Technische Universität München
TUM School of Natural Sciences

Experimental quantification of radial impurity transport in the tokamak pedestal

Tabea Katharina Gleiter

Vollständiger Abdruck der von der TUM School of Natural Sciences der Technischen Universität München zur Erlangung einer Doktorin der Naturwissenschaften (Dr. rer. nat.) genehmigten Dissertation.

Vorsitz: Prof. Dr. Nora Brambilla

Prüfende der Dissertation:
1. Prof. Dr. Ulrich Stroth
2. Prof. Dr. Eleonora Viezzer

Die Dissertation wurde am 24.01.2025 bei der Technischen Universität München eingereicht und durch die TUM School of Natural Sciences am 20.02.2025 angenommen.

Abstract

For the operation of magnetically confined fusion plasmas, it is essential to combine high confinement of energy in the plasma with tolerable stress on the vessel components caused by the exhaust power. Suitable impurity distributions are crucial for achieving this in future tokamak devices. In the plasma core, impurities are undesired because they limit the fusion performance. However, the metallic walls foreseen for reactors will introduce heavy impurities, and lighter species will need to be intentionally added to cool the plasma edge by radiation. Thus, the radial impurity transport must be well controlled. Of special relevance is the narrow edge region with steep plasma temperature and density gradients, known as pedestal, since it sets the boundary conditions for the impurity content in the plasma core.

Experimental assessments of impurity distributions cannot be directly transferred to other devices that exhibit different pedestal background plasma profiles. To predict the impurity behavior in larger and hotter reactors, it is therefore necessary to gain a solid understanding of the underlying physics governing radial impurity transport in the pedestal. However, the pedestal impurity dynamics in confinement regimes that are currently considered reactor-relevant are largely unexplored. This is because they naturally differ significantly in their plasma edge physics from the standard high-confinement mode (H-mode), as they need to avoid its large edge localized modes (ELMs), which will be detrimental in reactors.

This thesis contributes a new analysis routine to experimentally quantify the radial impurity transport in the pedestal of ASDEX Upgrade (AUG) discharges. It is in particular capable of separating the flux surface-averaged diffusion and convection, which together build the radial impurity flux, and overcomes the challenges posed by the steep pedestal gradients, yielding profiles with unprecedented radial resolution. Comparing the corresponding transport coefficients to theoretical simulations allows for conclusions on the amount of collisional, also termed neoclassical, and turbulent transport.

The method is based on observations of spectral line radiation from ≥ 2 charge stages of an impurity in stationary plasmas, using a tailored setup of the charge-exchange recombination spectroscopy (CXRS). From this data, the transport coefficients are derived in an inverse inference procedure, which employs a complex forward model including a diffusive-convective transport solver. To provide a robust uncertainty quantification, the full probability distribution of the free parameters is inferred with a Bayesian sampling algorithm, which can handle high-dimensional, non-Gaussian error statistics.

After thorough tests with synthetic data, the novel framework has been successfully applied to infer pedestal neon transport in a series of AUG discharges. Investigations of H-mode phases between large ELMs confirm the strong suppression of impurity turbulence by the edge transport barrier (ETB) in the pedestal. Moreover, the ELMs are qualitatively shown to act as a diffusive process. Comparative results for a low confinement discharge (L-mode) show significant turbulent transport in the pedestal. The thesis further focuses on promising confinement regimes without large ELMs, namely the quasi-continuous exhaust (QCE) regime and the enhanced D-alpha (D_α) (EDA) H-mode. Both are characterized by different plasma edge fluctuations that are assumed to impact the impurity transport. The presented experimental results reveal especially substantial turbulent diffusion in the QCE pedestal, which is less evident in the studied EDA H-mode discharge, where instead the neoclassical transport is altered. These properties mitigate the impurity density peaking in the pedestal for both regimes.

Zusammenfassung

Für den Betrieb von magnetisch eingeschlossenen Fusionsplasmen ist es essenziell, einen hohen Energieeinschluss im Plasma mit einer tolerablen Belastung der Gefäßkomponenten durch die abgegebene Leistung zu kombinieren. Geeignete Verunreinigungsverteilungen sind entscheidend, um dies in zukünftigen Tokamak-Anlagen zu erreichen. Im Plasmakern sind Verunreinigungen unerwünscht, da sie die Fusionsleistung einschränken. Die für Reaktoren vorgesehenen Metallwände werden jedoch schwere Verunreinigungen einbringen, und leichtere Spezies werden absichtlich hinzugefügt werden müssen, um den Plasmarand durch Strahlung zu kühlen. Daher muss der radiale Verunreinigungstransport gut kontrolliert werden. Von besonderer Bedeutung ist der schmale Randbereich mit steilen Temperatur- und Dichtegradienten im Plasma, bekannt als Pedestal, da er die Randbedingungen für den Verunreinigungsgehalt im Plasmakern festlegt.

Experimentelle Begutachtungen von Verunreinigungsverteilungen können nicht direkt auf andere Maschinen übertragen werden, die andere Hintergrundplasmaprofile im Pedestal aufweisen. Um das Verhalten von Verunreinigungen in größeren und heißeren Reaktoren vorherzusagen, ist es daher notwendig, ein solides Verständnis der zugrundeliegenden Physik zu erlangen, die den radialen Verunreinigungstransport im Pedestal bestimmt. Die Dynamik der Verunreinigungen im Pedestal der Einschlussregime, die derzeit als reaktorrelevant angesehenen werden, ist jedoch weitgehend unerforscht. Dies liegt daran, dass sie sich in ihrer Plasmarandphysik deutlich vom üblichen Szenario mit hohem Einschluss (H-Mode) unterscheiden, da sie dessen große lokalisierte Randmoden (ELMs) vermeiden müssen, die in Reaktoren schädigend sein werden.

In dieser Arbeit wird eine neue Analyseroutine zur experimentellen Quantifizierung des radialen Verunreinigungstransports im Pedestal von ASDEX Upgrade (AUG)-Entladungen vorgestellt. Diese ist insbesondere in der Lage, die Flussflächen-gemittelte Diffusion und Konvektion zu trennen, die zusammen den radialen Verunreinigungsfluss bilden, und überwindet die Herausforderungen, die sich durch die steilen Gradienten im Pedestal ergeben, sodass sie Profile mit einer beispiellosen radialen Auflösung liefert. Der Vergleich der entsprechenden Transportkoeffizienten mit theoretischen Simulationen erlaubt Rückschlüsse auf den Anteil des stoßbedingten, auch neoklassischen, und des turbulenten Transports.

Die Methode basiert auf Beobachtungen von Spektrallinienstrahlung von ≥ 2 Ladungsstufen einer Verunreinigung in stationären Plasmen, unter Verwendung einer angepassten Konfiguration der Ladungsaustausch-Spektroskopie (CXRS). Aus diesen Daten werden die Transportkoeffizienten in einem inversen Inferenzverfahren abgeleitet, welches ein komplexes Vorwärtsmodell verwendet, das einen diffusiv-konvektiven Transportcode einschließt. Um eine robuste Quantifizierung der Unsicherheit zu liefern, wird die vollständige Wahrscheinlichkeitsverteilung der freien Parameter mit einem bayesianischen Sampling-Algorithmus hergeleitet, der mit hochdimensionalen, nicht-gaußschen Fehlerstatistiken umgehen kann.

Nach gründlichen Tests mit synthetischen Daten wurde das neue Framework erfolgreich angewandt, um den Neontransport im Pedestal einer Reihe von AUG-Entladungen zu erschließen. Untersuchungen von H-Moden-Phasen zwischen großen ELMs bestätigen die starke Unterdrückung von Verunreinigungsturbulenz durch die Randtransportbarriere im Pedestal. Außerdem wird qualitativ gezeigt, dass die ELMs als Diffusionsprozess wirken. Vergleichende Ergebnisse für ein Szenario mit geringem Einschluss (L-mode) zeigen einen erheblichen turbulenten Transport im Pedestal. Die Arbeit fokussiert sich außerdem auf vielversprechende Einschlussregime ohne große ELMs, namentlich das sogenannte QCE Regime und die EDA H-Mode. Beide sind

durch unterschiedliche Fluktuationen am Plasmarand gekennzeichnet, von denen angenommen wird, dass sie den Verunreinigungstransport beeinflussen. Die vorgestellten experimentellen Ergebnisse offenbaren vor allem wesentliche turbulente Diffusion im QCE-Pedestal, welche in der untersuchten EDA H-Moden-Entladung weniger deutlich ist, in der stattdessen der neoklassische Transport verändert ist. Diese Eigenschaften mildern den Anstieg der Verunreinigungsdichte im Pedestal für beide Regime.

Contents

List of Figures

List of Tables

1 Introduction

The realization of viable nuclear fusion power generation on Earth will tap a climate-neutral and inherently base-load capable energy source that does not entail large risks or difficulties due to radiotoxicity and is purely based on abundantly available resources. In short, "fusion has advantages that ensure sustainability, safety and security of supply" (Oost, 2023, preface). Since fusion is not yet commercially available, it is essential that renewable energy sources are advanced politically and technologically to mitigate climate change in the short term. In the long term, however, nuclear fusion has the potential to overcome many of the challenges emerging from the transformation of the energy system. Most evidently, it will strongly facilitate the reliable provision of base-load electricity without accepting the problems that come with nuclear fission technologies.

1.1 Nuclear fusion research

If not indicated otherwise, the following remarks on nuclear fusion research are based on a synthesis of the references Stroth, 2018, Dux, 2010, Wesson, 2011, Oost, 2023, and Zohm, 2019. The interested reader is referred to these sources for further information.

The fusion of light nuclei into nuclei with enhanced binding energy per nucleon releases energy equivalent to the mass difference between the fusion reactants and products. However, the repulsive Coulomb force between nuclei necessitates overcoming an energy barrier before the short-ranged nuclear forces can effectuate the fusion. This can be achieved by collisions with high kinetic energies and is fostered by quantum tunneling. Given the much higher cross-sections for Coulomb collisions at the energies typically involved in fusion experiments, numerous collisions are nevertheless necessary to reach significant fusion probabilities. Consequently, in addition to the acceleration of the particles, efficient confinement with small energy loss is required. In a confined system, the fusion reaction rate of two species with densities n_1 and n_2 per volume and time is determined by $f_{\mathrm{fus}} = n_1 n_2 \langle \sigma u \rangle$. The rate coefficient

$$\langle \sigma u \rangle = \int \int \sigma u \, f(\vec{v_1}) f(\vec{v_2}) \, \mathrm{d}^3 v_1 \mathrm{d}^3 v_2 \tag{1.1}$$

represents the average of the product of the cross-section σ and the relative velocity $u = |\vec{v_2} - \vec{v_1}|$ over the velocity distributions of the species, $f(\vec{v_1})$ and $f(\vec{v_2})$. In thermal equilibrium, i.e., given a Maxwellian velocity distribution, the reaction parameter $\langle \sigma u \rangle$ is solely temperature dependent for a given fusion reaction.

The proton fusion reactions that dominate the Sun's energy production have very low cross-sections. These are partly compensated by the high gravitational pressure in the Sun's core, which effectuates especially high densities, but the reaction rate is still comparably low. Thus, the Sun's fusion reactions are not viable for a fusion reactor on Earth. A fusion reaction with orders of magnitude higher cross-sections, which allows significant fusion rates at feasible temperatures (around $15\,\mathrm{keV}$) and densities (around $10^{20}\,\mathrm{m}^{-3}$), is the deuterium ($^2_1\mathrm{D}$) - tritium ($^3_1\mathrm{T}$) reaction $^2_1\mathrm{D} + {}^3_1\mathrm{T} \rightarrow {}^4_2\mathrm{He}\,(3.5\,\mathrm{MeV}) + {}^1_0\mathrm{n}\,(14.1\,\mathrm{MeV})$, which provides $E_{\mathrm{fus}} = 17.6\,\mathrm{MeV}$ of released energy per fusion reaction. This is the most promising reaction for civil energy production. Deuterium and tritium are readily available resources, found in seawater and bred from lithium, which is abundant in the Earth's crust. Moreover, a deuterium-tritium fusion power plant will be intrinsically safe from uncontrolled runaway reactions due to the small amount of fuel in the reactor and the absence of any neutron-amplifying reaction. Also, the resulting radiotoxicity will not require permanent waste disposal on a geological time span. It arises mainly from the tritium, which has a short half-life of 12.3 years, and from some materials activated by the fast neutrons born from the fusion reaction.

Due to the required high temperatures in a fusion reactor, a simple confinement of the fuels by solid walls is not feasible. However, a long-researched concept, which is in the focus of this thesis, is magnetic confinement fusion. It uses the fact that the matter is in plasma state, i.e., ionized, at the relevant temperatures, and thus can be contained in a magnetic field cage. In this concept, the energetic alpha-particle ($^4_2$He) born from the fusion reaction remains confined due to its charge and reheats the plasma via collisions. The neutron ($^1_0$n) instead leaves the plasma, and its kinetic energy can be harvested for electricity generation.

An important figure for research is the Q-factor, $Q = \frac{P_{\mathrm{fus}}}{P_{\mathrm{heat}}}$. It is the ratio of the fusion power $P_{\mathrm{fus}} = \int f_{\mathrm{fus}} E_{\mathrm{fus}} \, \mathrm{d}V$ generated in the plasma with volume V and the external heating power P_{heat}, which is required to compensate the loss P_{loss} from the plasma if it is not fully balanced by heating due to collisions with the alpha particles. The loss of thermal energy W in a plasma is due to transport processes, namely collisions, turbulence, and macroscopic instabilities, which are summarized in a global energy confinement time τ_{E}. Additional radiation losses depend crucially on the concentration of impurities, that is, other elements than the fusion main ions, which have higher atomic numbers. They contribute to the bremsstrahlung losses due to their stronger deflection of electrons and to the line and recombination radiation due to their higher full ionization potential. Thus,

$$P_{\mathrm{loss}} = P_{\mathrm{transp}} + P_{\mathrm{rad}} = \frac{W}{\tau_{\mathrm{E}}} + \int c_{\mathrm{Br}} n_{\mathrm{e}}^2 Z_{\mathrm{eff}} \sqrt{T} \, \mathrm{d}V + P_{\mathrm{line}} + P_{\mathrm{recomb}}, \tag{1.2}$$

where the bremsstrahlung's constant is given by $c_{\mathrm{Br}} = 1.66 \cdot 10^{-38} \, \mathrm{W\,m^3\,eV^{-\frac{1}{2}}}$, n_{e} signifies the electron density and T is the product of the temperature in Kelvin multiplied by the Boltzmann constant k_{B}, yielding the temperature in energy units. Z_{eff} is the effective plasma charge as a measure for the plasma dilution by impurities, calculated from the densities n_{i} and charges Z_{i} of all ion species in the plasma:

$$Z_{\mathrm{eff}} = \frac{\sum_i n_{\mathrm{i}} Z_{\mathrm{i}}^2}{n_{\mathrm{e}}} \tag{1.3}$$

Therefore, the main parameters that determine the performance of a fusion reactor are the plasma density and temperature, the energy confinement time, and the impurity content. $Q = 1$ is known as the scientific break-even, but a future reactor will require much higher values of $Q \gtrsim 30$ (EUROfusion, 2024b) in order to compensate for additional losses in the system and to operate more efficiently in a burning plasma regime where much of the plasma heating is self-sustained by the alpha particles.

Charged particles can move freely along magnetic field lines but not perpendicular to them due to deflection by the Lorentz force. It was found that the best magnetic confinement is reached in a torus-shaped configuration using a magnetic field with both a toroidal and a poloidal component, which produces helically twisted field lines. There are two main concepts for establishing such a field: the tokamak and the stellarator. The tokamak (Russian for 'toroidal chamber with magnetic coils') is in the focus of this thesis and schematically sketched in figure 1.1. Its toroidal field is effectuated by planar coils and the poloidal component is induced by a toroidally flowing plasma current I_{p}, which in turn is induced by a linear current ramp in a central solenoid transformer coil. Given the toroidal angle ϕ and the poloidal angle θ, the twisting of the field lines can be described with the relation

$$q_\mathrm{s} = \frac{\mathrm{d}\phi}{\mathrm{d}\theta} = \frac{rB_\mathrm{T}}{RB_\mathrm{P}}, \tag{1.4}$$

where r signifies the minor radius from the magnetic axis, R the major radius from the tokamak center, B_T the toroidal magnetic field strength, and B_P the poloidal magnetic field strength. q_s is also known as safety factor as it impacts the plasma stability.

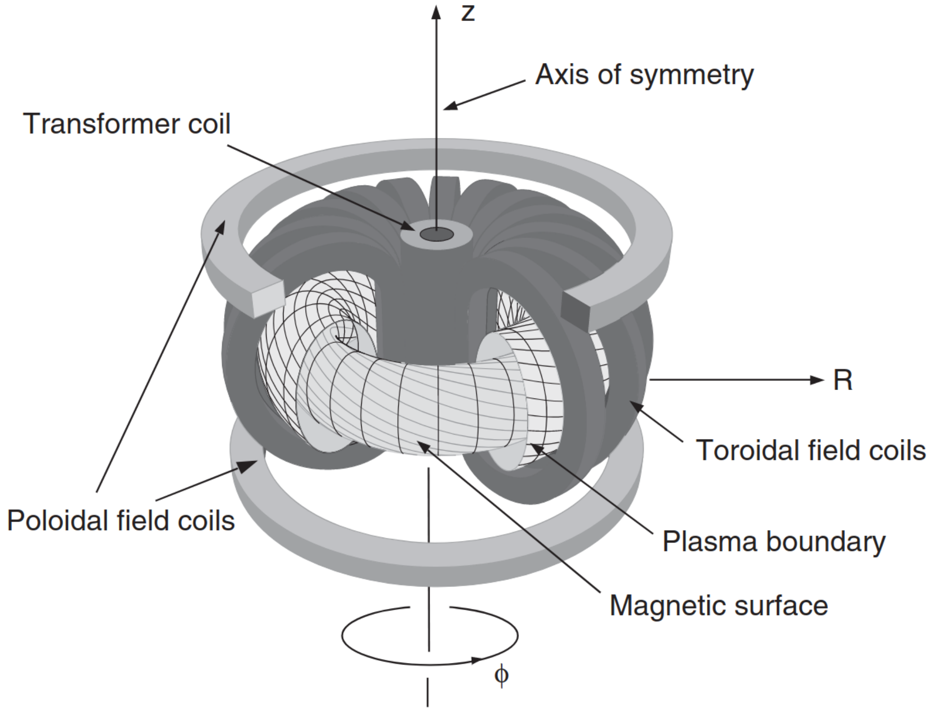

Figure 1.1: Schematic of a tokamak. The toroidal magnetic field coils generate the toroidal magnetic field component, and a linearly ramped current in the transformer coil induces a loop voltage, which generates the toroidal plasma current that induces the poloidal magnetic field component. The poloidal field coils add a vertical magnetic field, which is needed for shaping and stabilization of the plasma. The structure of the plasma edge is not shown in detail but simplified as plasma boundary. Figure reproduced from Zohm, 2014.

In equilibrium, the pressure gradient in the tokamak is balanced by the magnetic field according to the magnetohydrodynamic (MHD) force balance

$$\nabla p = \vec{j} \times \vec{B}, \tag{1.5}$$

where p is the kinetic pressure, $\vec{j}$ the plasma current density and $\vec{B}$ the total magnetic field. MHD describes the plasma as a single conducting fluid in order to study its macroscopic behavior. The force balance shows that the magnetic field lines establish nested magnetic surfaces with constant pressure. These flux surfaces are labeled according to their enclosed poloidal magnetic flux ψ with a normalized radial coordinate

$$\rho_\mathrm{pol} = \sqrt{\frac{\psi - \psi_\mathrm{axis}}{\psi_\mathrm{separatrix} - \psi_\mathrm{axis}}}, \tag{1.6}$$

reaching from 0 on the magnetic axis to 1 at the last closed flux surface, called the separatrix.

With respect to stellarators, which establish the full field via stationary currents in sophisticated 3D-shaped coils, tokamaks are more prone to current-driven MHD instabilities and have to deal with possible plasma current disruptions and their intrinsic pulsed operation. However, due to their better accessible axisymmetric physics and long research history, starting with the works of Dolgov-Saveliev et al., 1958 in the mid-20th century, the energy and particle confinement and power exhaust concepts are nowadays more mature. Detailed information on many facets of tokamaks can be found in Wesson, 2011.

Several tokamak devices have so far demonstrated the feasibility to generate relevant fusion rates, the record produced energy being 69 MJ and the record Q-factor 0.67, both achieved at the so far largest tokamak, the Joint European Torus (JET) (EUROfusion, 2024a; EUROfusion, 2024c). However, getting to reactor-relevant Q-factors necessitates a further improvement in energy confinement to reach τ_{E} in the order of a few seconds. With the currently available confinement regimes, this can be achieved along two major pathways. Either the torus volume is expanded by increasing the major radius R_0, which is the distance of the magnetic axis without plasma from the tokamak center. Here, changes in the aspect ratio, that is, the ratio of R_0 to the minor radius a, which describes half the horizontal diameter of the poloidal vessel cross-section, are not considered. Alternatively, the magnetic field strength B can be increased.

Following the first path, a new tokamak, the International Thermonuclear Experimental Reactor (ITER), is currently under construction with envisaged $R_0 = 6.2\,\mathrm{m}$ and $B = 5.2\,\mathrm{T}$. This is more than a doubling of R_0 and also a significant increase in B with respect to JET and is envisaged to allow the demonstration of a burning tokamak plasma with $Q = 10$. Subsequently, the even larger demonstration power plant DEMO is planned. The second path, building compact but high-field tokamaks, has become accessible only recently due to advances in high-temperature superconductor technology, such as rare earth barium copper oxide (REBCO) tapes, which have a higher critical current density. It is pursued mainly by the company Commonwealth Fusion Systems (CFS) in collaboration with the Massachusetts Institute for Technology (MIT) in their tokamak project ARC ('Affordable, Robust, Compact') and its demonstration predecessor SPARC ('Soonest/Smallest Possible ARC') (cf. Creely et al., 2020; Rodriguez-Fernandez et al., 2022; Sorbom et al., 2015; Kuang et al., 2018), which is currently under construction,.

So far, however, no devices with reactor-like R_0 or B are yet operational, such that fusion research has to rely on smaller experiments to address the remaining engineering and physics challenges. The latter include mainly improvements in core-edge integration, meaning the combination of high energy confinement in the core with a power exhaust solution that respects target strain thresholds. Moreover, a general aim of tokamak research is to resolve the weaknesses of tokamaks, thus improving the non-inductive current drive efficiency, avoiding current disruptions, and mitigating current-driven MHD instabilities.

1.2 The ASDEX Upgrade tokamak

The ASDEX (Axially Symmetric Divertor EXperiment) Upgrade, or AUG, tokamak is located at the Max Planck Institute for Plasma Physics in Garching, Germany. Currently, it is the operating device with the most similar configuration to the planned ITER tokamak. This includes a tungsten (W) wall and a very similar coil and vessel configuration. As such, it was designated the current “flagship facility” of the EUROfusion tokamak program in the most recent facilities

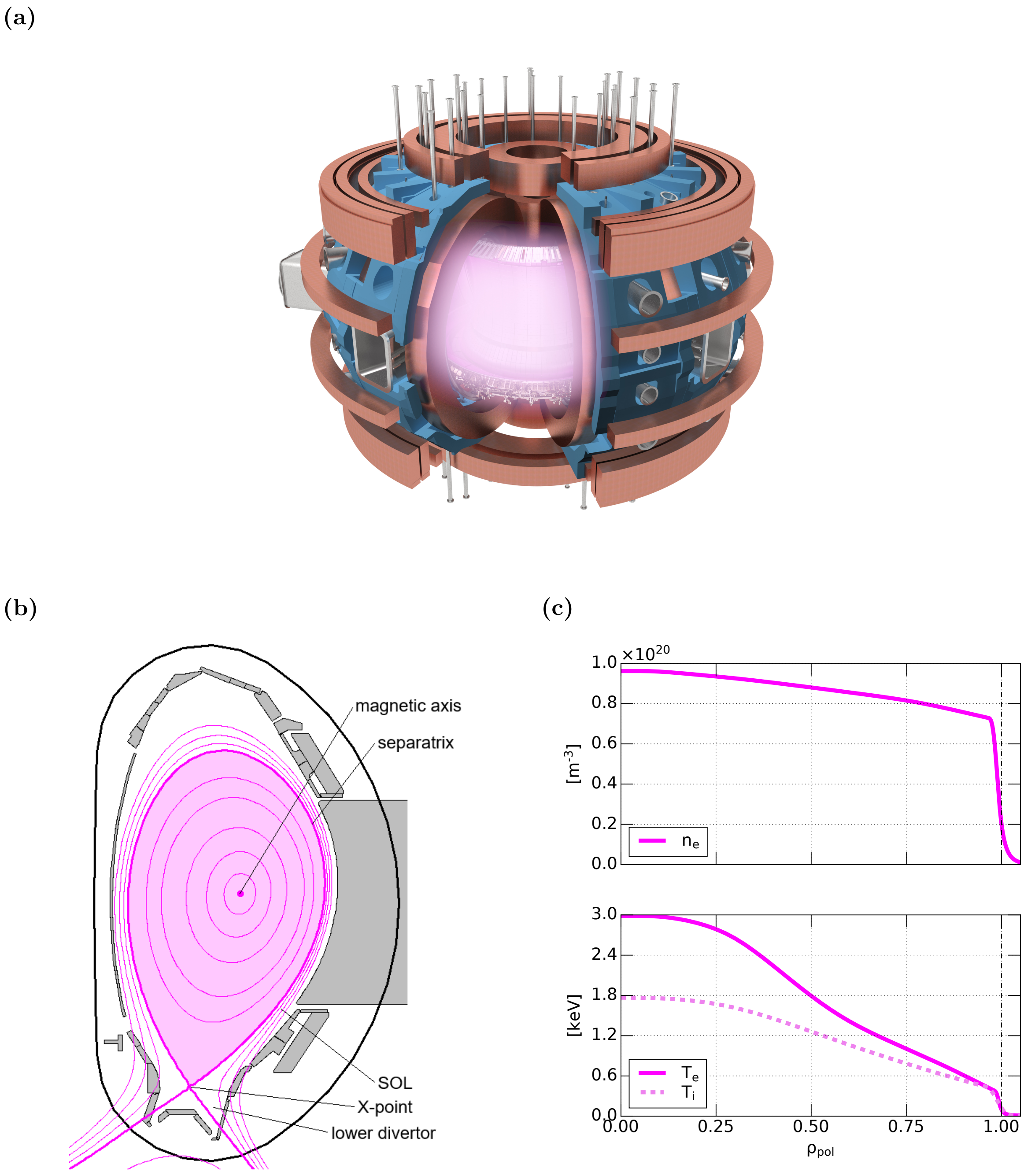

Figure 1.2: The schematic of AUG (a) shows the toroidal magnetic field coils, the transformer coil and the poloidal magnetic field coils (brown), the support structure for the coils (blue), and the vessel with ports and divertors (grey) filled with plasma (pink). The poloidal cross-section (b) shows a typical AUG plasma shape (here AUG #39086, 5.885 s) with the confined plasma with closed field lines around the magnetic axis, the separatrix as last closed flux surface featuring the X-point and the scrape-off layer (SOL) with open field lines to the lower divertor. The corresponding kinetic profiles (c) show the separation of the confined plasma into the core with small gradients, in particular in density, and the narrow pedestal with steep edge gradients. Schematic of AUG (a) reproduced from IPP, 2024a.

review (IPP, 2024b). Figure 1.2 shows a schematic of AUG together with the poloidal cross-section and kinetic profiles, of the electron density and the electron and ion temperatures T_e and T_i, for a typical plasma. The steep edge gradients define the narrow region known as pedestal. Important parameters are stated in table 1.1. As for all currently operating tokamaks worldwide, the experiments at AUG are executed without tritium to avoid the nuclear handling. No significant fusion energy is therefore produced. However, studies on the plasma confinement are done with pure deuterium (D), and isotope or mass effects can be investigated using hydrogen (H) or helium (He).

Parameter	Value
Major radius R_0	1.65 m
Minor radius a	0.5 m
Plasma volume	$\sim 14\,\mathrm{m}^3$
Plasma current I_p	≤ 1.4 MA
Magnetic field strength B	≤ 3.2 T
Available heating power	20 MW NBI, 6 MW ECRH, 5 MW ICRF
Fuel amount and species	~ 3 mg; D, sometimes He or H
First wall material	W
Available impurity species	He, N, Ne, Ar, Kr, Xe
Typical core electron density n_e	$10^{20}\,\mathrm{m}^{-3}$
Typical core electron temperature T_e	3–10 keV
Typical energy confinement time τ_E	0.2 s

Table 1.1: AUG machine parameters. The information is retrieved from IPP, 2023, Zohm et al., 2024, and private communication.

AUG is equipped with an upper and a lower divertor, which are special vessel components tailored for power and particle exhaust. When operated in a divertor configuration, the plasma is shaped such that the open field lines end in one or both of the divertors where the plasma-wall interaction takes place and the exhaust gas is pumped spatially well separated from the confined plasma. In the divertors, the magnetic field lines are expanded to reduce heat and particle fluxes, and the energies of incoming particles are reduced by atomic interactions with added ('seed') impurities and neutral gas.

During an experimental campaign, the vessel remains in an ultra-high vacuum throughout several months. On experimental days, individual discharges with a maximum pulse length of 10 s are executed. A longer duration is not feasible due to the heat-up of the copper coils. For the heating of the plasma, 3 options are available. Neutral beam injection (NBI) transfers the kinetic energy of fast injected neutrals to the plasma, electron cyclotron resonance heating (ECRH) heats the electrons via injected microwaves at their gyrofrequency, and ion cyclotron resonance frequency (ICRF) heating injects electromagnetic waves in the radio frequency range to heat the ions, which have a lower gyrofrequency due to their higher mass. The plasma fueling with the main species and possibly requested impurities is performed via gas valves in the divertor or at the midplane, or via injection of frozen pellets.

1.3 The role of impurities and their transport in tokamaks

Core-edge integration with tailored impurity distributions As mentioned above, a major remaining physics challenge in nuclear fusion research is the core-edge integration. This means that a long energy confinement time in the core must be combined with a power exhaust solution that prevents overheating of the plasma-facing components (PFCs). In current research devices, the first wall is typically not at significant risk, at least when some basic safety measures are applied, as described for AUG by Kallenbach et al., 2010. However, reactors will be hotter and will therefore require more sophisticated active moderation of the stationary power load and minimization of transient peak power fluxes. Demonstrating successful core-edge integration is therefore also an important objective to be achieved in the fusion power operation phase of ITER (Campbell et al., 2024). Specifically, the steady-state power load in the divertor should be kept below the engineering design point of $10\,\mathrm{MW\,m^{-2}}$ and the short-term power flux must not exceed $20\,\mathrm{MW\,m^{-2}}$ (ITER, 2024).

In order to achieve the first objective – namely a tolerable stationary power load on the PFCs in a tokamak reactor – a significant part of the outgoing power will need to be radiated at the plasma edge. Radiation distributes the power over an extended area of the first wall and thus reduces the power load on the divertor target plates. Ultimately, it is an important actuator to access a divertor condition with a strong pressure drop in front of the target, which minimizes the interaction between the plasma and the divertor target plates and is known as divertor detachment (Matthews, 1995; Krasheninnikov et al., 2017). Equation 1.2 shows that the radiative energy loss depends on the impurity content. Therefore, effective power exhaust in a reactor will require impurity radiation in the divertor, the SOL, and possibly even the confined plasma edge. For example, ITER is expected to operate with mainly divertor and SOL impurity radiation due to its moderate heating power, whereas DEMO is likely to rely on additional impurity radiation from the edge of the confined plasma (Kallenbach et al., 2013).

However, while impurity radiation is favorable in the outer plasma region, the allowable impurity content in the plasma center is limited. This is because impurity radiation degrades the energy confinement, and fuel dilution reduces the fusion rate. The former is particularly critical for impurities with high atomic number Z as they are not fully ionized at core temperatures, whereas the latter also restricts the concentration of low-Z impurities (Pütterich et al., 2019). Dealing with these competing demands, set by the impurity limits for plasma core performance and the required power dissipation pattern at the plasma edge, necessitates carefully balanced impurity distributions.

Impurity sources in tokamaks Impurities in a tokamak can arise from intrinsic sources, namely from the fusion process itself producing He, and from physical sputtering or chemical erosion from the first wall. Due to its very low Z, He does not substantially add to impurity radiation, but due to its strong source in the plasma center, it is a relevant contributor to fuel dilution. Efficient He removal from the plasma is therefore subject to ongoing research, see, e.g., Zito et al., 2023. Future devices are planned with metallic walls owing to several beneficial properties, namely small tritium retention, high stability against neutron irradiation, and small erosion rates (Neu et al., 2013). A promising candidate material is W, which is used for the AUG PFCs since 2007 and is also foreseen for the ITER first wall (Loarte et al., 2024). It was shown at AUG that a W wall reduces the intrinsic impurity content in the plasma, in particular when conditioned with a thin boron layer in a so-called boronization (Neu et al., 2013). However, the tolerable W core concentration is also very low since it is a strong radiator. Therefore, sputtering from the wall must be avoided.

For customized radiative power exhaust, additional extrinsic impurity seeding, usually via gas puffing or pellet injection, is required. Candidate impurities are in particular xenon (Xe), krypton (Kr), argon (Ar), neon (Ne), or molecular nitrogen (N_2) as they are suitable for puffing, chemically inert, and strongly recycling from the wall, which avoids co-deposition of tritium (Kallenbach et al., 2011). Their influences on the plasma and the PFCs are reviewed in Kallenbach et al., 2011. Importantly, they have a complex impact on the intrinsic impurity content, as sputtering of high-Z first wall materials is on the one hand mainly caused by impurities, but on the other hand also reduced due to the cooling by impurity radiation.

Importance of radial impurity transport in the pedestal In order to assess the influence of impurities on the plasma performance, it is essential to consider both the radiative properties and the density distributions of all charge stages of the various impurity species that may be present. Studies based solely on atomic data can provide boundary conditions for future reactors, such as measures for the permissible W concentration in the core presented by Pütterich et al., 2019, but cannot predict whether these constraints will be satisfied. Similarly, experimental studies on current devices can only give indications. For example, Kallenbach et al., 2012 and Kallenbach et al., 2013 point to the need to involve different seeding species with increasing Z for radiative cooling of the divertor, the SOL, and the edge of the confined plasma, and Kallenbach et al., 2022 and Lang et al., 2023 demonstrate a faster response and enhanced radiative efficiency for cooling the pedestal when injecting the seed species via impurity doped pellets, which could help to counteract transient divertor re-attachment. However, these experimental results cannot necessarily be directly scaled to future reactors.

Accurate predictions must instead rely on physics-based modeling of the impurity density distributions and the charge stage balances. In order to fill the gaps in the required physical understanding, priorities are the investigation of impurity behavior in the divertor, e.g., addressed in Makarov et al., 2024, and the comprehension of the relationship between the impurity content in the confined plasma and in the divertor. A simple empirical scaling for impurity compression and enrichment, that is, the ratios between the density or concentration of neutral impurity in the divertor with respect to impurity ions in the core, has been derived from AUG data by Kallenbach et al., 2024. Yet, these quantities are also not easily scalable to other devices. They depend critically on the radial impurity transport in the core-edge connecting pedestal, which needs to be thoroughly understood.

Impurity transport coefficients The transport of an impurity species acts on its charge stage densities $n_{\mathrm{I},Z}$ via the continuity equation

$$\frac{\partial n_{\mathrm{I},Z}}{\partial t} = -\nabla \cdot \vec{\Gamma}_{\mathrm{I},Z} + Q_{\mathrm{I},Z}, \tag{1.7}$$

where t is the time, $\vec{\Gamma}_{\mathrm{I},Z}$ represents the flux density of the impurity charge stage, which is determined by transport processes, and $Q_{\mathrm{I},Z}$ indicates the source term. Here, Z does not indicate the atomic number but the charge of the atom, i.e., the ionization stage. This double use is conventional in the literature and is therefore adopted here. The equations for all charge stages yield a coupled system since the source is determined by ionization and recombination processes from neighboring charge stages, except for the neutral one, which is released by the above-mentioned intrinsic or extrinsic sources. Since the ionization and recombination equilibration time can be longer than typical transport time scales, not only the total density of an impurity species but also its charge stage balance can be affected by the transport.

In the confined plasma, thus also in the pedestal, it is mainly the component of the transport directed perpendicular to the flux surfaces that is of interest, because the transport parallel to the magnetic field is typically fast enough to avoid large impurity density asymmetries on a flux surface. Thus, a radial coordinate r is defined, which is constant on a flux surface. Together with the angles ϕ and θ, it forms a complete set of coordinates in the torus. The transport processes defining the radial flux density can then be parameterized into a diffusive and a convective component with flux surface-averaged transport coefficients D and v, such that

$$\Gamma^r_{\mathrm{I},Z} = -D\frac{\partial n_{\mathrm{I},Z}}{\partial r} + v n_{\mathrm{I},Z}. \tag{1.8}$$

Thus, the flux surface-averaged radial continuity equation reads

$$\frac{\partial n_{\mathrm{I},Z}}{\partial t} = \frac{1}{r}\frac{\partial}{\partial r} r\left(D\frac{\partial n_{\mathrm{I},Z}}{\partial r} - v n_{\mathrm{I},Z}\right) + Q_{\mathrm{I},Z}. \tag{1.9}$$

In a steady state and without a neutral particle source, which usually applies to the confined plasma, the flux density of the total impurity, i.e., summed over all charge stages, must vanish. This yields the relation for the inverse of the gradient scale length $L_{n_{\mathrm{I,tot}}}$ of the total impurity density $n_{\mathrm{I,tot}}$:

$$\frac{v}{D} = \frac{1}{n_{\mathrm{I,tot}}}\frac{\partial n_{\mathrm{I,tot}}}{\partial r} = \frac{\partial \ln n_{\mathrm{I,tot}}}{\partial r} = \frac{1}{L_{n_{\mathrm{I,tot}}}}. \tag{1.10}$$

It shows that negative/positive values of convection, i.e., inward/outward drift velocities, lead to peaked/hollow density profiles of the total impurity, whereas diffusion always acts flattening on the profiles. Both diffusion and convection can be due to collisional, also termed neoclassical, and turbulent processes, the former setting the lower transport limit. A brief review of important impurity transport theory and in particular on these different transport processes contributing to diffusion and convection is provided in section 2.1.

It is important to quantify these underlying physical mechanisms in the pedestal based on experimental observations of D and v and their comparison with transport modeling. Only such knowledge allows the accurate scaling of impurity behavior in the pedestal to future reactors. This can be understood by the example of predictions for pedestal impurity transport in ITER when operated in the standard high-confinement regime (H-mode) (Dux et al., 2014; Dux et al., 2017) and observations in strongly heated JET plasmas (Field et al., 2022; Garcia et al., 2022). Here, the same underlying convection and diffusion mechanisms result in different phenomenological transport properties and impurity density distributions than typical in current devices due to different kinetic profiles of the background plasma. More simple assessments of impurity behavior, e.g., in terms of confinement times or density profiles, are not sufficient to predict or explain such effects.

Interest in H-modes without large ELMs So far, it has been discussed how to achieve a tolerable stationary power load on the PFCs via radiative cooling. However, the second objective introduced above has been neglected – namely to reduce transient peak power fluxes to the wall below the detrimental threshold. This is not possible by radiation, even with sophisticated impurity distributions, but rather requires the avoidance of MHD instabilities that endanger the first wall, in particular disruptions of the plasma current in the tokamak and large (type-I) edge-localized modes (ELMs). The former result in a loss of the total stored thermal and magnetic energy, whereas the latter are periodic relaxation events of the pedestal gradients, which occur in standard H-mode plasmas and flush energy and particles out of the confined plasma. Effective real-time disruption monitoring and control techniques are being developed for passive and active stabilization of disruptive modes (Strait et al., 2019). On the other hand, the development of an H-mode with either natural absence of large ELMs or compatibility with active ELM control techniques is inevitable. Good overviews of currently available promising candidate regimes are provided in Stroth, 2022 and Viezzer et al., 2023.

Whereas disruption avoidance is hardly related to impurity issues, the ELM characteristics of a regime and its impurity distribution mutually influence each other. ELMs can contribute to wall sputtering, in particular in case of high levels of light impurities in the plasma (Dux et al., 2009; Dux et al., 2011), and impurities can influence the pedestal stability (Beurskens et al., 2013; Dunne, 2016). Furthermore, and most importantly for this thesis, H-modes without large ELMs feature different MHD or turbulent instabilities at the plasma edge, which keep the pedestal stable but also influence the pedestal impurity transport. Thus, the radial impurity transport in the pedestal must be studied individually for the specific operational regimes to assess their compatibility with a metal wall, and with impurity seeding for edge radiative cooling and divertor detachment. As a side-effect, a better understanding of impurity transport in these regimes could also further the understanding of their general pedestal physics. A brief review of the standard H-mode, pedestal stability, and the current state of research on the most promising ELM-free, small-ELM, and ELM-suppressed or -mitigated regimes is provided in section 2.2.

Summary In summary, knowledge of the radial impurity transport, in particular in the core-edge connecting pedestal, is important for predicting the performance of reactor plasmas. It influences the choice of the first wall material and conditioning, the impurity seeding scheme, consisting of the species, amount, and method of extrinsic injection, and the operation scenario of a future tokamak reactor. For all regimes considered, experimental quantification of the transport in terms of diffusion and convection and its physical understanding by comparison with modeling is crucial.

1.4 Previous knowledge

Core impurity transport bounded by the pedestal There have been numerous studies on core impurity transport in the past years, such that this matter has by now reached a high level of understanding. A rather recent detailed review is provided in Angioni, 2021. In current devices, the transport of impurities in the core is governed by the balance between turbulent diffusion and neoclassical inward convection, which scales linearly with Z and thus becomes particularly relevant for high-Z elements. If the neoclassical transport is dominant, impurities may accumulate, meaning that they exhibit a stronger density peaking than the background plasma. This can typically be prevented by central wave heating of electrons or ions, the effects of which have been thoroughly investigated experimentally (Dux et al., 2003; Angioni et al., 2017; Sertoli et al., 2017; Odstrčil et al., 2020) and recently successfully modeled (Fajardo et al., 2024), revealing changes in the impurity transport coefficients.

In future reactor-like devices, however, the conditions will be more beneficial from the outset, because of lower collision frequencies, measured as collisionalities, in the hotter core, as well as a reduction in plasma rotation and central main ion source due to the minor role of NBI heating with respect to ECRH heating. Integrated modeling predictions for ITER using these constraints indicate that turbulence will dominate impurity transport throughout the plasma core, thus preventing impurity accumulation and yielding relatively flat impurity density profiles (Fajardo et al., 2024). Therefore, the impurity content in the core will be largely determined by the boundary impurity density at the pedestal top, which emphasizes the crucial role of impurity transport in the pedestal.

Pedestal impurity transport in type-I ELMy H-modes Yet, impurity transport studies specifically targeting the pedestal are rare. The most detailed understanding is available for H-mode plasmas with type-I ELMs. Already shortly after the discovery of the H-mode, it was proposed that the pedestal impurity transport is close to the neoclassical lower limit between ELMs, explaining the higher impurity confinement times compared to the low confinement regime (L-mode), whereas the ELMs themselves were observed to have a screening effect on impurities (ASDEX Team, 1989). Experimental investigations in several devices have since supported this hypothesis, with the most comprehensive study of pedestal impurity transport coefficients presented by Pütterich et al., 2011. In agreement with results from the tokamaks Alcator C-Mod, DIII-D, and JET, it proves for a set of different low- to medium-Z impurities in AUG H-modes the suppression of turbulent impurity transport by the edge transport barrier (ETB) that occurs during inter-ELM phases. Furthermore, it demonstrates the common approach to model ELMs as a diffusive process, namely with enhanced impurity diffusion above the neoclassical level in the pedestal during ELMs.

Given typical kinetic profiles in current devices, neoclassical transport normally causes inward convection of impurities in the plasma edge, which is balanced by impurity flushing during the ELMs. The impurity distribution is thus influenced by both the background plasma profiles and the ELM frequency and amplitude. However, as briefly touched upon above, due to the high core temperatures and high separatrix densities in ITER, the outward directed contribution to neoclassical convection, which driven by the temperature gradient, will dominate, leading to hollow edge impurity density profiles, in particular for high-Z impurities (Dux et al., 2014; Dux et al., 2017). Calculations with the extended MHD code `JOREK` have shown that, in this case, ELMs can drive impurities inward as they act diffusively (van Vugt et al., 2019). These reverse effects have been proven experimentally in plasmas using high heating power at JET (Garcia et al., 2022; Field et al., 2022).

Open questions Despite these findings, an extensive investigation of radial impurity transport in the type-I ELMy H-mode pedestal is still lacking. In particular, it should not impose coarse parameterizations on the transport coefficient profiles and furthermore comprise different collisionality ranges. Most experiments in current devices are conducted with much higher impurity collisionalities than expected in future hotter devices, especially at the pedestal top. For the ion heat transport, it has been shown at DIII-D that the pedestal may become more turbulent as the collisionality decreases (Haskey et al., 2022), and it is not clear whether the same applies to impurity transport.

Moreover, still poorly investigated is the pedestal impurity transport in the various operational regimes without large ELMs that are potential candidates for reactor operation. In the focus of this thesis are promising regimes in which large ELMs are naturally absent, in particular the so-called quasi-continuous exhaust (QCE) regime and the enhanced D-alpha (D_α) (EDA) H-mode. Both exhibit small MHD activity and turbulence in the plasma edge, which prevents type-I ELMs, while good energy confinement is maintained. Observations indicate that despite the absence of impurity flushing due to large ELMs, these regimes do not suffer from high-Z impurity accumulation and have shorter impurity confinement times (Faitsch et al., 2023; Pedersen et al., 2000). This suggests an altered impurity transport, probably related to the respective edge fluctuations.

Experimental studies have explored the integration of seed impurities with these regimes, examining the phenomenological impurity behavior such as the divertor enrichment (Kallenbach et al., 2020; Kallenbach et al., 2024). Yet, these findings are not directly scalable to other devices without an analysis of the pedestal impurity transport coefficients. There have only been very few investigations aimed at the determination of D and v, in particular Pedersen et al., 2000, indicating enhanced impurity diffusion in the EDA H-mode pedestal compared to typical ELM-free H-modes. However, these results are based on simplified assumptions about the transport coefficient profiles, which are unable to provide accurate profile shapes with the high resolution required for pedestal studies.

1.5 Experimental approaches

Experimental challenges The lack of experimental studies on radial impurity transport coefficients in the pedestal is mainly due to experimental challenges, in particular caused by the steep edge gradients in the background plasma and in the transport coefficient profiles. These conditions demand high spatial diagnostic resolution, precise alignment of different diagnostic data, and robust uncertainty quantification. Additionally, the changes in the ionization balance between the multiple charge stages, which are present in the pedestal on narrow spatial scales, and the proximity of the SOL with 3-D impurity density distributions can further complicate the task.

General approaches The transport coefficients can be estimated from observations of impurity densities if enough information is available such that the system of radial equations, stated in equation 1.9, is not highly underdetermined. The easiest approach is the so-called flux-gradient method. When measuring the time evolution of the total impurity density, the source term vanishes due to the sum over all charge stages, and a linear equation in D and v can be obtained:

$$\frac{1}{n_{\mathrm{I,tot}} r} \int_0^r \frac{\partial n_{\mathrm{I,tot}}}{\partial t} r' \mathrm{d}r' = \frac{1}{n_{\mathrm{I,tot}}} \frac{\partial n_{\mathrm{I,tot}}}{\partial r} D - v. \tag{1.11}$$

This approach is well suited for studies concerning low-Z impurities in the core, see, e.g., Bruhn et al., 2018 and McDermott et al., 2021, as they are fully stripped, thus only one charge stage has to be measured. The required impurity density time evolution can be induced by extrinsic perturbations, such as gas puff modulations, laser blow-off (LBO) or pellet injections, or also ICRF heating variations. However, the impurity must be in the trace limit, which is defined as

$$\frac{n_{\mathrm{I},Z} Z^2}{n_{\mathrm{D}^+}} \ll 1, \tag{1.12}$$

with the main ion density n_{D^+}. This condition ensures that impurities do not contribute much to any transport in the plasma (Angioni, 2021) and the impurity transport coefficients are therefore constant in time.

When there is more than one charge stage present, usually for high-Z impurities or in the pedestal, the derivation of D and v becomes more difficult since the system of coupled transport equations, as shown in equation 1.9, must be solved. Measuring only one charge stage and applying the flux-gradient method requires assumptions or modeling of the charge stage balance, as demonstrated by Sertoli et al., 2011. However, this is complicated by the fact that the charge stage balance is usually not in ionization equilibrium but is affected by the radial impurity transport. Furthermore, in the pedestal, it can be difficult to observe one charge stage that is prevalent throughout, as the charge stage balance changes significantly across this region.

Solving the system of transport equations analytically is only feasible in very simple cases (Dux, 2004). Generally a numerical diffusive-convective impurity transport solver, such as the codes `STRAHL` (Dux, 2021) or `Aurora` (Sciortino et al., 2021a; Sciortino, 2020), must be employed. These codes are forward modeling the impurity densities of all charge stages, focusing on the confined plasma without neutral impurity sources or losses, as they use rather simple models for the SOL and divertor. Their inputs consist of the magnetic equilibrium, the plasma background, the atomic rate coefficients for all relevant ionization and recombination processes, and specified D and v profiles. Thus, inferring the latter from experimental data which contains information on impurity densities, becomes an inverse problem.

A common simplification is to adopt equal transport coefficients for all prevailing charge stages, assuming them to be close in Z. Then, it is possible to constrain the problem if sufficient data on different charge stages is available. Typically, passive spectroscopic diagnostics, such as soft X-ray (SXR) or vacuum ultraviolet (VUV) measurements, are used to acquire information on multiple charge stages. The few studies of impurity transport in the pedestal presented above have used such approaches. However, since passive spectroscopic observations are line-integrated, tomographic inversion is needed to retrieve spatial information. The accuracy of the pedestal transport coefficient inferences, which are very sensitive to the radial resolution, is therefore limited.

Charge-stage method A different approach, called charge-stage method, is used here. It has not often been used so far, but overcomes the aforementioned problems in the pedestal. This method is based on stationary plasmas without modulation of the impurity content, such that the time derivative in equation 1.9 vanishes:

$$0 = \frac{1}{r}\frac{\partial}{\partial r} r \left(D \frac{\partial n_{\mathrm{I},Z}}{\partial r} - v n_{\mathrm{I},Z} \right) + Q_{\mathrm{I},Z}. \tag{1.13}$$

Thus, in the confined plasma without neutral impurity sources or losses, the unknowns in the system of equations are reduced to the densities of all charge stages plus the profiles of D and v, their number being equal to the number of equations + 2. Therefore, measurements of the density profiles of 2 charge stages are in principle sufficient to constrain the impurity transport coefficients.

Recent works, in particular Dux et al., 2020 and Nishizawa et al., 2022, have started to explore the charge-stage method, but it has not yet become widely established. Its use requires a specialized diagnostic setup that is capable of measuring accurate radial density profiles of ≥ 2 charge stages. Most suitable for this task is charge-exchange recombination spectroscopy (CXRS) because it can provide the highest radial resolution and data quality for impurity density observations. CXRS observes the radiance of specific line transitions, emitted by impurity ions after charge-exchange (CX) processes with NBI neutrals. The emission contains information about the density of the charge stage involved in the CX reaction, with good radial localization provided by the intersection between the line of sight (LOS) and the NBI path. Yet, to apply the charge-stage method, the CXRS system must possess a dense radial array of LOS in the pedestal and be capable of measuring multiple charge states, which usually requires the LOS to be distributed across different spectrometers.

With such a tailored diagnostic setup, very accurate inferences of pedestal impurity transport are possible with the charge-stage method. The CXRS setup already comes with high radial resolution and data quality by itself, but due to the steady-state condition, experimental techniques for further improvements are available. First, the trace limit condition is not imposed, as the transport coefficients cannot be altered by a time evolving impurity concentration. The stationary influence of impurities above the trace limit on the transport can be included in comparative theoretical simulations, such that accurate conclusions on the underlying transport mechanisms are still possible. This allows a higher impurity content to be established in order to obtain better signals, which can be particularly important at the pedestal foot where impurity densities are typically lowest. In addition, the data can be averaged over longer time spans. Therefore, NBI dips, i.e., short off-periods, can be used to separate passive contributions to the spectral lines, which improves the data quality, and finally, radial plasma sweeps, as suggested in Viezzer et al., 2012, can further improve the spatial resolution.

Fulfilling the steady-state condition is normally not a problem in regimes without large ELMs or with sufficiently long inter-ELM phases. The main caveat concerning the charge-stage-based approach, which also limits its widespread application apart from the complex diagnostic requirements, is that it is mostly only applicable in the pedestal. The use of medium-Z impurities, such as Ne, is suggested because their poloidal density asymmetries are less pronounced than for high-Z elements. Moreover, they have multiple charge stages for which effective CX-emission rate coefficients of specific spectral lines are available, such that their impurity densities can be evaluated from observed line radiances. However, in the core, such impurities are usually completely ionized. Thus, D and v cannot be disentangled based on the charge stage balance but the charge-stage method can only yield their ratio $\frac{v}{D}$. For pedestal studies with the charge-stage method, as with any impurity transport analysis at the plasma edge, it is important to ensure that the model for SOL and divertor impurity sources and losses, which cannot capture the real complex 3-D impurity distributions, does not influence the results. Moreover, the results are sensitive to the kinetic profiles of the background plasma and to the atomic data used to calculate ionization and recombination processes in the impurity transport solver. Thus, these inputs, and especially their alignment, should be handled with care.

Bayesian data analysis The complete forward model used to derive D and v in the pedestal from CXRS data with the charge-stage method consists of the coupled system of equations, simplified by the stationary state as shown in equation 1.13, together with the synthetic diagnostic equations mapping the charge stage densities onto the measured line radiances, as detailed in the chapters 3 and 4. The unknown, i.e., free, parameters comprise, in addition to the profiles of transport coefficients and charge stage densities, scalar-valued sources of neutral impurity and of thermal neutral D outside the confined plasma. They must be inferred since they are difficult to measure and also difficult to model as they involve recycling. These constraints yield a complex non-linear forward model, which poses a difficult inverse problem. Its solution may in particular feature high-dimensional, non-Gaussian error statistics, and potentially even multimodality, i.e., multiple local minima.

Previous studies on radial impurity transport, such as Dux et al., 2020, Howard et al., 2012, and Grierson et al., 2015, have often fitted D and v using least-squares minimization techniques such as the Levenberg-Marquardt algorithm. However, given the conditions outlined above, a more robust uncertainty quantification that is especially able to deal with non-Gaussian probability distributions is strongly recommended. This applies to most experimental analyses of impurity transport coefficient profiles, also those using time-dependent approaches, and can best be addressed by inferring the full probability distribution of the parameters according to Bayesian statistics (Chilenski et al., 2019). However, this distribution cannot be calculated analytically but must be sampled, which comes with a considerable computational computational demand (Chilenski et al., 2019).

For this reason, the code `Aurora` (Sciortino et al., 2021a; Sciortino, 2020) has been developed, which is strongly based on its predecessor `STRAHL` (Dux, 2021) but reduces the runtime of the numerical impurity transport solver. Moreover, based on `Aurora`, a new module aimed at Bayesian impurity transport inference, `ImpRad`, has been developed within the One Modeling Framework for Integrated Tasks (`OMFIT`) (Meneghini et al., 2013; Meneghini et al., 2015). So far, however, the `Aurora` code and the `ImpRad` module have mostly been used and optimized for inferring impurity transport in the plasma core, such as in Odstrčil et al., 2020, Sciortino et al., 2020, Sciortino et al., 2021b, and Sciortino et al., 2022, where transport coefficients have been derived from LBO impurity injections into different confinement regimes on DIII-D and Alcator C-Mod. Recently, progress has been made on several extensions, e.g., to use `ImpRad` also for main ion transport studies (Rosenthal et al., 2023). For impurity transport studies targeted at the pedestal, and in particular for using the charge-stage method, a simplified impurity transport solver for steady-state conditions has been developed and included in the `Aurora` package (Nishizawa et al., 2022).

1.6 Thesis objectives and outline

This thesis presents a novel data analysis routine for experimental quantification of radial impurity transport in the pedestal of AUG discharges. It builds on previous achievements, in particular the impurity transport solver `Aurora`, optimized for fast iterations based on the earlier diffusive-convective transport code `STRAHL`, and the `OMFIT` `ImpRad` module, designed for experimental analyses of impurity transport coefficients, as well as the AUG CXRS system and data evaluation codes. High-quality CXRS data is acquired with a special diagnostic setup to derive the transport coefficients with the charge-stage method, that is, based on spectral line radiance measurements from ≥ 2 impurity charge stages in steady-state plasmas. The sophisticated forward model mapping from the free parameters to the data includes the `Aurora` code and a synthetic diagnostic, linking individual charge stage densities with the observed impurity radiances. Thus, the method poses a high-dimensional non-linear inverse problem. It is solved with a sampling algorithm providing the full probability distributions of the parameters according to Bayesian statistics. The settings of the Bayesian inference are carefully configured.

Methodology tests using realistic synthetic data are done to prove the high radial precision of the inferred transport coefficients and the rigorous uncertainty quantification. They also assess the parameterization of the transport coefficient profiles, and the impact of potential data perturbations and model errors. The new framework is applied to analyze radial Ne transport in the pedestal of different confinement regimes. Type-I ELMy H-mode discharges are studied between ELMs and qualitatively also during ELMs, and compared to L-mode transport. Moreover, for the first time, high-resolution profiles of diffusion and convection in naturally ELM-free regimes, namely the QCE regime and the EDA H-mode, are presented. All experimental results are compared to collisional transport modeling, providing insights into the underlying transport processes.

The structure of the thesis is as follows. Chapter 2 introduces important background information, in section 2.1 on impurity transport, in section 2.2 on plasma edge physics, and in section 2.3 on Bayesian statistics. Subsequently, the specific experimental setup, as it is used for impurity transport inferences with the charge-stage method, is presented in chapter 3. The new inference framework to infer D and v profiles from this data is detailed in chapter 4, including in particular the individual elements of the forward model and the specifications for the Bayesian sampling. The methodology is tested with synthetic data in chapter 5. Thereafter, the framework is applied to deduce radial Ne transport coefficients in different confinement regimes at AUG. Chapter 6 shows the Ne transport results for type-I ELMy H-modes and L-mode, and chapter 7 for QCE discharges and an EDA H-mode. The thesis is summarized and concluded with a discussion on the implications of the findings for reactor-like tokamaks and directions for future work in chapter 8.

2 Background

This chapter summarizes important background information that is needed to understand the methodology and results of this thesis. It is structured into 3 sections on impurity transport (2.1), plasma edge physics (2.2), and Bayesian statistics (2.3).

2.1 Impurity transport

Impurity transport comprises all processes that contribute to the flux density of different impurity charge stages in the plasma ($\vec{\Gamma}_{\mathrm{I},Z}$ in equation 1.7). As it is an important and long-researched topic in magnetic confinement fusion plasma physics, several comprehensive reviews have been published over the years. Besides more general textbooks, such as Goldston et al., 2012 or Stroth, 2018, which include informative chapters on the subject, recommended are Helander et al., 2002 and Hinton et al., 1976 on collisional impurity transport theory, Fußmann, 1992 for general insights into particle transport, Dux, 2004 for an introduction to impurity transport focusing on aspects relevant to experimental studies, and Angioni, 2021 which provides an overview of the current knowledge and recent research developments concerning all aspects of impurity transport.

This section is oriented on these publications. It first introduces some general properties of transport in magnetized plasmas (section 2.1.1), before detailing the characteristics of radial impurity transport, subdivided into classical and neoclassical collisional transport (section 2.1.2), and anomalous transport due to turbulence and MHD activity (section 2.1.3). Thereafter, the relevance of poloidal asymmetries of impurity transport coefficients and densities is discussed (section 2.1.4), and modeling approaches for radial impurity transport are outlined (section 2.1.5).

2.1.1 General properties of transport in magnetized plasmas

The motion of a single charged particle in a plasma to which an external magnetic field is applied is influenced by the Lorentz force. Its velocity component perpendicular to the field lines $v_\perp$ is deflected, resulting in a gyration around the field lines. This fundamental gyromotion is characterized by its gyroradius, also called Larmor radius. For a particle with charge q and mass m it is given as

$$r_{\mathrm{L}} = \frac{m v_\perp}{|q| B}. \tag{2.1}$$

A tokamak plasma is usually magnetized, meaning that the Larmor radius is very small compared to typical system sizes or gradient scale lengths L in the plasma. Hence, a small ordering parameter

$$\rho^* = \frac{r_{\mathrm{L}}}{L} \ll 1 \tag{2.2}$$

can be defined. L is often specified as the pressure gradient scale length

$$L_p = |\nabla \ln p|^{-1}, \tag{2.3}$$

or sometimes also as the minor tokamak radius a. The small ρ^* effects that particles can move rather freely along the field lines spanning the magnetic flux surfaces, but radial transport, i.e., perpendicular to the flux surfaces, is hampered and occurs on much slower time scales than parallel transport.

The motion of many particles in the plasma is described statistically by the distribution function in phase space $f(\vec{r}, \vec{v})$ for each particle species, which represents the density of particles with velocity $\vec{v}$ at position $\vec{r}$. A common assumption is that the velocity distribution is influenced only by electric and magnetic fields, $\vec{E}$ and $\vec{B}$, and by collisions with other particle species, in particular neglecting gravity. Since Coulomb collisions dominate, other types of collisions are as well typically neglected. Coulomb collisions are in fact also interactions due to electric fields, but on spatial scales smaller than the Debye length λ_{Debye}, which is the characteristic length scale at which the plasma maintains quasineutrality. Their effect on $f(\vec{r}, \vec{v})$ can therefore be separated into a collision operator C_b for collisions with each other particle species b, which is usually specified as the Fokker-Planck operator due to the dominance of small-angle collisions. Then, $\vec{E}$ and $\vec{B}$ only describe fields on scales larger than λ_{Debye}. If furthermore any sources of particles or heat are neglected, this yields the kinetic equation for a particle species with mass m and charge q:

$$\frac{\partial f(\vec{r}, \vec{v})}{\partial t} + \vec{v} \cdot \nabla f(\vec{r}, \vec{v}) + \frac{q}{m}\left(\vec{E} + \vec{v} \times \vec{B}\right) \cdot \nabla_v f(\vec{r}, \vec{v}) = \left(\frac{\partial f(\vec{r}, \vec{v})}{\partial t}\right)_{\text{coll}} = \sum_b C_b(f). \tag{2.4}$$

The electromagnetic field in a tokamak is partly externally induced, such as the toroidal magnetic field and the toroidal electric field driving the plasma current. But in addition there are fields caused by the plasma itself, such as the poloidal magnetic field induced by the plasma current. Therefore, the kinetic equations for all particle species must be combined with Maxwell's equations to form a closed system that determines $f(\vec{r}, \vec{v})$, given suitable boundary conditions. The density and mean velocity of a single species follow directly from $f(\vec{r}, \vec{v})$ as the first two velocity moments:

$$n(\vec{r}) = \int f(\vec{r}, \vec{v})\, \mathrm{d}^3 v, \tag{2.5}$$

$$\vec{u}(\vec{r}) = \frac{\int \vec{v}\, f(\vec{r}, \vec{v})\, \mathrm{d}^3 v}{n(\vec{r})}. \tag{2.6}$$

Together, they yield the particle flux density

$$\vec{\Gamma}(\vec{r}) = n(\vec{r})\vec{u}(\vec{r}). \tag{2.7}$$

However, solving the coupled system of equations with the kinetic equation is very complicated. Therefore, it is usually simplified by approximations or other methods are used to derive important properties of particle transport in the plasma.

In the following, some general properties of particle transport are derived from the velocity moments of the kinetic equation, known as fluid equations. In the lowest two orders, these yield the particle and momentum conservation equations, also known as continuity equation and equation of motion, providing relations for n and $\vec{u}$:

$$\frac{\partial n}{\partial t} + \nabla\left(n\vec{u}\right) = 0, \tag{2.8}$$

$$mn\left(\frac{\partial \vec{u}}{\partial t} + \vec{u}\cdot\nabla\vec{u}\right) = qn\left(\vec{E} + \vec{u}\times\vec{B}\right) - \nabla p - \nabla\pi + \sum_b \vec{F}_b. \tag{2.9}$$

Here, p is the scalar pressure and π the viscosity tensor, which together form the pressure tensor. The friction force due to collisions is defined as

$$\vec{F}_b = \int m\vec{v}\,C_b \mathrm{d}^3v. \tag{2.10}$$

The infinite number of fluid equations are inherently coupled because each equation involves the next-order moment of $f(\vec{r},\vec{v})$. For instance, $\vec{u}$ appears in equation 2.8 and the pressure appears in equation 2.9. Solving the system of equations thus requires a closure that approximates higher-order moments in terms of lower-order moments.

However, some basic transport properties can also be more easily derived by ordering the equations in ρ^*. For this purpose, a temporal equilibrium with only a small deviation $f' \sim \mathcal{O}(\rho^*)$ of $f(\vec{r},\vec{v})$ from a Maxwellian velocity distribution $f_\mathrm{M}(T)$, defined by a local temperature T with thermal velocity

$$v_\mathrm{th} = \sqrt{\frac{2T}{m}}, \tag{2.11}$$

can be assumed.

The zeroth-order contributions in ρ^* to equation 2.9 yield the stationary ideal MHD equilibrium fluxes, namely the $E\times B$-drift and the diamagnetic drift:

$$\vec{u}_\perp^{(0)} = \frac{\vec{E}\times\vec{B}}{B^2} - \frac{\nabla p\times\vec{B}}{qnB^2}. \tag{2.12}$$

The diamagnetic drift causes the diamagnetic current, which flows poloidally, perpendicular to the field lines. In a tokamak, $B \propto 1/R$, such that the poloidal cross-section has an outboard low-field side (LFS) and an inboard high-field side (HFS). Therefore, the diamagnetic current is not divergence free and a top-down charge separation occurs. However, due to the helically twisted magnetic field lines, this charging can be counteracted by a parallel current, the so-called Pfirsch-Schlüter current, driven by the emerging vertical electric field.

Since collisional transport arises only from the perturbations of the Maxwellian velocity distribution, it is not included in the zeroth-order equation. Consequently, the zeroth-order drift velocities can also be understood qualitatively in part from the collisionless motion of single particles. Their guiding centers can move perpendicular to the field lines due to changes in the gyroradius during the gyroorbit. The $E\times B$-drift can be explained by the acceleration of individual particles in the electric field, whereas the flows of the diamagnetic drift cannot be fully recognized in the particle picture. Yet, the charge separation effect is captured in the torus drifts, namely the curvature drift caused by the centrifugal acceleration on the trajectory along the curved magnetic field lines, and the ∇B-drift caused by the radial gradient of the magnetic field:

$$\vec{v}_{\mathrm{curv}} = \frac{mv_{\|}^2}{q}\frac{\vec{R}_{\mathrm{curv}} \times \vec{B}}{R_{\mathrm{curv}}^2 B^2}, \tag{2.13}$$

$$\vec{v}_{\nabla B} = -\frac{mv_{\perp}^2}{2qB}\frac{\nabla B \times \vec{B}}{B^2}, \tag{2.14}$$

where $v_{\|}$ is the velocity component parallel to the field lines and R_{curv} the curvature radius of the magnetic field. In a torus, these drifts result in drift surfaces of the particles in the poloidal plane that are shifted with respect to the actual flux surface.

In the parallel direction, the particles can in principle move freely. However, $v_{\|}$ is altered by the inhomogeneity of the magnetic field since, in the absence of accelerating forces except for the Lorentz-force, both the kinetic energy of a particle

$$E_{\mathrm{kin}} = \frac{1}{2}mv_{\|}^2 + \frac{1}{2}mv_{\perp}^2 \tag{2.15}$$

and its magnetic moment

$$\mu = \frac{mv_{\perp}^2}{2B}, \tag{2.16}$$

which is an adiabatic invariant, are conserved. As a result, $v_{\|}$ decreases for a particle moving from the LFS towards the HFS. If the decrease is sufficient to reduce $v_{\|}$ to zero, the particles are trapped and cannot reach the HFS, but reverse the direction of their parallel motion. For the typical magnetic field configuration in a tokamak, the condition for a particle to become trapped can be approximated with the local inverse aspect ratio

$$\epsilon = \frac{r}{R} \tag{2.17}$$

as a condition for the velocity ratio at the LFS where $v_{\|}$ is maximal:

$$\left.\frac{v_{\|}}{v_{\perp}}\right|_{\mathrm{LFS}} \leq \sqrt{2\epsilon}. \tag{2.18}$$

This results in a trapped particle fraction $f_{\mathrm{t}} = \sqrt{2\epsilon}$. Trapped particles spend the most time near their turning points since $v_{\|}$ is lowest there. Together with the vertical displacement caused by the torus drifts, stated in equations 2.13 and 2.14, this leads to orbits that are banana-shaped when projected onto the poloidal plane, giving them the name banana particles. The banana particles give rise to a current in the direction of the plasma current, which is therefore known as bootstrap current

$$j_{\mathrm{BS}} \approx -\sqrt{\epsilon}\frac{\nabla p}{B_{\mathrm{P}}}. \tag{2.19}$$

The fluid velocity described by equation 2.12 is perpendicular to the magnetic field lines, but lies within a flux surface. This is because ∇p and the electrostatic potential gradients generating $\vec{E}$ are always orthogonal to the flux surfaces, while the additional induced toroidal electric field is small enough to be negligible. Consequently, a radial particle flux density Γ^r, directed perpendicular to the flux surfaces, can only be derived from higher order contributions in ρ^* to equation 2.9. It is caused by collisions between different particle species or by instabilities of the equilibrium, in particular turbulent fluctuations of pressure and electrostatic potential on small scales above λ_{Debye}. Coulomb collisions are always present and set the lower limit for the radial transport. Perpendicular to the field lines, they increase the particle transport, which is in contrast to the situation in neutral gases or along the magnetic field. The additional turbulent transport is often referred to as anomalous transport since it was discovered as unexpected transport required in simulations to match the observed order of magnitude of heat conductivity. Macroscopic instabilities of the MHD equilibrium can also contribute to anomalous radial particle transport, though these are often treated separately from collisions and turbulence.

All collisional transport of particles, energy/heat, and electric charge arises from gradients in density, temperature, or electrostatic potential within the plasma. These gradients cause the velocity distributions of different particle species to deviate from Maxwellian distributions with identical temperatures, such that collisions drive transport by exchanging momentum between the species. Collisions among particles of the same species, however, do not alter the fluid velocity of that species due to momentum conservation. Being close to a thermodynamic equilibrium, with a thermal velocity as defined in equation 2.11, the relations between the radial fluxes and the gradients can be linearized, resulting in a matrix relation. This relation can be reformulated into a symmetric matrix that satisfies the Onsager symmetry principle, thus known as the Onsager matrix. The fluxes in this formulation are referred to as generalized fluxes, and the gradients as thermodynamic forces.

The diagonal elements of the transport matrix relate the flux of each quantity to its own gradient. Therefore, they can be regarded as diffusion coefficients D, generating diffusive fluxes according to Fick's law of diffusion. For the density it is the diffusive particle flux

$$\Gamma^r_{\mathrm{diff}} = -D\frac{\partial n}{\partial r}. \tag{2.20}$$

The off-diagonal elements contributing to the particle flux instead relate it to the particle density itself. Thus they are termed convection coefficients as they contribute a convective particle flux

$$\Gamma^r_{\mathrm{conv}} = vn. \tag{2.21}$$

Turbulent particle transport can be equally subdivided into diffusive terms, which are proportional to the density gradient, and convective terms, which are proportional to the density itself. The general objective of plasma transport theory is to determine the diffusion and convection coefficients for both collisional and anomalous transport. In contrast to the ion heat flux, which is known to be almost purely diffusive, convection plays a substantial role in the impurity particle flux. Consequently, the radial impurity transport can be parameterized by a diffusive-convective equation, also called advective-diffusive or drift-diffusive equation, stated in equation 1.8.

The collisional and turbulent transport processes contributing to the particle transport coefficients generally act on different spatial and temporal scales, such that their coupling effects are mostly negligible and they are typically treated as additive. It should be noted, however, that some interactions may occur, e.g., due to turbulence influencing the plasma background profiles, which in turn affect collisional transport (Angioni, 2021). For main ions or light impurities and in most regions of the plasma core, turbulent transport dominates because collisional transport is in principle small in tokamak plasmas. Nonetheless, collisional transport can become relevant in regions of suppressed turbulence, like the H-mode pedestal in phases between type-I ELMs, or in regions with very weak pressure gradients, especially near the magnetic axis. Furthermore, for high-Z impurities, collisional transport can be significant across the entire plasma, since the collisional convection scales $\propto Z$.

Finally, the magnitude of collisional transport also depends on the probability for collisions. The effective 90° scattering frequency ν_eff is mainly caused by small-angle collisions. It is summed over the scattering frequencies with all other particle species b, given as

$$\nu_{\mathrm{eff},b} = \frac{1}{(4\pi\epsilon_0)^2}\frac{4\sqrt{\pi}}{3}\frac{q^2 q_b^2 \sqrt{m_\mathrm{red}}\, n_b \ln\Lambda_b}{m\sqrt{T^3}}, \tag{2.22}$$

with the vacuum permittivity ϵ_0, when assuming equal temperatures T of both colliding species, which have the reduced mass

$$m_\mathrm{red} = \frac{m\cdot m_b}{m+m_b}. \tag{2.23}$$

$\ln\Lambda_b$ is the Coulomb logarithm, which gives a measure for the importance of small-angle scatterings in the Coulomb collisions. It is defined as

$$\Lambda_b = \frac{\lambda_\mathrm{Debye}}{b_{90}}, \tag{2.24}$$

where b_{90} is the impact parameter for 90° Coulomb collisions when the particles are moving at the thermal speed. λ_Debye replaces the maximum impact parameter since the plasma becomes quasineutral at this scale. Typical values for $\ln\Lambda_b$ are between 10–20. The collision probability is typically quantified in the dimensionless parameter of collisionality ν^*, which is based on the frequency with which the banana particles are freed from their trapped paths by collisions

$$\nu_\mathrm{tr} = \frac{\nu_\mathrm{eff}}{\epsilon}, \tag{2.25}$$

and the frequency with which they complete their banana orbits

$$\omega_\mathrm{tr} = \frac{\sqrt{\epsilon}v_\mathrm{th}}{q_\mathrm{s}R}. \tag{2.26}$$

The collisionality is defined as the ratio of these two frequencies:

$$\nu^* = \frac{\nu_\mathrm{tr}}{\omega_\mathrm{tr}} = \frac{\nu_\mathrm{eff}q_\mathrm{s}R}{\epsilon^{3/2}v_\mathrm{th}}. \tag{2.27}$$

2.1.2 Classical and neoclassical collisional transport

Collisional transport arises from friction forces due to interspecies Coulomb collisions. The forces are a consequence of the collisionless particle motion, which introduces perturbations and shifts to the Maxwellian velocity distributions of the individual species. Here, the lowest order collisionless motion is regarded, neglecting in particular small scale turbulent perturbations. It comprises the gyromotion, the perpendicular drifts within the flux surface, and the parallel motion including trapped particles, as explained in section 2.1.1. Throughout, an approximate temporal equilibrium is assumed, implying that the gradient relaxation due to transport occurs on a much longer timescale than the collision time. For impurities, collisional transport is primarily caused by collisions with main ions, although collisions with other impurity species can also contribute. Collisions with electrons are negligible due to the significantly lower mass. The exact solution for collisional impurity transport from the kinetic theory presented in equation 2.4 is highly complex. Therefore, calculations usually rely on simplifications. The following discussion presents the common approaches and results, alongside simple random walk arguments in the particle picture, which illustrate some main features but cannot provide the exact fluid velocities.

Different contributions to radial collisional transport can be distinguished. First, there is a basic level of transport, commonly referred to as classical (CL) transport. The friction force $\vec{F}$ caused by the diamagnetic flow velocities in the flux surface perpendicular to the magnetic field lines, included in equation 2.12, results in a fluid velocity in $\vec{B} \times \vec{F}$-direction. In addition, the toroidal geometry introduces significant collisional transport, termed neoclassical transport. It originates from the friction caused by the parallel flow velocities in the tokamak, in particular by the Pfirsch-Schlüter current and the banana orbits. Since the classical transport is usually much smaller than the neoclassical contribution, the term neoclassical is often also used to refer to the sum of both transport contributions, though this usage is somewhat imprecise.

First, the classical transport is discussed. As it does not depend on the larger field structure, it can be derived from local arguments. Specifically, the kinetic description is not needed, but the fluid equations can be used, with a closure based on the assumption of a short mean free path λ relative to the system size. These equations are often referred to as Braginskii equations, since they were first derived by Braginskii, 1965. In a magnetized plasma, the gyroradius, which dominates the perpendicular motion length scale, is typically much shorter than the perpendicular system length scale $L_\perp$. The condition for the derivation of classical transport therefore concentrates on the ratio between the mean free path and the parallel system length scale $L_\parallel$,

$$\frac{\lambda}{L_\parallel} \ll 1. \tag{2.28}$$

With Braginskii's closure, the classical radial impurity flux can be derived from the first-order contributions in ρ^* to the momentum balance, stated in equation 2.9. The resulting flux due to collisions with another particle species b is

$$\Gamma_b^{r,\mathrm{CL}} = -D_b^{\mathrm{CL}} \frac{\partial n}{\partial r} + D_b^{\mathrm{CL}} \frac{q}{q_b} \left(\frac{1}{n_b} \frac{\partial n_b}{\partial r} + H_b^{\mathrm{CL}} \frac{1}{T} \frac{\partial T}{\partial r} \right) n, \tag{2.29}$$

with

$$H_b^{\mathrm{CL}} = -\frac{3}{2} \frac{m_{\mathrm{red}}}{m_b} + 1 + \frac{q_b}{q} \left(\frac{3}{2} \frac{m_{\mathrm{red}}}{m} - 1 \right) \tag{2.30}$$

and

$$D_b^{\mathrm{CL}} = \frac{mT}{q^2 B^2} \nu_{\mathrm{eff},b}. \tag{2.31}$$

H_b^{CL} quantifies the influence of the temperature gradient on the classical convection. It is outward-directed for collisions with main ions because of the larger impurity charge. Such an outward convection due to the temperature gradient is also called thermo-diffusion or temperature screening. Conversely, the convection term that is proportional to the density gradient of the other species b, is always inward-directed if the profile of species b is peaked, which is the case for main ions. It is therefore known as (main ion) density peaking contribution to the convection. Overall, the classical impurity convection scales with the impurity charge.

The classical diffusion coefficient D_b^{CL} can be intuitively understood since the diffusion is equal to a random walk where the step width is given by the Larmor radius of the particles:

$$D_b^{\mathrm{CL}} = \frac{1}{2} r_{\mathrm{L}}^2 \nu_{\mathrm{eff},b}. \tag{2.32}$$

Moreover, the dependency of the classical convection on the temperature and density gradients can be qualitatively understood by considering the gyromotion which generates the diamagnetic flow and the corresponding friction. A stronger temperature or density gradient increases the diamagnetic velocity of a species. This modifies the friction between different species, as it is determined by the velocity difference between them. In the case of main ion-impurity collisions, the diamagnetic velocity of the main ions is typically larger due to their smaller charge. Therefore, the friction force points in the direction of the main ion diamagnetic drift if all particles have the same collision efficiency. The resulting collisional transport is aligned with the main ion density gradient. The temperature screening effect stems from the higher efficiency of collisions with slower particles. Due to the temperature gradient, the guiding centers of slower particles are located further outward. Their local velocities, and therefore the resulting friction force, point in the opposite direction to the diamagnetic drift. This is well illustrated in Dux, 2004.

If the local transport assumption in equation 2.28 does not hold, neoclassical transport must be considered. Its contribution to the radial impurity flux is typically significantly larger then the classical component. It arises from changes to the guiding center motion of the particles in the torus geometry, induced by collisions. The derivation of the neoclassical transport requires a kinetic approach because Braginskii's fluid equations, which rely on the closure assumption given in equation 2.28, are not valid for non-local transport considerations. However, the gyromotion is not relevant to neoclassical transport, and the kinetic plasma description in equation 2.4 can therefore be simplified. The distribution function is decomposed as $f = \overline{f} + \tilde{f}$, where $\overline{f}$ describes the gyro-averaged motion of the guiding center and $\tilde{f}$ the gyration. Moreover, fluctuations of $\vec{E}$ or $\vec{B}$ on scales smaller than the Larmor radius, which are attributed to turbulent transport, are neglected. These conditions yield the drift kinetic equation for $\overline{f}$:

$$\frac{\partial \overline{f}}{\partial t} + \vec{v}_{\parallel} \cdot \nabla_{\parallel} \overline{f} + \vec{v}_D \cdot \nabla_{\perp} \overline{f} + \frac{q}{m} \vec{E}_{\parallel} \nabla_{v\parallel} \overline{f} = \left(\frac{\partial \overline{f}}{\partial t} \right)_{\mathrm{coll}} \tag{2.33}$$

Here, $\vec{v}_D$ is the sum of all particle drift velocities, i.e., the $E \times B$-drift and the torus drifts, which are detailed in equations 2.13 and 2.14. The neoclassical transport can be calculated by solving this equation for the first order perturbation in ρ^* of $\overline{f}$. Within the neoclassical transport, two regimes can again be distinguished based on the mean free path of the impurity particles. They result in different terms being dominant in the solution of the drift kinetic equation.

At rather high collision frequencies, i.e., short mean free paths, the neoclassical transport is in the Pfirsch-Schlüter (PS) regime. The Pfirsch-Schlüter transport is due to the collisional friction caused by the Pfirsch-Schlüter current, which is introduced in section 2.1.1. Due to the finite resistivity of the plasma, a poloidal variation of the electrostatic potential remains, creating an $\vec{E}$-field with a component perpendicular to $\vec{B}$ in the flux surface. This field gives rise to a radial $E \times B$-drift. Using the random walk argument in the particle picture, the transport arises due to the drift surfaces of the passing particles, which are shifted with respect to the flux surfaces, as described in section 2.1.1. The diffusion coefficient in the PS regime is given as

$$D^{\mathrm{PS}} \approx q_{\mathrm{s}}^{2} D^{\mathrm{CL}}. \tag{2.34}$$

When the mean free path is long, additional radial transport is caused by the banana particles, whose properties are introduced in section 2.1.1. These particles generate parallel friction because the density gradient leads to a local difference in the number of co-current and counter-current moving particles. Their significant transport contribution, even at low collision frequencies and despite the limited trapped particle fraction, can be understood from the random walk picture. Collisions can cause trapped particles to be freed by altering their ratio between $v_{\|}$ and $v_{\perp}$. Small scattering angles are often sufficient for this, leading to an increase in the effective collision frequency. Moreover, the random walk step size corresponds to the banana orbit width, which is much larger than the Larmor radius. However, once the collisionality becomes too high for the banana particles to complete their orbits, the banana transport decreases. Thus, the neoclassical transport transitions into the Pfirsch-Schlüter regime via an intermediate plateau regime, where the transport remains approximately constant over a finite range of collision frequencies. The banana regime and the plateau regime are often summarized as banana-plateau (BP) transport. Its diffusion coefficient, which is mainly applicable in the banana regime, is

$$D^{\mathrm{BP}} \approx \frac{q_{\mathrm{s}}^{2}}{\epsilon^{\frac{3}{2}}} D^{\mathrm{CL}}. \tag{2.35}$$

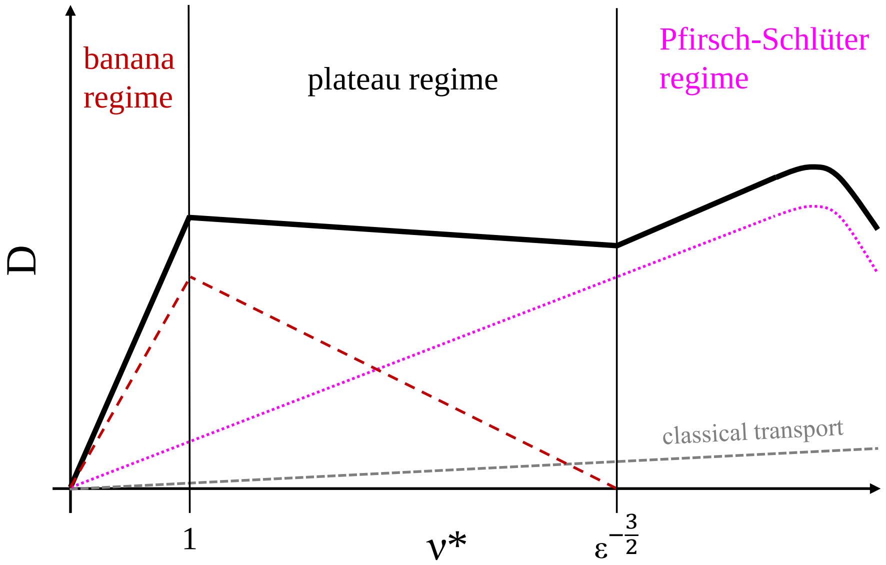

Figure 2.1: Idealized schematic of the different collisional transport regimes as a function of the collisionality. ϵ is the inverse aspect ratio. For very high collisionalities, which are typically not reached in tokamaks, the transport approaches the classical level, which describes the effect of local collisions without influences of the toroidal geometry.

Figure 2.1 shows a simplified picture of the diffusion coefficient as a function of collisionality for the different contributions to collisional transport, indicating the different transport regimes. Due to the definition of the collisionality as stated in equation 2.27, the trapped particles cannot anymore complete their orbits for $\nu^* \geq 1$, and the banana transport consequently decreases. The transport then remains in the plateau regime until the Pfirsch-Schlüter transport at $\nu^* = \epsilon^{-\frac{3}{2}}$ becomes as strong as the banana transport at $\nu^* = 1$. At very high collisionalities, the Pfirsch-Schlüter transport also decreases, and the local classical transport dominates, but such collisionality regimes are typically not reached. The different regimes of collisional transport can thus be summarized as follows:

$$\begin{aligned} \nu^* < 1 &: \text{banana regime} \\ 1 < \nu^* < \epsilon^{-\frac{3}{2}} &: \text{plateau regime} \\ \epsilon^{-\frac{3}{2}} < \nu^* &: \text{Pfirsch-Schlüter regime} \end{aligned} \tag{2.36}$$

The total collisional radial impurity flux due to collisions with another particle species b is the sum of the different contributions, which can all be written in the same form, analogous to equation 2.29:

$$\Gamma^{r,\text{coll}} = \sum_{\text{x=CL,BP,PS}} \sum_b D_b^x \left(-\frac{\partial n}{\partial r} + \frac{q}{q_b} \left(\frac{1}{n_b} \frac{\partial n_b}{\partial r} + H_b^x \frac{1}{T} \frac{\partial T}{\partial r} \right) n \right). \tag{2.37}$$

Here, the coefficients H_b^x again quantify the influence of the temperature gradient on the convective velocities. The total temperature screening coefficient (TSC) is defined as

$$\text{TSC} = \frac{\sum_{\text{x=CL,BP,PS}} \sum_b \frac{D_b^x}{q_b} H_b^x}{\sum_{\text{x=CL,BP,PS}} \sum_b \frac{D_b^x}{q_b}}. \tag{2.38}$$

It is negative if the temperature gradient has an overall screening effect and positive if the temperature gradient contributes an inward convection. In general it is a complex function of ν^*, being negative for low ν^* and positive for high ν^*. In current devices, where the main ions are typically in the banana regime and the impurities in the Pfirsch-Schlüter regime, the TSC for collisions between main ions and high-Z impurities usually has values around $-\frac{1}{2}$. The direction of the total convection depends in addition on the normalized density gradients of the other species. In the case of a negative TSC, i.e., temperature screening, it is directed outwards if

$$\frac{\sum_{\text{x=CL,BP,PS}} \sum_b \frac{D_b^x}{q_b} \frac{1}{n_b} \frac{\partial n_b}{\partial r}}{\sum_{\text{x=CL,BP,PS}} \sum_b \frac{D_b^x}{q_b}} \bigg/ \frac{1}{T} \frac{\partial T}{\partial r} < -\text{TSC}. \tag{2.39}$$

2.1.3 Anomalous transport

Excluding large-scale MHD activity, any radial transport in a tokamak above the collisional level is attributed to turbulence. Turbulence arises from small-scale instabilities caused by perturbations in the electromagnetic field around ion and electron Larmor radius scales, in combination with a background density or temperature gradient that exceeds a critical threshold. If these perturbations are only due to electrostatic potential variations, resulting from stochastic fluctuations in the plasma density or temperature, the turbulence is termed electrostatic. If, instead, magnetic field perturbations, induced by the time-evolving electric field, also contribute significantly to the instability, the turbulence is classified as electromagnetic. For simplicity, this discussion focuses on the basic mechanisms of electrostatic turbulence arising from density fluctuations superimposed on a large-scale density gradient. In this scenario, the plasma density

n and the electrostatic potential ϕ can be expressed as

$$n(\vec{r}) = n_0(\vec{r},t) + \tilde{n}(\vec{r},t), \tag{2.40}$$

$$\phi(\vec{r}) = \phi_0(\vec{r},t) + \tilde{\phi}(\vec{r},t), \tag{2.41}$$

where $\tilde{}$ indicates the deviations from the background states denoted by the subscript $_0$. If $\tilde{n}$ and $\tilde{\phi}$ are not in phase and the background density gradient exceeds a critical threshold, the $E \times B$-drift due to the electric field emerging from $\tilde{\phi}$ can amplify $\tilde{n}$. Such a self-enhancement of a perturbation is known as an instability. It can result in eddies with complex flows that interact non-linearly, leading to turbulence, which typically has a broad-band frequency/power spectrum. From the random walk perspective, turbulent diffusion can be understood as guiding center motion due to the $E \times B$-drifts resulting from the fluctuating field.

There are two main mechanisms by which an electrostatic potential perturbation can arise from density fluctuations and lead to an instability: In the drift-wave instability, the density perturbation exhibits a parallel gradient, to which the electrons respond faster than the ions because their velocity is higher. This produces a $\tilde{\phi}$ that is in principle in phase with $\tilde{n}$, however, a non-zero cross-phase can occur if the electrons are slowed down by effects such as resistivity between ions and electrons, trapped electrons, or Landau damping. In the MHD-like interchange instability, the density perturbation is constant along the field lines. $\tilde{\phi}$ is generated by the curvature drift, as given in equation 2.13, which points in opposite directions for ions and electrons. Therefore, the absolute value of the cross-phase with $\tilde{n}$ is naturally $\pi/2$. As the curvature radius of the magnetic field points outwards on the LFS and inwards on the HFS, an instability is only caused on the LFS, which is thus referred to as bad curvature region.

Since the curvature drift is also temperature dependent, a temperature perturbation can as well drive an interchange instability. Turbulent modes that can be attributed to the just presented mechanisms are for instance:

- ITG (ion temperature gradient modes): ion temperature gradient-driven interchange instability
- ETG (electron temperature gradient modes): electron temperature gradient-driven interchange instability
- TEM (trapped electron modes): drift-wave instability with a phase shift between $\tilde{n}$ and $\tilde{\phi}$ caused by trapped electrons

In addition, there are electromagnetic instabilities, such as MTMs (micro-tearing modes). These resistive instabilities create magnetic islands through reconnection, i.e., field stochastization, which act as shortcuts for the radial transport. Another example are KBMs (kinetic ballooning modes), which are interchange-type instabilities that are specifically relevant in the pedestal region. A more comprehensive overview of micro-instabilities in tokamaks can be found in Manz, 2018 and Kalis, 2024. Experimentally, the mechanisms causing turbulence can be distinguished through the cross-phase between the fluctuations, as well as the spatial and temporal evolution of the eddies. In the core, the temperature gradient dominates over the density gradient, resulting in predominantly temperature gradient-driven turbulence.

Although the fundamental mechanisms driving turbulence are well known, stationary, i.e., saturated, turbulent transport is a very complex non-linear phenomenon that cannot be described analytically and is generally not understood. To approximate turbulent transport numerically, the kinetic equation, stated in equation 2.4, is simplified to the gyrokinetic equation. This involves omitting the collision operator, thereby reducing it to the Vlasov equation, and averaging over the gyromotion, except for finite Larmor radius corrections that account for variations of the electromagnetic field across one Larmor radius. Turbulent transport is then calculated by solving the gyrokinetic equation to first order in ρ^*. The distribution function can be decomposed into equilibrium and fluctuating contributions of different order in ρ^* as follows:

$$f = f_{\mathrm{M}} + f_{\mathrm{equil}}[\mathcal{O}(\rho^*)] + f_{\mathrm{fluct}}[\mathcal{O}(\rho^*)] + f_{\mathrm{equil}}[\mathcal{O}({\rho^*}^2)] + f_{\mathrm{fluct}}[\mathcal{O}({\rho^*}^2)] + \dots \tag{2.42}$$

While the classical and neoclassical transport calculations contribute the gyromotion and guiding center contributions to $f_{\mathrm{equil}}[\mathcal{O}(\rho^*)]$, turbulent transport calculations can contribute $f_{\mathrm{fluct}}[\mathcal{O}(\rho^*)]$. Together, they therefore describe the full first order deviation of the distribution function from a Maxwellian equilibrium (`NEO` homepage, 2024).

Similar to the collisional transport, the result for turbulent impurity transport can be differentiated by multiple terms arising from the gradients of different quantities (Angioni et al., 2012):

$$\Gamma^{r,\mathrm{turb}} = -D^{\mathrm{turb}} \frac{\partial n}{\partial r} + \left(-D_T \frac{1}{T} \frac{\partial T}{\partial r} - D_\Omega \frac{R}{v_{\mathrm{th}}} \frac{\partial \Omega}{\partial r} + V \right) n. \tag{2.43}$$

Turbulence is also driven by density and temperature gradients, but this connection is less clear in the equation. D^{turb} represents the diffusion coefficient for the impurity particle transport and the term in brackets can be summarized as the convection coefficient. The latter can be subdivided into three distinct contributions, proportional the temperature gradient (thermo-diffusion D_T), the gradient of the toroidal angular velocity Ω (roto-diffusion D_Ω), and one term independent of any gradients (pure convection V). However, this simplified linear relation does not fully hold in reality, because the gradients impact also the types of turbulence that are present, which influence the coefficients in equation 2.43 (Angioni et al., 2012). In contrast to what was stated for collisional transport, this is not only the case far from thermodynamic equilibrium.

The turbulent impurity convection can be directed outwards or inwards, depending on the dominant turbulent modes and the plasma conditions. However, in contrast to the collisional transport, it does not involve any terms directly proportional to the impurity mass A or charge Z, of which it is only a weak function. For more details, see Angioni et al., 2012. Thus, strong high-Z impurity accumulation is less likely with turbulent transport, which rather produces flat impurity density profiles.

Turbulent microinstabilities typically saturate at small amplitudes. However, larger-scale MHD-instabilities, such as sawtooth profile relaxations in the core or ELMs in the pedestal, can also affect the impurity transport. Since such instabilities are not continuous but rather abrupt, it is unclear whether they can be adequately described within the diffusive-convective parameterization. ELMs are often modelled as radial diffusion and simulations using the non-linear MHD code `JOREK` with a kinetic particle extension confirmed that the mechanism for particle transport during ELMs is, as in turbulent transport, the $E \times B$-drift caused by the electric field that is generated by the MHD interchange-type instability (van Vugt et al., 2019). However, the particle transport during ELMs happens much faster than via collisions or turbulence, and it moreover depends on the mode phase and not only on the radial position, such that this simplified approach cannot not capture all properties of ELM impurity transport (van Vugt et al., 2019).

2.1.4 Poloidal asymmetries of impurity transport coefficients and densities

The radial transport of impurities varies in its magnitude and can even differ in sign across a flux surface due to the non-uniform magnetic field strength. This is particularly evident for the Pfirsch-Schlüter contribution to neoclassical transport, as the Pfirsch-Schlüter current flows in opposite directions on the LFS and HFS. Hence, also the direction of the associated radial transport is reversed. Turbulent transport may also be inhomogeneous on a flux surface, although this is less thoroughly validated. Despite these poloidal changes in radial transport, the impurity densities are typically assumed to be rather constant within the flux surfaces due to the fast parallel transport. Consequently, radial transport can be described as a 1-D problem using flux surface-averaged transport coefficients.

Given a general radial coordinate r, being constant on a flux surface, the average of a scalar quantity F on a flux surface S enclosing the volume V is defined as (Hinton et al., 1976)

$$\langle F\rangle = \left(\frac{\partial V}{\partial r}\right)^{-1} \oint F\frac{1}{|\nabla r|}\mathrm{d}S, \tag{2.44}$$

with the flux surface average denoted as $\langle\rangle$. For a toroidally symmetric quantity that depends only on the poloidal angle, this reduces to

$$\big\langle F(\theta)\big\rangle = \left(\frac{\partial V}{\partial r}\right)^{-1} \int_0^{2\pi} F(\theta)\frac{1}{|\nabla r|}\frac{dS}{d\theta}\mathrm{d}\theta. \tag{2.45}$$

Furthermore, the flux surface average for the divergence of a vector field $\vec{F}$ is given by (Hinton et al., 1976)

$$\langle\nabla\cdot\vec{F}\rangle = \left(\frac{\partial V}{\partial r}\right)^{-1} \frac{\partial}{\partial r}\frac{\partial V}{\partial r}\langle\vec{F}\cdot\nabla r\rangle. \tag{2.46}$$

Therefore, the general continuity equation for the impurity charge stage density, equation 1.7, can be reformulated into a radial equation:

$$\frac{\partial\langle n_{\mathrm{I},Z}\rangle}{\partial t} = \left(\frac{\partial V}{\partial \rho}\right)^{-1} \frac{\partial}{\partial r}\frac{\partial V}{\partial r}\langle\vec{\Gamma}_{\mathrm{I},Z}\cdot\nabla r\rangle + \langle Q_{\mathrm{I},Z}\rangle, \tag{2.47}$$

$$\frac{\partial\langle n_{\mathrm{I},Z}\rangle}{\partial t} = \left(\frac{\partial V}{\partial r}\right)^{-1} \frac{\partial}{\partial r}\frac{\partial V}{\partial r}\langle\Gamma_{\mathrm{I},Z,r}|\nabla r|\rangle + \langle Q_{\mathrm{I},Z}\rangle. \tag{2.48}$$

The diffusive-convective parameterization of the radial component of the flux density $\Gamma_{\mathrm{I},Z,r}$ gives

$$\frac{\partial\langle n_{\mathrm{I},Z}\rangle}{\partial t} = \left(\frac{\partial V}{\partial r}\right)^{-1} \frac{\partial}{\partial r}\frac{\partial V}{\partial r}\left\langle\left(-D(\theta)\frac{\partial n_{\mathrm{I},Z}}{\partial r}|\nabla r| + v(\theta)n_{\mathrm{I},Z}\right)|\nabla r|\right\rangle + \langle Q_{\mathrm{I},Z}\rangle. \tag{2.49}$$

When assuming constant densities on a flux surface, this yields

$$\frac{\partial n_{\mathrm{I},Z}}{\partial t} = \left(\frac{\partial V}{\partial r}\right)^{-1} \frac{\partial}{\partial r}\frac{\partial V}{\partial r}\left(-\langle D(\theta)|\nabla r|^2\rangle\frac{\partial n_{\mathrm{I},Z}}{\partial r} + \langle v(\theta)|\nabla r|\rangle n_{\mathrm{I},Z}\right) + \langle Q_{\mathrm{I},Z}\rangle. \tag{2.50}$$

In the following, D and v are defined as flux surface-averaged transport coefficients, i.e.,

$$D = \langle D(\theta)|\nabla r|^2\rangle, \tag{2.51}$$

$$v = \langle v(\theta)|\nabla r|\rangle. \tag{2.52}$$

Then, after dropping the flux surface average on the source term, and with a radial coordinate definition based on the volume enclosed by the respective flux surface

$$r_{\mathrm{vol}} = \sqrt{\frac{V}{2\pi^2 R_{\mathrm{axis}}}}, \tag{2.53}$$

where R_{axis} is the major radius of the magnetic axis, equation 1.9 for the radial impurity transport is retrieved (Dux, 2021). $|\nabla r|$ and $|\nabla r|^2$ are metric coefficients.

For the above derivations, poloidally homogeneous impurity densities have been assumed. This is often a valid approximation because the parallel transport redistributes the impurities on a flux surface on short time scales. However, poloidal asymmetries can still develop, especially due to the centrifugal force in a rotating plasma, but also due to electrostatic potential perturbations or parallel friction. The centrifugal force and the electrostatic potential are partly related, since electrons and ions are subject to opposite centrifugal asymmetries and the generated potential difference counteracts these asymmetries (Angioni, 2021). Electrostatic potential perturbations can however also be caused by other processes, such as temperature anisotropies resulting from ICRH or NBI heating. The extent of poloidal asymmetries is largely determined by the strength of the centrifugal force, which depends on the plasma rotation and the impurity mass. Moreover, the impact of electrostatic potential perturbations is related to the impurity charge. Thus, heavy and highly charged impurities, such as Kr, Xe, or W, are generally more affected. For low- to medium-Z impurities, including Ne and Ar, the approximation of constant impurity densities within the flux surfaces is valid (Dux, 2003), although minor asymmetries, primarily due to friction, may remain (Viezzer et al., 2015).

Since substantial poloidal impurity density asymmetries can significantly influence the neoclassical transport (Odstrčil et al., 2017; Angioni et al., 2014a; Fajardo et al., 2023), they must be taken into account when interpreting experimental observations of high-Z impurity transport. Thus, if studying the effects of poloidal asymmetries is not the objective, the use of lower-Z impurities with negligible asymmetries is advantageous for transport investigations and therefore done in this thesis. Otherwise, more complex transformations are required to convert the transport coefficients derived from the densities measured at a specific poloidal position into flux surface-averaged transport coefficients. This procedure is described in the appendix of Angioni et al., 2014b.

2.1.5 Modeling

Several codes with different approaches are available to model collisional, and turbulent radial impurity transport. Typically, the classical, neoclassical and turbulent transport coefficients are calculated separately and then summed, as their interactions are generally small. Therefore, multiple codes are usually combined for integrated modeling of impurity transport, as done in Fajardo, 2024. MHD phenomena, such as sawteeth or ELMs, are however often not included or only treated with simplified approaches, like enhanced impurity diffusion during ELMs, because the underlying mechanisms are not yet fully understood.

Classical transport can be calculated directly according to equation 2.29. In contrast, modeling neoclassical transport is more complex. It can be achieved most accurately by solving the drift kinetic equation, as derived in equation 2.33, to first order in ρ^*. This is done without further approximations by the code `NEO` (Belli et al., 2008; Belli et al., 2009; Belli et al., 2011), but comes at a significant computational cost. Therefore, the fast analytical model `FACIT` has recently been developed (Fajardo et al., 2022; Fajardo et al., 2023). `FACIT` reproduces `NEO` results across a wide range of collisionalities, trapped particle fractions, impurity charges, and masses, including the effects of plasma rotation. In addition, simpler fluid approaches are available to approximate the neoclassical transport coefficients, such as the two similar codes `NEOART` (Peeters, 2000; Dux et al., 2000) and `NCLASS` (Houlberg et al., 1997). They are based on the approach for calculating the transport coefficients by Hirshman et al., 1981, which solves a set of linear coupled equations for the parallel velocities. These fluid codes are fast, but lack the ability to account for toroidal rotation and its poloidal density asymmetry effects, which are discussed in section 2.1.4. Thus, their results are less accurate, especially for high-Z impurities. Generally, it should be kept in mind that all approaches for collisional transport modeling rely on the Larmor radius ordering introduced in equation 2.2. Due to the steep gradients in the kinetic plasma profiles, this ordering may lose its validity in the pedestal.

For the work presented here, the computational expense of transport simulations is not a limiting factor. Therefore, `NEO` is used as it provides in principle the most accurate results. However, since the mass and charge of Ne, the impurity studied, are low enough to neglect poloidal density asymmetries, the fluid approach is also valid. Calculations with `NEOART` are thus performed to complement the `NEO` results. An advantage of `NEOART` is that it includes the classical transport arising from the impurity gyromotion, whereas `NEO` calculates only the actual neoclassical transport contribution caused by parallel friction in the toroidal geometry. Moreover, `NEO` does not calculate transport coefficients for the individual contributions to collisional transport (classical, banana-plateau, Pfirsch-Schlüter). Instead, it returns the total radial impurity flux, calculated from the distribution function using the equations 2.5, 2.6, and 2.7. D and v can be disentangled with two separate `NEO` runs, in one of which the density gradient of the concerned species is set to zero in order to extract the purely convective flux. The banana-plateau and Pfirsch-Schlüter contribution, however, can only be distinguished with `NEOART`.

Both `NEO` and `NEOART` can account for collisions with multiple species, though `NEO` is limited to a maximum of 11 species. This capability is important in cases with significant impurity content involving multiple charge stages that interact through collisions, such as the Ne puffed experiments presented in this thesis. `NEO` offers two modes of operation: a profile mode, where it automatically reads many parameters from experimental data, using the routine `profiles_gen`, and a local mode, where calculations are only done for specified radial locations and all inputs must be provided by the user in the way specified in the manual (`NEO` homepage, 2024). Since the focus of this thesis is on pedestal transport, runtime is saved by operating `NEO` in its local mode. Finally, it is important to be aware that different transport codes utilize different radial coordinate definitions. Whereas the impurity transport solver `Aurora` and `NEOART` use the radial coordinate defined in equation 2.53, the radial coordinate of `NEO` is based on the maximum and minimum major radii of a flux surface, R_{LFS} and R_{HFS} on the LFS and HFS, respectively. It is defined as

$$r_{\mathtt{NEO}} = \frac{R_{\mathrm{LFS}} - R_{\mathrm{HFS}}}{2}. \tag{2.54}$$

Consequently, for a direct comparison of transport coefficients based on different radial coordinates, transformations must be applied. To convert between two arbitrary radial coordinate bases, from r_1 to r_2, the diffusion coefficient must be multiplied by $\left(\frac{\partial r_2}{\partial r_1}\right)^2$ and the convection coefficient by $\left(\frac{\partial r_2}{\partial r_1}\right)$.

Turbulent transport is most accurately modeled with non-linear gyrokinetic codes, such as `GYRO` (`GYRO` homepage, 2024) or `GENE` (`GENE` homepage, 2024), which solve the gyrokinetic equation to first order in ρ^*. However, these codes are computationally very expensive. To reduce the computational cost, quasilinear gyrofluid or quasilinear gyrokinetic codes with different models for the turbulence saturation, such as `TGLF` or `QuaLiKiz`, have been developed (Staebler et al., 2024). A rather new approach to improve the trade-off between accuracy and efficiency in turbulence modeling are neural network based models, such as `QLKNN`, which has been trained on `QuaLiKiz` output (Plassche et al., 2020). Moreover, advances are made in developing codes that are specifically tailored for the difficult task of simulating turbulent transport in the pedestal, where the background plasma profile gradients are steep. Notable examples include `CGYRO` (`CGYRO` homepage, 2024), `GENE-X` (Michels et al., 2021), and `GRILLIX` (Stegmeir et al., 2019). Yet, robust simulations of pedestal turbulence across different confinement regimes remain an unsolved challenge. The experimental results presented in this thesis are therefore not compared to turbulent transport calculations.

2.2 Plasma edge physics

To understand the mechanisms underlying the observed pedestal impurity transport in different confinement regimes, knowledge of the fundamental plasma edge physics in these regimes is essential. In this section, the main properties of regimes with high and low confinement are detailed (section 2.2.1), and the MHD stability of the pedestal is discussed (section 2.2.2), with a particular focus on the formation of type-I ELMs. Moreover, several currently investigated confinement regimes that may be compatible with reactor requirements, in particular due to the absence of large ELMs, are introduced (section 2.2.3).

2.2.1 Properties of H- and L-modes

In former times, a major challenge in nuclear fusion research was to demonstrate tokamak operation with high temperatures and high energy confinement since increasing the heating power had been observed to degrade the confinement time. A major improvement in the plasma performance was achieved with the breakthrough discovery of the so-called high-confinement regime (H-mode) in 1982 in diverted plasmas at ASDEX, the predecessor of ASDEX Upgrade (Wagner et al., 1982). It was shown that with heating powers above a certain threshold the pressure gradient suddenly steepens in a narrow, only a few cm wide, region at the plasma edge, forming the so-called pedestal (cf. figure 1.2), which enhances the pressure boundary condition for the plasma core. The energy and particle confinement times increased by about a factor of 2 compared to the previous low-confinement regime (L-mode) (ASDEX Team, 1989). Thus, the ratio between the stored kinetic energy and the heating power suddenly increases. The threshold power for H-mode access $P_{\mathrm{L-H}}$ empirically shows a hysteresis with higher powers needed to access H-mode than where H-mode can be sustained.

The confinement degradation with increased heating power in L-mode can be understood from the prevalence of turbulence that is driven by the temperature gradient, as described in section 2.1.3. The transition to H-mode is caused by the formation of an edge transport barrier (ETB), where turbulence is suppressed. It is located just inside the separatrix and is classically attributed to sheared $E \times B$-velocities, hindering the development of turbulent eddies (Burrell, 1997). This $E \times B$-shear is due to a well in the edge radial electric field E_r, which is the dominant component of the $\vec{E}$-field in equation 2.12. As explained in section 2.1.1, E_r is caused by gradients in the electrostatic potential between flux surfaces. A cross product of equation 2.12 with $\vec{B}$ yields the following relation, which holds for each species:

$$E_r = \frac{\nabla p}{qn} + \vec{u}_{\perp}^{(0)} \times \vec{B}. \tag{2.55}$$

Since $\vec{u}_{\perp}^{(0)}$ lies within a flux surface, E_r can be experimentally determined from measurements of the poloidal and toroidal velocities, the pressure gradient, and the magnetic field. However, many details of the development of the edge E_r well remain an active area of research, including, e.g., its dependence on the drift-configuration determined by the direction of the $\vec{B}$-field (Plank et al., 2023). Consequently, predictions of $P_{\mathrm{L-H}}$ must rely on empirical scaling laws, based on data from different devices. The widely recognized scaling law by Martin et al., 2008 captures the dependency on the electron density, the magnetic field, and the plasma size. More recent scaling laws, in particular by Schmidtmayr et al., 2018, are based on findings of the power threshold corresponding to a critical ion heat flux crossing the separatrix (Ryter et al., 2014). Simulations highlight the role of finite ion orbit effects to explain this observation (Kramer et al., 2024).

The H-L back-transition depends not only on the threshold power but also occurs once the plasma density exceeds a certain limit. Empirically, the line integrated density $\overline{n}$ in tokamak plasmas is constrained below what is known as the Greenwald density (Greenwald et al., 1988; Greenwald, 2002)

$$n_{\mathrm{GW}} = \frac{I_{\mathrm{p}}}{\pi a^2}[10^{20}\,\mathrm{m}^{-3}]. \tag{2.56}$$

While L-mode plasmas with too high densities typically disrupt, the H-mode density limit is a soft boundary, as a back-transition into L-mode usually occurs slightly below n_{GW} (Bernert et al., 2014). Although $\overline{n}$ is line-integrated, these density restrictions are suspected to originate from transport processes at the plasma edge. This has motivated the reconsideration of the operational boundaries in H- and L-mode in the recent semi-empirical concept of the separatrix operational space, which suggests an interplay of multiple processes connected to different turbulent modes (Eich et al., 2021; Manz et al., 2023). Moreover, it has led to the development of a new scaling law for the limit of the density close to the separatrix (Giacomin et al., 2022).

The primary challenge preventing the operation of future reactors in standard H-mode is the occurrence of large ELMs. These MHD instabilities cause a rapid collapse of the ETB, flattening the pedestal pressure profile on time scales of $\tau_{\mathrm{ELM}} \sim 1\,\mathrm{ms}$ by expelling energy and particles from the plasma edge. This strong radial edge transport is largely driven by filaments, that is, poloidally and toroidally localized structures elongated along the field lines (Kirk et al., 2008; Griener et al., 2020). ELMs occur in repetitive limit-cycles, with a recovery of the pedestal profiles during inter-ELM phases, which typically last 10–100 ms. It was found that the electron temperature gradient recovers on slower time scales than the electron density and ion temperature gradients (Cavedon et al., 2017; Cavedon et al., 2019) due to different heat flux dynamics of electrons and ions (Viezzer et al., 2020). During an ELM, the power flux on the PFCs scales as

$$P_{\mathrm{PFC}} \propto \frac{\Delta W_{\mathrm{ELM}}}{A_{\mathrm{vessel}}\sqrt{\tau_{\mathrm{ELM}}}}. \tag{2.57}$$

Since the energy content in the ELM W_{ELM} is proportional to the energy content in the plasma, which is determined by the plasma volume, while the wetted vessel area A_{vessel} is only proportional to the radius, P_{PFC} increases with the device size, making ELMs problematic, e.g., for ITER (Zohm, 2014).

The large ELMs observed in standard H-modes, which come with high peak power fluxes to the edge, are classified as type-I ELMs. Other types of ELMs with smaller amplitudes and higher frequencies have also been identified. They are typically categorized on the basis of phenomenological properties, as their underlying physics are only partially understood. The most common ones, that have been observed on several devices, are type II ELMs, sometimes also referred to as grassy ELMs, and type-III ELMs. Type-II ELMs typically exist in highly shaped plasmas, while type-III ELMs can occur close to the H-L transition (Zohm, 2014). Scenarios involving type-III ELMs usually exhibit very modest heat loads in the divertor, but also an empirically limited pedestal top temperature, which questions their applicability to reactor-like devices (Zohm, 2014).

2.2.2 MHD stability of the pedestal

A comprehensive overview of MHD theory and stability properties of tokamaks can be found in Zohm, 2014, which serves as the foundation for this section. In general, two fundamentally different types of MHD instabilities can be distinguished: pressure gradient-driven and current-driven instabilities. Both are directly evident from the intuitive form of the energy principle of ideal MHD, considered here for the bulk plasma with surface and vacuum terms neglected for simplicity. This principle investigates the change in the potential energy of the plasma δW_p, given a small excursion, described by the vector $\vec{\xi}$. $\vec{\xi}$ can be expressed as a sum of harmonics with poloidal and toroidal mode numbers m and n:

$$\vec{\xi}(r,\theta,\phi) = \sum_{m,n} \vec{\xi}_{m,n}(r) \exp\left(i\left(m\theta + n\phi\right)\right). \tag{2.58}$$

Flux surfaces where the magnetic geometry satisfies a rational relationship

$$q_\mathrm{s} = \frac{m}{n} \tag{2.59}$$

are more prone to the development of MHD instabilities and are therefore referred to as resonant surfaces.

Pressure gradient-driven instabilities appear in the equation for δW_p as a term

$$\propto - \int 2\left(\vec{\xi}_\perp \cdot \nabla p_0\right) \cdot \left(\vec{\kappa}_\mathrm{curv} \cdot \vec{\xi}^*_\perp\right) \mathrm{d}V, \tag{2.60}$$

where the subscript $_0$ denotes unperturbed equilibrium quantities, * the complex conjugate, and $\vec{\kappa}_\mathrm{curv}$ is the curvature vector of the magnetic field. The term is negative, i.e., contributes to instability, only when $\vec{\kappa}_\mathrm{curv}$ and ∇p_0 are parallel, which is the case at the LFS. Pressure gradient-driven MHD instabilities are therefore subject to a good and a bad curvature region in the same way as explained for the turbulent interchange instability in section 2.1.3. The overall stability depends crucially on the integral of the curvature along the field lines. In particular, instabilities likely occur if pressure gradient-driven modes with different m but the same n, which live on nearby flux surfaces, interfere. The interference can amplify the mode on the LFS while reducing its amplitude on the HFS, causing the bad curvature contribution to dominate. The resulting instability is called a ballooning mode, as it increases the plasma dimensions by extending the plasma surface on the LFS. Since the distance between neighboring resonant surfaces decreases with increasing n, ballooning instabilities are often analyzed in the infinite-n ($n \to \infty$) limit, e.g., with the code `HELENA` (`HELENA` homepage, 2024).

Besides the pressure gradient, which is typically specified as the normalized pressure gradient

$$\alpha = -\frac{2\mu_0 R_0}{B^2} q_\mathrm{s}^2 \frac{\mathrm{d}p}{\mathrm{d}r}, \tag{2.61}$$

where μ_0 denotes the vacuum permeability, the most relevant factor for ballooning stability is the magnetic shear indicated by the shear parameter

$$s = \frac{r}{q_\mathrm{s}} \frac{\mathrm{d}q_\mathrm{s}}{\mathrm{d}r}. \tag{2.62}$$

Higher shear narrows the region that is susceptible to MHD instabilities around each resonant surface. It therefore has a stabilizing effect, as shown in the schematic stability diagram for ballooning modes in figure 2.2. However, the diagram also shows the existence of a second stability region for small flux surface-averaged magnetic shear, where conversely an increasing pressure gradient acts stabilizing. This condition arises due to the natural radial outward shift of the tokamak equilibrium, known as Shafranov-shift. The magnitude of this shift depends on the plasma pressure and impacts the poloidal variation of the magnetic shear. In cases of small average shear, a significant variation across a flux surface can reverse the shear locally, and negative local shear can increase the absolute value of the shear, which enhances stability. The connection between the first and second stability regions, as depicted in figure 2.2, exists only for plasmas with non-circular poloidal cross-section.

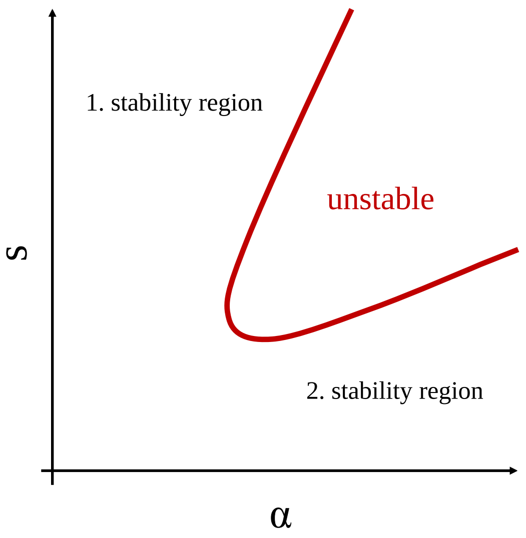

Figure 2.2: Stability diagram for ballooning modes. The second stability region is only accessible in plasmas with non-circular poloidal cross-sections. It is limited by the shear parameter s instead of the normalized pressure gradient α.

Since the shaping of the plasma influences the length of the field line path on the HFS relative to the LFS, it also affects the ballooning stability. It is typically measured in terms of elongation, κ, and upper and lower triangularities, δ_u and δ_l. They can be defined as

$$\kappa = \frac{Z_\mathrm{max} - Z_\mathrm{min}}{R_\mathrm{max} - R_\mathrm{min}}, \tag{2.63}$$

$$\delta_\mathrm{u} = \left(\frac{R_\mathrm{max} + R_\mathrm{min}}{2} - R|_{Z_\mathrm{max}} \right) \Bigg/ \left(\frac{R_\mathrm{max} - R_\mathrm{min}}{2} \right), \tag{2.64}$$

$$\delta_\mathrm{l} = \left(\frac{R_\mathrm{max} + R_\mathrm{min}}{2} - R|_{Z_\mathrm{min}} \right) \Bigg/ \left(\frac{R_\mathrm{max} - R_\mathrm{min}}{2} \right), \tag{2.65}$$

where the subscripts $_\mathrm{max}$ and $_\mathrm{min}$ indicate the maximum and minimum values of the radial position R and the vertical position Z on a given flux surface.

Current-driven instabilities appear in the intuitive equation for δW_p as a term

$$\propto -\int \frac{j_{0,\|}}{B_0}\left(\vec{\xi}_\perp^* \times \vec{B}_0\right) \cdot \vec{B}_1 \,\mathrm{d}V, \tag{2.66}$$

where $j_{0,\|}$ is the unperturbed current density parallel to the magnetic field and $\vec{B}_1$ is the perturbation of the magnetic field due to the displacement $\vec{\xi}$. Of particular relevance for pedestal stability are so-called peeling modes, which occur due to high current densities at the plasma edge and perturb the plasma boundary.

The pedestal stability of standard H-modes is governed by a combination of these two types of instabilities, such that type-I ELMs can be well described by the peeling-ballooning model. As explained in section 2.2.1, the pressure gradient at the edge rises due to the suppression of turbulence by the ETB. Along with it, the current density at the edge also rises since the increased pressure gradient enhances the bootstrap current, as evident from equation 2.19. Finally, an ELM occurs once the combined peeling-ballooning stability boundary is crossed, causing both the pressure gradient and the current density to collapse.

The peeling-ballooning stability of the pedestal can be calculated with linear MHD stability codes. However, only non-linear modeling with codes like `JOREK` (`JOREK` homepage, 2024) can simulate the breakdown of the pedestal and the formation of filaments, which emerge from non-linear coupling of modes. Moreover, the peeling-ballooning theory captures many but not all of the characteristics of ELMs. In particular, it does not uniquely determine the pedestal width and its height, which sets the boundary condition for the plasma core. To address this, the EPED model (Snyder et al., 2009; Snyder et al., 2011) has been developed, which successfully explains several experimental observations by additionally considering the KBM turbulence in the pedestal, briefly mentioned in section 2.1.3. First, KBMs are destabilized at a critical pressure gradient and locally limit its further increase. Subsequently, the pedestal width grows until the peeling-ballooning boundary is reached. The complete present understanding of type-I ELMs therefore combines a global stability constraint due to peeling-ballooning modes with a local stability/transport constraint imposed by KBMs with high mode numbers.

2.2.3 H-modes without type-I ELMs

Since type-I ELMs cause major problems for reactor-like devices, significant effort in current tokamak research is dedicated to identifying and investigating operational regimes that maintain high energy confinement, while being naturally ELM-free or having only small ELMs, and to developing methods for active ELM suppression. These regimes must exhibit sufficient pedestal transport to relax the pedestal gradients such that they stay away from the peeling-ballooning boundary, but at the same time the pedestal transport must be small enough to stay above the H-L backtransition threshold (Zohm et al., 2024). Their confinement properties are typically assessed by H-factors, comparing the energy confinement to empirical H-mode scaling laws, such as the widely used IPB98(y,2) scaling (ITER Physics Expert Group on Confinement and Transport et al., 1999). Moreover, for compatibility with reactor requirements, they must support high separatrix densities to enable divertor detachment. This means that high collisionalities must be reached at the pedestal foot, while the pedestal top collisionalities in a reactor will be low due to the high temperatures. Such profiles with a strong collisionality change in the pedestal are challenging to achieve in current devices. Consequently, extrapolations to reactor conditions must rely on models based on knowledge of the underlying pedestal physics.

For impurities, such regimes often show favorable properties in current devices, especially the absence of impurity accumulation in contrast to ELM-free phases of type-I ELMy H-modes. It is therefore hypothesized that the edge fluctuations that stabilize the pedestal against peeling-ballooning modes also affect the impurity transport. However, as for the general plasma behavior, a more detailed understanding of the underlying physics is required to reliably scale the impurity behavior and its consequences for core-edge integration, outlined in section 1.3, to reactor conditions.

An overview of the current knowledge on ELM-free regimes and their reactor relevance is provided in Viezzer, 2018, Stroth, 2022, and Viezzer et al., 2023, which form the basis for this section where not indicated otherwise. ITER is foreseen to be operated primarily with ELM suppression by resonant magnetic perturbations (RMPs) or pellet ELM pacing. However, the recent progress on regimes with natural absence of large ELMs has led to some of them being also considered for ITER operation. Due to their relevance for this thesis, the following discussion of the most important high confinement regimes without type-I ELMs concentrates mainly on the quasi-continuous exhaust (QCE) regime and the enhanced D-alpha (D_α) (EDA) H-mode. The operating conditions achieved with the QCE regime are currently closest to those required for future reactors (Stroth, 2022).

2.2.3.1 Operational regimes with natural absence of large ELMs

QCE regime The QCE regime is a promising small-ELM H-mode without significantly degraded confinement relative to type-I ELMy H-mode plasmas. It has been demonstrated in several devices, recently also at JET (Faitsch et al., 2025), and is best established at AUG (Harrer et al., 2018; Faitsch et al., 2021) and TCV (Tokamak à Configuration Variable) (Labit et al., 2019). As it is accessed at high densities around the separatrix, the QCE regime naturally complies with the collisionalities required at the pedestal bottom for power exhaust in reactor-like devices, such as ITER (Harrer et al., 2022). Yet, the compatibility of its small ELMs with the heat flux thresholds of the PFCs in a reactor is not fully guaranteed (Faitsch et al., 2023). Experiments with fueling by pellet injection compared to gas puffing have proven the sensitivity of the QCE access specifically to the density at the separatrix and in the SOL (Harrer et al., 2018). The second access condition for the QCE regime is strong plasma shaping close to double-null configurations, and especially a high triangularity, as shown in experiments at TCV (Harrer, 2020).

The small ELMs in QCE plasmas, which are also known as type-II or grassy ELMs, come at high frequencies $> 300\,\mathrm{Hz}$ (an example time trace can be seen in figure 7.1). They can coexist with type-I ELMs, as they have a different underlying mechanism (Harrer et al., 2018). Ideal $n \to \infty$ ballooning stability analyses with `HELENA` indicate that QCE discharges are locally unstable to high-n ballooning modes, typically located at $0.99 \lesssim \rho_\mathrm{pol} \lesssim 1.00$, this means mostly at the pedestal bottom (Radovanovic et al., 2022). The ballooning mode nature of the small QCE ELMs was confirmed with the more realistic non-linear, resistive MHD code `JOREK`, where ballooning modes occurred under QCE-like conditions (Hoelzl et al., 2021; Harrer et al., 2022). Experimentally, a coherent structure with a frequency around 30–40 kHz is observed at the plasma edge in QCE discharges (Griener et al., 2020), referred to as quasi-coherent mode (QCM). This fluctuation is indeed localized near the separatrix and propagates in the ion diamagnetic direction, which is consistent with the properties of ballooning modes (Kalis et al., 2023).

The stability analyses by Radovanovic et al., 2022 provide deeper insights into the reasons for the good energy confinement without large ELMs in the QCE regime. These qualities are due to a fine balance of the ballooning stability, whose distinct stability regions are illustrated in figure 2.2, across the pedestal. The pedestal bottom is in the first stability region (Radovanovic et al., 2022), such that the small-ELM ballooning modes, which are very localized due to their high n, are destabilized by lower magnetic shear or increased pressure gradient. This explains the QCE access conditions, namely the high edge densities, which result in steep local pressure gradients, and the strong shaping, which results in small local magnetic shear at the pedestal bottom (Harrer et al., 2018; Harrer, 2020; Harrer et al., 2022). With increasing shaping, the pressure gradient threshold for peeling-ballooning modes rises more rapidly than that for the QCE ballooning modes, creating a larger operational space for the QCE regime (Dunne et al., 2024). The additional transport by the ballooning modes at the plasma edge is efficient due to the high densities in this region and flattens the local gradients such that the pedestal width is reduced sufficiently to keep the entire pedestal away from the peeling-ballooning boundary (Harrer, 2020). As the pedestal middle is in the second stability region, its gradients can in contrast be locally steep without provoking ballooning modes (Radovanovic et al., 2022). This ensures the good confinement in the QCE regime.

The small ELMs are observed to come with high-frequency, i.e., quasi-continuous, filamentary transport in the SOL. These filaments exhibit velocities up to 3× higher compared to H-mode phases between type-I ELMs (Griener et al., 2020). Their transport causes a density shoulder in the SOL, characterized by flatter density gradients in the far SOL than closer to the separatrix (Faitsch et al., 2021). Moreover, it increases the SOL power fall-off length, defined as the exponential decay length to $1/e$, by a factor of up to 4 compared to H-mode phases between type-I ELMs (Faitsch et al., 2021). The high SOL densities, together with the broadened heat flux, facilitate detachment and reduce the power load on the PFCs, potentially lowering the required edge impurity radiation in a reactor (Faitsch et al., 2021). However, individual filaments may have substantial local heat and particle impacts on the wall (Faitsch et al., 2021).

In the past, the QCE regime has not been considered for reactor operation because it is only achievable with rather high pedestal top collisionalities in present-day devices, which will not prevail in reactors. However, this limitation arises from the inability of smaller devices to decouple the collisionalities at the pedestal top and bottom. The rather recently discovered localized dependence of the QCE regime on the separatrix density thus invalidates this argument (Harrer et al., 2022), and the compatibility of QCE operation with lower collisionalities at the pedestal top is supported by experimental findings at JET, where the QCE regime has recently been established (Faitsch et al., 2025). Nevertheless, further requirements must be met in order to operate ITER in a QCE regime. The pedestal middle must remain in the second stability region to ensure good confinement, and the small ELM filaments must be compatible with the heat fluxes that are tolerable for the PFCs. Furthermore, the strong shaping needed to access the QCE regime must not endanger the upper vessel tiles (Pitts, 2024). At AUG, the QCE regime is usually operated at 0.8 MA, several example discharges are presented in chapter 7. Extensions of the QCE operational space are subject of ongoing research.

EDA H-mode The EDA H-mode was discovered on the compact, high-field tokamak Alcator C-Mod (Greenwald et al., 1999; Marmar et al., 2000) and has since then been established on several devices, including AUG (Gil et al., 2020). It is named after the enhanced D_α radiation observed at the plasma edge, which is related to an increased particle transport compared to

H-mode phases between type-I ELMs. This increased transport prevents impurity accumulation in present-day devices and keeps the pedestal away from the peeling-ballooning boundary, such that it is practically ELM-free (an example time trace can be seen in figure 7.1). Nevertheless, the particle confinement in EDA H-mode plasmas is high enough to build a clear density pedestal with high core densities. Additionally, it provides excellent energy confinement, with H-factors that can be even > 1.

The EDA H-mode is accessed primarily by strong electron heating via ECRH, and it is more easily achieved with additional high fueling, i.e., high collisionality, and high shaping, in particular high triangularity. In AUG, EDA H-modes are typically operated at rather low plasma currents, as the discharge presented in chapter 7 with 0.7 MA, and NBI heating contributing up to 50 % of the heating power is tolerable.

A key characteristic of EDA H-mode plasmas is the QCM, which appears similar to the QCM in the QCE regime. Although with a narrower frequency bandwidth, it is also observed near the separatrix and propagating in the ion diamagnetic direction, identifying it as related to electromagnetic ballooning modes (Kalis et al., 2023). Thus, as in the QCE regime, ballooning-like fluctuations are assumed to be responsible for the enhanced plasma edge particle transport. This hypothesis is supported by non-linear MHD stability calculations with `JOREK` for an AUG EDA H-mode, which find modes with a poloidal rotation velocity compatible with resistive ballooning modes, and a ballooning-like localization at the LFS (Cathey et al., 2023). The increased edge transport is probably also connected to filamentary activity, although the filament velocities in the SOL are found to be smaller than those generated by the small ELMs in the QCE regime (Griener et al., 2020).

Due to their similar parameter space, which is directly compared in Viezzer et al., 2023, and the presence of a QCM, albeit with slightly different characteristics, in both the QCE regime and the EDA H-mode, the connection or distinction between these regimes is not fully understood. Typically, the regimes are distinguished by the higher ELM activity in the QCE regime and the narrower frequency bandwidth of the QCM in the EDA H-mode. Further investigation of the EDA H-mode physics, and also of the QCE regime, is required to assess their differences and for robust scaling to future devices. In the EDA H-mode, in particular, the appearance of ELMs can occur when the heating power is increased above a certain threshold. Thus, its compatibility with higher heating powers, but also with lower collisionalities, needs to be proven and remains a topic of current research.

XPR regime The X-point radiator (XPR) regime, demonstrated at AUG, TCV, and JET (Bernert et al., 2017; Bernert et al., 2020; Bernert et al., 2023), is accessed by strong impurity seeding. A highly radiating region, which is poloidally localized close to the X-point, is established in the confined plasma, and the associated radiative cooling relaxes the pedestal gradients such that type-I ELMs are suppressed. The ELM suppression depends on the position of the XPR region, and usually occurs in AUG for heights of the XPR above the X-point of > 7 cm. Therefore, in order to operate a stable XPR regime, a real-time control for the XPR position via the seeding level has been developed. The XPR model proposed by Stroth et al., 2022 captures further parameter dependencies of the XPR access and stability, which are in good agreement with experimental observations. At AUG, a stable XPR regime with high energy confinement can be operated without detrimental impurity accumulation. Due to the large radiated power fraction, it is typically inherently fully detached. This allows the X-point to be placed closer to the divertor targets, which motivates the concept of the compact radiative divertor (CRD) (Lunt et al., 2023).

I-mode The improved energy confinement mode (I-mode) (Whyte et al., 2010), found on several tokamaks including AUG (Ryter et al., 2016; Happel et al., 2016), is characterized by the combination of good energy confinement with L-mode-like particle confinement, thus the absence of a density pedestal. As a result, the pedestal is peeling-ballooning stable, i.e., ELM-free, and impurity accumulation is prevented. Similar to the QCE regime and the EDA H-mode, a plasma edge fluctuation, the weakly coherent mode (WCM), is observed, but at higher frequencies than the QCM. The I-mode is typically accessed via an unfavorable ion ∇B-drift configuration, where the ion particle drift given in equation 2.14 is directed away from the active X-point. This can be achieved by operating in upper single-null (USN), that is, with the X-point at the upper divertor, or with a reversed B-field direction. It leads to a higher threshold power for H-mode access and the I-mode is also established at high powers, though below $P_{\mathrm{L-H}}$, with an operational power window that increases with the magnetic field. Close to $P_{\mathrm{L-H}}$, pedestal relaxation events appear, which however have lower power fluxes than type-I ELMs and cannot be described as peeling-ballooning instabilities (Silvagni et al., 2020). The reversed field operation and the high access power pose challenges for future reactors. Moreover, the integration of the I-mode with impurity seeding without transitioning into L-mode is challenging. Hence, its compatibility with divertor detachment needs to be further investigated.

Negative triangularity L-mode Negative triangularity plasmas have a poloidal cross-section that is opposite to the vessel shape at AUG. These plasmas can be operated in L-mode without ELMs even at H-mode-like heating powers. However, even without a pedestal, they can achieve high energy confinement with an H-factor around 1. They have first been studied on TCV (Camenen et al., 2007), and have been shown to be able to reach reactor-relevant pressure on DIII-D (Austin et al., 2019). Since its potential reactor relevance was only discovered rather recently, this regime is not yet well studied and many other reactor-relevant criteria, such as the integration with impurity seeding and divertor detachment, but also the vertical stability, cannot yet be rated. A review is provided by Marinoni et al., 2021, and initial studies at AUG are presented in Happel et al., 2022.

QH mode The quiescent H-mode (QH-mode) (Burrell et al., 2001; Suttrop et al., 2003) is established via strong plasma rotation combined with low edge densities. It exhibits a similar energy confinement as the type-I ELMy H-mode but no ELMs. Instead, additional edge transport is driven by a kink-peeling type MHD instability, the edge harmonic oscillation (EHO). It is saturated close to the peeling-ballooning boundary and keeps the pedestal peeling-ballooning stable. Yet, in AUG with the W wall, as in metal-wall devices in general, impurity accumulation is not prevented, such that QH-modes can only be reached transiently before a radiative collapse occurs. Moreover, due to the low edge densities, compatibility with divertor detachment is not ensured. The QH mode can, however, be operated stably in other devices, such as the tokamak DIII-D, where even a new wide-pedestal QH-mode (WPQH-mode) was discovered rather recently (Burrell et al., 2016; Burrell et al., 2020). This mode has a wider and higher pedestal and thus also a higher energy confinement than the previous QH-mode, and is accessed by particularly high shaping.

2.2.3.2 Active ELM control techniques

ELM mitigation and suppression with RMPs With the use of tailored control coils, 3-D, i.e., non-axisymmetric, magnetic fields can be generated that perturb the magnetic topology at the plasma edge such that ELMs are mitigated or even fully suppressed. This was first discovered on DIII-D by Evans et al., 2004. Although the exact mechanism of the ELM suppression is complex and not fully understood, it is thought to be related to the formation of magnetic islands near resonant surfaces at the pedestal top due to magnetic re-connection. Such an island acts as a transport shortcut, therefore reducing the pedestal pressure gradient and stabilizing the pedestal against peeling-ballooning modes. With RMPs, especially the pedestal density is lowered, which is known as density pump-out. The existence of magnetic islands in RMP plasmas has recently been proven experimentally and is supported by non-linear free-boundary `JOREK` simulations (Willensdorfer et al., 2024).

RMP ELM suppression has been found to significantly reduce the accumulation and confinement time of high-Z impurities with respect to ELM-free phases without RMPs (Grierson et al., 2015). The experimentally observed impurity diffusion in the pedestal is increased (Victor et al., 2020; Vogel et al., 2021), which is supported by `JOREK` simulations showing an increase in pedestal impurity diffusion by a factor of about 2 during RMP ELM-suppressed operation (Korving et al., 2024). This modeling indicates that the impurity diffusion cannot be explained by neoclassical transport alone, although the reduced density gradient in RMP plasmas could contribute to reduced neoclassical impurity inward convection in the pedestal. However, further and more detailed quantitative validation of these results is required for a thorough understanding and ITER predictions.

ELM pacing via pellet injection Instead of ELM suppression, ELMs can also be intentionally triggered, called ELM pacing. This is favorable since frequent small ELMs can provide sufficient transport to avoid large type-I ELMs. ELMs can be released by injection of frozen fueling pellets, as they locally perturb the pedestal pressure. For ITER, this is foreseen as an alternative to RMP ELM suppression or ELM-free/small-ELM regimes, especially during the ramp-up and ramp-down of the plasma (Loarte et al., 2014). At AUG this technique was established by Lang et al., 2004.

Pellet ELM pacing is critically dependent on a number of parameters, which have been statistically assessed at JET by Lennholm et al., 2021. The dominant influence is the injection location, with injections from the HFS being favorable. Moreover, larger and faster pellets trigger ELMs more reliably, but also contribute undesirably more to core fueling and degrade the energy confinement more significantly. After each ELM, there is a lag time within which further pellet injections do not trigger another ELM, an observation that has been successfully modeled with `JOREK` by Futatani et al., 2021. Finally, the required pellet size depends on the collisionality of the plasma, as the effect is connected to a pressure perturbation. The required pellet size in reactor-like pedestals with low collisionality has been evaluated experimentally at DIII-D by Wilcox et al., 2021 and is in good agreement with the MHD simulations by Wingen et al., 2021.

ELM pacing via vertical plasma kicks As an alternative to pellet injection, ELM pacing is also possible with vertical kicks, as first found by Degeling et al., 2003 and described in Zohm, 2014. These are generated by changes to the radial magnetic field, which is induced by the poloidal field coils used for stabilization of the vertical plasma position. Controlled vertical plasma displacements with sufficient velocity and magnitude can trigger small ELMs. However, this method has several drawbacks for reactor operation. Most importantly, the plasma is more prone to vertical displacement events (VDEs), which are instabilities that lead to a loss of vertical position control. VDEs cause the plasma to move rapidly towards the wall, often resulting in disruptions.

2.3 Bayesian statistics

This section is concerned with the extraction of information from experimental data in a statistically accurate manner with robust uncertainty quantification. It is structured into a general discussion of inverse problems and their solution using Bayesian statistics (section 2.3.1), and an introduction to sampling algorithms (section 2.3.2). Special attention is given to nested sampling methods, and especially the algorithm `MultiNest`, which is employed in this work. More information can be found in Sivia et al., 2006 and Toussaint, 2011, on which this chapter is based.

2.3.1 Solving inverse problems

Experimental studies aim to obtain information about physical quantities, here referred to as parameters $\mathcal{P}$, for which some prior information $\mathcal{I}$ may already exist, from measured data $\mathcal{D}$. However, the parameters are often not directly measurable, but the observed quantities depend on the parameters via a known or hypothesized (forward) model $\mathcal{M}$. Estimating the parameters based on the data therefore poses an inverse problem, which can be complex to solve if the model is not invertible. Moreover, especially for non-linear models, there may be multiple distinct solutions for the parameters in fairly good agreement with the data, and additionally, the data may be affected by large noise or may be sparse. In sum, it can be difficult to determine a single narrowly constrained solution of the inverse problem and it is therefore insufficient to use optimization methods such as χ^2-minimization, which minimizes

$$\chi^2 = \sum_i \frac{(f_i - d_i)^2}{\sigma_i^2}, \tag{2.67}$$

where f_i are the elements of the solution, d_i the corresponding data points, and σ_i their univariate standard deviations. In these cases, it is recommended to infer a probability estimate for the full parameter space, which also takes a priori knowledge explicitely into account. This can be done according to Bayesian statistics with Bayesian inference methods. As such, they provide an accurate quantification of the uncertainty.

Bayes' theorem provides the following relation for the probability of the parameters given the prior information, the measured data, and the forward model:

$$p(\mathcal{P}|\mathcal{D},\mathcal{M},\mathcal{I}) = \frac{p(\mathcal{D}|\mathcal{P},\mathcal{M},\mathcal{I})p(\mathcal{P}|\mathcal{M},\mathcal{I})}{\int p(\mathcal{D}|\mathcal{P},\mathcal{M},\mathcal{I})p(\mathcal{P}|\mathcal{M},\mathcal{I})\mathrm{d}\mathcal{P}} \propto p(\mathcal{D}|\mathcal{P},\mathcal{M},\mathcal{I})p(\mathcal{P}|\mathcal{M},\mathcal{I}). \tag{2.68}$$

Here, $p(\mathcal{P}|\mathcal{M},\mathcal{I})$, typically called prior (probability), is the probability assigned to the parameters prior to the experiment due to a priori knowledge, e.g., about the physical process. $p(\mathcal{D}|\mathcal{P},\mathcal{M},\mathcal{I})$, typically called (data) likelihood, is the probability of the data, given a specific parameter set, meaning that it describes the measurement noise. $p(\mathcal{P}|\mathcal{D},\mathcal{M},\mathcal{I})$ is often referred to as posterior (probability). For an inference of the parameters, known as parameter estimation, the denominator in equation 2.68 does not need to be computed, as it is simply a normalization constant.

From the posterior, several summary statistics can be derived, such as its mean or confidence intervals, which contain a certain percentage of the probability mass. Also, posterior distributions for a parameter subset can be calculated, marginalizing the other parameters. The mode of the posterior is the point with the highest probability, called maximum a posteriori (MAP).

However, in the case of strongly non-Gaussian or even multimodal posteriors, and in high-dimensional parameter spaces, simple estimators, including the MAP, may not be particularly representative of the high-probability region. This highlights again the advantages of Bayesian inference over optimization methods that infer a single point in the parameter space.

Bayesian statistics can not only be used for parameter estimation but also to compare the applicability of different models. The denominator in equation 2.68 is the likelihood integrated over the prior space, so it depends only on the prior information and the given model, which can be written as $p(\mathcal{D}|\mathcal{M},\mathcal{I})$. Since the parameters are marginalized, it is also known as marginalized likelihood. Multiplied by the prior probability of the model $p(\mathcal{M}|\mathcal{I})$ it yields the posterior probability of the model $p(\mathcal{M}|\mathcal{D},\mathcal{I})$ (Knuth et al., 2015). Assuming same prior probabilities for two models, their relative posterior probabilities are thus directly indicated by the marginalized likelihood, which is therefore also known as Bayesian (model) evidence. It measures how well the data can be matched by a model, while favoring simpler models over more complex ones (Knuth et al., 2015). The ratio between the Bayesian evidence values of two different models is usually referred to as Bayes factor, and the approach of selecting an appropriate model via its Bayesian evidence is known as model selection.

Calculating the posterior or the Bayesian evidence analytically is often impossible. Instead, alternative approaches, usually sampling methods, are employed for their approximation. However, these can be costly and it is particularly challenging to accurately capture the integration required to retrieve the Bayesian evidence, i.e., the denominator in equation 2.68 because the parameter space region that strongly contributes to the evidence is typically small. In addition to choosing an inference algorithm, setting up a Bayesian inference in practice requires the definition of a model, a prior, and a likelihood. The model should incorporate the physical understanding of the mapping from the parameters to the ideal measured quantities. Moreover, it often includes further parameterizations, e.g., of profiles, in order to reduce the dimensionality of the parameter space. Non-parametric inference, e.g., with Gaussian-process regression, can become computationally expensive in high dimensions. The prior should reflect any information about the parameters before conducting the experiment. Following the principle of maximum entropy, it should contain as little information about the parameters as possible while satisfying all known properties, e.g., a positivity constraint. Finally, the likelihood should capture all knowledge about the measurement noise, in particular any correlations in the data error statistics, non-Gaussian error distributions, or systematic offsets.

2.3.2 Sampling algorithms

Sampling algorithms approximate the posterior distribution by drawing a sample set to represent it. A common choice are Markov chain Monte Carlo (MCMC) methods, which are designed such that their equilibrium chain samples are distributed according to the posterior. MCMC methods are often efficient even in high dimensions, but if they are not run for a sufficient number of steps, the sample set can be correlated, and if they start in an unfavorable region, they may need a rather long burn-in time to reach the regions of high posterior probability density. Hence, very complex posterior shapes may not be well captured by MCMC methods. In addition, while parameter estimation only needs to approximate the unnormalized posterior, i.e., the right-hand side of equation 2.68, model selection studies require an estimate of the integral in the denominator of the equation, which is not easily feasible with MCMC methods.

Particularly useful for both dealing with strongly non-Gaussian posteriors and accurately estimating the Bayesian evidence is the nested sampling method first introduced by Skilling, 2004 and Skilling, 2006. For comprehensive recent reviews, see Ashton et al., 2022 and Buchner, 2023. The basic principle of nested sampling is to iteratively update a set of n_{live} samples, the so-called live points. They are initially drawn uniformly from the prior, and updated by rejecting the sample with the lowest likelihood L_i at iteration i and sampling a replacement uniformly from the prior regions with higher likelihood. In the case of a simple likelihood space, peaking at a central point, this yields nested shells. Each region or shell encloses a prior volume, i.e., prior probability mass, X_i, the shrinkage of which determines the prior volume or weight w_i that the rejected sample represents. The posterior weight of the sample i is therefore

$$p_i = \frac{L_i w_i}{\sum_i (L_i w_i)}. \tag{2.69}$$

The posterior is approximated by all samples together with their posterior weights and the Bayesian evidence is calculated as

$$p(\mathcal{D}|\mathcal{M},\mathcal{I}) = \sum_i (L_i w_i). \tag{2.70}$$

The multi-dimensional integration over the posterior space has thus been transformed into a 1-D integral. The MAP is obtained directly as the sample with the highest p_i.

There are different methods for estimating the prior weight of each sample. In the nested sampling code `MultiNest` (Feroz et al., 2008; Feroz et al., 2009; Feroz et al., 2019), which is used in this work, w_i is calculated as

$$w_i = \frac{X_{i-1} - X_{i+1}}{2}. \tag{2.71}$$

The expectation value for the shrinkage of the prior volume in each iteration is estimated in `MultiNest` by a statistical argument (Feroz et al., 2008) as

$$\frac{X_i}{X_{i-1}} = \exp\left(\frac{-1}{n_{\text{live}}}\right). \tag{2.72}$$

Thus, starting in the first iteration with a normalized prior volume of 1, the prior volume at iteration i has the size

$$X_i = \exp\left(\frac{-i}{n_{\text{live}}}\right). \tag{2.73}$$

The method for drawing new samples above the current likelihood threshold can also vary between different implementations of nested sampling. `MultiNest` uses a region-based approach, namely ellipsoidal rejection sampling. The current live point set is enclosed by multiple ellipsoids, from which samples are drawn randomly until a sample with high enough likelihood is found, while those below the threshold are rejected. The ellipsoids are optimized to have a high probability of covering the remaining parameter space defined by the likelihood threshold, but to avoid including large regions with lower likelihood in order to reduce the sampling overhead. Since with increasing dimensionality an increasing fraction of the sampling volume lies at its boundaries, region based sampling can become inefficient in particular in high-dimensional parameter spaces. The overview paper by Buchner, 2023 shows how ellipsoidal sampling scales with dimensionality.

`MultiNest` is well suited to identify multimodal posterior distributions by detecting distinct groups of ellipsoids without overlaps. These regions can then be treated individually in the rest of the sampling process. Alternatively, the multimodality detection can also be done on specific parameters only or completely disabled, which saves computational cost. Complex non-Gaussian posterior shapes, that means high-dimensional curved, i.e., banana-like, shapes, can still be well captured by many overlapping ellipsoids.

The main critical factors for the runtime of a nested sampling evaluation are the number of live points, the speed of the likelihood evaluation, the efficiency of the generation of new samples, which depends on the specific sampler used, and the distance between prior and posterior, which can be measured as their Kullback-Leibler divergence, D_{KL} (Handley, 2023). The accuracy of the nested sampling result instead depends mainly on n_{live} and D_{KL} (Handley, 2023), which emphasizes especially the importance of an appropriate prior definition.

3 Experimental setup

Parts of the content, figures, and text of this chapter are included in a publication that I have submitted as first author to Nuclear Fusion. I was the main contributor to all the new aspects described, in particular the extension of the Bayesian framework within the `OMFIT ImpRad` module to handle AUG data and to infer pedestal impurity transport using the charge-stage method, the testing of the novel methodology with synthetic data, the execution of the presented discharge with the refined CXRS setup, and the analysis and interpretation of the pedestal Ne transport in the QCE regime. The co-authors contributed by providing advice in discussions and technical support. All co-authors read, commented on, and approved the text.

This chapter describes the diagnostics employed in this work to infer pedestal impurity transport coefficient profiles with the charge-stage method, as outlined in section 1.5. Section 3.1 details the charge-exchange recombination spectroscopy (CXRS) diagnostic, which provides information on the impurity densities of multiple charge stages. The observed spectra also yield the ion temperature profile. Moreover, the radial profiles of electron density and temperature are important for the evaluation of the impurity transport coefficients, as explained in section 4.1.2.1. Therefore, the diagnostics that are routinely used at AUG to determine these quantities are introduced in section 3.2.

3.1 CXRS diagnostic

3.1.1 General principle

CXRS observes spectral line radiance of an impurity I after a charge-exchange (CX) reaction with neutral D from the NBI, when the electron decays from the initial excited state, i.e.,

$$\mathrm{D}^0_{\mathrm{NBI}} + \mathrm{I}^{Z+} \overset{\mathrm{CX}}{\to} \mathrm{D}^+_{\mathrm{NBI}} + \mathrm{I}^{(Z-1)+^*} \to \mathrm{D}^+_{\mathrm{NBI}} + \mathrm{I}^{(Z-1)+} + \text{photon}. \tag{3.1}$$

The radiance (in photons $(\mathrm{Ph}) \cdot \mathrm{m}^{-2} \cdot \mathrm{s}^{-1} \cdot \mathrm{sr}^{-1}$) captured by each line of sight (LOS) is given by the integration along the intersection region of LOS and neutral beam

$$L_{\mathrm{CXline,LOS}} = \frac{1}{4\pi} \sum_n \sum_{j=1}^{4} \int_{\mathrm{LOS}} n_{\mathrm{I},Z} n_{\mathrm{b},n,j} \left\langle \sigma_{\mathrm{CXline},n} u_j \right\rangle_{\mathrm{eff}} \mathrm{d}l. \tag{3.2}$$

Here, $n_{\mathrm{b},n,j}$ is the density of the NBI neutrals in an excitation state with main quantum number n and with a velocity indexed by j. $\langle \sigma_{\mathrm{CXline},n} u_j \rangle_{\mathrm{eff}}$ is the effective CX-emission rate coefficient, calculated from the CX cross-section $\sigma_{\mathrm{CXline},n}$, which is a function of the relative velocity,

$$u_j = |\vec{v}_{\mathrm{b},j} - \vec{v}_{\mathrm{I}}|, \tag{3.3}$$

between the concerned beam neutrals with velocity $\vec{v}_{\mathrm{b},j}$ and impurity ions with velocity $\vec{v}_{\mathrm{I}}$. $\langle\rangle$ indicates the integral over their velocity distributions. The beam consists of several energy/velocity populations since charged D molecules (D^+, D^{2+}, D^{3+}) are accelerated with the same voltage, and subsequently break up during their neutralization, yielding beam neutrals with full, 1/2, and 1/3 beam energy. Besides these three components, there is a population of neutrals with thermal velocity distribution produced by CX between beam neutrals and main ions, the beam halo. It forms the fourth velocity component in equation 3.2.

As the equation shows, the impurity emission observed with CXRS is directly related to the impurity densities. In addition to the impurity transport solver, this relation is included as a synthetic diagnostic in the forward model $\mathcal{M}$ mapping from parameter space to data space. The calculation of $n_{\mathrm{b},n,j}$ and $\langle \sigma_{\mathrm{CXline},n} u_j \rangle_{\mathrm{eff}}$, and the LOS integration are detailed in section 4.1.4. This chapter focuses on the acquisition of the high quality radiance data.

Detailed information on CXRS as a plasma diagnostic can be found in Isler, 1994. Unlike passive spectroscopy, CXRS is able to measure fully ionized impurities and to provide good spatial resolution due to the defined intersection region between NBI and LOS. Furthermore, in addition to determining impurity densities, CXRS can provide ion temperatures and also the (typically toroidal) plasma rotation. It observes radiation in the range of visible wavelengths, which are long enough to resolve the Doppler broadening and wavelength shifts of the spectral lines with sufficient accuracy. Since the plasma is optically thin in this wavelength range, there is moreover no need to account for attenuation of the radiation within the plasma.

3.1.2 Specific setup

The transport analyses in this thesis focus on Ne, although the framework can, in principle, be applied to other impurities as well, such as Ar or N. Since the charge-stage method requires a stationary impurity content, best eligible are impurities that can be puffed. Moreover, multiple charge stages must be present in the pedestal, with spectral lines that can be observed with CXRS, and for which the effective CX-emission rate coefficients are determined. Ne is advantageous due to its moderate atomic number (10), which is high enough to have significant densities of non-fully stripped ions throughout the pedestal, in particular the He- and H-like charge stages, but low enough to provide good interpretability of the CXRS signal due to known effective CX-emission rate coefficients. In addition, Ne is likely to be used for radiative power exhaust in ITER (Campbell et al., 2024), hence its transport properties are of particular interest.

Figure 3.1 shows a schematic of the experimental setup. It is similar to the one in Dux et al., 2020, which also uses the AUG CXRS system with a radial array of toroidally looking LOS to measure multiple Ne charge stages. Due to the CX-reaction that induces the observed line radiation, as stated in equation 3.1, the density of the Ne^{Z+} charge stage, which will further be used to refer to the data, is represented by the radiance of a $\mathrm{Ne}^{(Z-1)+}$ transition. The spectral lines used to provide information about the Ne^{10+}, Ne^{9+} and Ne^{8+} densities are NeX $n = 11 \rightarrow 10$ at 524.88 nm, NeIX $n = 14 \rightarrow 12$ at 610.44 nm and NeVIII $n = 10 \rightarrow 9$ at 606.82 nm. Additional CX-lines (NeVIII $n = 13 \rightarrow 11$ at 606.41 nm and carbon CVI $n = 8 \rightarrow 7$ at 529.0 nm), which are not used, are also visible in the spectra.

The Ne^{8+} CX-line can hardly be distinguished from the equivalent CX-line of fully ionized oxygen (O) since the Doppler broadening differs only by 10 % (Dux et al., 2020). However, also the effective CX-emission rate coefficients of these spectral lines are approximately the same since the atoms are Rydberg-like for the high principal quantum number (14) into which the CX takes place. Thus, the impurity density information retrieved according to equation 3.2 from the combined $\mathrm{Ne}^{8+} + \mathrm{O}^{8+}$ spectral line when assuming Ne^{8+} rate coefficients can be attributed to the sum of the Ne^{8+} and O^{8+} densities. Therefore, the impurity transport solver in the forward model is additionally run for O and the summed densities are compared to the radiance data

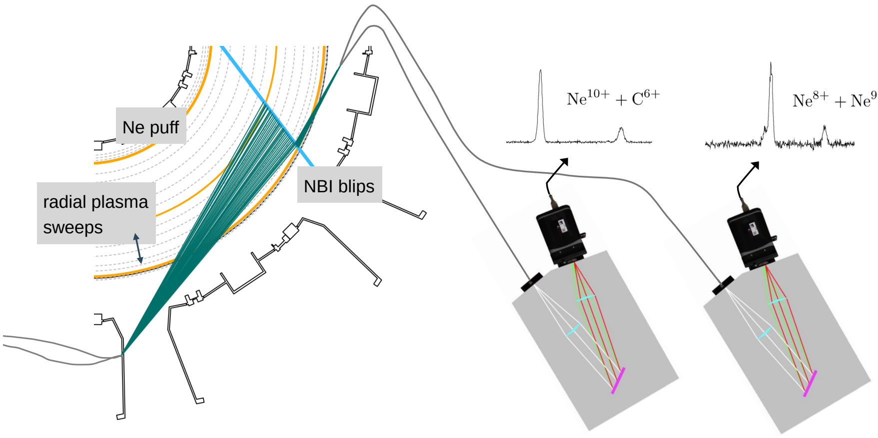

Figure 3.1: Schematic of the diagnostic setup. The top-down view of a torus segment shows the toroidally looking LOS of the core and edge CXRS systems (dark green, looking on the beam from different sides), from their intersection points with beam 3 of NBI box 1 in sector 16 (blue) to the respective optical heads. The plasma is indicated by the magnetic axis and separatrix (orange) and further flux surfaces (light grey). The LOS of each optical head are alternately imaged on 2 spectrometers, which observe spectral lines that contain information on the densities of the 3 charge stages 10+, 9+ and 8+ of the puffed Ne impurity. Beam 3 is used for the diagnostic, and all other beams from box 1 are turned off. NBI dips and, where possible, radial plasma sweeps are applied to improve the data quality.

using the Ne^{8+} effective CX-emission rate coefficients.

At AUG, the NBI system consists of 8 beams, 4 of which are injected from each of the 2 beam boxes, located on opposite sides of the torus. The maximum extraction voltages are 60 kV and 93 kV for box 1 and box 2, respectively. Each beam can deliver an individually adjustable power of maximally 2.5 MW. Optical heads for CXRS measurements are installed on both torus sides, allowing beams from either box to be used for diagnostic purposes. However, the optical heads whose LOS specifically observe the plasma edge are located in sector 16, designed to observe beams from box 1. As the LOS go through the center of beam 3 and their focal points are optimized for this beam, this beam is employed for the CXRS data acquisition in this work.

Beam 3 is observed with a radial array of toroidally looking LOS from different optical heads. In both campaigns concerned in this thesis (2021 and 2022), the LOS of the CER optical head, observing the plasma core, were imaged on two spectrometers, called CER and CAR. This setup is in the following referred to as core CXRS system. In the setup used for the presented discharges, the plasma edge was observed with the CMR-1 and CMR-2 optical heads, and additionally with the CMR-3 optical head in the 2022 campaign. Their LOS were imaged on two spectrometers, called CMR and CPR, which is in the following referred to as edge CXRS system. The core CXRS system consisted of 45 LOS in both campaigns and the edge CXRS system consisted of 22 LOS in the 2021 campaign and 32 LOS in the 2022 campaign. Figure 3.2 shows an example of the LOS viewing geometry in the pedestal with respect to beam 3. It demonstrates that the region observed with the LOS of the edge CXRS system is more tangential to the flux surfaces and therefore better resolved in the radial direction.

All the spectrometers are of the Czerny-Turner type, with 2400 l/mm gratings and charge-coupled device (CCD) cameras. The minimal exposure times depend on the cameras and are

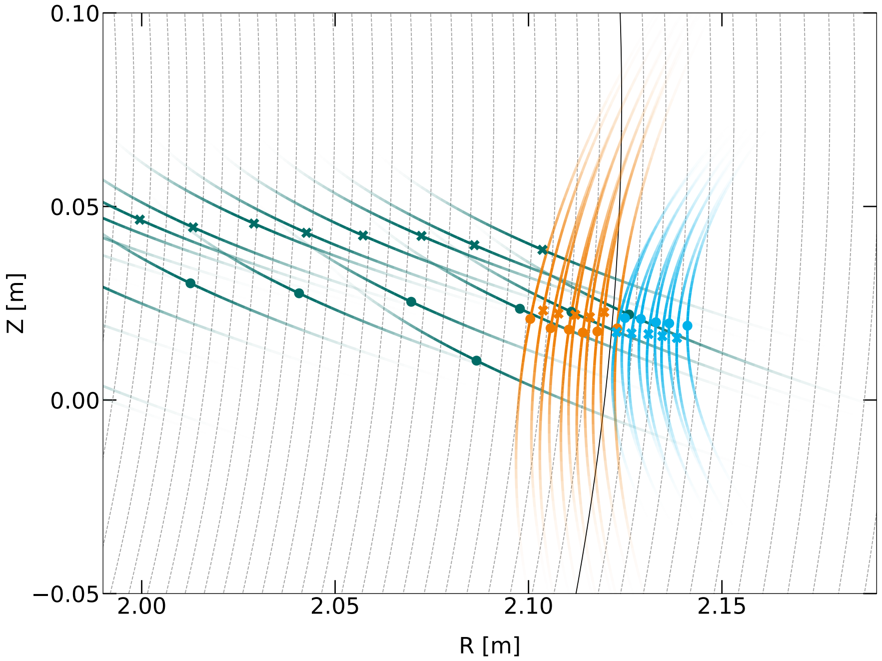

Figure 3.2: Example of the LOS configuration in the poloidal plane. The projections of the LOS onto the poloidal plane appear as curved trajectories. The transparency indicates the density of the first energy component of the NBI beam normalized to its maximum along each LOS. The points of maximum beam density are indicated by the markers. This example shows the setup of the 2021 campaign, specifically for #39461, observing beam 3. 3 optical heads are used, CER (dark green) for the core CXRS system, and CMR-1 (orange) and CMR-2 (blue) for the edge CXRS system. Their LOS are distributed on different spectrometers, CER and CPR measuring Ne^{10+} (crosses), and CAR and CMR measuring Ne^{8+} and Ne^{9+} (dots). The graphic shows the plasma edge region with the separatrix (black) and the other flux surfaces in distances of $\rho_{\text{pol}} = 0.01$ (grey), calculated from the equilibrium at 5.38 s.

about 5 ms for the core CXRS system and about 2.5 ms for the edge CXRS system. Since the fibers are arranged in a vertical stack in front of the spectrometer entrance slit, the CCD chip is binned into vertical regions of interest (ROIs), which define the spectrometer channels. The light is transmitted from the optical heads in the torus to the spectrometers in the laboratory through a series of two (or more) optical (quartz glas) fibers, which are connected at a fiber connector board. Prior to all the presented discharges, the configuration for the connection of the LOS to the spectrometer channels was modified by dis- and re-connections at this connector board. Namely, the LOS of the edge CXRS system were distributed alternately on the CMR and CPR spectrometers. This is because the CPR spectrometer is usually dedicated to measuring the poloidal plasma rotation for radial electric field studies, which require poloidally looking LOS. In contrast, the LOS of the core CXRS system were consistently imaged on the CER and CAR spectrometers without changes in LOS-channel attributions throughout the campaigns.

The steady-state approach with constant impurity densities supports a high data quality. It allows the data to be averaged in time, and moreover NBI dips can be used for subtraction of passive contributions to the spectra, and radial plasma sweeps can be performed for measurements at more radial positions. More details on the data evaluation are provided in section 3.1.4.

3.1.3 Calibrations

3.1.3.1 Geometry calibrations

The geometry of all LOS is determined using a robot arm provided by FARO (FARO Technologies, 2024), which is installed in the vessel during its openings. The fibers are backlit in the laboratory, and several spatial points in the center of the LOS light cone are measured around the focus point of the LOS with the robot arm. A straight line is then fitted through these points to define the LOS geometry. This method achieves an accuracy $\leq 1\,\mathrm{mm}$.

3.1.3.2 Spectrometer calibrations

The grating equation for a spectrometer is given by

$$n \cdot g \cdot \lambda = \cos\epsilon \cdot (\sin\alpha + \sin\beta)\,. \tag{3.4}$$

Here, n is the diffraction order, g the grating constant (in this case 2400 l/mm), λ the wavelength, α the horizontal angle of incidence on the grating, and β the horizontal diffraction angle. ϵ represents the vertical angle between the incident light and the horizontal plane, which results in a parabolic vertical image of a straight vertical line. This parabola is particularly important as the fibers imaged to the different spectrometer channels are arranged in a vertical stack in front of the entrance slit. The dispersion and the vertical parabola are measured using spectral arc lamps. The size of the image on the CCD chip depends on two factors, namely the ratio between the focal lengths of the two lenses or mirrors that collimate the light and focus it onto the CCD chip, called image ratio, and on the magnification in dispersion direction due to the angle of the grating.

Apart from the ideal grating equation, the image is influenced by the spectrometer optics, in particular the finite width of the entrance slit, which is typically between 50–100 μm, and other imperfections, which are together summarized in the instrument function. These factors broaden the measured spectral lines, meaning that a single wavelength is imaged onto a larger wavelength range. The image of the entrance slit produces an intesity profile in the form of a square function, while all other influences are well approximated by a Gaussian because the lenses in the spectrograph produce Gaussian profiles. The width of the square function and the full width at half maximum (FWHM) of the Gaussian are also calibrated using spectral arc lamps.

The finite frame transfer time of the CCD camera, which is determined by the shift speed and the size of the CCD chip in the shift direction, causes the actual exposure time to be shorter than the set value. This offset is quantified by a linear fit of the count rate along a scan in exposure time, using a constant light source. For both edge CXRS spectrometers, the exposure time is approximately 0.3 ms shorter than the repetition time.

The photons arriving at the CCD chip pixels are converted into (photo-)electrons, which can be amplified with an electron-multiplying gain (EM-gain) controlled by an adjustable voltage. After amplification, the electrons are converted into digital counts by an analog-to-digital (AD) converter. Its controller gain provides three predefined settings for low (1), medium (2) and high (3) count rate, based on the electrons acquired on the CCD chip after potential electron multiplication. Since the EM-gain leads to additional noise, it should only be applied when necessary.

For the calibration of the controller gain and the readout noise of the AD-converter, the count noise σ_c is measured for different count numbers n_c. It is assumed that the count noise depends on the electron noise σ_e and the readout noise σ_AD as

$$\sigma_\mathrm{c}^2 = \Phi^2 \sigma_\mathrm{e}^2 + \sigma_\mathrm{AD}^2, \tag{3.5}$$

where Φ represents the counts per electron resulting from the AD converter. When the EM-gain is disabled, the electron noise equals the photon noise, which follows a Poisson distribution. Therefore, the variance σ_e^2 is equal to the number of electrons acquired on the CCD pixel n_e. Substituting this into equation 3.5 yields

$$\sigma_\mathrm{c}^2 = \Phi^2 n_\mathrm{e} + \sigma_\mathrm{AD}^2 = \Phi n_\mathrm{c} + \sigma_\mathrm{AD}^2. \tag{3.6}$$

Instead, if the EM-gain is enabled, the associated noise statistics must be included, introducing an additional factor of $2g$ in the electron noise variance, where g is the EM-gain (Ryan et al., 2021). Φ and σ_AD can be directly determined as slope and intercept of a linear fit. This calibration procedure is repeated for all possible controller gain settings in combination with the EM-gain set to 0 and 1.

Moreover, the actual EM-gains g corresponding to the set EM-gains g_set must be calibrated. The actual EM-gain is determined for a range of EM-gain settings by calculating the ratio of the count rate with respect to the count rate with the EM-gain set to 1. The AD offset count rate, measured with closed shutter, is therefore subtracted. In a double logarithmic plot, the result is an approximately straight line with

$$\ln(g) = f_\mathrm{g} \cdot \ln(g_\mathrm{set}), \tag{3.7}$$

from which a correction factor f_g can be obtained. This factor was found to be approximately 0.729 for the CPR spectrometer and approximately 0.942 for the CMR spectrometer. However, f_g has a non-linear dependence on the total number of counts. To account for this, the measurement is repeated several times with n_c approximately fixed at different values by decreasing the exposure time accordingly as the EM-gain increases. For a given n_c of a signal, f_g is then interpolated from its values at different n_c to retrieve g.

The spectrometer calibrations, and in particular the gain calibrations, are not always repeated between experimental campaigns. However, for this thesis, they were repeated specifically for the edge CXRS spectrometers due to suspected issues.

3.1.3.3 Spectral radiance calibrations

In order to obtained absolutely calibrated spectral radiance measurements, the calibration constants that relate the measured count rate with the emitted spectral radiance for different wavelengths must be determined. Therefore, the optical heads in the vessel are irradiated with a well-characterized light source. An Ulbricht sphere of known spectral radiance $L_{\mathrm{sphere},\lambda}$ is used for this purpose. It is positioned approximately at the focus position of the LOS, using fiber backlighting to ensure that its opening covers the whole focus spot. The signal is measured over a scan across the full range of wavelengths for which the CXRS diagnostic can be used. From this data, the sensitivity of each channel is calculated, depending not only on the wavelength but also on the specific pixel, as

$$S_{\lambda,\mathrm{pixel}} = \frac{n_\mathrm{c}}{\Delta t_\mathrm{exp} \cdot L_{\mathrm{sphere},\lambda} \cdot \Delta\lambda_\mathrm{pixel}} \left[\frac{\mathrm{counts}}{\mathrm{Ph} \cdot \mathrm{m}^{-2} \cdot \mathrm{sr}^{-1}}\right]. \tag{3.8}$$

Here, Δt_exp is the exposure time, and $L_{\mathrm{sphere},\lambda} \cdot \Delta\lambda_\mathrm{pix}$ is the number of photons emitted per unit time, area, and solid angle in the wavelength range that is seen by the concerned pixel. The entrance slit width and the gain settings of the calibration are saved. Thus, if the gain is changed during later measurements, correction factors can be applied.

The intensity calibration is also repeated by irradiating the fibers at the connector board in the laboratory, instead of the optical heads in the vessel. Thereby, the transmission from the vessel to the connector board can be separated from the intensity calibration starting at the connector board. As a result, it is possible to redistribute LOS to different spectrometer channels during the campaign, while still being able to retrieve an absolute calibration. However, it should be noted that when LOS are unplugged to connect them to other spectrometer channels, their calibration may be affected by poor connections at the fiber connector board, as well as by newly introduced dust and scratches. If only few LOS are affected while others remain perfectly calibrated throughout the campaign, cross-calibration between channels can be used to correct for the introduced calibration errors. In doing this, it should be kept in mind that the errors may be wavelength-dependent.

Moreover, since the optics typically experience some degradation during a campaign, the intensity calibrations are repeated both before and after each campaign, resulting in pre- and post-campaign calibration data. The selection of which calibration to use for evaluating CXRS data depends on the observed degradation and the time point of the discharge during the campaign. This includes both the degradation of the optical head and of individual channels due to unplugging.

Table 3.1 summarizes the choices regarding the calibrations used for the data evaluation in this thesis. They are based on comparisons of the data profiles with both respective calibration options and on the analyses of the optics degradations in the respective campaigns. In the 2021 campaign, the CER optical head, which is used for the core CXRS system, showed minimal degradation, with a decrease of $\leq 5\,\%$ across all relevant wavelengths. In the 2022 campaign in contrast, a stronger degradation was observed. This degradation was reconstructed using the evolution of routine Z_eff calculations, which are derived from B CXRS measurements on the CER spectrometer, with the pre- and post-campaign calibrations serving as boundary conditions. The corresponding correction was implemented in the data loading routine to be automatically applied. The optical heads used for the edge CXRS system did also not degrade much in the 2021 campaign. In the 2022 campaign, however, in particular those LOS that were frequently switched to be imaged on the CPR spectrometer suffered from degradation. Moreover, for all data acquired on the CPR spectrometer, the calibrations are retrieved from calibrations of the LOS on the CMR spectrometer in combination with the calibrations starting at the fiber connector board on the CPR spectrometer. Thus, these LOS were never consistently calibrated without any unplugging.

3.1.3.4 Shot-to-shot calibrations

To calibrate the exact wavelength axis on the CCD chip, which changes when the grating is turned, a spectral Ne lamp is switched on after each discharge. Its spectrum is observed on one

	CER	CAR	CMR	CPR
#39084	pre	pre	pre	pre
#39086	pre	pre	pre	pre
#39456	pre	pre	post	post
#39461	pre	pre	post	post
#39463	pre	pre	post	post
#40014	shot dependent correction based on Z_{eff}	shot dependent correction based on Z_{eff}	pre	pre
#40219	shot dependent correction based on Z_{eff}	shot dependent correction based on Z_{eff}	pre	pre

Table 3.1: Pre- or post-campaign calibration choices for the evaluated discharges. Which calibration data is used depends on several factors, such as the point of time within the campaign and the observed degradation of the optical head. For all discharges, the measured radiance profiles were compared using both calibration options, and the better one was selected.

of the spectrometer channels and averaged over several frames. The wavelengths of strong Ne lines in the typical spectral ranges of the CXRS diagnostic are known and identified by their approximate positions in the averaged spectrum. The lines are fitted as Gaussians, and the shifts of their means with respect to the theoretical wavelengths of the lines are compared. If these shifts are similar, their mean is taken as correction for the wavelength axis.

The channel observing the Ne lamp is also used to acquire background frames after the discharge, i.e., without any light, measuring the AD offset counts. This signal is subtracted from the data of all channels. The background-subtracted data is thereafter further corrected for the cross-talk due to illumination during the frame transfer, also known as smear. During the plasma phase, the Ne lamp channel should not detect any signal, making it suitable to represent the smear contribution. The measured intensity in this channel is thus subtracted from all other channels, at matching horizontal pixels along the wavelength axis and matching time frames. To account for potential differences in the width of the ROIs of different channels, the smear contribution is weighted according to the respective ROI sizes, thus assuming that the cross-talk per vertical pixel is constant.

3.1.4 Data evaluation

Figure 3.3 illustrates the evaluation of the spectral lines. It shows that even in the case where there are many passive lines around the active lines, cleaned spectra containing only the CX-lines can be retrieved. This is achieved through averaging in time and subtraction of passive background contributions to the spectra, which originate from processes such as radiative recombination, dielectronic recombination, or electron impact excitation.

The time intervals with stable voltage of beam 3 are identified as beam-on phases, and the time intervals with no beam power of beam 3 as beam-off phases. In scenarios with non-stationary conditions caused by ELMs, only those spectra which are within the time range of interest relative to the ELM onset are included. This ELM synchronization procedure is described in more detail in section 6.2.1. The spectra from both beam-on and beam-off phases are then sorted by the outermost radius on the separatrix R_{aus} at the time they were acquired. Afterwards, they can be averaged in groups of a few spectra and their corresponding R_{aus} is also averaged. The averaging of their data points y_i is done weighted by their variances σ_i^2, which are returned by

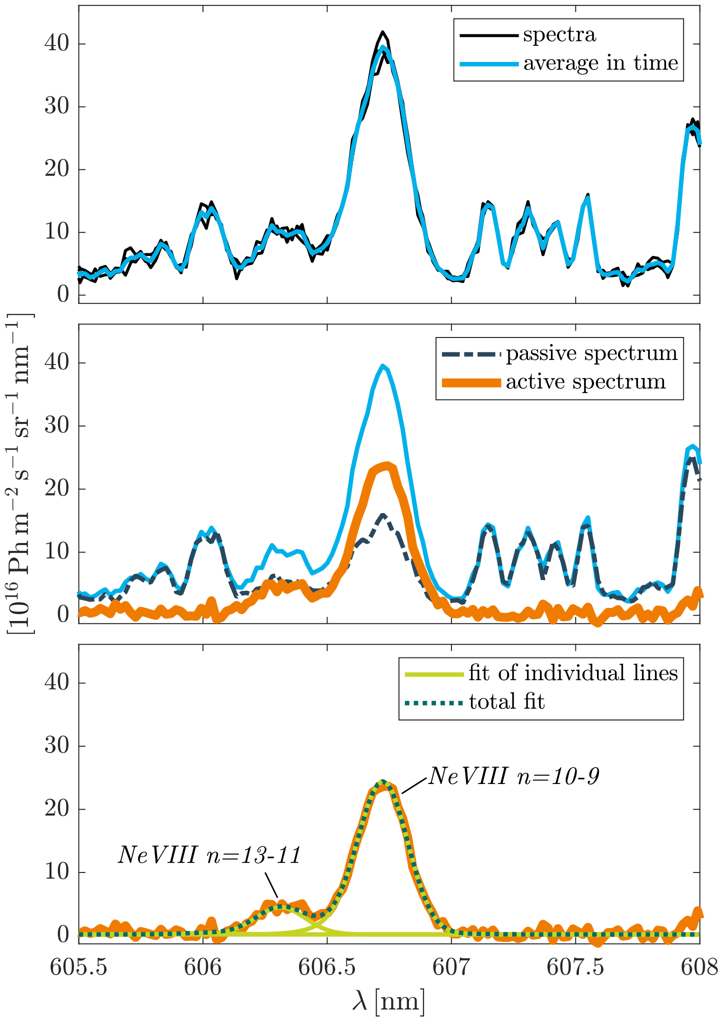

Figure 3.3: Example of the evaluation of the observed spectra. Due to the steady-state condition the spectra can be averaged in time (top), subsequently, the passive spectra, measured during the phases without NBI, are subtracted (middle), and finally, the spectral lines are fitted, taking the fine structure and Zeeman splitting into account (bottom). The spectra shown are examples of data frames from the LOS CMR-1-3 in #39461, which was observing the pedestal top, and the averaging was done over 3 spectra.

the data reading routine according to the photon statistics and the AD-converter noise, i.e.,

$$\overline{y} = \frac{\sum \frac{y_i}{\sigma_i^2}}{\sum \sigma_i^2}. \tag{3.9}$$

Next, the averaged passive spectra are interpolated to the positions of the averaged active spectra based on R_{aus}, and are subtracted. Moreover, a wavelength range without dominant spectral lines is selected, and a mean background level is calculated for each spectrum from the signal in this range. This background is subtracted from the entire spectrum.

The fits of the so prepared spectral lines are based on the interpolation of line shapes that were precalculated on a logarithmic temperature grid. This grid covers temperatures from 60 eV to

8000 eV and consists of 23 values evenly spaced on the logarithmic scale. For each temperature value on the grid, the line shapes are calculated for all LOS, including the Doppler broadening, the instrument function (cf. section 3.1.3.2), the Zeeman effect due to the magnetic field, and the fine structure splitting. The magnetic field is approximated by the field at the intersection of the LOS with the beam center, evaluated at the median time of the time interval considered.

For the calculation of the Zeeman effect, the typical set of quantum numbers is used to describe the energy levels of the ion:

$$\text{main quantum number: } n = 1, 2, 3, ... \tag{3.10}$$

$$\text{orbital angular momentum quantum number: } l = 0, 1, 2, ..., n-1 \tag{3.11}$$

$$\text{spin quantum number: } s = \pm\frac{1}{2} \tag{3.12}$$

$$\text{total angular momentum quantum number: } j = |l+s| = |l \pm 0.5| \tag{3.13}$$

$$\text{projection of the total angular momentum quantum number: } m = -j, -(j-1), ..., j-1, j \tag{3.14}$$

An observed spectral line corresponds to a specific transition between an upper and a lower n-state, but includes contributions from various combinations of the other quantum numbers. This is because their wavelengths are very close, such that the broadened spectral lines overlap strongly. However, the only transitions that are allowed are those that satisfy the quantum mechanical selection rules

$$\Delta l = \pm 1, \tag{3.15}$$

$$\Delta m = 0, \pm 1. \tag{3.16}$$

The wavelengths of all allowed transitions are determined from the energy differences between the corresponding quantum states, and are subsequently divided by the refractive index of air, which is calculated using the Edlén equation.

For the calculation of the energy differences, the ion is approximated to be Rydberg-like. For such an ion, the basic energy levels, determined by the main quantum number, are

$$E_0 = -\frac{R_\infty}{1 + \frac{m_\mathrm{e}}{m_\mathrm{ion}}} \frac{Z^2}{n^2}, \tag{3.17}$$

where R_∞ is the Rydberg constant, m_e is the electron mass, and m_ion and Z are the mass and charge of the ion. The fine structure splitting, which arises from the spin-orbit interaction caused by their magnetic moments, modifies the energy levels to

$$E_\mathrm{f} = E_0 \left(1 + \frac{Z^2\alpha^2}{n}\left(\frac{1}{j+\frac{1}{2}} - \frac{3}{4n}\right)\right), \tag{3.18}$$

where

$$\alpha = \frac{e^2}{4\pi\epsilon_0 \hbar c} \approx \frac{1}{137} \tag{3.19}$$

is the Sommerfeld fine structure constant. α is defined by the elementary charge e, the speed of light c, and $\hbar = \frac{h}{2\pi}$ with the Planck constant h. The fine structure splitting results in every l-level except for $l = 0$ being split into two sublevels. Furthermore, neighboring values of l can have the same energy level. Any hyperfine structure effects and the Lamb shift corrections are not included as they are very small.

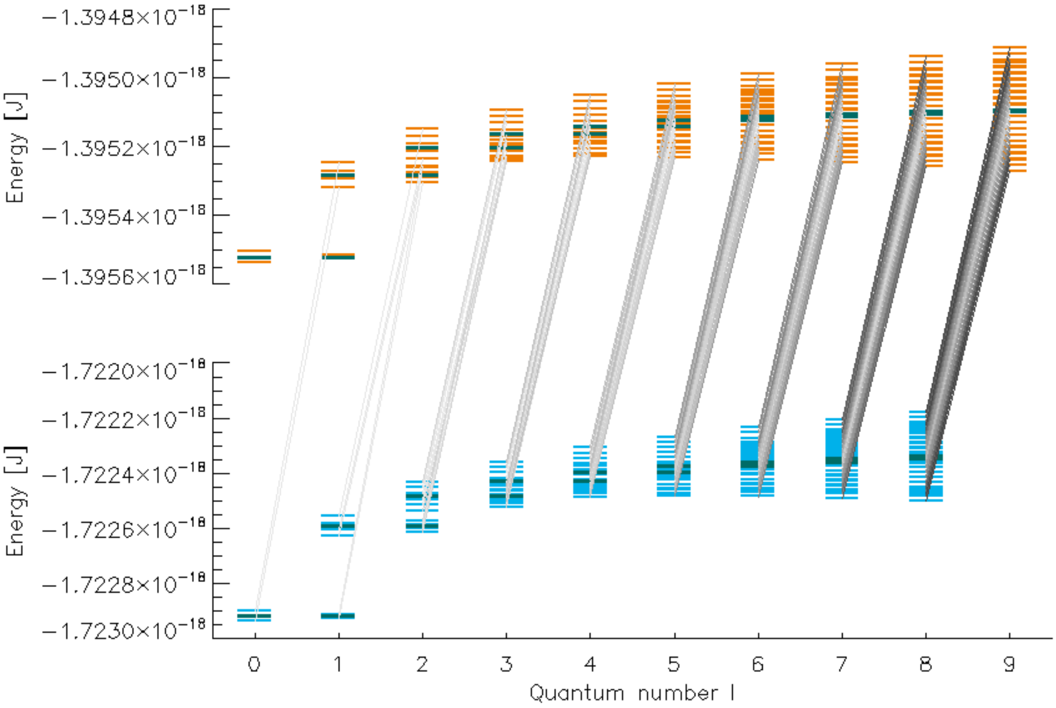

Figure 3.4: Example of the electron transitions included in the spectral line shape calculations. For the spectral line NeVIII $n = 10 \to 9$, the energy levels of the fine structure splitting (dark green), and the final energy levels used for the spectral line shape calculation (orange and blue), including the Zeeman splitting, are shown, for the $n = 10$ level (top, orange) and the $n = 9$ level (bottom, blue), for different quantum numbers l each. The relative intensities of the individual spectral line components are indicated by the transparency of the lines connecting the respective energy levels (grey). All transitions with less than 10 % of the maximum line intensity are not plotted. Evidently, transitions with $\mathit{\Delta} l = +1$ contribute much less than transitions with $\Delta l = -1$. The magnetic field used for the calculation of the Zeeman splitting was retrieved from the equilibrium of #39461 at 5.38 s, at the point of maximum NBI beam density along the LOS CMR-1-3, i.e., at the pedestal top.

The Zeeman splitting is due to the interaction of spin and orbit with the external magnetic field. To calculate it, the Landé g-factors are defined as

$$g_s = 2 + \frac{\alpha}{\pi} - 5.946\frac{\alpha^2}{\pi^2} \approx 2, \tag{3.20}$$

$$g_l = 1 - \frac{m_\mathrm{e}}{m_\mathrm{ion}} \approx 1, \tag{3.21}$$

and the Bohr magneton as

$$\mu_\mathrm{B} = \frac{e\hbar}{2m_\mathrm{e}}. \tag{3.22}$$

The exact solution for the Zeeman splitting, without any approximation for the magnetic field strength B, depends on l and m, and yields the following energy levels:

$$E_{l,m} = \begin{cases} E_{\mathrm{f}} + \mu_B B g_s m & \forall\, l = 0 \\ E_{\mathrm{f},+} + \mu_B B \left(g_l m - 0.5(g_s - g_l)\right) & \forall\, l > 0,\ m = -l - 0.5 \\ E_{\mathrm{f},+} + \mu_B B \left(g_l m + 0.5(g_s - g_l)\right) & \forall\, l > 0,\ m = l + 0.5 \\ \left(E_{\mathrm{f},+} + E_{\mathrm{f},-}\right)/2 + \lambda_{\mathrm{eig}}[M_{l,m}] & \forall\, l > 0,\ -l + 0.5 \leq m \leq l - 0.5, \end{cases} \tag{3.23}$$

with

$$M_{l,m} = \begin{bmatrix} \frac{1}{2}\Delta E_{\mathrm{f}} + \mu_B B \left(g_l m + \frac{(g_s - g_l)m}{2l+1}\right) & \frac{\mu_B B (g_s - g_l)\sqrt{(2l+1)^2 - 4m^2}}{2(2l+1)} \\ \frac{\mu_B B (g_s - g_l)\sqrt{(2l+1)^2 - 4m^2}}{2(2l+1)} & -\frac{1}{2}\Delta E_{\mathrm{f}} + \mu_B B \left(g_l m - \frac{(g_s - g_l)m}{2l+1}\right) \end{bmatrix}. \tag{3.24}$$

Here, $E_{\mathrm{f},+}$ and $E_{\mathrm{f},-}$ represent the two fine structure energy levels for a given $l > 0$, as stated in equation 3.18, $\Delta E_{\mathrm{f}} = E_{\mathrm{f},+} - E_{\mathrm{f},-}$, and $\lambda_{\mathrm{eig}}[M_{l,m}]$ are the eigenvalues of the matrix $M_{l,m}$. By applying the approximations for g_s and g_l as stated in equation 3.20, the formula that is often found in the literature, such as in Bethe et al., 1977, p. 211, is recovered. The relative intensities of the allowed transitions between the different energy levels are derived from their dipole radiation. Figure 3.4 shows an example of the energy levels and transition intensities corresponding to an observed spectral line.

The individual spectral line components determined by the fine structure and Zeeman splitting are subject to Doppler broadening caused by the thermal motion of the ion, which yields a Gaussian with FWHM

$$\Delta\lambda_{\mathrm{FWHM},T} = 2\sqrt{2\ln 2}\,\frac{\lambda_0}{c}\sqrt{\frac{T_{\mathrm{i}}}{m_{\mathrm{ion}}}}, \tag{3.25}$$

for a central wavelength λ_0. Additionally, the instrument function of the spectrometer, calibrated as described in section 3.1.3.2, broadens the image of the spectral line on the CCD chip. These two contributions are convolved into a common line broadening function. The complete spectral line shape used to fit the data is then obtained as the sum of the individual broadened spectral components, weighted according to their relative intensities.

The fits of the spectral lines are done with a Levenberg-Marquardt χ^2-minimization, making use of the IDL function `MPFITFUN`. Since the signal-to-noise ratio is better for the Ne^{10+} data in the core and for the Ne^{8+} and Ne^{9+} data in the edge, the temperature fits of the other CX-lines are constrained by the fitted temperatures of these CX-lines in the core and edge CXRS systems, respectively. This ensures that all spectral line fits have approximately the same temperatures at the same radial positions. The maximum allowed discrepancy is set to be $\pm 100\,\mathrm{eV}$. While the temperatures and spectral line radiances follow directly from the fits, the plasma velocity v_{P}, although not needed in this work, can be calculated from the wavelength shift $\Delta\lambda$ using the relation

$$\frac{\Delta\lambda}{\lambda} = \cos(\theta)\frac{v_{\mathrm{P}}}{c}, \tag{3.26}$$

where θ is the angle between the (approximately toroidal) B-field and the LOS.

Any other effects that could influence the CXRS signal, in particular the CX cross-section effect and the gyro-motion effect, are not included since they are small (Viezzer, 2012). Also the plume effect, which is an additional signal contribution not originating from the NBI CX, but from re-excitation of the recombined CX ions after the NBI CX (Kappatou et al., 2018), is neglected. As it is connected to the NBI CX, it is not subtracted with the spectra acquired during beam-off phases. However, its contribution is only substantial for light impurities, especially He.

3.2 Background plasma diagnostics

3.2.1 Thomson scattering

The Thomson scattering diagnostic is based on the elastic scattering of light injected into the plasma with a laser by the electrons in the plasma. Due to their small mass, the electrons are accelerated in the electromagnetic field of the laser. Their oscillation emits dipole radiation at the laser frequency, which is detected with a double Doppler shift, due to the movement of the electrons relative to the laser and relative to the detector. n_e can be determined from the intensity and T_e from the Doppler broadening of the measured radiation. Since Thomson scattering is the only diagnostic that allows for the simultaneous observation of both n_e and T_e, it plays a crucial role in ensuring the correct relative alignment of their profiles.

AUG has two Thomson scattering systems observing the plasma core and edge, respectively, the details of which are described in Murmann et al., 1992 and Kurzan et al., 2011. Both systems utilize pulsed Nd:YAG lasers with a wavelength of $1.06\,\mu$m. The core Thomson scattering system consists of 16 channels, while the edge system consists of 11 channels, which measure at different radial positions. The temporal resolution is limited to at least 8 ms due to the repetition time of the laser pulses, and the radial resolution is around 25 mm for the core system and around 3 mm for the edge system.

3.2.2 Electron cyclotron emission radiometry

The electrons in the plasma emit cyclotron radiation at their cyclotron frequency and its harmonics due to the gyromotion. Assuming a Maxwellian electron velocity distribution and an optically thick plasma, the electron cyclotron emission (ECE) intensity complies with Planck's law for black body radiation due to absorption and re-emission of the light. Therefore, the signal strength depends directly on T_e. Furthermore, due to the approximately radial variation of the magnetic field and the linear dependence of the emission frequency on the magnetic field, the frequency can be matched to a radial position.

As the ECE diagnostic relies on the assumption of an optically thick plasma, it can provide inaccurate results at the plasma edge, where the densities are too low to maintain this condition. This effect is known as ECE shine through. A correction for it was developed for AUG in Rathgeber et al., 2012. Additionally, issues can arise if the plasma density is too high, causing the ECE emission frequency to be below the cut-off frequency of the plasma, thus preventing the propagation of the electromagnetic wave.

The fundamentals of the ECE diagnostic setup at AUG are detailed in Salmon, 1994. The diagnostic employs a heterodyne radiometer as receiver, which is capable of measuring 60 frequencies in the range from 89 GHz to 187 GHz. The diagnostic therefore has 60 channels measuring at different radial positions with a high radial resolution of $< 1\,\mathrm{cm}$, and a high temporal resolution of $< 1\,\mathrm{ms}$.

3.2.3 Lithium beam emission spectroscopy

A neutral lithium (Li) beam is injected into the plasma, where it undergoes collisional excitation or ionization. The excitation processes give rise to line radiation as electrons decay from excited states. This emitted light can be observed and, by applying collisional-radiative modelling, n_e can be derived from this data, as explained in Schweinzer et al., 1992. Typically, the LiI line at 670.8 nm is used for this purpose.

Since the Li beam is attenuated in the plasma by the ionization processes, the diagnostic is primarily useful at the plasma edge. The system at AUG is described in Willensdorfer et al., 2014. Its beam is injected horizontally in the upper half of the torus on the LFS. Two different optics observe the beam, one from above with 35 channels, and a newer one from the side with shorter LOS and 26 channels. The beam is modulated to subtract passive contributions to the signal, so data are only available for the beam-on time intervals. Due to the large number of channels measuring at the plasma edge, the Li beam diagnostic provides a high radial resolution $< 1\,\mathrm{cm}$. Moreover, it has a high temporal resolution $< 1\,\mathrm{ms}$.

3.2.4 Deuterium cyanide laser interferometry

The refractive index of the plasma depends on n_e, since the plasma frequency is density dependent. Interferometry measures the phase shift of a laser beam passing through the plasma relative to a reference beam that does not pass through the plasma. The line-integrated density can be calculated very exactly from this shift. However, the measurement is prone to so-called fringe jumps, which occur if the number of phase shifts is not correctly tracked during the discharge. Post-discharge corrections are sometimes necessary, making use of data from other diagnostics.

At AUG, a far-infrared deuterium cyanide (DCN) laser with a wavelength of $195\,\mu\mathrm{m}$ is used. The system includes 5 different injection paths ranging from the plasma core to the edge and has a high temporal resolution $< 1\,\mathrm{ms}$.

3.2.5 Integrated data analysis

An integrated data analysis (IDA) framework (Fischer et al., 2010) is routinely employed at AUG. This framework uses Bayesian statistics to combine data from the diagnostics presented above. It infers the MAP profiles of n_e and T_e as functions of ρ_pol.

4 Inference framework

Parts of the content, figures, and text of this chapter are included in a publication that I have submitted as first author to Nuclear Fusion. For further details, see chapter 3.

The impurity transport coefficients D and v are derived in the pedestal of AUG discharges from radial profiles of impurity line radiances measured with CXRS, as detailed in section 3.1. With such observations, providing information on the density profiles of ≥ 2 impurity charge stages in stationary plasmas with stable impurity content, the number of unknowns in the coupled system of transport equations, given in equation 1.13, is reduced to fewer than the number of equations. This relies on the assumption that D and v are identical for all charge stages, which is justified when charge stages with similar Z dominate. Yet, the forward model mapping the transport coefficients to the impurity line radiances is non-linear, and it includes additional unknowns, in particular the neutral impurity source in the SOL, which involves recycling, and the level of thermal neutral D density, which is difficult to measure. For these reasons, complex non-Gaussian error statistics can occur. Consequently, the inverse problem is more robustly addressed with appropriate uncertainty quantification by inferring the full probability distribution of the parameters according to Bayesian statistics using Bayesian sampling.

Figure 4.1 provides an overview of the full inference framework. The forward model is detailed in section 4.1, while the details of the inverse inference are described in section 4.2. Finally, the `ImpRad` module within the One Modeling Framework for Integrated Tasks (`OMFIT`), into which much of the framework is embedded, is introduced in section 4.3.

4.1 Forward model

4.1.1 Magnetic geometry reconstruction

The magnetic geometry of the plasma equilibrium is essential for various components of the inference framework. It can be obtained by solving the Grad-Shafranov equation, which describes the poloidal magnetic flux in the tokamak according to ideal MHD (Zohm, 2014):

$$R\frac{\partial}{\partial R}\left(\frac{1}{R}\frac{\partial\psi}{\partial R}\right)+\frac{\partial\psi^2}{\partial z^2}=-\mu_0\left(2\pi R^2\right)\frac{\mathrm{d}p}{\mathrm{d}\psi}-\mu_0^2\frac{\mathrm{d}I_\mathrm{p}}{\mathrm{d}\psi}I_\mathrm{p}. \tag{4.1}$$

Here, z is the vertical position in the plasma. This equation can be solved based on experimental data, such as magnetic measurements outside the plasma and observations of kinetic quantities. For this thesis, the routinely written EQH shotfiles were used. They contain the output of equilibrium reconstructions performed with the code `CLISTE` (McCarthy et al., 1999; McCarthy, 1999), short for CompLete Interpretive Suite for Tokamak Equilibria, at a temporal resolution of 1 ms. The reconstructions are called interpretive because they rely exclusively on magnetic measurements. To ensure reliability, the equilibria for all discharges were verified using the newer `IDE` (Integrated Data analysis Equilibrium) data analysis framework (Fischer et al., 2016). For the IDE evaluations, the Grad-Shafranov equation is coupled to the current diffusion equation to ensure a smooth temporal evolution of the equilibrium. Moreover, IDE also takes into account kinetic data. The comparisons, in particular of R_aus and of the kinetic stored energy W_MHD, showed only minor discrepancies for the concerned discharges.

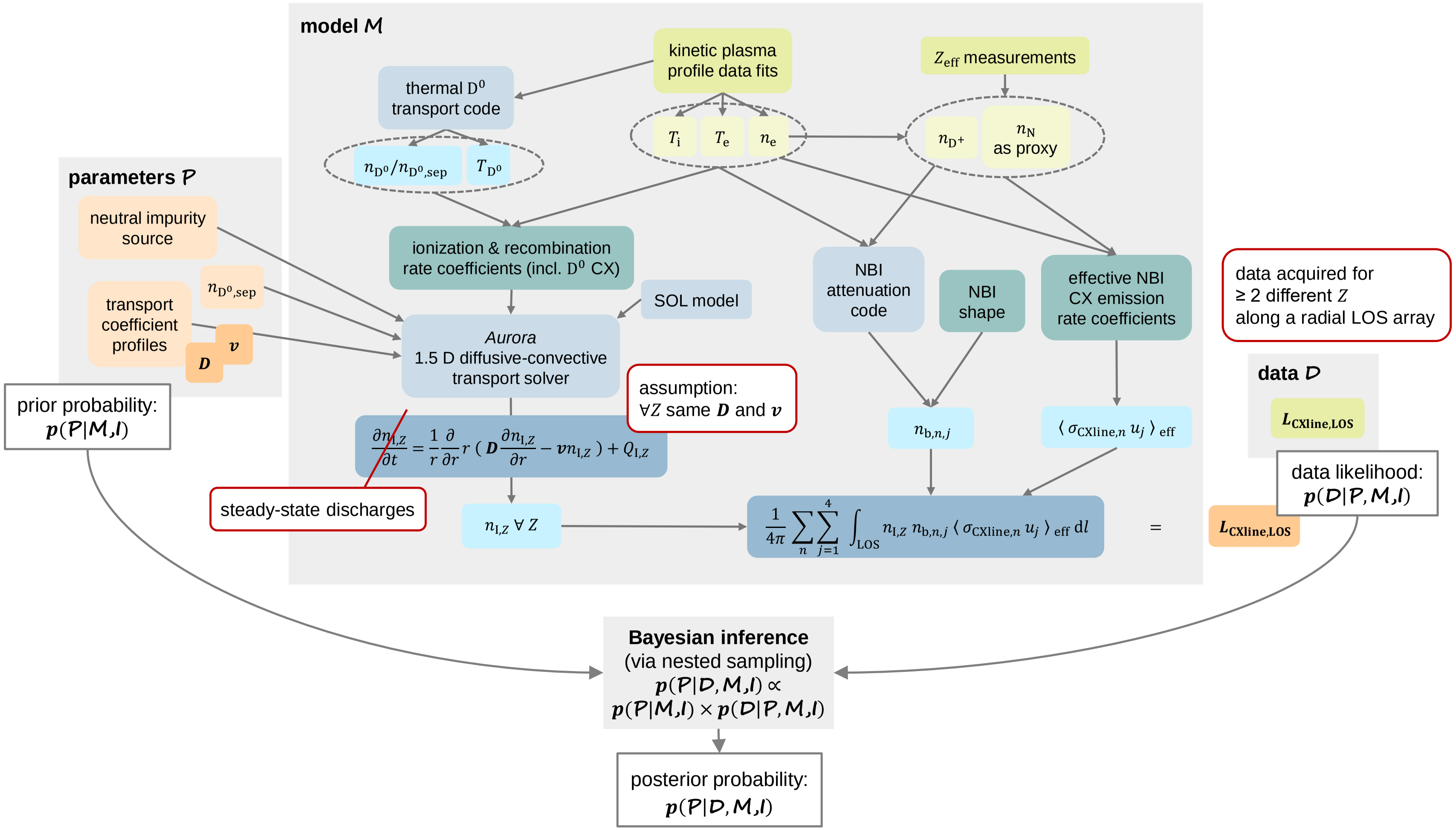

Figure 4.1: Schematic of the inference framework. All individual elements are described in detail in chapter 4. The plasma equilibrium, which is needed for all parts of the inference framework, is obtained from routinely written EQH shotfiles. $\mathcal{I}$ signifies the prior information on the parameters.

4.1.2 Plasma background

Information on the background plasma profiles is important for the many atomic processes involved in the forward model, and thus of particular relevance for the inference approach based on data from multiple charge stages. Furthermore, comparative theoretical transport simulations, e.g., of neoclassical convection, also rely heavily on the kinetic profiles. However, accurately capturing the profiles in the steep gradient region of the pedestal is challenging.

4.1.2.1 Main ion and electron background

n_e, T_e, and T_i, are fitted by an exponential cubic spline interpolation with manually selected spline knot positions. Figure 4.2 shows an example of such a fit for n_e. Different diagnostics, which are presented in section 3.2, are used for the fits, and a major challenge lies in achieving accurate alignment of their data. This difficulty is due to uncertainties in the equilibrium reconstruction, as discussed in Illerhaus, 2017, combined with the different viewing geometries of the diagnostics.

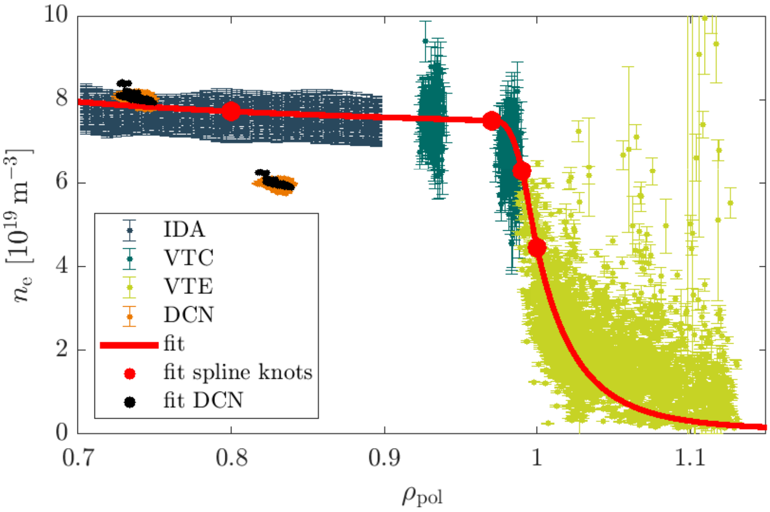

Figure 4.2: Example of a kinetic profile fit. The data are taken from #39461 in the time range 3.95–6.81 s. In this example, the fit relies mainly on the IDA profiles in the core, whereas the core and edge Thomson scattering systems (VTC and VTE) are used for the pedestal fit. Additionally, the line-integrated DCN laser interferometry data are employed. The n_e profile is fitted using an exponential cubic spline interpolation, the results of which (red) are shown in addition to the corresponding synthetic data for the DCN signal (black). The VTE data has been shifted radially outward by 7.5 mm, as determined with the corresponding fit of T_e.

Both the T_e and n_e fits use Thomson scattering data. For the T_e fit, the ECE diagnostic can be used in addition, but the data are neglected outside of an individually determined radial position, as they can suffer from ECE shine through in regions with small optical depth at the plasma edge. For the n_e fit, line-integrated density measurements from the DCN laser interferometry are additionally used. Data from the Li beam diagnostic, which provides information on n_e in the pedestal, are not used because the diagnostic was not operated in some of the discharges and its data quality is poor in other discharges. Where good IDA profiles are available, they are used in the core, but the pedestal profiles are obtained directly from the diagnostic data. The edge Thomson scattering data is shifted such that T_e is 100 eV at the separatrix since it is known to be typically in the range of 80–120 eV at AUG (Pütterich et al., 2011). This shift is done equally in T_e and n_e to ensure good alignment. Subsequently, all other diagnostic data are shifted such that they are in agreement with the Thomson scattering data. Moreover, if Li beam data were available, they were checked for consistency with the other diagnostics to confirm that the applied alignment shifts are reasonable.

The T_i fits are based on the temperatures obtained from the Ne CXRS measurements, which ensures good alignment with the impurity radiance data. The assumption of equal main ion and impurity temperatures is justified by the fact that the thermal equilibration is fast compared to transport time scales (Viezzer et al., 2013). The temperatures are obtained from the fits of those CX-lines with better signal-to-noise ratio in the core and edge, respectively, which are also used to constrain the fits of the other spectral lines (cf. 3.1.4). Their data are assigned to their emissivity-weighted mean radial position. Some works, such as Pütterich et al., 2011, further align the steep gradient regions of T_i and T_e. This has not been done in this work, but has been checked to be approximately the case.

4.1.2.2 Thermal neutral deuterium

It was first shown by Dux et al., 2020, and confirmed by Sciortino et al., 2021a and Sciortino et al., 2021b that recombination due to CX of impurity ions with recycling thermal neutral deuterium contributes significantly to the charge stage balance at the plasma edge. It was also shown in Dux et al., 2020 that although the CX processes may be local, this effect mostly acts globally on flux surfaces due to slow enough impurity re-ionization. Whereas the thermal neutral D CX was previously suspected to be only relevant in the SOL, these works highlight its relevance for the pedestal. The strength of the effect in the pedestal depends on the sources of thermal neutrals, in particular the amount of recycling at the wall, and on the plasma density profile in the SOL and the pedestal, which determines how far the neutrals penetrate into the confined plasma.

Measurements of the thermal neutral D density profile are not available. In principle, observations of D_α radiation at the edge could be used, but they do not provide quantitative results due to strong reflections at the W wall. Instead, in this framework, the flux surface-averaged thermal neutral D density n_{D^0} and temperature T_{D^0} are calculated with `KN1D` (LaBombard, 2001), a 1-D kinetic transport code for atomic and molecular hydrogen, using the `KN1D OMFIT` module. `KN1D` requires as inputs some simple SOL geometry specifications, similar to the `Aurora` SOL model explained in section 4.1.3.2, the electron and main ion background profiles as specified in section 4.1.2.1, and the midplane molecular neutral pressure as is obtained from a pressure gauge (AUG IOC shotfile, manometer 14).

However, merely the profile shape but no absolute densities can be obtained since the recycling source at the edge is unknown. Therefore, an additional scalar parameter is introduced for the absolute density at the separatrix $n_{\mathrm{D}^0,\mathrm{sep}}$. Moreover, reflected particles can have other starting energies at the edge than the room temperature assumed in `KN1D`, which could impact the profile shape. However, this effect is estimated to be small based on the calculations presented in Dux et al., 2020, where profile shapes are compared for different starting energies between 10–160 eV.

4.1.2.3 Impurity content

The beam attenuation calculation in the synthetic diagnostic includes collisions with impurities, which necessitates an estimate of the impurity content. Furthermore, the effective CX-emission rate coefficients depend on the effective plasma charge Z_eff. At AUG, a Z_eff value for the plasma core is routinely determined via integrated data analysis (Rathgeber et al., 2010) based on the bremsstrahlung background seen in the CXRS diagnostic. It is saved in the IDZ shotfile. For the beam attenuation calculation, a fully stripped nitrogen (N) density n_N with a profile shape proportional to n_e, thus a constant N concentration, is estimated as proxy for the impurity content. It is determined such that Z_eff is matched together with the corresponding n_{D^+}.

4.1.3 Impurity transport solver

The forward model is based on the impurity transport solver `Aurora` (Sciortino et al., 2021a; Sciortino, 2020; `Aurora` Website, 2024; `Aurora` Github Repository, 2024), which solves the system of transport equations, stated in equation 1.9, for all charge stages. It thus returns the charge stage density profiles of the impurity when provided with diffusion and convection profiles. As additional inputs, it requires the magnetic equilibrium, the kinetic profiles T_i, T_e, n_e, n_{D^0}, and T_{D^0}, the ionization and recombination rate coefficients for atomic processes affecting the charge stage balance, and assumptions on the impurity sources and losses in the SOL. From the derived charge stage densities, `Aurora` can moreover calculate the impurity radiation, in particular line radiation, continuum radiation, and bremsstrahlung, using atomic rate coefficients obtained from the Atomic Data and Analysis Structure (ADAS) (Summers, 2004; OPEN ADAS, 2024) and the input kinetic profiles. Since `Aurora` relies on the full 2-D tokamak equilibrium to solve the 1-D radial transport equation, it is also referred to as 1.5-D code.

The `Aurora` code is heavily based on and benchmarked against the successful impurity transport solver `STRAHL` (Dux, 2021), which has been developed over several decades from its first version introduced by Behringer, 1987. Both codes use the same radial grid coordinate as defined in equation 2.53, and rely on very similar Fortran 90 routines for the numerical solution of the coupled system of equations. `Aurora` is designed to enable Bayesian impurity transport inference, which requires many iterations of the forward model. In particular, it avoids file I/O operations to reduce the computational expense. In addition, it offers modern, user-friendly interfaces in Python 3 and JULIA.

4.1.3.1 Ionization and recombination rate coefficients

The source term in equation 1.9 is due to ionization and recombination processes from neighboring charge stages, that is,

$$\begin{aligned} Q_{\mathrm{I},Z} = &-(n_\mathrm{e} S_{\mathrm{I},Z} + n_\mathrm{e}\alpha_{\mathrm{I},Z} + n_{\mathrm{D}^0}\alpha^\mathrm{cx}_{\mathrm{I},Z}) \cdot n_{\mathrm{I},Z} \\ &+ n_\mathrm{e} S_{\mathrm{I},Z-1} n_{\mathrm{I},Z-1} \\ &+ (n_\mathrm{e}\alpha_{\mathrm{I},Z+1} + n_{\mathrm{D}^0}\alpha^\mathrm{cx}_{\mathrm{I},Z+1}) \cdot n_{\mathrm{I},Z+1}, \end{aligned} \tag{4.2}$$

where S, α, and α^cx indicate the effective rate coefficients for ionization, radiative and dielectronic recombination, and recombination via CX with thermal neutral D (cf. section 4.1.2). In contrast to the thermal neutrals, CX reactions with non-thermal NBI neutrals are neglected. This contribution plays a minor role in the pedestal since the flux surface-averaged densities of the NBI neutrals are small due to the large size of the flux surfaces (Dux et al., 2020). Typical values and temperature dependencies of S, α, and α^cx are shown in figure 4.3.

For Ne, S is retrieved according to Mattioli et al., 2007, and α from the ADAS adf11 acd96_ne file. The α^cx data were calculated based on the CX cross-sections for thermal D with principal quantum numbers $n = 1, 2, 3, 4$ as given in Janev et al., 1993, pp. 172 and 174, together with the excited state populations due to electron impact excitation as provided by Geiger, 2013, appendix B. To retrieve the CX rates with the recycling neutrals, the reduced temperature $T_{\mathrm{red}} = (T_{\mathrm{i}} m_{\mathrm{D}^0} + T_{\mathrm{D}^0} m_{\mathrm{I}}) \,/\, (m_{\mathrm{D}^0} + m_{\mathrm{I}})$, i.e., weighted by the neutral and impurity masses, m_{D^0} and m_{I}, is used.

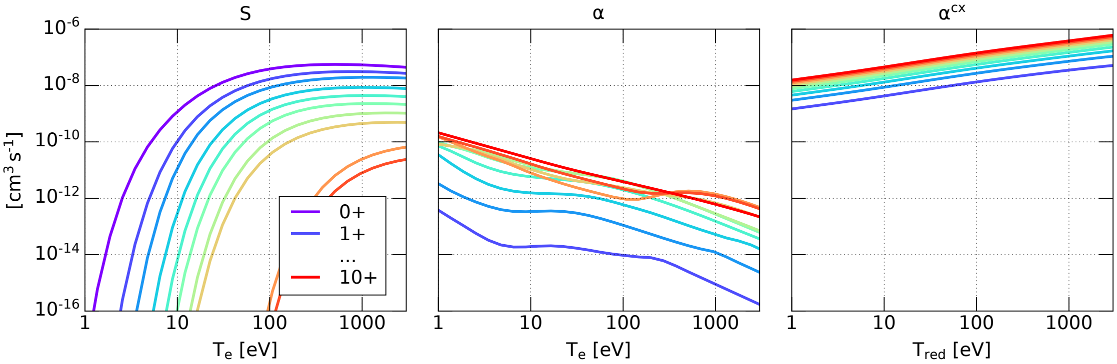

Figure 4.3: Atomic ionization and recombination rate coefficients for Ne. S, α, and α^{cx} are shown as functions of T_{e} and T_{red} at constant $n_{\mathrm{e}} = 10^{20}\,\mathrm{m}^{-3}$. The colors indicate the different Ne charge stages.

The recombination of the singly ionized impurity is artificially set to zero, in order to prevent particle losses since the neutral impurity is not evolved in time but serves solely as a source function. An option to calculate the temporal evolution of the neutral charge stage is included in `Aurora`, but is not employed here.

4.1.3.2 SOL model

In the SOL, the radial coordinate cannot be calculated according to equation 2.53 since V is not defined. Therefore, the grid is extrapolated beyond the separatrix by approximating V based on the midplane flux surface width ΔR_{mid}, which is the difference between the LFS and HFS radii in the horizontal plane of the magnetic axis. To approximate V for a SOL flux surface, the separatrix shape is scaled up in the horizontal and vertical coordinates of the poloidal plane according to the ratio of ΔR_{mid} between the flux surface and the separatrix.

Moreover, the impurity densities in the SOL have complex 3-D distributions, which cannot be accurately captured by a 1.5-D transport model but their flux surface average must be approximated. The neutral impurity distributions (of Ne and O) in the SOL, which are the sources of the ionized impurities, are calculated with `Aurora`'s simple neutral penetration model based on a specified neutral impurity source location and strength, particle starting energy, and the neutral ionization rate coefficients. Here, the neutral impurity source location is chosen as 4.5 cm outside the separatrix and the particle starting energy as 0.5 eV, while the source strengths are fitted for both impurity species. In addition to the radial transport, parallel transport in the SOL results in particle losses to the limiter and the divertor. These losses are calculated in `Aurora` from the plasma flow velocity specified by a Mach number, here set to 0.05, together with geometry estimations on the radial extent of the SOL and limiters and on the average connection lengths to the limiters and the divertor. The limiters are assumed to be always positioned at $^2/_3$ of the distance from the separatrix to the first wall, for which the minimum distance at the LFS is calculated from the equilibrium. The connection length to the limiters is approximated as $^1/_5$ of the machine height, thus at AUG 0.5 m, and the connection length to the divertor is estimated based on the equilibrium as

$$c_{\mathrm{div}} = \pi R_0 \; q_{\mathrm{s}}\big|_{\rho_{\mathrm{pol}}=0.95} \, . \tag{4.3}$$

The decay length λ determining the boundary condition at the last grid point, which is the wall position, in `Aurora` is set to 1 cm.

Recycling can be modelled with `Aurora`'s 0-D reservoir model, which uses time constants for wall retention, divertor pumping, and the backflow from the divertor into the SOL. However, in order to reduce the number of free parameters, all recycling options are disabled such that any particles that are lost from the radial domain to limiters, divertor, or the wall cannot return. Instead the valve flux (of Ne) and the recycling fluxes (of Ne and O) are combined into the neutral impurity source strengths (of Ne and O). As these are unknown, two additional scalar parameters are added, namely a scaling factor of the Ne valve flux to account for the much higher recycling flux, and the neutral O particle source strength to model the O content in the device. For this to be valid, the impurity sources are assumed to be entirely located in the SOL, as can be expected for a divertor plasma. All other quantities of the SOL model are fixed.

Because of these rather crude assumptions about SOL geometry, parallel transport, and plasma-wall interaction, the framework is only able to infer reliable impurity transport coefficients within the confined plasma. The tests in section 5.4 demonstrate that the results do not depend crucially on the fixed SOL parameters.

4.1.3.3 Algorithm

`Aurora` is typically run with a numerical time evolution of the impurity charge stage densities according to equation 1.9. It employs a first-order, vertex-centered, finite-volume scheme developed by Linder et al., 2020. In particular in the pedestal, where the impurity density gradients are strong, this scheme is numerically more stable than the previously used finite-differences scheme (Sciortino et al., 2021a). The grid points along the radial coordinate given in equation 2.53 are defined equally to `STRAHL` (Dux, 2021) as

$$\Delta r = \left(\frac{1}{\Delta r_{\mathrm{center}}} + \left(\frac{1}{\Delta r_{\mathrm{edge}}} - \frac{1}{\Delta r_{\mathrm{center}}} \right) \left(\frac{r}{r_{\mathrm{max}}} \right)^{k_r} \right)^{-1} . \tag{4.4}$$

The distance between the innermost gridpoints $\Delta r_{\mathrm{center}}$, between the outermost gridpoints Δr_{edge}, and the grid exponent k_r are in this work set to 1 cm, 0.05 cm, and 6, respectively, resulting in a finer resolution near the plasma edge. r_{max} is the simplified estimation for the first wall position, calculated as explained in section 4.1.3.2. The temporal grid is constructed such that the time step width increases progressively. The initial Δt_0 is multiplied by a factor k_t each n_t time steps (Sciortino, 2020). In this work, these parameters are chosen as 10^{-5} s, 1.01, and 1, respectively, meaning that each time step is 1.01 times longer than the previous one. More details on the numerical algorithm can be found in Sciortino et al., 2021a. To assess the numerical accuracy, `Aurora` includes a particle conservation test. This compares the total number of particles in the system, including those lost to the wall, against the time-integrated particle source. If the squared deviation is smaller than 5 % of the squared time integrated particle source, the particle conservation test is considered passed.

Specifically for inferences based on steady-state impurity densities, an analytic solution scheme has been developed by Nishizawa et al., 2022, which is also implemented in `Aurora`. This algorithm is based on the fact that under stationary conditions, the system of equations described in equation 1.13 can be reformulated to

$$\begin{aligned} n_{\mathrm{I},Z}(r) =& \exp\left(-\int_r^{r_{\max}} \frac{v(r')}{D(r')}\mathrm{d}r'\right)\cdot \\ & \left(n_{\mathrm{I},Z}(r_{\max}) + \int_r^{r_{\max}} \frac{1}{D(r')r'} \exp\left(\int_{r'}^{r_{\max}} \frac{v(r'')}{D(r'')}\mathrm{d}r''\right) \int_0^{r'} Q_{\mathrm{I},Z}(r'')r''\mathrm{d}r''\mathrm{d}r'\right). \end{aligned} \tag{4.5}$$

This is not in strict sense an analytical solution of the system of equations since the impurity densities still appear on the right-hand side within the term $Q_{\mathrm{I},Z}$. However, by discretizing the integrals as summations over Δr, the impurity density profiles can be obtained through a straightforward matrix calculation. This steady-state solver also incorporates the impurity source and parallel loss terms of the simple SOL model, as described in section 4.1.3.2, in $Q_{\mathrm{I},Z}$.

Both the time-dependent `Aurora` code and the steady-state solver are available for use with this framework and have been checked for consistency. Only when `Aurora`'s recycling model was used, small differences in absolute impurity densities could occur since this is not included in the analytic solution scheme. In terms of runtime, there is no clear advantage of one method over the other. Their difference in speed depends on the length of the simulation time interval. For very short intervals of around 0.2 s, which is the minimum needed to ensure convergence, the time-dependent solver can perform the `Aurora` simulations for this thesis up to twice faster, whereas both methods take around 0.1 s for a single simulation if the interval spans a few seconds. Although using the time-dependent `Aurora` model may offer slight runtime improvements, the benefit of the steady-state solver is that it does not require convergence checks for stationary impurity densities. It is therefore used in this thesis.

4.1.4 Synthetic diagnostic

The synthetic diagnostic maps the impurity charge stage densities that are obtained with the impurity transport solver to the diagnostic data, namely the radiances of the CX-lines measured with CXRS, according to equation 3.2. It thus requires knowledge on the NBI shape and attenuation and on the effective NBI CX-emission rate coefficients, as well as on the geometry of the LOS intersection with the neutral beam, along which the signal has to be integrated.

4.1.4.1 NBI shape and attenuation

The AUG beam shape, that is, the beam density distribution without attenuation, is provided by an analytical beam model, whose parameters are determined to match beam emission spectroscopy (BES) measurements (Lebschy, 2014). This model describes the beam path originating from two extraction grids, which are treated as homogeneously emitting surfaces. The mean velocities of the beam particles are assumed to be directed towards a horizontal and a vertical focus point with a small Gaussian spread of the velocity direction, i.e., a small divergence. As free parameters in the beam model, the position of the extraction grids, the vertical and horizontal focus points, and the Gaussian divergence width are obtained from fits to Doppler velocity measurements along different BES LOS. The plasma is located at a distance of approximately 7–9 m from the extraction grids, thus close to the focus points, where the beam shape perpendicular to the beam direction can be well approximated as a 2-D Gaussian with a vertical and a horizontal standard deviation. This approximation is used for all further calculations in this work.

The densities calculated with the beam model are scaled according to the attenuation of the beam in the plasma, which is simulated with the collisional-radiative model `COLRAD`. This code additionally provides the excitation state populations of the beam, and has been validated against experimental data and against other beam attenuation codes, `FAST` and `FIDASIM`, in McDermott et al., 2018. With `COLRAD`, the beam attenuation can be calculated along several beamlets, meaning on the beam axis, but also along beam pencils following a constant angle in the perpendicular plane and a radial distance according to a constant density fraction with respect to the beam axis. However, in this work, only the attenuation along a single beamlet on the beam axis is used, as this was found to yield the equally accurate results as the multi-beamlet approach. The numerical points along the beamlets are evenly spaced, in this work 167 points are used. An example for the Gaussian beam shape, as well as for the results of the beam attenuation is shown in figure 4.4.

The collisional-radiative model includes mixing between excited states due to spontaneous decay according to Einstein rates and due to electron-, main ion-, and impurity- impact excitation and de-excitation, as well as losses due to electron-, main ion-, and impurity- impact ionization and due to main ion- and impurity- CX. Thus, the code is relying on n_{e}, n_{D^+}, T_e, T_i, and the impurity density, which is estimated as n_{N} from Z_{eff} (cf. section 4.1.2.3). N is used as impurity in the beam attenuation calculation since only atomic data for He, B or N are available in `COLRAD` and in particular Ne is not available. All rate coefficients are retrieved from Geiger, 2013, appendix B, and summarized in a matrix C with the losses as the diagonal terms and the mixing processes between excitation states as the off-diagonal terms. Thus, the time evolution of the beam excitation state populations $\vec{f}$ is (Geiger, 2013, appendix A)

$$\mathrm{d}\vec{f}/\mathrm{d}t = C\vec{f}. \tag{4.6}$$

In this work, 10 excited states are resolved, and the truncation is compensated by increasing the losses from the highest resolved state by a factor of 8. All beam neutrals start in the ground state when arriving at the plasma, and the equation is solved in discrete time steps, which are matched to positions along the beam according to the beam velocity determined from the beam energy.

The halo, that is, the thermal neutral population that originates from the beam due to CX between beam neutrals and main ions, is also calculated. The halo birth rate $\vec{S}$ is obtained in `COLRAD` at each discrete point along the beam from excitation state resolved CX rates, meaning that the CX reactions into different halo excitation states are treated individually. The subsequent mixing of the excitation states due to spontaneous decay, due to electron-, main ion-, and impurity- impact excitation and de-excitation, and due to CX with main ions, and the losses due to electron-, main ion-, and impurity- impact ionization and due to impurity- CX are again summarized in a matrix C_{halo}. Since the halo is assumed to be in equilibrium, the equation

$$\mathrm{d}\vec{f}/\mathrm{d}t = C_{\mathrm{halo}}\vec{f} + \vec{S} \tag{4.7}$$

is solved as

$$\vec{f} = -C_{\mathrm{halo}}^{-1}\vec{S}. \tag{4.8}$$

All atomic data are again retrieved from (Geiger, 2013, appendix B).

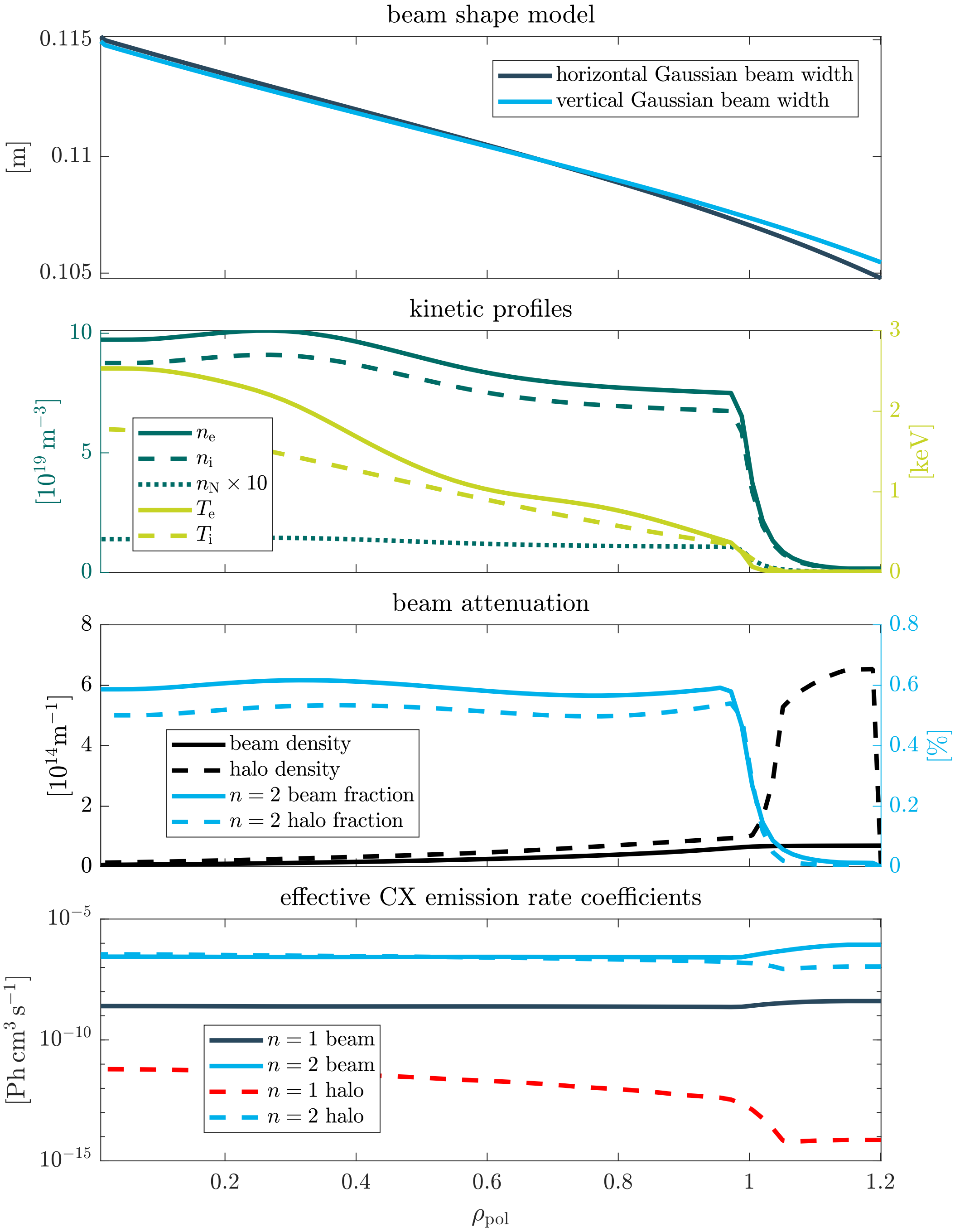

Figure 4.4: Example of the NBI shape, attenuation and effective NBI CX-emission rate coefficients. 1. plot: Gaussian beam widths along beam 3 as approximated from the results of the AUG beam shape model. Since beam 3 crosses the magnetic axis almost exactly, the profiles are shown as a full function of ρ_pol at the LFS. The mapping to ρ_pol was done according to the equilibrium of #39461 at 5.38 s. 2. plot: Kinetic profiles fitted for #39461 in the time range 3.95–6.81 s. The N density is calculated to represent the overall impurity density according to Z_eff. 3. plot: Densities of beam and halo, and fractions of the n=2 excitation states as calculated with the beam attenuation code COLRAD based on the kinetic profiles, here for the first energy component of beam 3. The fraction of the n=1 excitation state is above 99 % throughout in both, beam and halo. 4. plot: Effective CX-emission rate coefficients for the NeVIII $n = 10 \rightarrow 9$ spectral line, retrieved based on the kinetic profiles. The $n = 1$ excitation state of the halo is not included in further calculations due to the very low effective CX-emission rates.

As for the NBI beam, the halo birth and attenuation is only calculated along the 1-D beam axis in `COLRAD`. Its spatial distribution due to the movement of the neutrals is instead obtained from interpolations of precalculated Monte Carlo simulations. For the Monte Carlo simulations, a Gaussian decay length of the beam in perpendicular direction λ_{beam}, a mean free path for CX processes between halo neutrals and main ions λ_{cx} (which produces new halo neutrals), and a mean free path for electron impact ionization of halo neutrals λ_{ion} are estimated. λ_{beam} is approximated from the beam shape model, and λ_{ion} and λ_{cx} are calculated assuming a Maxwellian velocity distribution according to T_{i} and loss and CX rates that are calculated in `COLRAD`. The halo particles start at each point along the beam with a density distribution according to λ_{beam}. From there, they move into random directions, changing their direction into a new random direction after the path length λ_{cx}, or being removed after the path length λ_{ion}. For this random walk calculation, the plasma parameters are assumed to be constant, equal to those at the starting position along the beam on the beam axis.

4.1.4.2 Effective NBI CX-emission rate coefficients

As shown in equation 3.2, the CX reactions between the impurity ions and the NBI neutrals are summed over the velocity components j and excitation states n of the neutrals. The sum over j includes the 3 NBI energy components and the halo. The sum over n includes different principal quantum numbers of the NBI atoms. Given typical plasma parameters, most atoms are in the ground state and the fraction of atoms with $n = 2$ is only about 0.5 % at its maximum along the NBI path, both for the beam and the halo. However, the effective CX-emission rate coefficients are higher for the excited states. Therefore, only the $n = 1$ and $n = 2$ states of the beam neutrals and the $n = 2$ state of the halo neutrals contribute significantly, thus only these are included in the calculations. This is shown in figure 4.4. The product of the beam density and the effective CX-emission rate coefficient for the $n = 1$ halo contribution is more than 2 orders of magnitude smaller than the other plotted contributions.

The effective beam and halo CX-emission rate coefficients are usually strongly based on theoretical calculations, since there are only few measurements available, as, e.g., for Ar^{15+} by McDermott et al., 2020. For Ne^{8+}, Ne^{9+}, and Ne^{10+}, they are obtained as in McDermott et al., 2018 from interpolations of data calculated with the ADAS 309 code (Summers, 2004) for different n_{e}, T_{i}, Z_{eff}, and NBI energies, assuming $T_{\mathrm{e}} = T_{\mathrm{i}}$ and n_{D^+} consistent with n_{e} and Z_{eff}. This code runs a collisional-radiative model to determine the principal quantum number populations taking into account transitions from higher excited states. The initial excitation state populations are obtained based on adf01 data (OPEN ADAS, 2024), which provides CX cross-sections into different n and l quantum states. For the calculations of the radiative cascades into lower n-states, the atoms are assumed to be Rydberg-like. A relevant effect for such atoms, especially for high n, is l-mixing (Isler, 1994; Dux, 2004). The nearly degenerate states with different l (cf. section 3.1.4), can be mixed by the influence of electric and magnetic fields without radiative transitions. Since this mixing depends on the plasma background parameters, especially n_{e}, T_{i}, and Z_{eff}, these quantities are important for the effective CX-emission rate coefficients, besides the relative velocity of the beam neutral and the impurity ion.

4.1.4.3 LOS integration

As shown in equation 3.2, the product of the impurity and NBI beam densities with the effective CX-emission rate coefficients is integrated along each LOS to forward model the line radiance. This means that the CXRS measurement is semi-local, in the sense that each LOS observes light emission from the small intersection region of the LOS and the beam, which is visualized in figure 3.2. The more tangential the LOS is to the flux surfaces in this region, the narrower is the flux surface range contributing to the signal. In the inverse inference, this is equivalent to a small tomographic inversion, which becomes particularly relevant for less tangential LOS. The inclusion of the fully accurate LOS integral without constraints on the impurity density profiles in the forward model is an improvement with respect to earlier codes for impurity density evaluation from CXRS data, such as `CHICA`, which approximates the pedestal impurity density profiles by a simple functional form for the evaluation of the LOS integral (McDermott et al., 2018). As implemented already in `CHICA` (McDermott et al., 2018), in the course of this work, a finer splitting of the LOS for the LOS integration was tested, to account for the finite cone width from which light is collected. This, however, did not yield any relevant differences.

For the integration along the LOS, the beam attenuation is calculated for each data point individually. It is based on the plasma shape in the concerned time range that has the R_{aus} value closest to the mean R_{aus} of all spectra contributing to the averaged spectral line (cf. section 3.1.4). The trajectory of the LOS through the beam is subdivided into a predefined number of distinct points, which is set to 71 in this work. At these points, the beam density for all beam velocity components and the relevant excitation states of beam and halo are evaluated. Subsequently they are multiplied with the distance to the next point, divided by 4π, and multiplied with the effective CX-emission rate coefficient according to the kinetic profile values at the respective ρ_{pol} position. Then, the radiance is retrieved for a unit impurity density of $1\,\mathrm{m}^{-3}$. Multiplication with the impurity density profile at the ρ_{pol} positions along the LOS and summation over all elements yields the forward modeled spectral line radiance, which is compared to the measured data in the inference.

4.2 Inverse inference

In the following, the details of the Bayesian inverse inference, namely the sampling algorithm and the prior and likelihood definitions, are presented. The inference is based on the CXRS data and the forward model, which are explained in section 3.1 and section 4.1, respectively. A visualization of the sampling process is shown in figure 4.5.

4.2.1 Posterior sampling

Specifically for impurity transport inference, the nested sampling algorithm `MultiNest`, which has been briefly introduced in section 2.3.2, is suggested in Chilenski et al., 2019. In this framework, its version v3.10, wrapped with the python code `PyMultiNest` (Buchner, J. et al., 2014), is used. `MultiNest` is capable of handling complex non-Gaussian, if enabled even multimodal, posterior shapes, which may arise due to the non-linearity of the model introducing non-linear correlations between the parameters. Moreover, the algorithm does not rely on any gradient information, which would be prone to the round-off error of finite differences as long as the time-dependent numerical `Aurora` model is used (Chilenski et al., 2019). And lastly, as with any nested sampling algorithm, in contrast to MCMC methods, good estimates of the Bayesian evidence are provided.

However, as stated in section 2.3.2, the region-based sampling approach of `MultiNest` loses efficiency with increasing dimensionality, such that `MultiNest` can only easily handle up to around 30 parameters (`MultiNest` Github Repository, 2024). Therefore, a parametric inference of the transport coefficient profiles is required. The chosen spline parameterization is explained in section 4.2.2. In principle, such approach imposes prior constraints on the solution and risks

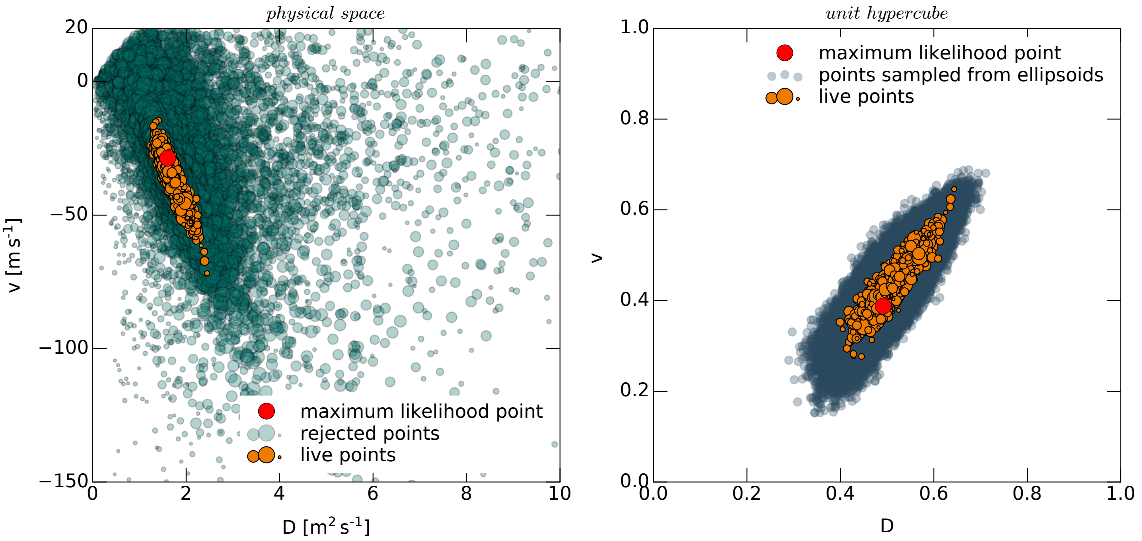

Figure 4.5: Visualization of the Bayesian sampling process with `MultiNest` (using case 8 in table 5.2 as example). A 2-D cut through the parameter space shows the transport coefficients at $\rho_{\mathrm{pol}} = 0.99$. Left: Sampling history in the physical space. Every third rejected point is shown, with the size of the dots increasing linearly with the iteration of their rejection, i.e., increasing with likelihood. The live points at the sampling termination are plotted with the size of the dots now increasing linearly with logarithmic likelihood. Right: Sampling process in the unit hypercube. Random samples from the current ellipsoids at the sampling termination are plotted to indicate their combined shape. This inference was done without smoothness constraint in the prior, such that the mapping between the unit hypercube and the physical space is given by the univariate inverse prior CDFs.

to produce correlated residuals, i.e., systematic errors in the inferred profiles (Chilenski et al., 2019). Alternatively, non-parametric inference of smooth profiles is possible using Gaussian process regression and has been tried for impurity transport coefficient analyses in Nishizawa et al., 2022. However, the high dimensionality of the non-parametric parameter space (around 200 parameters in Nishizawa et al., 2022) demands other sampling methods, such as gradient-based MCMC algorithms, e.g., also used in Victor et al., 2020, which do not come with the above mentioned advantageous properties of `MultiNest`. To ensure that large systematic errors can be excluded, the framework has been thoroughly tested, as presented in chapter 5. It has been shown to be capable of handling enough spline knots in the pedestal to reconstruct realistic D and v profiles with good accuracy. This justifies the use of `MultiNest`, and implementing an option for non-parametric inference is not considered essential.

In `MultiNest`, the samples are drawn uniformly in a unit hypercube space with each parameter ranging between 0 and 1. Subsequently, the hypercube sample $\vec{s}_{\mathrm{unit}}$ is transformed into the physical space sample $\vec{s}_{\mathrm{phys}}$, respecting the prior mass conservation

$$\int p(\vec{s}_{\mathrm{phys}})\mathrm{d}\vec{s}_{\mathrm{phys}} = \int \mathrm{d}\vec{s}_{\mathrm{unit}}, \tag{4.9}$$

with the prior probability p, such that uniform samples from the prior are obtained. In case of univariate parameter priors, this is straightforward by applying their inverse cumulative distribution functions (CDFs), which is also known as inverse transform sampling. The implementation of the univariate prior distributions of the individual parameters, and the implementation of additional correlations that are consistent with equation 4.9 is further detailed in section 4.2.2. General possibilities for the implementation of prior correlations are outlined in `UltraNest` Documentation, 2024

Since the number of free parameters in the inferences performed with this framework is at the edge of `MultiNest`'s capability, `MultiNest`'s constant efficiency mode can be used to ensure convenient runtimes. This limits the size of the ellipsoids within which new samples are searched to meet a specified target sampling efficiency. It was found to yield reliable posterior distributions when applied in our framework, as demonstrated in chapter 5, but can compromise the estimation of the Bayesian evidence. Moreover, in this thesis, `MultiNest` was not used in its multimodal mode, as in several test runs, no real multimodal posterior distributions could be detected, but the ellipsoidal decomposition was mainly useful to capture the non-Gaussianity of the posterior. Further, the `MultiNest` stopping criterion has to be selected. `MultiNest` stops if the ratio between the approximate contribution of the remaining prior volume to the Bayesian evidence, estimated as $L_i X_i$, and the Bayesian evidence calculated from the sample set Z_{cal}, is smaller than a set tolerance value δ_{tol}, i.e.,

$$\log\left(\frac{L_i X_i}{Z_{\mathrm{cal}}}\right) < \log(\delta_{\mathrm{tol}}), \tag{4.10}$$

or if the likelihood span in the live point set becomes too small

$$\log(L_i) - \log\left(L_{i-(n_{\mathrm{live}}-1)}\right) < 10^{-4}. \tag{4.11}$$

The second condition means that `MultiNest` also stops if a large region of parameter space is left but all solutions in this parameter space have very similar likelihood, meaning that some parameters are strongly underdetermined. δ_{tol} is set to 0.5 in this work, as recommended in `MultiNest` Github Repository, 2024.

Run with a target sampling efficiency of 0.05, as suggested in `MultiNest` Github Repository, 2024, and with 1000 live points, a typical inference, like the reference inference presented in section 5.1, requires around 500 core hours on IPP's TOK batch cluster, which provides nodes with 2 Intel Xeon Gold 6130 (Skylake) CPUs each. As the inference can be run using MPI parallelization, the amount of time needed on such an HPC cluster is manageable. However, for good performance, the specifications of prior and likelihood, presented in sections 4.2.2 and 4.2.3, are of crucial importance. A well chosen prior and likelihood increase the accuracy of the sampling and can significantly reduce the number of iterations needed to complete the sampling. Each individual iteration is however mostly constrained by the runtime of the impurity transport solver and the sampling efficiency.

The posterior weights of the newly drawn samples typically first increase during the sampling, as the likelihood threshold increases faster than the shrinking of the prior volume attributed to the samples. Once a high likelihood region is reached, the threshold increases less in each iteration and the prior volume, which is typically shrinking with increasing likelihood, dominates the evolution of the posterior weights. Thus, they decrease again before the convergence of the algorithm is reached (Feroz et al., 2008). This behavior has also been observed in the inferences done in this thesis.

4.2.2 Prior

The prior probability should represent the prior knowledge on the parameters that are inputs of the forward model. These are in particular the transport coefficient profiles, the neutral impurity sources, and $n_{\mathrm{D}^0,\mathrm{sep}}$ (cf. figure 4.1).

In general, the framework provides the choice of a univariate normal, a log-normal, a uniform, or a log-uniform prior distribution for each parameter, with mandatory and optional parameter boundaries for the uniform and normal distributions, respectively. In this work, the priors for the neutral impurity sources (of Ne and O) and for $n_{\mathrm{D}^0,\mathrm{sep}}$ are chosen as log-normal distributions to cover multiple orders of magnitude. The Ne source rate prior is based on the rate read from the gas valve shotfile. This rate is scaled with a scalar factor, whose prior maximum is chosen to be 10 to account for the high wall recycling of Ne. The n_{D^0} profile is calculated with `KN1D` and also scaled with a scalar factor, whose prior is specified such that $n_{\mathrm{D}^0,\mathrm{sep}}$ is most likely around $10^{16}\,\mathrm{m}^{-3}$, which is a typical value. All priors are shown in figure 4.6.

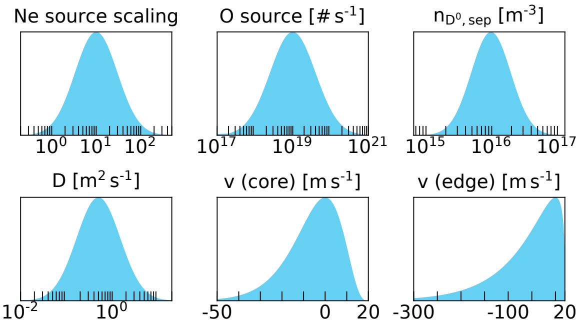

Figure 4.6: Univariate prior probability distributions for the model parameters. Log-normal distributions are chosen for the scalar parameters and D, whereas a customized distribution is used for v, with stronger skewness in the edge ($\rho_{\mathrm{pol}} \geq 0.95$) than in the core ($\rho_{\mathrm{pol}} < 0.95$), reflecting the typical impurity density gradients. In addition, parameter boundaries are applied in the priors for the Ne source scaling (0.2–500), the O source (10^{17}–$10^{21}\,\#\,\mathrm{s}^{-1}$), $n_{\mathrm{D}^0,\mathrm{sep}}$ (10^{15}–$10^{17}\,\mathrm{m}^{-3}$), and D (0.01–$20\,\mathrm{m}^2\,\mathrm{s}^{-1}$).

The impurity transport coefficient profiles are parameterized by a piecewise monotonic cubic spline interpolation. This allows the number of free parameters to be kept small, by using only a few spline knots in the core but placing more spline knots specifically in the steep gradient edge region. As it restricts the possible profile shapes, this parameterization is part of the prior. Yet, it leaves more freedom to the profile shape than the pedestal profile parameterizations used in many previous studies, such as the parameterization of the v profile with a Gaussian dip in the pedestal, e.g., in Sciortino et al., 2020. Optional free parameters are the spline knot values and positions (implemented as in Sciortino, 2021, pp. 113–115), but not their number. Since $\frac{v}{D}$ is better constrained by the experimental data than v and D individually, the latter are spline parameterized to ensure reasonable, in particular smooth, profiles for all quantities v, D, and $\frac{v}{D}$. The strong constraint of $\frac{v}{D}$ can be seen in the correlation of the physical live points in figure 4.5. In line with Chilenski et al., 2019, the boundary conditions for the splines are chosen to be $v(0) = 0$ and $\frac{\partial D}{\partial r}\big|_{r=0} = 0$. The former ensures that $\frac{v}{D}\big|_{r=0} = 0$ since this ratio determines the total impurity density gradient, as shown in equation 1.10, which vanishes on axis. The latter prevents large scatter of the underdetermined D on axis. Since D is a purely positive quantity, the spline interpolation is done on $\ln D$.

In case of poor data quality, in particular sparse data and systematic errors, profiles with unphysical undulations, which are caused by spline overshoots in areas with dense spline knots, can have high likelihoods. To mitigate this, an additional optional smoothness constraint can be applied by introducing radial distance-dependent correlations in the prior of the spline knot values. These correlations are introduced using a Gaussian copula, so for the spline knot values of each profile, the unit hypercube sample $\vec{s}_{\mathrm{unit}}$ is transformed as

$$\vec{s}_{\mathrm{unit}} = \mathrm{CDF}_{\mathcal{N}(0,1)}\left(\sqrt{M_{\mathrm{cov}}} \cdot \mathrm{CDF}^{-1}_{\mathcal{N}(0,1)}\left(\vec{s}_{\mathrm{unit}}\right)\right), \tag{4.12}$$

with

$$M^{i,j}_{\mathrm{cov}} = \exp\left(-\frac{1}{2}\left(\frac{|\rho_{\mathrm{pol,i}} - \rho_{\mathrm{pol,j}}|}{\lambda_{\rho_{\mathrm{pol}}}}\right)^2\right). \tag{4.13}$$

The CDF of the normal distribution with mean 0 and standard deviation 1 ($\mathcal{N}(0,1)$) is applied element-wise to $\vec{s}_{\mathrm{unit}}$. However, the product with the square root of a covariance matrix M_{cov} with radial correlation length $\lambda_{\rho_{\mathrm{pol}}}$, which introduces the correlations, is a multidimensional transformation. This breaks the direct traceability of the mapping between the original unit hypercube and the physical parameter space. In the sampling process shown in figure 4.5, which was done without smoothness constraint, this immediate mapping is retained. $\lambda_{\rho_{\mathrm{pol}}}$ can be adjusted individually for each inference, depending on the data quality. $\sqrt{M_{\mathrm{cov}}}$ is a matrix A such that $M_{\mathrm{cov}} = AA^T$. It is computed via Cholesky decomposition, or alternatively, via eigendecomposition.

After performing the Gaussian copula correlation in unit hypercube space, each spline knot value is transformed into a physical parameter by applying the inverse CDF of its univariate prior distribution. In this work, a log-normal distribution is used for D, as shown in figure 4.6. For v, especially in the pedestal, negative values are much more likely than positive values, due to the typically observed peaked impurity density profiles, which are due to inward convection. Therefore, a special skewed prior distribution, which, however, still covers flat or even hollow impurity density profiles, is defined as

$$p(v, \alpha, \beta) = \frac{\beta^{\alpha}\left(-(v + v_{\mathrm{max}})\right)^{\alpha-1} \mathrm{e}^{\beta(v+v_{\mathrm{max}})}}{\Gamma(\alpha)}, \tag{4.14}$$

with

$$\begin{aligned} \alpha &= \frac{\left(2\frac{\sigma_v^2}{v_{\mathrm{max}}^2} + 1 + \sqrt{4\frac{\sigma_v^2}{v_{\mathrm{max}}^2} + 1}\right)}{2\frac{\sigma_v^2}{v_{\mathrm{max}}^2}}, \\ \beta &= \frac{\alpha - 1}{v_{\mathrm{max}}}. \end{aligned} \tag{4.15}$$

This is a gamma distribution, mirrored around 0, and shifted such that the maximum possible value is v_{max}, the standard deviation is σ_v, and the maximum probability is at $v = 0$. In this work, v_{max} is chosen as $20\,\mathrm{m\,s^{-1}}$, and σ_v as $12.5\,\mathrm{m\,s^{-1}}$ in the core and $75\,\mathrm{m\,s^{-1}}$ in the edge.

If v and D are sampled independently, physically reasonable values of $\frac{v}{D}$ cannot be ensured. To achieve this, v can be sampled not directly from the above presented univariate prior distribution but conditionally on the value of D if the spline knot positions of the profiles are set to be equal. A maximum and standard deviation are therefore also defined for $\frac{v}{D}$, in this work

$\frac{v}{D}_{\max}$ is $20\,\mathrm{m}^{-1}$, and $\sigma_{\frac{v}{D}}$ is $12.5\,\mathrm{m}^{-1}$ in the core and $75\,\mathrm{m}^{-1}$ in the edge, as for v. Then, for each sample, the prior from which v is sampled is adapted based on the value of the sample for D, such that the constraints for v and $\frac{v}{D}$ are respected, i.e.,

$$\begin{aligned} v_{\text{max,samp}} &= \min(v_{\max}, \left(\frac{v}{D}\right)_{\max} \cdot D_{\text{samp}}), \\ \sigma_{v,\text{samp}} &= \min(\sigma_v, \sigma_{\frac{v}{D}} \cdot D_{\text{samp}}). \end{aligned} \tag{4.16}$$

Thus, the total univariate prior distribution for v, which is shown in figure 4.6, is the integral of the conditional prior for v over the prior for D:

$$p(v|\mathcal{M},\mathcal{I}) = \int p(v|D,\mathcal{M},\mathcal{I})p(D|\mathcal{M},\mathcal{I})\mathrm{d}D. \tag{4.17}$$

The conditional prior is evident in the rejected samples in the physical space in figure 4.5, e.g., the top left region does not contain any samples as they are excluded by the constraint on the maximum of $\frac{v}{D}$.

The univariate priors for all parameters, as well as the Gaussian copula transformation and the conditional prior for v, all ensure the prior mass conservation stated in equation 4.9. Moreover, prior predictive checks confirmed that the prior covers the range of physically reasonable solutions.

4.2.3 Likelihood

The data likelihood defines the probability of observing the actual CXRS data based on the synthetic data that is calculated with the forward model from the parameters as ground truth (cf. figure 4.1). Thus, it should represent the spectroscopic measurement error.

In this work, uncorrelated Gaussian measurement errors are used. The variances σ^2 are estimated for each spectrometer channel individually via bootstrapping, that is, from the standard deviation between a subset of N data points x_i, and interpolations made from the rest of the data to the corresponding radial positions, giving estimated data points x_{est}:

$$\sigma^2 = \sum_{i=1}^{N} \frac{(x_i - x_{\text{est}})^2}{N}. \tag{4.18}$$

In reality, systematic measurement errors can be present in addition to this random scatter, in particular due to calibration issues of individual channels or spectrometers. These can be included either as additional inferred scaling parameters or by using a profile likelihood, that is, automatically estimating and applying the best scaling parameters in each likelihood evaluation, which marginalizes these parameters. However, the inclusion of systematic errors is not routinely done, rather only in the case of apparent data offsets, since it significantly complicates the sampling. Moreover, if the data quality of individual channels is obviously poor, their weight in the likelihood may also be reduced manually.

In principle, the likelihood can also be used to account for model errors, in particular in the background plasma profiles, the atomic data, and the NBI shape and attenuation. Since these induce radially correlated deviations of the synthetic data, they suggest a multivariate Gaussian with a radial correlation length as likelihood. However, such a likelihood significantly complicates the posterior space and consequently convergence of the `MultiNest` sampling to the maximum likelihood point could no longer be achieved in tests of this approach. Yet, a simpler approach is used to avoid unreasonably small posterior distributions, which arise if no correlations are assumed in the large data sets. Namely, the variance of all data acquired by one spectrometer channel is scaled by the total number of data points acquired by that channel. The weight of the total data of each channel in the posterior is then equal to the weight of a single data point with the original variance. This approximation broadens the posterior distribution and, due to the general smoothness constraints in the prior (cf. section 4.2.2), in particular increases the probability of radially correlated offsets.

4.3 **`OMFIT ImpRad`** module

`OMFIT` (Meneghini et al., 2013; Meneghini et al., 2015) is a software tool that was developed to enable users to easily combine various modeling and data analysis work steps, and to perform them interactively. Its basic idea is the collection of all needed components, such as data, scripts, and parameters in a python dictionary, whose uniform tree structure facilitates the access to all objects. Multiple elements that are mostly used together can be grouped into predefined modules. `OMFIT` provides a python interface and functions to easily create graphical user interfaces (GUIs). Moreover, the `OMFIT` classes can be installed alone for programming in python. The `OMFIT` software is developed in a collaborative way. When merging into the main branch, automated regression tests have to be passed, such that a stable `OMFIT` version is maintained. More information is available in `OMFIT` Website, 2024.

The presented framework is embedded in the `OMFIT` module `ImpRad`, which is designed for modeling of impurity radiation and inferences of impurity transport based on `Aurora`. Its graphical user interface facilitates the selection of the required `Aurora` parameters, sampler configuration, and prior and likelihood specifications, as well as the visualization of settings, diagnostic data, sampling, and results. The module is generalized to be usable at multiple devices by minimization of device-specific tasks. In this work, it has been substantially extended for routines to infer impurity transport coefficients based on AUG CXRS data with the charge-stage method. Most of the inference workflow presented here is done within `ImpRad`. Only the evaluation of the spectral line radiances from the raw spectra, as well as the calculations of the NBI distribution, which is determined by the beam attenuation and beam shape, are done outside of `ImpRad`, based on AUG CXRS data analysis codes. `ImpRad` could be easily extended in the future, e.g., for including other diagnostics, other sampling algorithms, or more visualization routines. A Levenberg-Marquardt fitting routine is already included for least-squares fitting. However, its functionality is limited due to the complex non-linear inverse problem, which strongly recommends Bayesian sampling.

5 Methodology tests

Parts of the content, figures, and text of this chapter are included in a publication that I have submitted as first author to Nuclear Fusion. For further details, see chapter 3.

In this chapter, the capabilities of the novel inference framework are tested with synthetically generated data, also known as method of manufactured solutions. Such tests can in particular validate the inverse inference procedure, which is done in section 5.1. The influence of different configurations of the spline parameterization for the v and D profiles, which is part of the prior (cf. section 4.2.2), is moreover assessed in section 5.2. However, these tests cannot reveal error sources in the forward model or systematic errors in the data acquisition since those are automatically ruled out when the synthetic data is generated from an outcome of the exact forward model (cf. section 4.1), and with an error pattern precisely matching the likelihood definition (cf. section 4.2.3). By deliberately introducing specific model errors or data perturbations, it is nevertheless possible to analyze their effects on the inference results. This approach provides indications of which aspects of model accuracy and data quality are most critical, also in view of future experiments. Potential error sources include any components of the forward model, such as the magnetic geometry reconstruction, the kinetic profiles, the ionization and recombination rate coefficients, the SOL model in `Aurora`, the NBI shape and attenuation, and the effective CX-emission rate coefficients. Section 5.3 focuses specifically on the impact of systematic calibration errors in individual CXRS channels, as this is a frequently observed issue. Furthermore, section 5.4 investigates the influence of errors in the atomic ionization data, in the n_e and T_e profiles, and in the parallel transport in the SOL. The first two are particularly critical for impurity transport analyses based on the charge-stage method, as they directly affect the impurity charge stage balance, and the latter demonstrates that the results for the pedestal remain robust against changes in the sources and losses in the close SOL, which is essential since they are not realistically captured in the simple SOL model.

5.1 Setup and general validation

The tests with synthetic data are based on the QCE discharge #39461, which is analyzed in section 7.1. `Aurora` was run with the plasma equilibrium and background of this discharge and reasonable choices for the fixed parameters, which are listed in table 5.1. Realistic, that is, not just spline-interpolated, transport coefficient profiles were used as ground truth. v was chosen close to the neoclassical profile, and D such that there is a transport barrier in the pedestal, but the diffusion remains above the neoclassical value, as could be expected for the QCE regime based on the results presented in section 7.1.2. For the other free parameters, the ground truth values were chosen similar to the inference result for #39461. A synthetic data set was generated according to the pattern of the original data, namely with the same amount of data at the same LOS positions. The percentage errors of the original data were determined via bootstrapping (cf. section 4.2.3), and applied to the synthetic data as univariate Gaussian perturbations. The raw data evaluation for #39461 was repeated after the completion of the synthetic tests, but this resulted in only minimal differences between the data pattern of the ground truth and the #39461 data presented in section 7.1. In addition to the Gaussian scatter, realistic calibration offsets, similar to those inferred for #39461, were introduced for both edge spectrometers and added as free parameters, with Gaussian priors around the values that can be estimated by eye from the blank data set. The settings for all other priors and the likelihood were set up as explained in sections 4.2.2 and 4.2.3. In the likelihood, additionally to weighting the data according to the number of data points for each channel, the weight of the core CXRS LOS was halved, which yields approximately equal weight to the edge and core CXRS systems. The ground truth and the priors are also shown in figure 5.1.

Parameter	Value
algorithm	steady-state analytical
radial grid: *k, dr_0, dr_l*	6.0, 1.0, 0.05
Ne and O neutral source energy	0.5 eV
distance of sources to separatrix	4.5 cm
decay length outside last grid point	1.0 cm
SOL Mach number	0.05
distance of last grid point to separatrix	9.0 cm
distance of limiters to separatrix	6.0 cm
connection length to limiters	0.5 m
connection length to divertor	29.4 m

Table 5.1: `Aurora` settings used in the tests with synthetic data. The parameters in the upper part of the table were chosen freely, whereas the geometry parameters in the lower part were approximated from the magnetic equilibrium of #39461 at 5.38 s. For the definitions of the quantities, see Sciortino, 2020 and Dux, 2021. The parameters for `Aurora`'s recycling model are not listed since the recycling was switched off.

Settings	Bayes factor	ped. MAP $\frac{\chi^2}{n_{\mathrm{DOF}}}$	ped. $\overline{\left(\frac{v_{\mathrm{MAP}}-v_{\mathrm{truth}}}{\sigma_{v,\mathrm{post.}}}+\frac{D_{\mathrm{MAP}}-D_{\mathrm{truth}}}{\sigma_{D,\mathrm{post.}}}\right)^2}$
(1) reference case	1.00	1.05	0.05
(2) as (1), but without Ne^{9+} data	not comparable	1.09	0.09
(3) -1 edge knot	0.56	1.15	0.18
(4) -2 edge knots	0.05	1.21	0.31
(5) +1 edge knot	0.36	1.11	0.15
(6) + $\lambda_{\rho_{\mathrm{pol}}} = 0.01$	3.21	1.10	0.12
(7) + $\lambda_{\rho_{\mathrm{pol}}} = 0.03$	0.09	1.25	0.26
(8) Fixed edge knots at ρ_{pol} = 0.96, 0.975, 0.99, 1.01	0.63	1.09	0.05
(9) Fixed edge knots at ρ_{pol} = 0.965, 0.98, 0.995, 1.015	0.43	1.13	0.21
(10) with channel offsets	not comparable	1.65	0.11
(11) Ne^{8+} ionization × 1.5	$5.11 \cdot 10^{-5}$	1.13	0.31
(12) n_{e} and T_{e} shift $\rho_{\mathrm{pol}} - 0.005$	0.65	1.07	0.27
(13) SOL losses × 2	0.95	1.11	0.07

Table 5.2: Comparison of inferences from synthetic data with different settings. In the reference case (1), 4 knots are placed in the core, which are free to move between minimum boundaries of ρ_{pol} = 0.05, 0.1, 0.35, 0.75 and maximum boundaries of ρ_{pol} = 0.25, 0.65, 0.9, 0.95, and another 4 knots are placed in the edge, which are all free to move in the range $0.95 < \rho_{\mathrm{pol}} < 1.03$, keeping a minimum distance of $\rho_{\mathrm{pol}} = 0.01$, and bounded from above by a fixed knot at $\rho_{\mathrm{pol}} = 1.03$. Also, in the reference case, the smoothness prior, set by $\lambda_{\rho_{\mathrm{pol}}}$, was disabled. The Bayes factors can only be compared for inferences with the same likelihood, thus especially when using the same data set. The data match and the accuracy of the MAP in the pedestal ($0.95 < \rho_{\mathrm{pol}} < 1.0$) are measured by the reduced χ^2, and by the mean squared deviation of the v and D profiles from the ground truth, weighted by half the size of the posterior $1\,\sigma$-quantile, as defined in figure 5.1.

All tests are summarized in table 5.2 for comparison with their Bayes factors (cf. section 2.3.1) and quantities to measure the data match and accuracy of the MAP. The inferences were performed in `MultiNest`'s constant efficiency mode (cf. section 4.2.1), with a target sampling efficiency of 0.05 and 1000 live points. The stability of the posterior against these sampler settings was tested for the reference inference (case 1), which was repeated with a sampling efficiency of 0.01 and with 1500 live points, both of which yielded consistent results. This reference inference, which has the best MAP data match and accuracy, is shown in figure 5.1, and demonstrates that our framework is able to reconstruct the correct D and v profiles and additional free parameters from a typical data set. It was also repeated without Ne^{9+} data (case 2), providing a similar posterior, and thus proving that data from 2 charge stages is in principle sufficient for an inference. The reduced χ^2 of the MAP, i.e., its χ^2 divided by the number of degrees of freedom, $n_{\mathrm{DOF}} = n_{\mathrm{data}} - n_{\mathrm{parameters}}$, is in both cases close to the ideal value of 1.0, which can however not be reached exactly due to the inherent limitations of the spline parameterization, which prevents the profiles from perfectly reproducing the ground truth. Finally, it was also tested that a different random seed in an inference does not significantly influence the result.

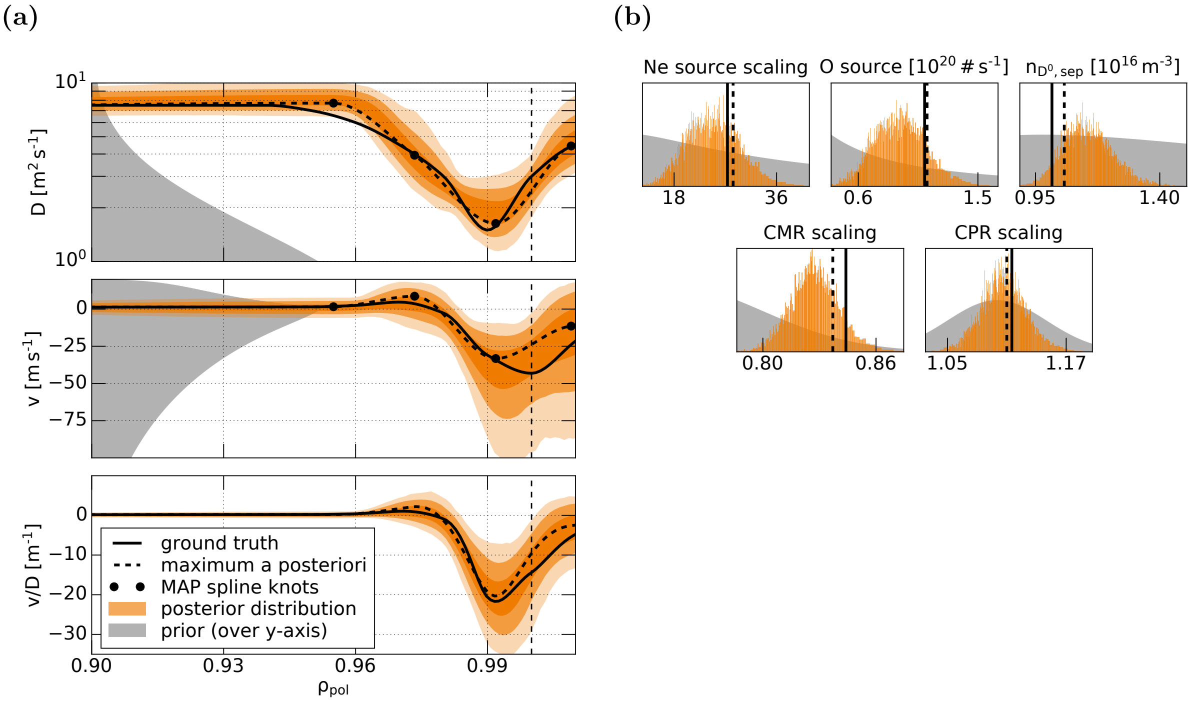

Figure 5.1: Inference result from synthetic data with the setup of the reference case, as specified in table 5.2. The reference case denotes the inference in which the best MAP data match and accuracy of the transport coefficient profiles were achieved. (a) Transport coefficient profiles at the plasma edge. The orange shadows indicate the 1, 2 and $3\,\sigma$-quantiles of the posterior probability distribution, i.e., in the non-Gaussian case the ranges covering 68.3 %, 99.4 % and 99.7 % of the probability, likewise to both sides of the probability mean. The normalized prior distributions are plotted over the y-axis. The vertical dashed line indicates the separatrix. (b) Additional scalar parameters. The posterior probability distributions (orange) and the normalized prior distributions (grey) are shown. The ground truth (solid) and the MAP (dashed) are indicated by vertical lines (black).

To illustrate the precision of the results for v and D compared to $\frac{v}{D}$, as well as in the pedestal compared to the core, an additional inference from the synthetic data was performed. Its settings were mainly consistent with the reference inference (case 1), but all spline knots were radially fixed, allowing the correlations between v and D at certain radial positions to be more easily visualized. The fixed knot positions were selected near their MAP positions in the reference case, at $\rho_{\mathrm{pol}} = 0.05,\ 0.2,\ 0.4,\ 0.8,\ 0.96,\ 0.975,\ 0.99,\ 1.01,\ 1.03$. Figure 5.2 shows the correlations of v and D in the posterior probability for distinct locations in the core, at the pedestal top, and where Ne density gradient in the ground truth is steepest. As expected for inferences based on the charge-stage method, the uncertainty, especially in D, increases significantly in the core. This is because the transport coefficients cannot be disentangled once the impurity becomes fully ionized and only one charge stage remains in substantial amounts. In the pedestal, v and D can be clearly disentangled, but $\frac{v}{D}$ is still better constrained. This is not surprising, since $\frac{v}{D}$ follows directly from the profile shape of the total impurity density according to equation 1.10, without any need for knowledge of atomic processes. The measurements of the 3 Ne charge stages therefore provide a strong constraint.

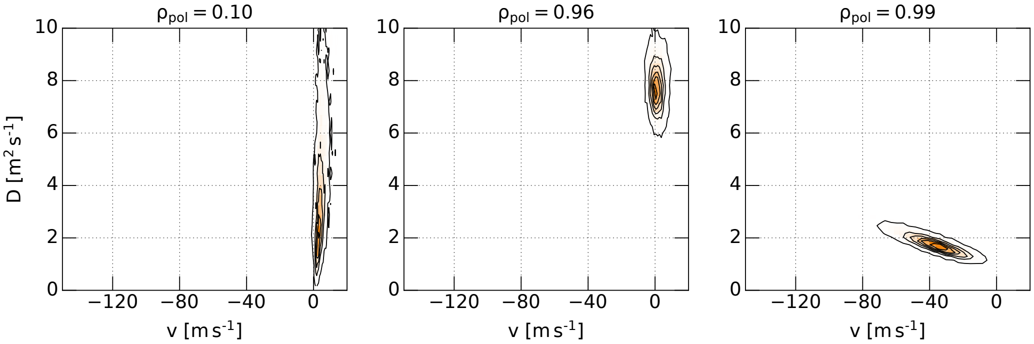

Figure 5.2: Visualization of posterior correlations between v and D at different radial positions. 2-D marginal posterior probability densities of an inference from the synthetic data are shown. The inference used the settings of the reference inference in table 5.2, except for fixed spline knots at $\rho_{\text{pol}} = 0.05, 0.2, 0.4, 0.8, 0.96, 0.975, 0.99, 1.01, 1.03$. Three radial spline knot positions in the core, at the pedestal top, and at the location of the steepest Ne density gradient in the ground truth are selected. The probability density values at which the contours are drawn and which determine the transparency of the coloring are the same in all subplots.

The following tests are aimed at assessing the spline parameterization of the transport coefficient profiles, and the influence of data perturbations and model errors on the inference. However, it should be noted that this study remains selective since not all possible settings and influences can be tested. Moreover, the Bayes factors are used for comparison, employing the Jeffreys' scale (Jeffreys, 1998, appendix B), according to which a Bayes factor $\gtrsim 3$ indicates substantial evidence for the model with higher Bayesian evidence. In doing so, it must be kept in mind that the accuracy of the Bayesian evidence estimates is compromised by the use of `MultiNest`'s constant efficiency mode. Thus, the values shown in table 5.2 should be taken as indicative rather than relying on their absolute values.

5.2 Assessment of the spline parameterization

The inference from the synthetic data was repeated with different settings for the spline knot locations and the smoothness prior of the D and v profiles (cf. section 4.2.2), listed in table 5.2. This model selection test in particular suggests not to use too few spline knots (case 4), and not to apply a too strong smoothness prior (case 7). The use of free knots is slightly more favorable than fixed knots (case 8 vs. case 1), and the positions of the fixed knots are also slightly relevant (good positions, i.e., close to the MAP from case 1, in case 8 and worse positions in case 9). That none of this is strongly indicated, can be understood by the high number of knots, which are densely packed in the pedestal in all three cases. Furthermore, the tests indicate that the reference case (1) is using the optimum number of spline knots, as both the removal (case 3) and the addition (case 5) of knots reduce the evidence, the latter probably due to an unnecessary increase of the parameter space dimensionality. Finally, the use of a weak radial correlation length for the smoothness prior (case 6) seems to be slightly suggested by the Bayes factor, but its application results in a worse MAP data match and accuracy. This can be understood as the good data quality, i.e., dense data without systematic errors, does not pose any risk of spline overshoots. Additional imposed smoothness is therefore not necessary but rather hinders the capture of the actual profiles.

In summary, the presented inferences show that the framework is able to handle a sufficient number of spline knots in the pedestal to capture profile shapes of realistic complexity. Moreover, the inference quality is not severely degraded when a small smoothness prior is imposed, which may be useful in the case of poorer data quality.

5.3 Influence of data perturbations

In the inferences presented above, the error pattern of the synthetic data matches the likelihood definition exactly. In reality, however, data perturbations that are not captured in the likelihood can occur. In the case of the CXRS data used, such perturbations are most likely systematic errors in the form of calibration issues of individual channels, which are difficult to correct or infer as free parameters, as they are often not well constrained by the profile shape. Therefore, the reference inference, case 1 in table 5.2, shown in figure 5.1, was repeated with realistic additional channel offsets (case 10). The data of three channels, CMR-1-2, CMR-1-10, and CMR-1-11, were divided by factors of 0.90, 1.30, and 0.85, respectively, which is similar to the offsets that were found in the original data of #39461. The comparison of the transport solution with the reference case is presented in figure 5.3, column 1 and row 1 in the top and bottom, respectively. It shows the sensitivity of the inferred diffusion profile and stresses the importance of accurate calibrations.

5.4 Influence of model errors

In the inferences presented above, no model error was assumed, although it could exist in the background plasma equilibrium and profiles, the atomic data, the SOL transport approximation, or the NBI strength calculation. For our inferences based on data from multiple charge stages in the steep gradient region of the pedestal, a particularly important error source is the impurity charge stage balance. It is calculated in `Aurora` from sophisticated atomic data (cf. section 4.1.3.1) together with the kinetic plasma profiles (cf. section 4.1.2), mainly T_e, which are difficult to determine with good alignment in the pedestal. Moreover, due to the proximity of the SOL, it is essential to ensure that the results do not depend crucially on the exact settings for the fixed parameters in the approximate SOL model (cf. section 4.1.3.2). For these reasons, the reference inference, case 1 in table 5.2, shown in figure 5.1, was repeated with artificially introduced model error according to the following model modifications (cases 11, 12 and 13):

- Ne^{8+} ionization rate coefficients increased × 1.5
- n_e and T_e shifted inward by $\rho_\mathrm{pol} = -0.005$
- SOL Mach number, i.e., parallel losses, increased × 2

The comparisons of the transport solutions with the reference case are presented in figure 5.3, columns 2–4 and rows 2–4 in the top and bottom, respectively. They show that the inference result is indeed mostly independent of the SOL losses. The increased SOL losses are simply

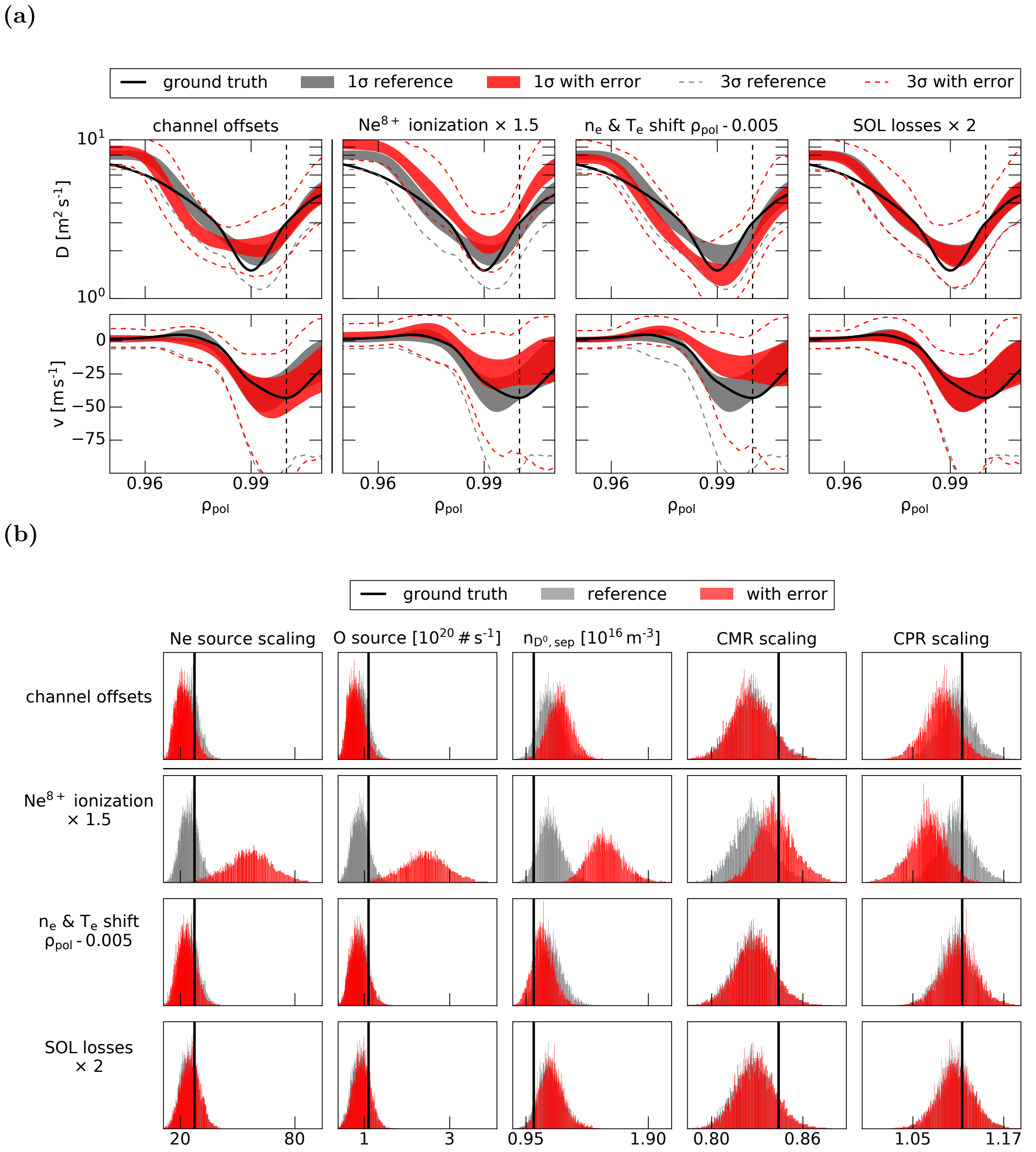

Figure 5.3: Inferences from synthetic data with channel offsets or different model errors. For the test with data perturbations (column 1 and row 1), realistic offsets of individual channels were introduced in the data. For the tests with different types of model error (columns 2–4 and rows 2–4), the Ne^{8+} ionization rate coefficients, the alignment of the n_e and T_e profiles, and the amplitude of the SOL losses were altered. All results are compared to the reference inference (case 1 in table 5.2, shown in figure 5.1). (a) Comparison of the transport coefficient profiles at the plasma edge. The shown quantiles are defined as in figure 5.1. (b) Comparison of the univariate posterior distributions of the additional scalar parameters.

balanced by a reduction of the diffusion coefficient in the far SOL, where it is not constrained by CXRS data. This region is not shown in the figures, and does not affect the pedestal. In contrast, the inferred D and v profiles are both sensitive to inaccuracies in the atomic data and in the kinetic profiles. The scalar parameters are most influenced by the increased ionization of Ne^{8+}, which is in particular balanced by an increased recombination via CX with thermal neutral D, whose density is inferred to be higher. Potential model errors in the synthetic diagnostic (cf. section 4.1.4) were not tested. However, Dux et al., 2020 showed that the error in the beam attenuation can be estimated to be, at most, 15 % and the error in the relative effective CX-emission rate coefficients when comparing two ionization stages to be, at most, 20 %.

6 Investigation of type-I ELMy H- and L-modes

As outlined in section 1.4, several previous studies on impurity transport in type-I ELMy H-mode plasmas have found evidence for impurity transport at the neoclassical level during inter-ELM phases, and thus for complete suppression of turbulent impurity transport by the ETB. However, an experimental derivation of the disentangled transport coefficients D and v with high radial resolution in the pedestal, and a thorough uncertainty quantification have been lacking. This is addressed in this chapter, which presents Ne transport analyses for dedicated AUG discharges in type-I ELMy H-mode and L-mode, applying the novel inference framework. Previous results are verified and the impurity transport barrier in H-modes with large ELMs is quantitatively compared to the higher transport level in L-mode. Furthermore, the impurity transport during an ELM is estimated in terms of D and v to assess the typical description of the ELM effect on impurities as anomalous diffusion. Yet, these results cannot be interpreted quantitatively due to the inaccurate approximation of the ELM as stationary state and the insufficient diagnostic temporal resolution.

The analyzed discharges are presented in section 6.1, and the specific settings for the data analysis are detailed in section 6.2. For all discharges, the neoclassical transport was calculated as explained in section 6.3. The experimental results are compared to the neoclassical modeling in section 6.4 for the inter-ELM phases of the ELMy H-mode discharges and for the L-mode. Section 6.5 shows the estimation of Ne transport during ELMs. Finally, all results are discussed in section 6.6.

6.1 Discharges

	#39084 (3.60–6.90 s) type-I ELMy H-mode (∼ 6 Hz ELMs)	#39086 (4.30–7.47 s) type-I ELMy H-mode (∼ 65 Hz ELMs)	#40014 (8.13–8.50 s) L-mode
I_p	1.00 MA	1.00 MA	0.84 MA
B_T	−2.50 T	−2.50 T	−2.45 T
D gas puff rate	$4.0 \cdot 10^{21}\,\mathrm{el\,s^{-1}}$	$5.7 \cdot 10^{21}\,\mathrm{el\,s^{-1}}$	$3.9 \cdot 10^{21}\,\mathrm{el\,s^{-1}}$
Ne gas puff rate	$8.9 \cdot 10^{20}\,\mathrm{el\,s^{-1}}$	$3.5 \cdot 10^{20}\,\mathrm{el\,s^{-1}}$	$8.7 \cdot 10^{20}\,\mathrm{el\,s^{-1}}$
Ne gas valve	divertor valve Du01X	divertor valve Du01X	divertor valve Du01X
ICRF heating	–	–	–
ECRH power	2.4 MW, 3 gyrotrons	3.9, 3.6 MW, 6, 5 gyrotrons	2.8 MW, 4 gyrotrons
NBI power	2.4 MW, 1 beam	2.4 MW, 1 beam	2.4 MW, 1 beam
δ_up	0.05	0.03	0.29
κ	1.70	1.71	1.70
W_MHD	0.56 MJ	0.50 MJ	0.37 MJ
Greenwald fraction $\overline{n}/n_\mathrm{GW}$	0.80	0.68	0.70

Table 6.1: Plasma parameters in the type-I ELMy H- and L-mode discharges. The relevant time ranges, in which the discharges were stationary (except for the ELMs), are indicated. These phases were used for the data analysis. In #39086, one gyrotron dropped out at approximately 5.16 s, resulting in slightly reduced ECRH heating power, which however did not significantly affect the plasma parameters.

For the investigation of the type-I ELMy H-mode and L-mode, 3 dedicated discharges were conducted, the main parameters of which are given for the analyzed time ranges in table 6.1. #39084 and #39086 are ELMy discharges with different ELM frequencies of approximately 6 Hz and approximately 65 Hz, respectively. The ELMs in #39084 occurred less regularly than in #39086 due to their very low frequency. #40014 entered an L-mode for a few hundred milliseconds towards the end of the discharge, which is the time range examined here. Originally, this discharge was planned as a stepwise transition from the QCE regime to a type-I ELMy H-mode by ramping down the gas puff. This is the reason for the high upper triangularity, which was used to access the QCE regime. However, large ELMs at the end of the discharge were not achieved but the L-mode phase occurred instead. It is a radiative L-mode, which is established at high heating power in combination with strong radiation. Since the Ne gas puff was not reduced equally with the D fueling during the pulse, the Ne content and its contribution to the total radiation increased throughout the discharge. This could explain that the heat flux across the separatrix dropped below the H-L backtransition threshold.

Radiative L-modes differ from typical L-modes in the sense that they are observed to have H-mode-like confinement, as the smaller pedestal gradients are compensated for by an increased pressure gradient further inwards. Fable et al., 2021 found that in particular the T_i gradient is enhanced in the outer core region at normalized radii $0.7 < \frac{r}{a} < 0.9$. Integrated modeling showed that the steepened core gradients can be explained by a decrease in ITG turbulence due to fuel dilution by impurities (Fable et al., 2021). Therefore, in spite of the good confinement, radiative L-modes are likely not a viable scenario for a reactor. In #40014, the gradients of T_e, T_i and n_e inside the pedestal top are indeed all larger than the respective gradients in the inter-ELM phases of #39086, and the electron pressure reaches the same level in the inner core. This is illustrated in figure 6.1. Yet, the localization of the gradient enhancement in the outer core region, as well as its main effect on the T_i profile, are not obvious. It should be noted, however, that the two discharges differ in relevant plasma parameters, such as the plasma current, and a quantitative comparison must therefore be treated with caution.

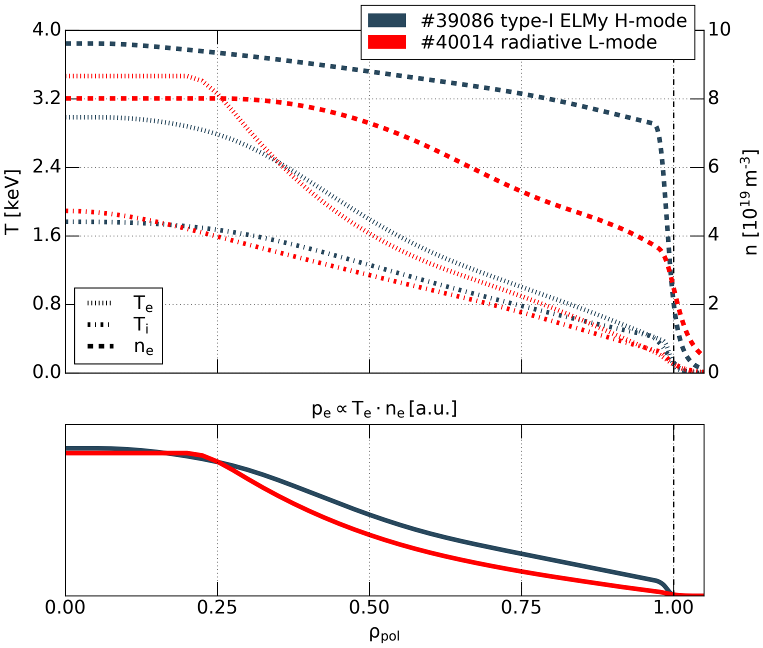

Figure 6.1: Kinetic profiles of the radiative L-mode #40014. All quantities are shown for the full radial range and compared to the respective quantities during the inter-ELM phases of the type-I ELMy H-mode #39086. The profiles of the individual temperature and density profiles (top), lead to a pressure profile, here shown for the electrons, which reaches the H-mode level at the magnetic axis (bottom).

The presented impurity transport analyses focus on the pedestal, where the kinetic profiles are not affected by the specific radiative characteristics of the L-mode. Therefore, the results obtained should be similar to those in typical L-modes and the discharge can be used for a comparative study of pedestal Ne transport in type-I ELMy H-mode and L-mode. The analyses of the ELMy discharges are mainly targeted at the quasi-stationary phase after the pedestal build-up and before the next ELM crash in the inter-ELM phases. In these time intervals, the observed Ne charge stage densities are constant on transport time scales and neoclassical transport is expected in the pedestal. In order to separate these phases, the data were evaluated ELM-synchronized, as explained in section 6.2.1. Moreover, a rough estimate of pedestal Ne transport during ELMs using the ELM synchronized data is presented in section 6.5. However, these results should be considered with caution due to the lack of an actual steady state, on which the inference method relies, and due to the coarse temporal averaging. They should therefore only be interpreted as indicative.

The pedestal kinetic profiles of the inter-ELM phases in the type-I ELMy H-mode plasmas and of the L-mode plasma are plotted in direct comparison in figure 6.2. For the thermal neutrals, they were calculated with the code `KN1D` and the absolute densities at the separatrix were inferred, whereas the other quantities were fitted from measurement data (cf. section 4.1.2). The L-mode pedestal gradients and pedestal top values are significantly smaller in all profiles. Moreover, the densities of the thermal neutrals in the plasma edge are considerably lower. For all discharges, their temperatures are lower than the ion temperatures throughout, since they originate mainly from further outward CX reactions.

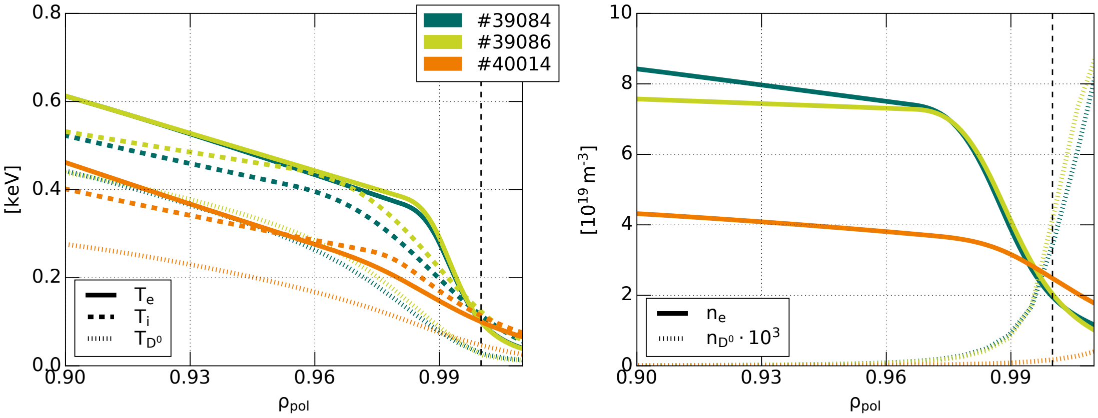

Figure 6.2: Kinetic profiles of the type-I ELMy H- and L-mode discharges at the plasma edge. For each discharge, the plotted n_{D^0} profile corresponds to the profile calculated with `KN1D`, scaled such that the separatrix density is equal to the posterior mean of the corresponding inferred scalar parameter. T_{D^0} is also obtained from `KN1D`. The fits of the other quantities are based on all data in the data analysis time ranges, in the ELMy plasmas restricted to the selected inter-ELM phases. #39084 and #39086 are H-mode discharges with type-I ELMs, in #39084 with particularly low ELM frequency, #40014 is a radiative L-mode.

The two H-mode discharges were not carried out particularly close to a previous boronization, but at a distance of 9 full shotdays, providing the potential for a higher content of other impurities. In contrast, #40014 was conducted only one full shotday after a boronization. Of special relevance for the Ne transport analyses is in particular the O content since the CX-emission of O^{8+} cannot be separated from the corresponding Ne^{8+} CX-emission. The measured spectral line radiances are therefore compared to the summed contribution from both species (cf. section 3.1.2). This requires an additional `Aurora` run for O in the forward model, using the same transport coefficients, and the O density profile is therefore also returned as an inference result. A comparison of the O concentrations in the analyzed discharges is given in table 6.2. From these values, it is not evident that the longer time span since the last boronization had a significant influence on the O content in the ELMy discharges.

	#39084	#39086	#40014
$\rho_{\mathrm{pol}} = 0.00$	0.047 %	0.047 %	0.048 %
$\rho_{\mathrm{pol}} = 0.96$	0.105 %	0.075 %	0.085 %

Table 6.2: Oxygen concentrations in the type-I ELMy H- and L-mode discharges. Listed are the posterior mean values of the inference results for two radial positions, at the magnetic axis and approximately at the pedestal top.

In all discharges, the NBI beam 3, which the CXRS LOS observe, and 8, on the opposite side of the torus, were operated alternately as the only beams, such that always one beam was turned on. The dips of beam 3 were used to clean the spectral data from passive background contributions, which are measured during the beam-off phases (cf. section 3.1.4). As beam 3 was always the only beam used from box 1, no neutrals from other beams contributed to the CX-signal. It was operated at an extraction voltage of 59 kV and at an injection power of 2.4 MW in all discharges. In #39084 and #39086, the beam-on phases lasted 230 ms, and the beam-off phases 170 ms, whereas in #40014, the beam-on phases were extended to 330 ms and the beam-off phases shortened to 70 ms. To obtain a higher radial resolution of the data, the plasma was radially shifted in #39084 and #39086 at 6.25 s, moving the target value for R_{aus} from 2.140 m to 2.145 m. Since the L-mode phase in #40014 was achieved by chance and was rather short, changes in the radial plasma position were not intentionally applied but R_{aus} had a constant target value of 2.140 m. In all discharges, the actual R_{aus} read from the reconstructed equilibrium is approximately 2 mm less than the set value.

The exposure times of the spectrometers were in all discharges set to 2.5 ms for the edge CXRS measurements on CMR and CPR and to 5 ms for the core CXRS measurements on CER and CAR, except for an exposure time of 10 ms on CER in #40014. The cameras of the core CXRS system were always operated without EM-gain, while the EM-gains of the edge CXRS cameras were set to 20 in #39084 and #39086. In #40014, the edge CXRS cameras were as well operated with EM-gain, but the gain was accidentally set to 1. This is a non-ideal setting, as it does not help to increase the count rate but rather accuracy is lost due to the electron multiplication (cf. section 3.1.3.2). The data quality in #40014 is therefore below optimal. It is particularly bad for the Ne^{9+} measurement, as can be seen in figure 6.5, since this spectral line has the lowest intensities. Moreover, in #39084 and #39086 the wavelength range observed by the CPR spectrometer was by mistake set such that the NeIX spectral line was not imaged in addition to the NeVIII spectral line in the edge CXRS system. Hence, the Ne transport inferences for these discharges are based on data for the 2 charge stages Ne^{10+} and Ne^{8+} only. Such a data set is however sufficient for accurate inferences, as was demonstrated using synthetic data in section 5.1.

6.2 Data analysis

6.2.1 Data averaging and ELM synchronization

The time trace of the outer divertor shunt current, which indicates the ELM activity, is shown for #40014 in figure 6.3. As it is an L-mode, no ELMs but a steady low divertor current are observed. Therefore, the spectra can be averaged in time before they are fitted. As a compromise between good data quality and high radial resolution, the averaging was done in groups of 3, sorted by the R_{aus} of their corresponding equilibria (cf. section 3.1.4).

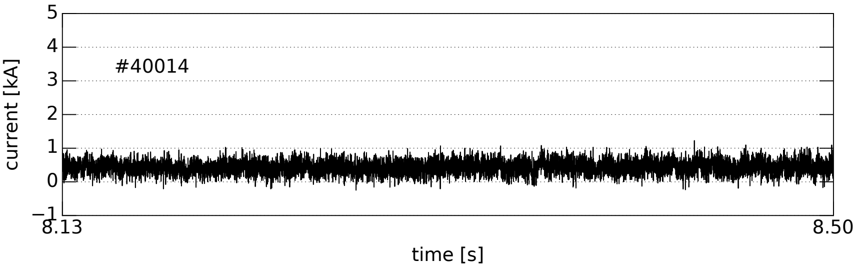

Figure 6.3: Time trace of the outer divertor shunt current in the L-mode discharge. The outer divertor shunt current is an indicator for the particle flux arriving in the divertor, and can therefore be used as ELM proxy.

The data of the ELMy discharges #39084 and #39086 were evaluated ELM-synchronized. For the analysis of inter-ELM Ne transport, only data from the nearly constant plasma phases preceding the ELM crashes is used. It is assumed that the plasma is stationary on transport time scales, such that the required steady-state condition for both the background plasma and the impurity densities is fulfilled, and the data can be mapped onto a single time point.

For the ELM synchronization, the onset times of all ELMs in the concerned time interval are read from the ELM shotfile, and the outer divertor shunt current signal is read as ELM proxy. Then, for each ELM, a time trace of the signal around the ELM is cut out, with a specified length and distance of its start from the ELM onset. The correlation between all pairs of these time traces is calculated in terms of the Pearson correlation coefficient

$$c_{\mathrm{Pearson}} = \frac{\sum_i (x_i - \overline{x}) \cdot (y_i - \overline{y})}{\sqrt{\sum_i (x_i - \overline{x})^2 \cdot \sum_i (y_i - \overline{y})^2}}, \tag{6.1}$$

where x and y are the two signal arrays with individual elements x_i and y_i and means $\overline{x}$ and $\overline{y}$. This is done for different amounts of relative time shifts up to 1 ms in both directions, and the maximum correlation of each pair is determined. Thereafter, the time trace for which the mean of all the maximum correlations with all other ELMs is the highest is used as a reference. All other time traces that have a maximum correlation with this reference above a given threshold are selected, and shifted to reach the maximum correlation. Finally, all edge CXRS data points whose full exposure time is within a specified relative time range in the time traces are used for the analysis. For the core CXRS data, which are less affected by the ELMs and usually have longer integration times, this condition is relaxed individually to ensure a sufficient number of data points.

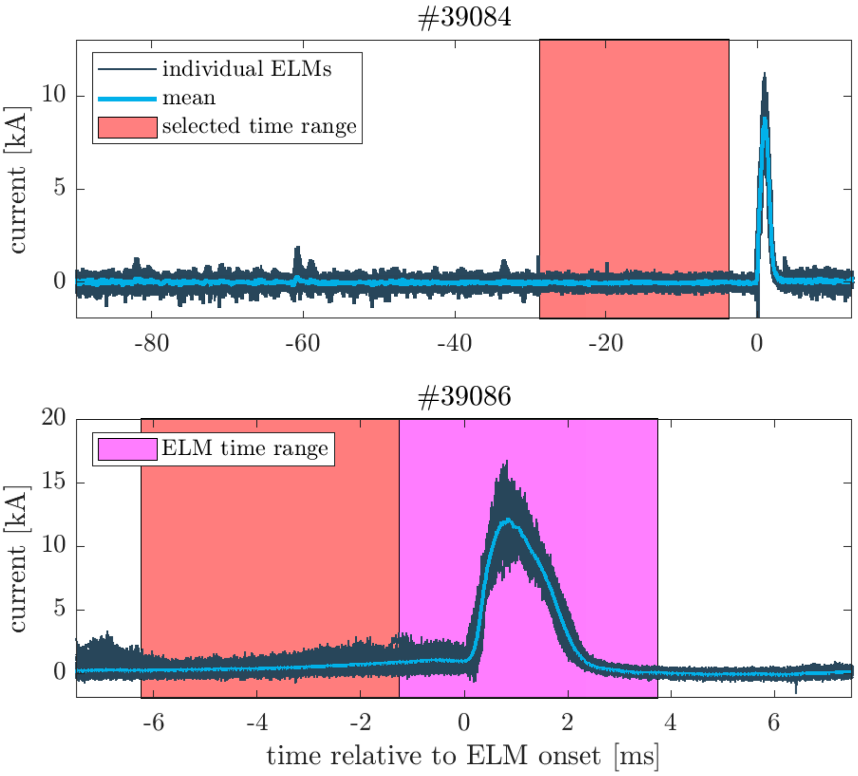

Figure 6.4: ELM synchronization and selection of time ranges between and during ELMs. The individual time traces of the outer divertor shunt current are overplotted after being shifted to have maximum correlation. For the data analysis, all edge CXRS frames with an exposure time fully within the marked time ranges were selected.

The ELM-synchronization for the ELMy discharges is illustrated in figure 6.4, showing the individual time traces, their mean, and the relative time ranges from which the data for the analysis of Ne transport in inter-ELM phases and during ELMs are taken. The correlation threshold was manually adjusted to 0.92 in #39084 and 0.98 in #39086, such that only time traces with a similar pattern are retained. Due to the low ELM frequency, the analyzed inter-ELM time range is much longer in #39084, but in turn, only 12 time traces are selected compared to 153 in #39086. In #39084, the relative time range was chosen based on the stationarity of the impurity radiances, whereas in #39086 the time ranges, both inter-ELM and during the ELMs, were chosen as short as possible. Although part of the pedestal build-up may be captured in the selected inter-ELM time range, and short time intervals before and after the ELMs are included in the ELM time range, stronger constraints were not used as they would have significantly reduced the number of data points due to the minimal exposure time of 2.5 ms in the edge CXRS system. This diagnostic is therefore not suitable for a finer resolution of impurity transport dynamics during an ELM cycle. However, the fitted radiances in the pedestal have sufficiently clear and distinct profile shapes in the two time ranges, which indicates that the spectra are well selected. They were not further averaged in #39084 and #39086. For all analyzed time ranges of all discharges and all charge stages, the fitted radiances in the pedestal are shown in the figures 6.8 and 6.11.

6.2.2 Correction of calibration offsets

The measurement of multiple charge stages requires the distribution of the toroidally looking CXRS LOS on 2 spectrometers. In contrast to the core CXRS system, this has not been the standard setup for the edge CXRS system in the campaigns concerned, but the CPR spectrometer was routinely used with other LOS (cf. section 3.1.2). Therefore, the LOS imaged on the CPR spectrometer were only connected to the spectrometer channels right before the discharges, and in #40014 additionally also most of the LOS imaged on the CMR spectrometer had been dis- and reconnected since the pre-campaign calibration. This procedure can easily violate the absolute calibration and introduce calibration offsets of individual channels (cf. section 3.1.3.3), which influence the inference result as demonstrated in section 5.3. In some cases, such offsets can be corrected manually, if only few channels are affected and their data overlap sufficiently with neighboring channels due to a radial plasma sweep. In addition, if several different discharges were done in a sequence, or if diverse discharge phases are present, the true offset pattern can become more obvious from the different radiance profile shapes. Finally, dedicated cross-calibration discharges, where both spectrometers are set to the same wavelength, such that the measured spectral line radiance profiles should match, can be helpful.

In the ELMy discharges, there are clear channel offsets towards the pedestal top in the Ne^{8+} data that was measured with the CPR spectrometer, as visible in figure 6.8. However, since several channels are affected, the offset pattern is not obvious. As there are moreover no helpful other discharges or discharge phases available, and no cross-calibration discharge was done, the offsets are not corrected. Fortunately, the Ne transport inferences are only marginally affected, since the profile shapes are still reasonably clear, especially in the regions of the steep gradients.

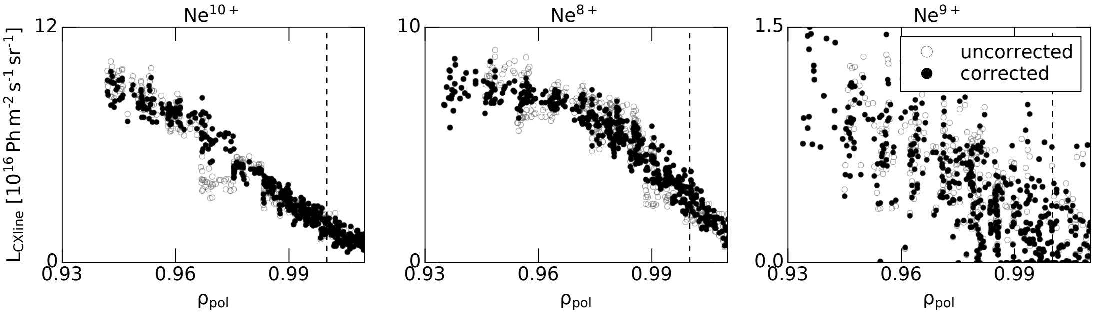

Figure 6.5: Correction of calibration offsets in individual channels in #40014. The CXRS radiance data are shown before and after application of the manually derived correction factors.

1-2	0.95	1-3	0.90	1-4	0.95	1-5	1.10	1-6	1.05	1-7	0.95
1-8	1.55	1-9	0.90	1-10	1.05	1-11	0.90	2-1	0.95	2-2	0.95
2-3	0.95	2-4	1.05	2-6	0.90	2-7	1.05	2-10	0.95	3-1	1.10
3-2	1.40	3-5	1.20	3-6	0.90	3-7	1.10	3-10	1.40		

Table 6.3: Correction factors for individual channels in #40014. The factors for the LOS were derived manually by looking at the CXRS data from different discharge phases of #40013 and #40014, and from the cross-calibration discharge #40016. The numbers in the first columns indicate the optical heads (CMR-1, CMR-2 and CMR-3) and their respective LOS.

In #40014, there are also several channel offsets, which were corrected as shown in figure 6.5, and listed in table 6.3. In this case, multiple discharge phases with different radiance profiles are available from the pulses #40013 and #40014, as these were attempts to transition between different confinement regimes. In #40013, the CXRS system also observed the different Ne charge stages. Therefore, calibration correction factors could even be derived for all channels, not only for those with the most obvious offsets. These factors were moreover checked using the cross-calibration discharge #40016, where both spectrometers measured the same spectral line of B. The fitted radiances with and without the calibration correction factors applied are shown in figure 6.6. Here, an additional factor of 0.8 was applied to all data measured with the CPR spectrometer. With these scalings, the CMR and CPR data in #40016 are in good agreement and draw a smooth radiance profile, which gives confidence in the derived corrections.

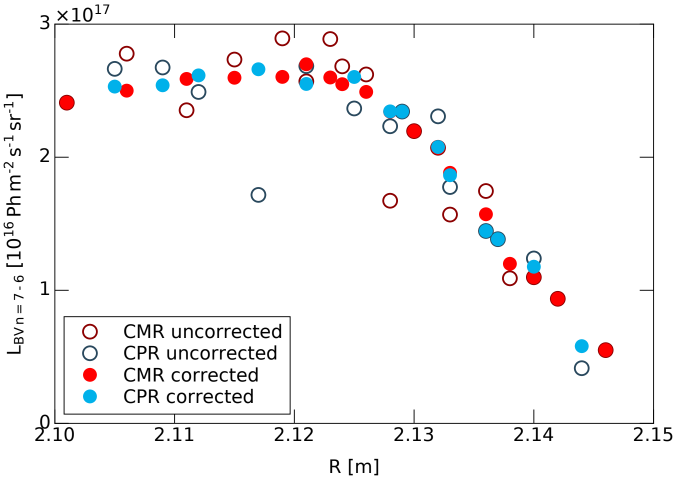

Figure 6.6: Data of the cross-calibration discharge #40016. Both edge spectrometers measured the spectral line BV $n = 7 \rightarrow 6$ at 494 nm. All spectra in the stationary time range between 3.6–4.2 s were averaged and fitted. The CXRS radiances are plotted with and without application of the correction factors used for #40014. The CPR data is additionally scaled by a factor of 0.8.

The scaling factor of 0.8 for the CPR data with respect to the CMR data is close to the ratio between the MAP values for the respective scaling factors in the inference result for #40014, which is 0.84. Such channel-independent scaling factors were included for both edge CXRS spectrometers as free parameters in all inferences since mismatches in the absolute radiances measured in the core CXRS system and the edge CXRS system were observed. It is assumed that the mismatches are due to calibration issues because other reasons were systematically excluded. In particular, since the two spectrometers CMR and CPR often show different offsets although they employ the same optical heads, any issues with the geometry of LOS and NBI are unlikely the cause. Moreover, errors in the background plasma profiles, atomic data, or the beam attenuation, would also affect the core CXRS system, and not lead to an offset between the different spectrometers. The core CXRS radiance data was used as fixed reference because the core CXRS system LOS were not subject to any dis- and re-connections during the campaigns, they maintained their absolute calibrations, and their optical head degradation was either very small (in the 2021 campaign) or could be corrected after the campaign (in the 2022 campaign) (cf. section 3.1.3.3). Moreover, the relative agreement of the core CXRS spectrometer calibrations was assessed in the 2022 campaign with the discharge #40700, where the same spectral line of N was observed on both, CAR and CER, and the relative difference between the measured radiances was $\leq 5\,\%$. Finally, the good agreement between the relative scalings of CPR and CMR in the inference result for discharge #40014 and in the cross-calibration discharge

#40016, which were both also done in the 2022 campaign, provides additional evidence for the viability of this approach, and further for the accuracy of the inference framework. In the 2021 campaign, which concerns the discharges #39084 and #39086, however, unfortunately no tests of the agreement between any of the spectrometer calibrations were done.

6.2.3 Inference settings

The equilibria used for the inferences correspond to the time points listed in table 6.4. These times were selected from the middle of the data analysis time ranges. However, for the ELMy discharges, care was taken to use equilibria from inter-ELM phases after the pedestal had built up, such that they are representative of the plasma phases from which the data originates. For the investigation of Ne transport during the ELMs in #39086, the equilibrium time point was chosen to be in the moment of an ELM at 5.880 s. All equilibria are retrieved from equilibrium reconstructions performed with `CLISTE`, which are routinely stored with a high time resolution of 1 ms in the EQH shotfiles. The resulting R_{aus} and W_{MHD} time traces show good agreement with IDE results, indicating consistency in the equilibria retrieved from the two codes (cf. section 4.1.1). The equilibria are mainly needed for mapping ρ_{pol} to `Aurora`'s radial coordinate r_{vol} as defined in equation 2.53. Besides, they are used for determining the variable geometry parameters of the simple SOL model (cf. section 4.1.3.2), which are used in `Aurora` and similarly in `KN1D`. Although the results are not very sensitive to these values, they are nevertheless listed in table 6.4.

equilibrium time point	#39084 4.740 s	#39086 5.885 s	#40014 8.300 s
distance of last grid point to separatrix	7.6 cm	7.8 cm	7.7 cm
distance of limiters to separatrix	5.1 cm	5.2 cm	5.1 cm
connection length to limiters	0.5 m	0.5 m	0.5 m
connection length to divertor	22.3 m	22.1 m	28.8 m
mean of CPR scaling factor prior	0.75	0.75	0.8
standard deviation of CPR scaling factor prior	0.05	0.05	0.05
mean of CMR scaling factor prior	0.95	0.95	1.0
standard deviation of CMR scaling factor prior	0.05	0.05	0.05

Table 6.4: Inference settings used for the type-I ELMy H- and L-mode discharges. The geometry parameters in the middle part of the table were approximated from the magnetic equilibria.

All other `Aurora` parameters used for the analyses were chosen as listed in the upper part of table 5.1. Moreover, also the `MultiNest` settings, the spline parameterization, and the other prior and likelihood settings were chosen identical to those used in the reference inference of the synthetic data tests presented in section 5.1, based on the general prior and likelihood settings (cf. sections 4.2.2 and 4.2.3). Specifically, 1000 live points and a sampling efficiency of 0.05 were employed, constraining the smoothness with radial spline knot correlations in the prior was not needed due to the high quality of the data, and an additional factor of 0.5 was applied to the weight of the core CXRS LOS in the likelihood to give approximately equal importance to the edge and core CXRS systems. The priors for the scaling factors of the data from both edge CXRS spectrometers, which are additional free parameters, as explained in section 6.2.2, were also again chosen as Gaussians, with means estimated from the radiance data by eye. Their means and standard deviations are listed in table 6.4, and they were additionally truncated at 0.5 and 1.5 to exclude very small or large scaling factors. Since #39084 and #39086 were both performed in the same session, changes to the calibration offsets due to fiber re-connections or optical head degradation can be excluded. Therefore, the same scaling factors are expected in both discharges, and the priors are accordingly set to be the same.

6.3 Neoclassical transport modeling

The neoclassical transport in the analyzed discharges is calculated based on the equilibria at the time points given in table 6.4, the kinetic profiles as shown in figure 6.2, and all available impurity density profiles. For Ne, the inferred posterior mean densities were used, as presented in figure 6.10. In addition, fully ionized N was added at the concentration that is required to match the Z_{eff} estimate from IDZ in order to account for other impurities present in the plasma (cf. section 4.1.2.3). Therefore, first, a concentration profile for N^{7+} was calculated, such that the Z_{eff} value is matched all along the profile (unless it is already over-fulfilled by the Ne impurity density). The concentration was then averaged along the profile, weighted with r_{vol}^2, i.e., volume averaged. This scalar concentration was finally multiplied by the n_{e} profile to obtain a N density profile that is proportional to the n_{e} profile.

Both the fluid code `NEOART` and the drift-kinetic code `NEO` were used for the neoclassical transport calculations. These codes can handle multi-species collisions, which is important in order to include collisions between the different charge stages of Ne since the Ne concentration is above the trace limit, as defined in equation 1.12, in all discharges. However, due to its drift-kinetic nature, `NEO` does not include the classical transport contribution. Furthermore, the `NEO` calculations were only done for specific radial points in the pedestal using its local mode to reduce the runtime. Also, only the 8 Ne charge stages $\geq 3+$ were included since the maximum number of species that `NEO` can handle is limited to 11, and includes the main ions, electrons, and the N^{7+}. The `NEOART` calculations, instead, include all Ne charge stages and are available for the full radial profile.

The plasma rotation was not included in the neoclassical transport calculations because the mass of Ne is small enough to avoid significant poloidal density asymmetries due to the centrifugal force. `NEO` was run with the full linearized Fokker-Planck collision operator, and with an approximation of the equilibria by 6 Fourier modes of the Miller extended harmonic (MXH) parameterization (Arbon et al., 2020). The resolution of the algorithm was set to the default values of 17 points in the poloidal direction, 18 polynomials in the cosine of the velocity pitch angle, and 7 energy polynomials. This setting was found to provide sufficient accuracy also in the steep gradient region. Nevertheless, it should be noted that the small ρ^*-ordering can become invalid, especially close to the separatrix, and can thus introduce errors in all neoclassical simulations. However, the results are accurate enough for the intended impurity transport studies.

The neoclassical transport profiles calculated with `NEOART` are presented in figure 6.7, differentiated into the contributions of different transport mechanisms to the diffusion and convection coefficients. In all discharges, the neoclassical transport in the pedestal is clearly in the Pfirsch-Schlüter regime, as $\nu^* \cdot \epsilon^{\frac{3}{2}} \gg 1$, namely more than an order of magnitude larger than the Pfirsch-Schlüter limit. Therefore, the contribution of the Pfirsch-Schlüter transport is dominant in both D and v. In Dux et al., 2014, it was shown that for very high collisionalities of $\nu^* \cdot \epsilon^{\frac{3}{2}} \gtrsim 100$, the temperature gradient contribution to the neoclassical convection can be reversed into an inward convection, instead of the temperature screening. However, the presented discharges still show a screening effect of the temperature gradient contribution. The `NEO` results, which cannot be easily separated into different contributions to the transport coefficients, are included in figure 6.9. The `NEOART` results in the figures 6.7 and 6.9 exhibit very small differences, especially close to the separatrix, since the values plotted in figure 6.7 are averaged over all Ne charge stages, weighted with their respective densities, while the values plotted in figure 6.9 are only averaged

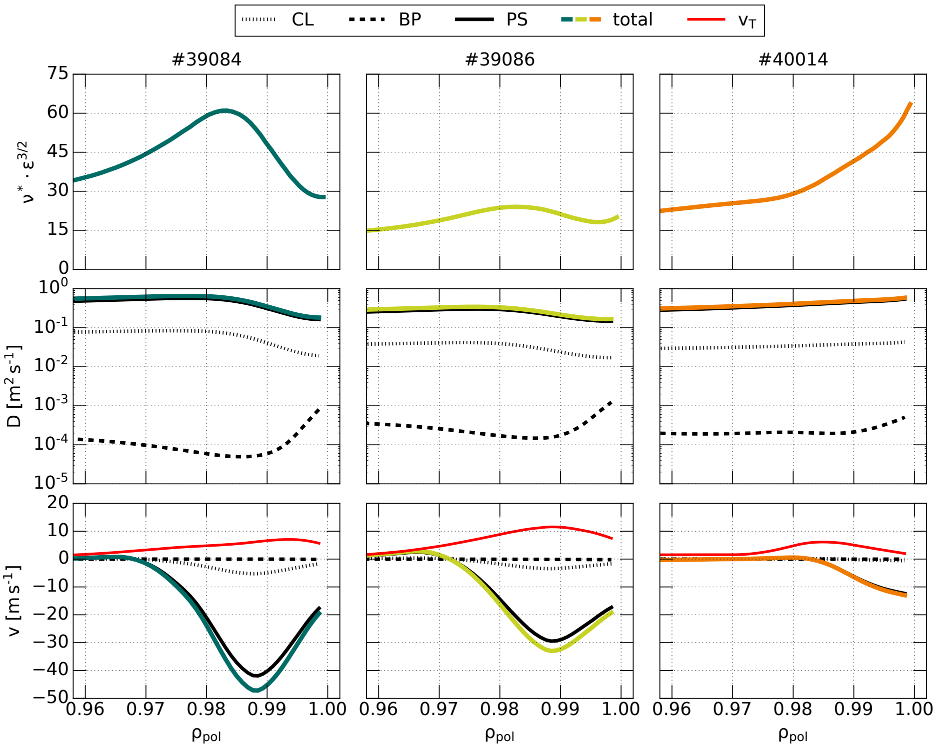

Figure 6.7: `NEOART` simulations for the type-I ELMy H- and L-mode discharges. The plasma edge profiles of the total transport coefficients are shown, as well as the individual contributions due to classical transport (CL), banana-plateau transport (BP), and Pfirsch-Schlüter transport (PS). Moreover, the total contribution of the temperature gradient term to the convection (v_{T}) is shown. The transport coefficients are averaged over all Ne charge stages, weighted with their respective densities.

over the highest 3 charge stages. The latter is more representative for the transport coefficients inferred from CXRS data of these charge stages, but cannot directly be retrieved as output from `NEOART` with disentangled contributions to the transport coefficients.

6.4 Neon transport in inter-ELM phases and L-mode

This section presents the results obtained for the pedestal Ne transport in the quasi-stationary inter-ELM phases of the two type-I ELMy H-mode discharges #39084 and #39086 and in the radiative L-mode phase of discharge #40014. Figure 6.8 shows the underlying spectral line radiance data in the pedestal. These data result from the spectral line fits of the CXRS measurements, after application of data averaging and ELM synchronization as described in section 6.2.1, and with corrections of individual channel offsets in #40014 as described in section 6.2.2. In addition, the synthetic data corresponding to the MAPs of the inferences, i.e., the samples that have the highest posterior probability, are shown. All settings of these inferences are described in section 6.2.3. The good agreement with the data that is achieved increases the confidence in the method and results.

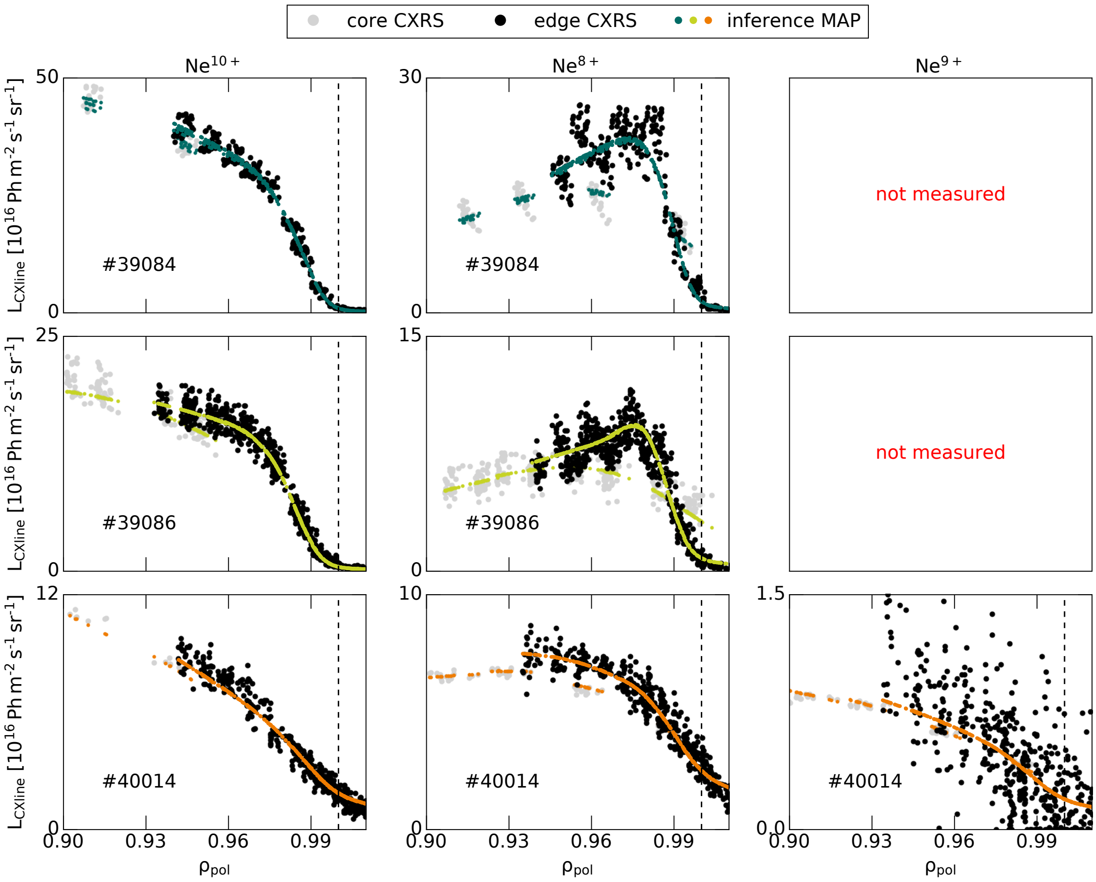

Figure 6.8: Comparison of the inference MAP with the data for the type-I ELMy H- and L-mode discharges. The radiance data of all measured spectral lines are shown, without error bars to avoid visual complication. Gaussian errors were used in the likelihood with standard deviations derived from the scatter in the individual channels using the bootstrapping method. All scaling factors are applied to the plotted data, i.e., the MAP of those inferred for the edge CXRS spectrometers, as well as the manually derived correction factors correcting for individual channel offsets in #40014. The radiance values calculated for each data point with the synthetic diagnostic from the inference MAP are overplotted. All data are plotted at the mean of the radial positions along the LOS weighted by their emissivity ϵ, i.e., $\rho_{\text{pol,plot}} = \int_{\text{LOS}} \rho_{\text{pol}} \epsilon \mathrm{d}l / \int_{\text{LOS}} \epsilon \mathrm{d}l$. The apparent mismatch between the LOS of the core and edge CXRS systems is an effect of their different viewing geometry. Their LOS capture light from different radial regions even if their emissivity-weighted mean radial positions are the same. The less tangential LOS of the core CXRS system are more affected by the pedestal density decay.

Figure 6.9 shows the inferred posterior distributions for the transport coefficients in the pedestal, compared to the neoclassical transport calculated with `NEOART` and `NEO` as detailed in section 6.3. Additionally, figure 6.10 shows the posterior mean densities of the individual charge stages in the pedestal. The differences between the results of the two neoclassical codes are small and can be partly explained by the missing classical transport in the `NEO` result.

The diffusion coefficient is much smaller and closer to the neoclassical level in the inter-ELM phases of the type-I ELMy H-modes than in the L-mode. In both ELMy discharges, the neoclassical solution is within the $3\,\sigma$-quantile of the posterior probability distribution for D at $\rho_{\text{pol}} \approx 0.98$, whereas in the L-mode, D is always at least a factor of 5 larger than the neoclassi-

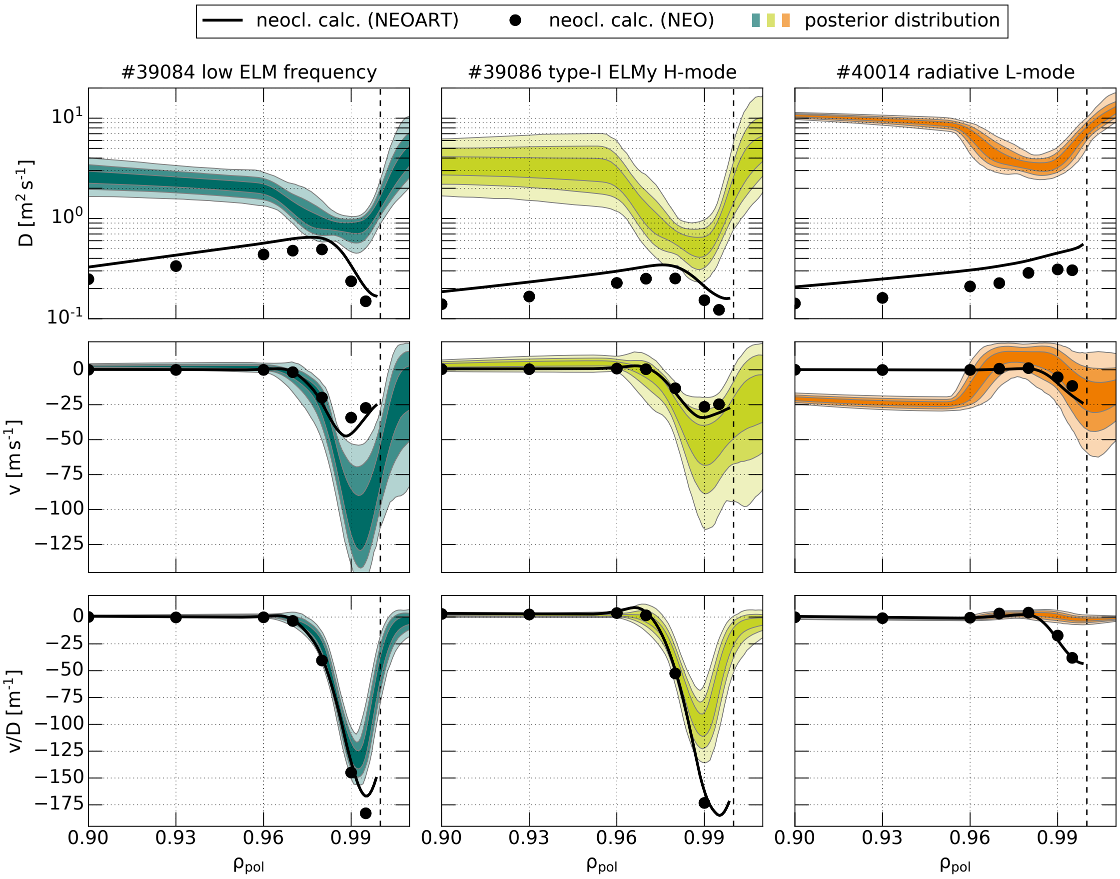

Figure 6.9: Inferred transport coefficients at the plasma edge compared to neoclassical simulations for the type-I ELMy H- and L-mode discharges. Here, D and v are defined with respect to the radial coordinate r_{vol} used in `Aurora` and `NEOART`. The results of `NEO` are converted to this radial coordinate definition. All transport coefficients are averaged over the highest 3 Ne charge stages, weighted by their densities. There are small differences between the `NEOART` and `NEO` results, which are partly due to the omission of classical transport in `NEO`. The posterior distributions are visualized with their 1, 2 and 3 σ-quantiles, as defined in figure 5.1.

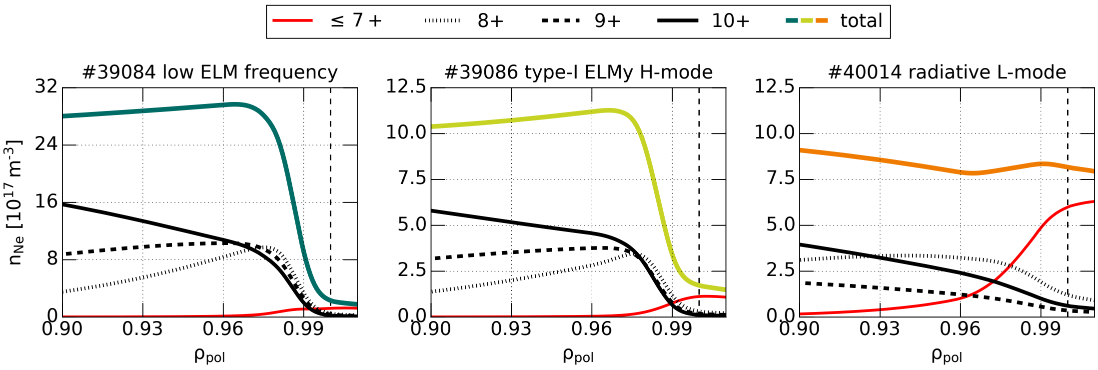

Figure 6.10: Posterior mean of the Ne charge stage densities in the type-I ELMy H- and L-mode discharges. The lower charge stages with $Z \leq 7$ are summed.

cal transport. For the convection, a slightly stronger than neoclassical inward drift is observed in the inter-ELM phases of the H-modes, but the uncertainty in v is large and this cannot be stated with much confidence. The ratio $\frac{v}{D}$, which is best constrained in the inference, is consistent with the neoclassical solution up to $\rho_{\mathrm{pol}} \approx 0.99$, whereas it is flat throughout in the L-mode pedestal. This is also reflected in the impurity densities, which show a substantial pedestal Ne peaking in the ELMy H-mode plasmas, in contrast to a flat Ne density profile in the L-mode plasma. In the latter, the higher charge stages exhibit some density gradients, but not so the total Ne density profile summed over all charge stages.

This difference in the pedestal impurity peaking can also be quantified in a scalar value as the pedestal peaking factor

$$F_{\mathrm{Ne}} = \frac{n_{\mathrm{Ne}}(\rho_{\mathrm{pol}} = 0.97)}{n_{\mathrm{Ne}}(\rho_{\mathrm{pol}} = 1.0)}. \tag{6.2}$$

It has values of 12.70 and 6.49 in the type-I ELMy H-mode discharges #39084 and #39086, compared to 0.97 in the L-mode discharge #40014.

Considering the charge stage densities, it should be noted that modeling the lower Ne charge stages with $Z \leq 7$ all with the same transport coefficients as inferred for the higher charge stages is not fully applicable, and may introduce errors in their density distributions. However, since especially the densities of the most affected charge stages with lowest Z are small in the confined plasma, the results for the transport coefficients of the higher Ne charge stages are only marginally affected. The inferred total Ne densities in all discharges are moreover in good agreement with the Z_{eff} estimates provided by IDZ (cf. section 4.1.2.3).

	#39084	#39086	#40014
O source	$4.6 \cdot 10^{19}\,\#\,s^{-1}$	$4.2 \cdot 10^{19}\,\#\,s^{-1}$	$55.5 \cdot 10^{19}\,\#\,s^{-1}$
Ne source scaling	14.9	21.1	139.5
CPR scaling factor	0.78	0.77	0.76
CMR scaling factor	0.98	0.96	0.91

Table 6.5: Posterior mean values of the scalar free parameters in the type-I ELMy H- and L-mode discharges.

The posterior mean values of the scalar free parameters are listed in table 6.5, except for the thermal neutral D densities at the separatrix, which are shown in figure 6.2. The scaling parameters for the edge CXRS spectrometers are moreover included in figure 6.8. They are indeed similar in #39084 and #39086, suggesting similar calibration error corrections, as it was the expectation for these discharges, outlined in section 6.2.3. The values for the Ne and O sources are not directly meaningful, since they include recycling, and also compensate for probable errors in the particle losses of the simple SOL model, such that the impurity particle flux crossing the separatrix matches the measurement data. Yet, the results for the source rates demonstrate that their priors leave enough freedom to infer very different values.

6.5 Neon transport during ELMs

This section presents the results obtained for the pedestal Ne transport in the type-I ELMy H-mode discharge #39086, specifically focusing on the phases during ELMs. These results must be interpreted with caution, since the analysis relies on two important stationarity assumptions: on the one hand, stationary background plasma profiles, implying constant transport coefficients in the analyzed time interval, and on the other hand, stationary impurity densities, allowing the application of the charge-stage method, since the time derivative in the transport equation vanishes, which yields equation 1.13. However, the exposure times of the CXRS diagnostic in the millisecond range necessitate the inclusion of signals from different phases during the ELMs, as shown in figure 6.4. Moreover, the transport coefficients and the impurity content both evolve dynamically during ELMs, without reaching a steady state. This poses a limitation that could not be fully addressed even with improved time resolution of the data. Consequently, the presented transport coefficients should be considered as indicative rather than quantitatively precise.

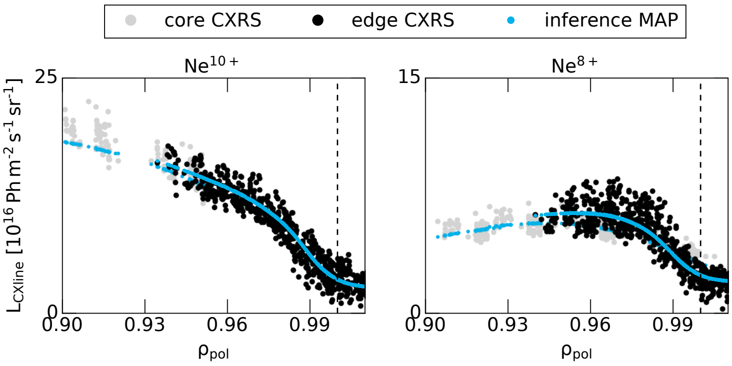

Figure 6.11: Comparison of the inference MAP with the data for the analysis of transport during ELMs. The data and inference result are plotted in the same way as in figure 6.8.

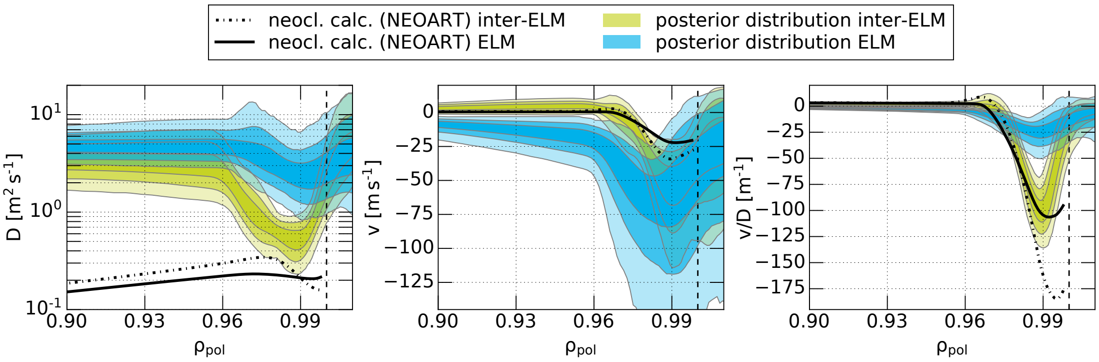

Figure 6.12: Inferred transport coefficients at the plasma edge during ELMs compared to neoclassical simulations. The posterior distributions and `NEOART` calculations are plotted in the same way as in figure 6.9. For direct comparison, the result for the Ne transport in the inter-ELM phases of the same discharge, #39086, is also plotted again.

Again, the MAP of the inference agrees well with the underlying spectral line radiance data, as shown in figure 6.11. Figure 6.12 shows the transport coefficient estimates, in direct comparison with the inter-ELM transport in the same discharge and with the respective `NEOART` simulations. Evidently, the ELMs have the effect of an additional diffusion. The influence of the ELMs on the convection is not clear due to the uncertainty in the inference result during the ELMs. This particularly large uncertainty is probably caused by the limited temporal resolution of the CXRS data, resulting in different data phases (just before, on, and just after the ELM) being included.

6.6 Discussion

The results presented in this chapter provide further evidence for neoclassical impurity transport in the inter-ELM phases of type-I ELMy H-mode plasmas, as suggested by previous studies, such as Pütterich et al., 2011. However, to the best of my knowledge, this is the first time that the disentangled transport coefficient profiles in the pedestal have been experimentally assessed with such high radial resolution. The two ELMy discharges analyzed have very different ELM frequencies, yielding inter-ELM phases of the order of 100 ms and 10 ms, respectively. Nevertheless, only a small difference was observed in the pedestal Ne peaking, which is slightly stronger and closer to the neoclassical level between the larger and lower frequent ELMs. This suggests that the ELM frequency or the duration of the inter-ELM phase, which determines the time available for the pedestal to rebuild, has only a limited influence on the impurity transport. In contrast, the diffusion was found to be strongly enhanced above the neoclassical level in the studied radiative L-mode plasma. This shows the turbulence at the plasma edge that acts in the absence of an ETB. It can be concluded that the H-mode ETB almost completely suppresses the turbulent impurity diffusion, which is dominant in L-mode. Finally, the transport during ELMs has been evaluated qualitatively. The inferred diffusion is clearly in line with studies describing ELMs as enhanced diffusion, such as, e.g., Dux et al., 2011, Pütterich et al., 2011 and van Vugt et al., 2019.

The above results strengthen the current understanding of the impurity dynamics in type-I ELMy H-modes. In present-day devices, a balance occurs between a neoclassical inward impurity pinch during the inter-ELM phases due to suppressed pedestal turbulence, and an outward impurity flushing during the ELMs, which can be modeled as enhanced diffusion. Indeed, a strong pedestal peaking of the Ne density was observed in the inter-ELM phases analyzed here, in contrast to a flat Ne density profile in the L-mode. As predicted by Dux et al., 2014 and Dux et al., 2017, the neoclassical impurity convection will most likely reverse in the pedestal in devices with reactor-like kinetic profiles, such as ITER, due to enhanced temperature screening. This would result in hollow impurity density profiles, and, as demonstrated by van Vugt et al., 2019, such profiles would cause ELMs to transport impurities inwards. The latter follows directly from the diffusive action of the ELM impurity transport, since diffusion always acts to flatten the impurity density gradient. First experimental evidence for these changed dynamics was found by Garcia et al., 2022 and Field et al., 2022 in JET plasmas with strong temperature pedestals.

7 Investigation of QCE and EDA H-modes

In this chapter, the radial Ne transport is studied in the pedestal of ELM-free and small-ELM regimes. Specifically, the QCE and EDA H-mode have been chosen as starting points for the investigations because they are well established on AUG, are not known to exhibit pronounced poloidal impurity density asymmetries or 3-D structures, and have promising characteristics as potential reactor scenarios. Particular emphasis is placed on the QCE regime. As explained in section 1.4, accumulation of high-Z impurities is not observed for either of these regimes, although the outward flushing effect of large ELMs is missing. This indicates an enhanced outward impurity transport even in the absence of significant ELM activity, in contrast to inter-ELM phases in type-I ELMy H-mode plasmas.

Section 7.1 presents analyses of stationary discharges, enabling a direct comparison with the results for the type-I ELMy H-mode and L-mode discharges discussed in chapter 6. A more detailed comparison of the QCE regime and the type-I ELMy H-mode is provided in section 7.2, which analyzes a discharge that is gradually transitioning between these two regimes.

7.1 Stationary discharges

7.1.1 Discharges and data analysis

	#39456 (4.80–8.50 s)	#39461 (3.95–6.81 s)	#39463 (6.70–8.20 s)
	QCE regime	QCE regime	EDA H-mode
I_p	0.83 MA	0.84 MA	0.72 MA
B_T	−2.45 T	−2.45 T	−2.50 T
D gas puff rate	$2.4 \cdot 10^{22}\,\mathrm{el\,s^{-1}}$	$2.4 \cdot 10^{22}\,\mathrm{el\,s^{-1}}$	$1.4 \cdot 10^{22}\,\mathrm{el\,s^{-1}}$
Ne gas puff rate	$0.89 \cdot 10^{21}\,\mathrm{el\,s^{-1}}$	$0.89 \cdot 10^{21}\,\mathrm{el\,s^{-1}}$	$1.3 \cdot 10^{21}\,\mathrm{el\,s^{-1}}$
Ne gas valve	divertor valve Du01X	divertor valve Du01X	A-port valve A03A
ICRF heating	–	–	–
ECRH power	1.6 MW, 3 gyrotrons	1.6 MW, 3 gyrotrons	3.1 MW, 4 gyrotrons
NBI power	4.9 MW, 2 beams	4.9 MW, 2 beams	4.9 MW, 2 beams
δ_up	0.27	0.27	0.33
κ	1.78	1.78	1.61
W_MHD	0.48 MJ	0.49 MJ	0.49 MJ
Greenwald fraction $\overline{n}/n_\mathrm{GW}$	0.90	0.89	0.90

Table 7.1: Plasma parameters in the QCE and EDA H-mode discharges. The relevant time ranges, in which the discharges were stationary, are indicated. These phases were used for the data analysis.

The main parameters of the 3 dedicated stationary discharges conducted to investigate the QCE and EDA H-mode are given in table 7.1 for the time ranges analyzed. The QCE discharges #39456 and #39461 are very similar, with only minor differences introduced to optimize the CXRS diagnostics. In #39456, the Ne gas puff was initiated only at 4.0 s in order to use the early discharge phase for measuring the O contribution to the spectral line radiances, which are compared to the summed CX-emissions of Ne^{8+} and O^{8+}. In #39461, instead, Ne was puffed starting already at 2.4 s. Moreover, the target R_aus was chosen further inward to improve the coverage of the pedestal with the edge CXRS LOS. In both discharges, the high density required to access the QCE regime was achieved through high D gas puffing, and the plasma was strongly shaped. The EDA H-mode discharge #39463 required less D fueling but still significantly more than the type-I ELMy H-mode and L-mode discharges in chapter 6. Compared to the QCE discharges, its shaping was similarly high, and it was heated with more ECRH power at the same NBI power. The QCE regime is routinely operated with 800 kA plasma current at AUG, which was adopted for the presented discharges, whereas the EDA H-mode was operated with an even lower plasma current of 700 kA. In #39463, one gyrotron dropped out at 6.2 s and was replaced by another soon after, resulting in a short dip in ECRH power. This phase was however not cut out from the analysis time range, as it did not significantly affect the plasma parameters.

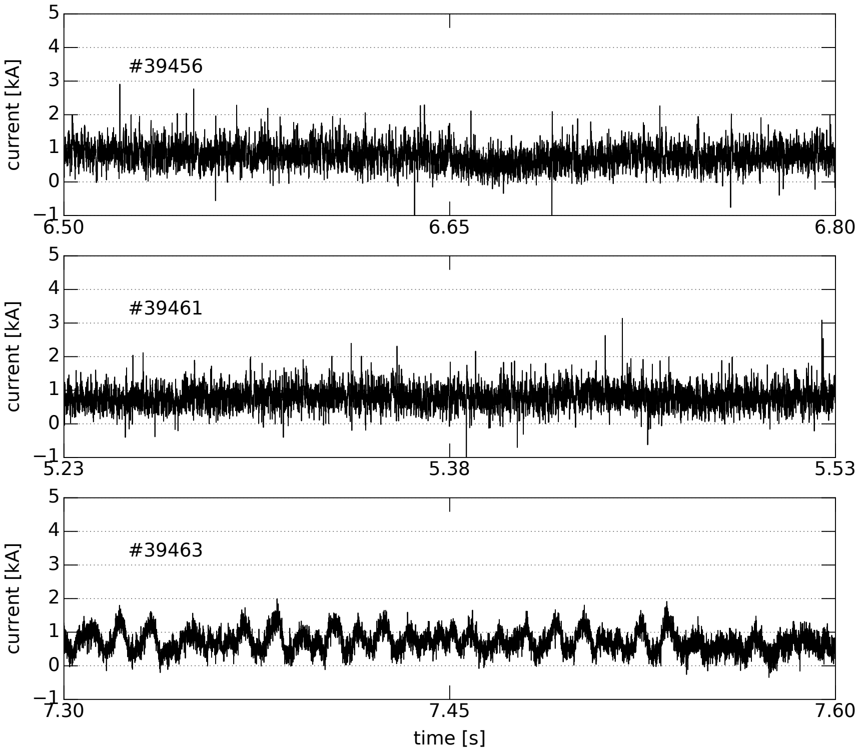

Figure 7.1: ELM activity in the QCE and EDA H-mode discharges. The outer divertor shunt current is shown as a proxy for the ELM activity. For higher time resolution, only the time traces of the central 300 ms in the data analysis time ranges are shown.

The data of all discharges can be analyzed time averaged, since the discharges are very stationary. The QCE discharges exhibit some small ELM activity, as expected, and also in the EDA H-mode discharge, some fluctuations of the divertor current, which is used as ELM proxy, are observed. Figure 7.1 shows that the amplitudes of these fluctuations are larger than in the time trace of the L-mode discharge #40014 shown in figure 6.3, but much smaller than type-I ELMs. These small ELMs and fluctuations are too fast to be resolved by the CXRS diagnostic system, and are therefore averaged in the impurity transport analyses. As described in section 6.2.1 for the L-mode discharge #40014, the spectra were again averaged before being fitted in groups of 3, based on the R_{aus} of their corresponding equilibria. The pedestal kinetic profiles of the QCE and EDA H-mode discharges are plotted together in figure 7.2. The higher separatrix densities in the QCE regime are immediately apparent, also in comparison to the respective profiles of the type-I ELMy H-mode and L-mode plasmas shown in figure 6.2.

The discharges were all carried out in a sequence, though spread over two different shotdays, approximately 2 full shotdays after the last boronization. The proximity to a boronization was intended to provide a low O concentration to reduce the influence of errors in the O density

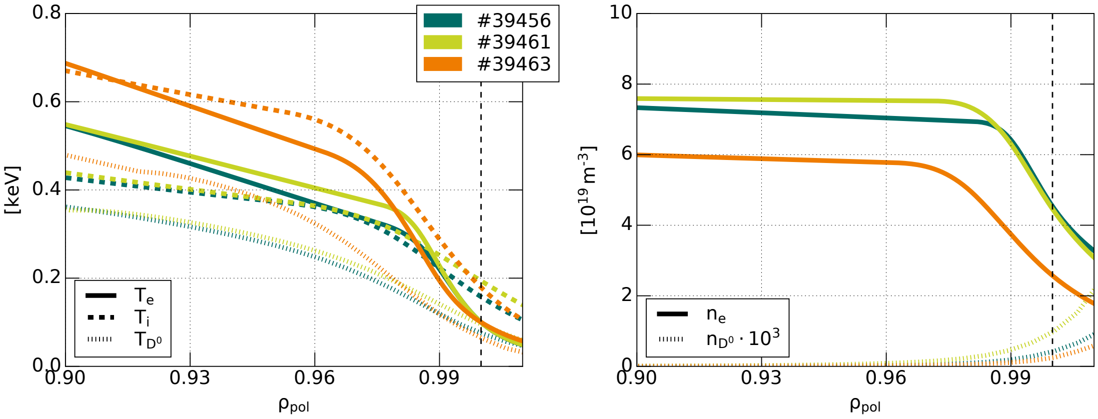

Figure 7.2: Kinetic profiles of the QCE and EDA H-mode discharges at the plasma edge. For each discharge, the plotted n_{D^0} profile corresponds to the profile calculated with `KN1D`, scaled such that the separatrix density is equal to the posterior mean of the corresponding inferred scalar parameter. T_{D^0} is also obtained from `KN1D`. The fits of the other quantities are based on all data in the data analysis time ranges. #39456 and #39461 are are very similar QCE discharges, #39463 is an EDA H-mode discharge.

profile, which is additionally inferred, on the Ne transport results. The O concentrations are compared for the analyzed discharges in table 7.2. They are indeed considerably lower than those in the type-I ELMy H-mode and L-mode discharges, which are presented in table 7.2, although the L-mode discharge #40014 was also carried out shortly after a boronization.

	#39456	#39461	#39463
$\rho_{\mathrm{pol}} = 0.00$	0.017 %	0.018 %	0.028 %
$\rho_{\mathrm{pol}} = 0.96$	0.030 %	0.026 %	0.056 %

Table 7.2: Oxygen concentrations in the QCE and EDA H-mode discharges. Listed are the posterior mean values of the inference results for two radial positions, at the magnetic axis and approximately at the pedestal top.

As mentioned above, in #39456, the radiance of the OVIII $n = 10 \to 9$ spectral line, which overlaps with the observed Ne^{8+} spectral line, was measured in an early discharge phase from 3.40–4.00 s, before the the Ne puff was turned on. The parameters of this plasma phase are very similar to the later data analysis time range when Ne was measured. Its data can therefore be mapped to data analysis time range and can be included in the inference for #39456 to improve the constraint on the Ne transport. However, due to the Ne content, the radiation in the plasma increased as soon as the Ne puff was turned on and the divertor temperature dropped. The n_{e} and T_{e} profiles used in the synthetic diagnostic (cf. section 4.1.4) for the O data, in particular for the calculation of the beam attenuation, were independently fitted based on the data in the early discharge phase. However, the impurity transport solver (cf. section 4.1.3) was necessarily run with the parameters of the later discharge phase, which may not be fully applicable to the O data. Figure 7.3 shows the agreement between the MAP of the inference and the O radiance data. The data are evidently less well matched than the Ne data shown in figure 7.6, but the order of magnitude of the O content and its profile shape could be reproduced.

The NBI settings were consistent across all discharges. Beam 3, which was operated as the only beam from box 1, was alternated with beam 8 to achieve the highest data quality, as also

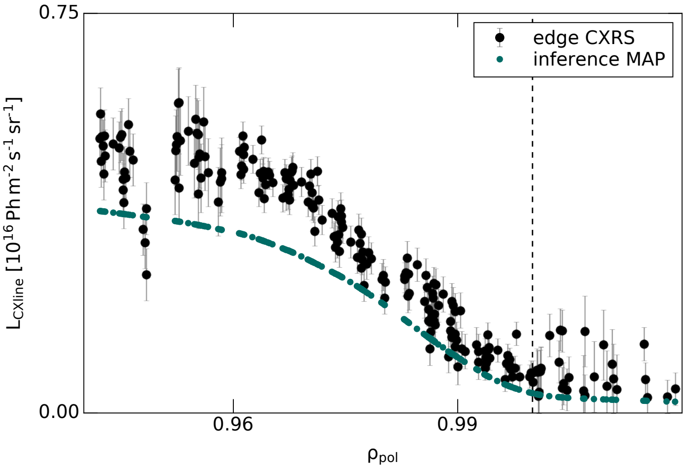

Figure 7.3: Comparison of the inference MAP with the oxygen radiance measurements in #39456. The radiance data are shown with their error bars indicating the standard deviations, which were estimated with the bootstrapping method for each channel and used in the univariate Gaussian likelihood.

described for the type-I ELMy H-mode and L-mode discharges in section 6.1. In addition, beam 5, which is also located on the other side of the torus, as beam 8, was operated continuously, such that 2 beams were always active. Beam 3 was operated with an extraction voltage of 59 kV and with an injection power of 2.4 MW. Its beam-on phases lasted 230 ms, and the beam off-phases 70 ms. Moreover, all discharges had large R_{aus} sweeps for increased radial resolution. The plasmas were shifted in discrete steps, with several of these steps covered by each of the analyzed time ranges, even by the O measurement phase in #39456. Figure 7.4 shows the pre-programmed target values and those resulting from the equilibrium reconstructions. The individual steps were set to last 300 ms to cover one beam-on and beam-off phase each.

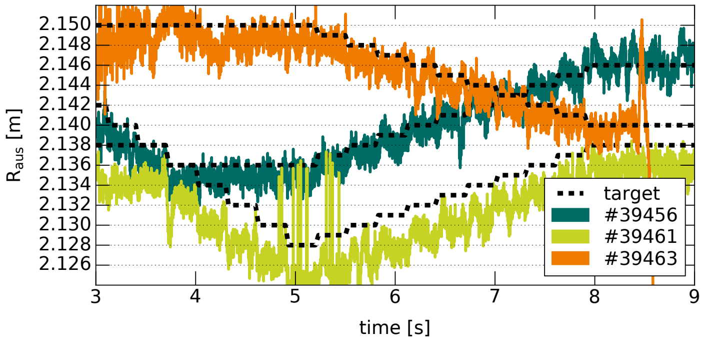

Figure 7.4: Radial plasma sweeps in the QCE and EDA H-mode discharges. The pre-programmed target values are overplotted over the values from the `CLISTE` equilibrium reconstructions saved in the EQH shotfiles.

The spectrometer settings were also consistent across all discharges. The exposure times of all spectrometers, including the edge CXRS system, were set to 5 ms. This is appropriate for these stationary discharges, as they do not require a high temporal resolution in the edge, unlike the type-I ELMy H-mode discharges. Also, all spectrometers were operated without EM-gain. The

Ne signal was strong enough to provide good data quality without additional amplification, even at the plasma edge. Moreover, all three Ne charge stages, Ne^{10+}, Ne^{8+} and Ne^{9+}, were observed. Thus, high quality data sets are provided for the inferences.

Nevertheless, calibration offsets of individual channels are present also in these data sets, similarly as those described in section 6.2.2 for the CXRS data of the type-I ELMy H-mode and L-mode discharges. However, since the QCE and EDA H-mode discharges were all performed in a sequence, without the possibility for optical head degradation and moreover without fiber re-connections, the same offsets should apply to the spectrometers as a whole as well as to the individual spectrometer channels in all discharges. Thus, the different profile shapes of the radiance data in the different discharges help to constrain the corrections. In addition, the large plasma sweeps performed in all discharges result in significant overlaps of data from neighboring channels, making offsets in individual channels more visible. Under these conditions it was possible to find a suitable set of correction factors that are likely to come close to correcting the actual calibration errors. The following factors were applied: CMR-1-2×0.90, CMR-1-10×1.25, CMR-2-1×0.95, CMR-2-3×1.05, and CMR-2-5×1.05, where the first number in the LOS name indicates the optical head (CMR-1, CMR-2), and the second number the respective LOS. These corrections are particularly relevant for the CPR data, which are the measurements of the Ne^{10+} radiances, towards the pedestal top in #39456 and #39463, while the profile shape of the CPR data in #39461 is less affected by the corrections. Figure 7.6 shows the data of all discharges with and without corrections for a direct comparison. In #39456, the measured spectral line radiances at the edges of the R_{aus} sweep, which coincide with the edges of the selected time range, were found to produce unrealistic profile shapes of all individual channels that do not match with their neighboring channels in the overlap regions, particularly in the Ne^{10+} data. Thus, some changes in the Ne distribution are suspected and these data were excluded. The remaining data, shown in figure 7.6, still provide sufficient overlap between neighboring channels.

	#39456	#39461	#39463
equilibrium time point	6.650 s	5.380 s	7.450 s
distance of last grid point to separatrix	7.7 cm	9.0 cm	7.1 cm
distance of limiters to separatrix	5.1 cm	6.0 cm	4.7 cm
connection length to limiters	0.5 m	0.5 m	0.5 m
connection length to divertor	29.7 m	29.4 m	30.8 m
mean of CPR scaling factor prior	1.15	1.15	1.15
standard deviation of CPR scaling factor prior	0.05	0.05	0.05
mean of CMR scaling factor prior	0.85	0.85	0.85
standard deviation of CMR scaling factor prior	0.05	0.05	0.05

Table 7.3: Inference settings used for the QCE and EDA H-mode discharges. The geometry parameters in the middle part of the table were approximated from the magnetic equilibria. The priors for the scaling factors of the edge CXRS spectrometers were chosen to be the same for all discharges as they were performed in subsequent sessions without changes in the fiber connections.

The general settings used for the inferences were the same as those specified for the type-I ELMy H-mode and L-mode discharges in section 6.2.3. Table 7.3 provides the discharge dependent settings, with its upper part listing the employed equilibrium time points and the derived geometry parameters for the SOL model. Its lower part details the parameters for the univariate Gaussian priors applied for the edge CXRS data scaling factors. The prior means for the spectrometer offsets were again estimated by eye, but kept identical across all discharges, as they were performed in directly consecutive sessions, such that newly introduced calibration errors between the discharges are unlikely. Again, the Gaussian priors were truncated at 0.5 and 1.5 to exclude unreasonable scaling factors.

7.1.2 Results

The neoclassical transport in the QCE and EDA H-mode discharges was modeled with `NEOART` and `NEO` in the same way as explained in section 6.3. The results from `NEOART` presented in figure 7.5 are qualitatively similar to those for the type-I ELMy H-mode and L-mode discharges shown in figure 6.7. Namely, the neoclassical transport in the pedestal is clearly in the Pfirsch-Schlüter regime, but the collisionalities are still low enough to have a temperature screening contribution to the neoclassical convection.

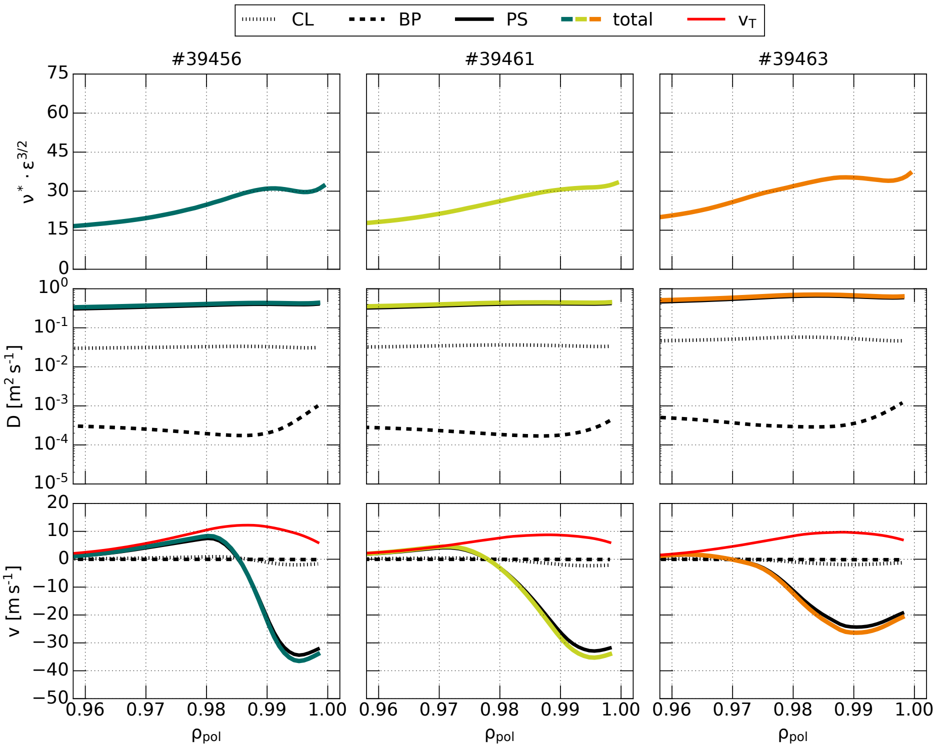

Figure 7.5: `NEOART` simulations for the QCE and EDA H-mode discharges. The plasma edge profiles of the total transport coefficients are shown as well as the individual contributions due to classical transport (CL), banana-plateau transport (BP), and Pfirsch-Schlüter transport (PS). Moreover, the total contribution of the temperature gradient term to the convection (v_T) is shown. The transport coefficients are averaged over all Ne charge stages, weighted with their respective densities.

Figure 7.6 shows the spectral line radiance data used in the inferences, obtained from the fits of the averaged spectral lines measured with CXRS. The figure highlights the excellent agreement between the MAPs from the inferences and the data, which is corrected for individual channel offsets. Figure 7.7 shows the posterior distributions inferred for the pedestal transport coefficients, compared to the neoclassical transport predictions from `NEOART` and `NEO`. The corresponding posterior mean densities of the different charge stages are shown in figure 7.8. The slight discrepancies between the `NEOART` and `NEO` results are again partially attributed to the exclusion of the classical transport in the `NEO` calculations.

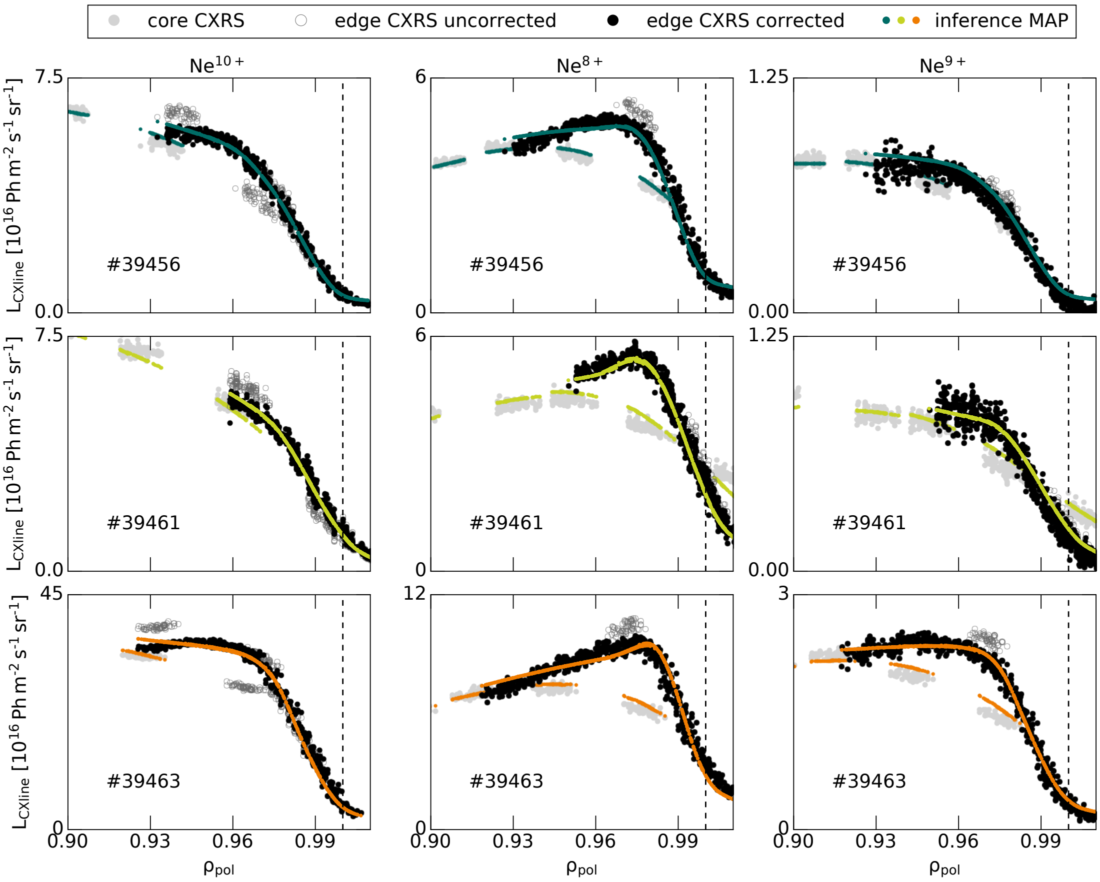

Figure 7.6: Comparison of the inference MAP with the data for the QCE and EDA H-mode discharges. The radiance data of all measured spectral lines are shown, without error bars to avoid visual complication. Gaussian errors were used in the likelihood with standard deviations derived from the scatter in the individual channels using the bootstrapping method. All scaling factors are applied to the plotted data, i.e., the MAP of those inferred for the edge CXRS spectrometers, as well as the manually derived correction factors correcting for individual channel offsets. The data before application of the individual channel corrections are shown in addition. The radiance values calculated for each data point with the synthetic diagnostic from the inference MAP are overplotted. All data are plotted at the mean of the radial positions along the LOS weighted by their emissivity ϵ, i.e., $\rho_{\mathrm{pol,plot}} = \int_{\mathrm{LOS}} \rho_{\mathrm{pol}} \epsilon \mathrm{d}l / \int_{\mathrm{LOS}} \epsilon \mathrm{d}l$. The apparent mismatch between the LOS of the core and edge CXRS systems is an effect of their different viewing geometry. Their LOS capture light from different radial regions even if their emissivity-weighted mean radial positions are the same. The less tangential LOS of the core CXRS system are more affected by the pedestal density decay.

The diffusion coefficient in the QCE pedestal is significantly enhanced above the neoclassical level. Although the inward convection is rather stronger than neoclassical, yet with large error bars, the pedestal Ne peaking is substantially reduced due to this anomalous diffusion. The consistency in the transport coefficients and the charge stage density profiles across both QCE discharges strengthens the confidence in this result. For the EDA H-mode, the situation is less clear. The Ne peaking in the pedestal is as well much lower than in the type-I ELMy H-mode inter-ELM phases presented in section 6.4. However, this is mainly attributed to altered neoclassical transport, instead of additional turbulent diffusion. The disentangled neoclassical transport components, which are presented for the `NEOART` simulations in figure 7.5, reveal, in comparison with figure 6.7, that the neoclassical diffusion is increased outside of $\rho_{\mathrm{pol}} \approx 0.98$

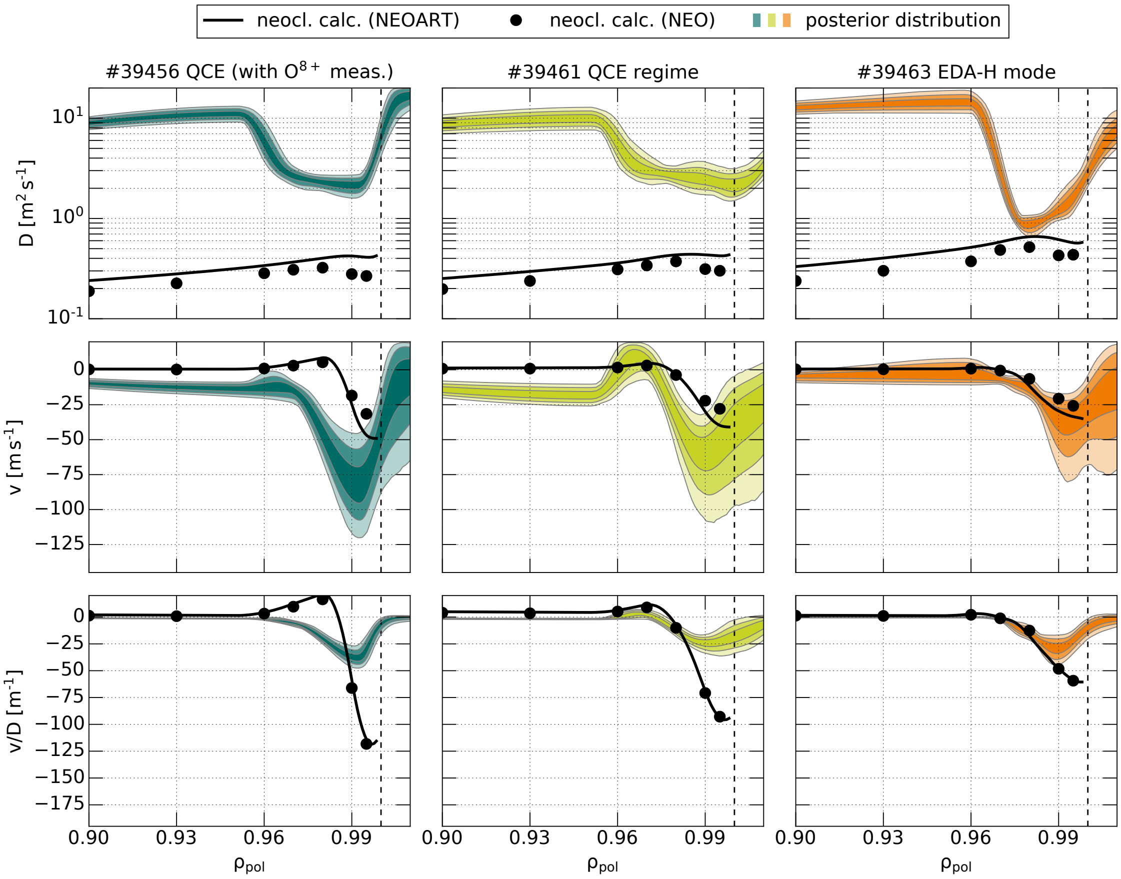

Figure 7.7: Inferred transport coefficients at the plasma edge compared to neoclassical simulations for the QCE and EDA H-mode discharges. Here, D and v are defined with respect to the radial coordinate r_{vol} used in `Aurora` and `NEOART`. The results of `NEO` are converted to this radial coordinate definition. All transport coefficients are averaged over the highest 3 Ne charge stages, weighted by their densities. There are small differences between the `NEOART` and `NEO` results, which are partly due to the omission of classical transport in `NEO`. The posterior distributions are visualized with their 1, 2 and 3 σ-quantiles, as defined in figure 5.1.

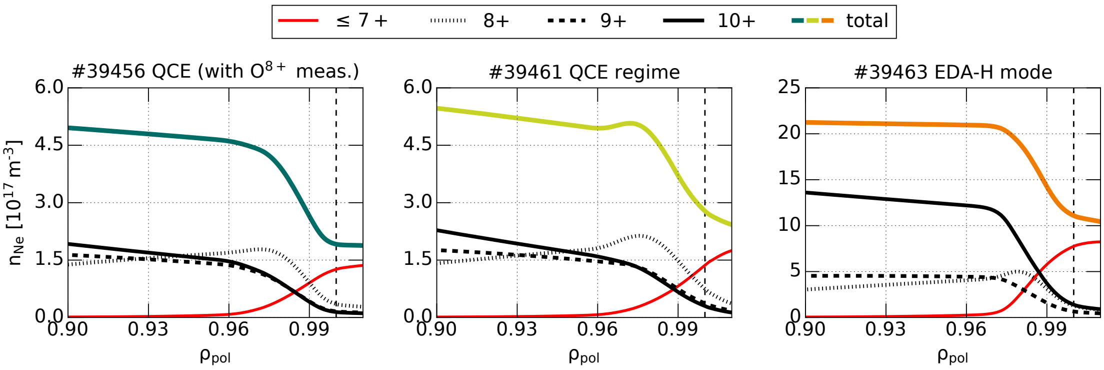

Figure 7.8: Posterior mean of the Ne charge stage densities in the QCE and EDA H-mode discharges. The lower charge stages with $Z \leq 7$ are summed.

compared to #39084 and in the whole pedestal compared to #39086, and the neoclassical main ion density peaking contribution to the convection is reduced inside of $\rho_{\mathrm{pol}} \approx 0.995$ compared to both ELMy discharges. The reduction in neoclassical convection is mainly due to a smaller main ion density peaking contribution, while the temperature screening remains active. These changes result in an overall decrease in neoclassical impurity peaking. Although the uncertainties indicate that some anomalous diffusion could be present, it is much less pronounced than in the QCE regime, and not the main cause for the decrease in $\frac{v}{D}$. $\frac{v}{D}$, which defines the total impurity density peaking, is most robustly determined and found to be very close to the neoclassical level. These different mechanisms in the QCE regime and the EDA H-mode are also reflected in the density profiles of the individual Ne charge stages. The enhanced diffusion in the QCE regime results in flatter pedestal gradients than the altered neoclassical transport in the EDA H-mode, which comes with smaller diffusion and smaller inward convection than in the QCE regime. In summary, all analyzed small-ELM and ELM-free discharges exhibit significantly reduced Ne density gradients in the pedestal, with pedestal peaking factors, as defined in equation 6.2, of 2.30 and 1.81 in the two QCE discharges #39456 and #39461 and 1.87 in the EDA H-mode discharge #39463. Again, it should be noted, that lower charge stages, which are not measured, may not be accurately modeled by the same transport coefficients. This can potentially introduce errors, in particular in the inferred total Ne density profiles. Yet, the inferred Ne densities show good agreement with Z_{eff} from IDZ.

	#39456	#39461	#39463
O source	$15.9 \cdot 10^{19}\,\#\,s^{-1}$	$13.0 \cdot 10^{19}\,\#\,s^{-1}$	$22.3 \cdot 10^{19}\,\#\,s^{-1}$
Ne source scaling	34.0	31.0	99.0
CPR scaling factor	1.29	1.14	1.31
CMR scaling factor	0.83	0.86	0.88

Table 7.4: Posterior mean values of the scalar free parameters in the QCE and EDA H-mode discharges.

Table 7.4 lists the posterior mean values of the scalar free parameters. The thermal neutral D densities at the separatrix are excluded here, as they are already shown in figure 7.2. The scaling parameters for the edge CXRS spectrometers, which are also included in figure 7.6, are explicitly stated for direct comparison. Although their posterior mean values are largely consistent, there are slight differences, most notably a lower scaling factor for the CPR in #39461. Since the scaling factors are theoretically expected to remain the same across all discharges, given their execution in consecutive sessions, these variations may point to uncertainties in the results. However, the consistent transport coefficient results between #39456 and #39461 suggest that any impact of these differences is minor.

Moreover, it should be noted that T_{e} was fixed to 100 eV at the separatrix as a boundary condition in the kinetic profile fitting to determine the alignment of the diagnostics (cf. section 4.1.2.1). This value is reasonably consistent with the data from the QCE database presented in Faitsch et al., 2023. However, particularly in the QCE regime, observations have shown that the separatrix temperatures can sometimes be lower (Faitsch et al., 2021; Griener et al., 2020). Hence, the alignment of T_{e}, and conditionally on it also n_{e}, introduces a potential source of error in the presented analyses. The sensitivity of the results to misaligned T_{e} and n_{e} profiles has been investigated in section 5.4.

7.2 Transition from QCE to type-I ELMy H-mode

7.2.1 Discharge and data analysis

In this section, the impurity transport in the QCE regime is compared to that in the inter-ELM phases of the type-I ELMy H-mode in more detail, in particular also in intermediate states between the two regimes and under identical machine conditions. Therefore, a discharge was performed that transitions from QCE to type-I ELMy H-mode in distinct steps. Important time traces of the analyzed discharge #40219 are presented in figure 7.9.

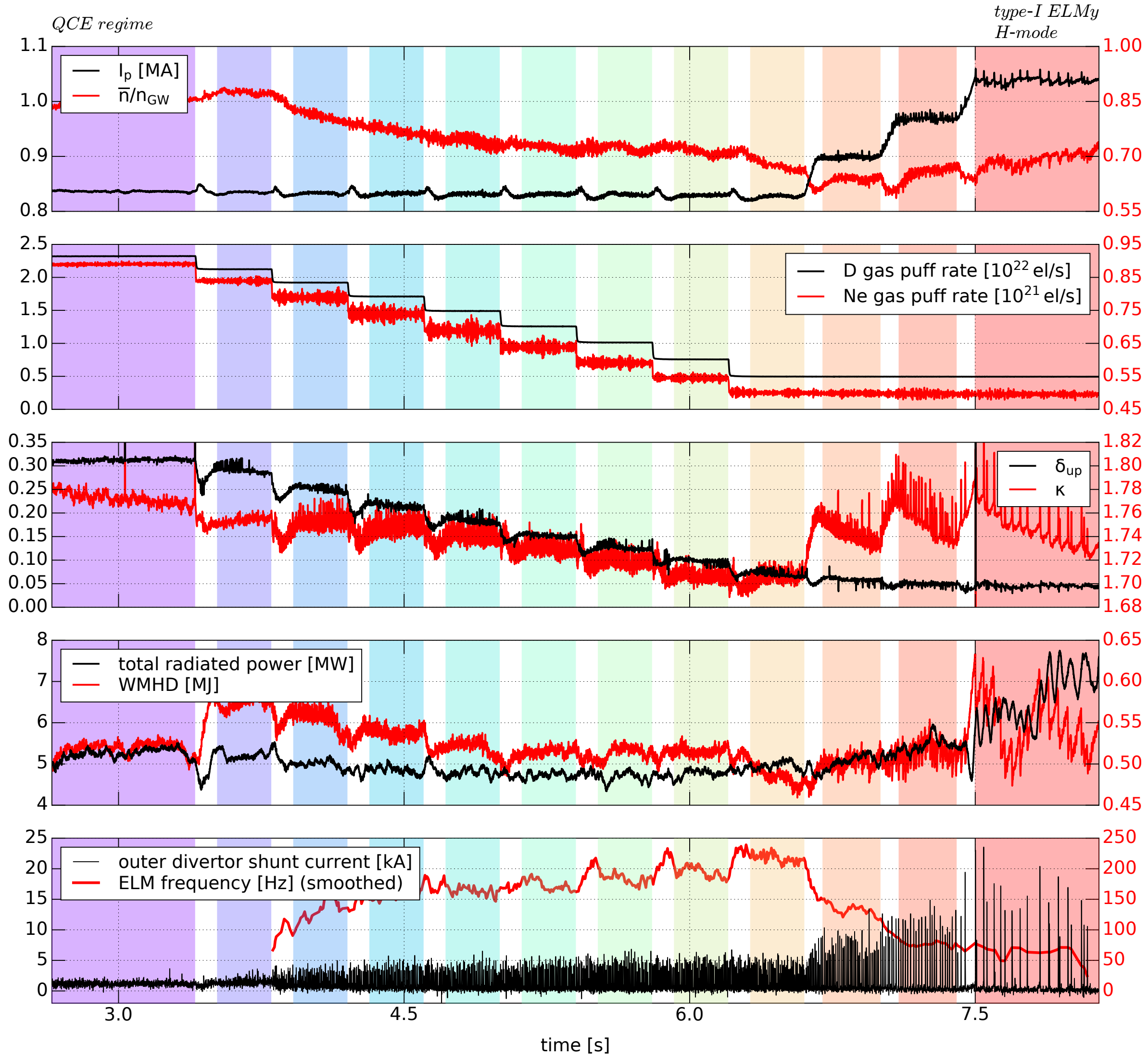

Figure 7.9: Time traces of discharge #40219 transitioning from QCE to type-I ELMy H-mode. The different data analysis time ranges are indicated by the shadings with different colors. These are also used in the following graphics to mark the concerned time ranges. For the regime transition, the fueling and the shaping (in particular the upper triangularity) of the plasma were reduced in the first part of the discharge, and the plasma current was increased starting at 6.6 s.

Similar to the discharges discussed in chapter 6 and section 7.1, the transition pulse was operated with a toroidal magnetic field $B_T = -2.50\,\mathrm{T}$, and heated with 2.3 MW of ECRH power provided by 3 gyrotrons and 4.9 MW of NBI power provided by 2 beams. This heating remained constant throughout the analyzed time range from 2.65 s to 8.15 s, with the exception of a brief dip in ECRH power when one gyrotron dropped out at 7.6 s and was replaced by another. This did not significantly affect the plasma parameters. The NBI beams 3 and 8 were operated alternately in phases lasting 330 ms and 70 ms, respectively, while beam 6 was operated continuously. Therefore, beam 3 was again the only active beam crossing the LOS of the CXRS systems. It was operated with an extraction voltage of 59 kV and with an injection power of 2.4 MW. The Ne impurity was puffed from the A-port valve A13A. Due to the relatively short duration of the individual discharge phases, an R_{aus} sweep in each of the phases was not feasible. Instead, the target R_{aus} was held constant at 2.146 m throughout the discharge. The discharge was conducted only 2 full shotdays after the previous boronization in order to minimize the O content in the plasma, thereby improving the quality of the CXRS data. The inferred posterior mean O concentration in the first discharge phase, i.e., the QCE-regime, is 0.050 % in the core and 0.068 % at the pedestal top, and in the last discharge phase, i.e., in the inter-ELM phases of the type-I ELMy H-mode, 0.069 % in the core and 0.145 % at the pedestal top, at $\rho_{\mathrm{pol}} = 0.00$ and $\rho_{\mathrm{pol}} = 0.96$, respectively.

As shown in figure 7.9, the transition from the QCE regime into a type-I ELMy H-mode was done in 12 distinct steps, with a duration of 400 ms each, such that each step covered exactly one beam-on and one beam-off phase. Initially, the fueling was ramped down in parallel with changes in the plasma shaping, reducing both the upper triangularity and the elongation. This resulted in an increase in ELM activity compared to the initial QCE phase with very small ELMs. However, the ELMs in these middle phases still have much higher frequencies and smaller divertor currents than those typical for type-I ELMs. Only after an additional ramp-up of the plasma current from 800 kA to 1.0 MA, which increased the radiated power, did large and low-frequent type-I ELMs appear.

Figure 7.10 displays the evolution of the kinetic profiles during the transition at selected radial positions at the pedestal top, middle, and at the separatrix. Additionally, the collisionalities that are returned by the neoclassical transport simulations with `NEOART` are shown, which were done as in the same way as described in section 6.3. Notably, as with all previously discussed discharges, the entire pedestal remains in the Pfirsch-Schlüter regime for the neoclassical transport throughout the whole transition. Moreover, it is evident that in particular the thermal neutral D density at the separatrix, which is an inferred parameter, increases significantly during the transition towards the type-I ELMy H-mode. This is probably caused by a better penetration of the neutrals due to lower plasma edge densities compared to the QCE phases.

A special challenge in the data analysis for discharge #40219 lies in handling the very different ELM activity. While the QCE regime at the beginning can only be analyzed by time-averaging over the small ELMs, the type-I ELMy H-mode at the end requires ELM synchronization to separate the inter-ELM phases of interest. In many of the transition steps in-between, there are clear inter-ELM phases that would be interesting to isolate, but they are too short to include at least one full integration time of the edge CXRS spectrometers. They were already set to their minimum exposure time of 2.5 ms, and operated with EM-gain values of 30 to ensure sufficient signal levels also at the plasma edge. The core CXRS spectrometers cannot even reach such exposure times, but have a minimal temporal resolution of 5 ms, at which they were operated without EM-gain. However, their signals are less influenced by the ELMs.

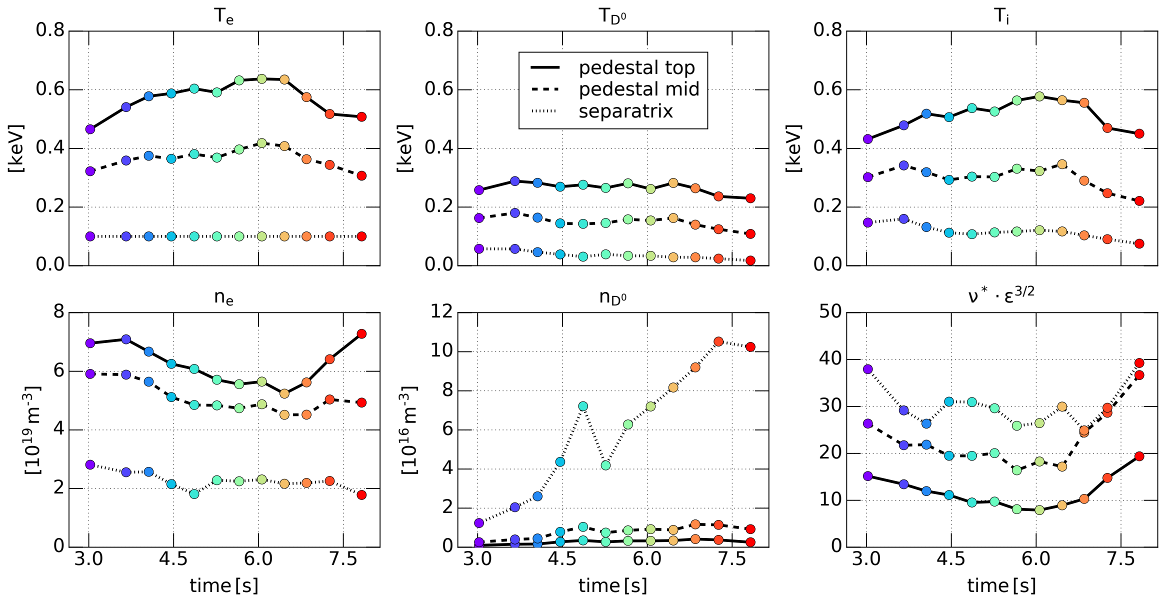

Figure 7.10: Evolution of the kinetic profiles in the different phases of #40219. The profile values are shown for distinct radial positions at the pedestal top ($\rho_{\mathrm{pol}} = 0.96$), at the middle of the pedestal in the region of strong gradients ($\rho_{\mathrm{pol}} = 0.98$), and at the separatrix. T_e was fixed to 100 eV at the separatrix as boundary condition for the diagnostic alignment in the kinetic profile fitting procedure. The collisionality calculated with `NEOART` is also plotted.

For the analysis of the first 9 plasma phases up to 6.6 s, the ELMs were too small for actual synchronization. To limit the data analysis nevertheless to relatively ELM-free periods, only those edge CXRS data frames were used, for which the exposure time range falls entirely within time ranges where the divertor shunt current was below an individually set threshold. The threshold values used were 2.5 kA, 2.75 kA, and 1.75 kA in the first three plasma phases and 1.5 kA in all of the following 6 plasma phases. For the core CXRS data, no frames were deselected, since they are less affected by the ELMs, and also have a longer exposure time, meaning that more data points would be lost. The thresholds for the first two phases with very small ELMs only removed a few spikes in the divertor current, while starting from 3.9 s, the thresholds were set to exclude most ELM time points. All remaining spectra were subsequently averaged in groups of 3 based on their radial positions before they were fitted, as described for the L-mode discharge #40014 in section 6.2.1.

In the last 3 plasma phases, starting at 6.6 s, a proper ELM synchronization was possible, using the approach described in section 6.2.1. Figure 7.11 shows the selected time traces and the relative time ranges used for the analyses. The correlation threshold for selecting the time traces was set to 0.9 for all 3 phases, yielding 14, 24 and 11 time traces contributing to the analyzed data, respectively. The spectra obtained from these phases were not further averaged before fitting. It was verified that the spread in the data points measured in the final discharge phase, as depicted in figure 7.12, could not be reduced by further restricting the inter-ELM time range. Therefore, the broad time range was chosen in order to include more data points.

The correction of individual channel offsets, as outlined in section 6.2.2, was facilitated by the many discharge phases with slightly varying profile shapes. Significant corrections were required for certain channels on both edge CXRS spectrometers, as shown in figure 7.12 and

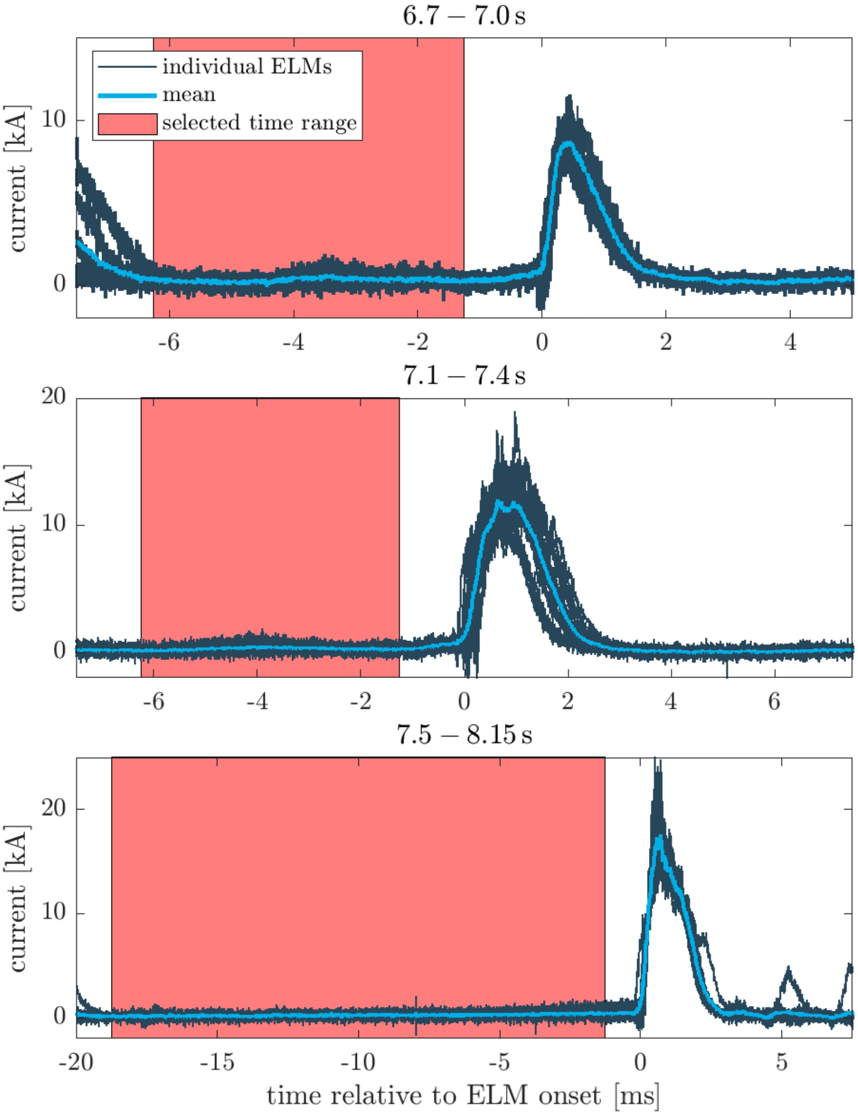

Figure 7.11: ELM synchronization in the ELMy phases of #40219. The individual time traces of the outer divertor shunt current are overplotted after being shifted to have maximum correlation. 14, 24, and 11 time traces were selected in the three discharge phases 6.7–7.0 s, 7.1–7.4 s, and 7.5–8.15 s, respectively. For the data analysis, all edge CXRS frames with an exposure time fully within the marked time ranges were selected.

listed in table 7.5. These calibration errors were caused by several fiber re-connections made earlier in the campaign, prior to this discharge. It was checked whether using the post-campaign calibration data would reduce the channel offsets, but this was not the case. Consequently, the pre-campaign calibration data were used (cf. section 3.1.3.3). The priors for the scaling factors of the edge CXRS spectrometers were set to be the same in all discharge phases as these factors are expected to correct for calibration errors, which cannot change during a discharge. They were selected as Gaussians with means estimated by eye from the radiance data as 0.65 and 1.0 for CPR and CMR, respectively, and with standard deviations of 0.05 each, and truncated at 0.5 and 1.5. As discussed in section 6.2.2, it was confirmed for the concerned 2022 campaign, to which this discharge belongs, that using the core CXRS spectrometers as a reference and scaling the edge data accordingly is a reliable approach.

1-6	1.15	1-8	1.60	1-9	1.05	1-11	0.85	2-2	0.90
2-4	4.60	3-3	0.85	3-6	0.85	3-8	0.80		

Table 7.5: Correction factors for individual channels in #40219. The factors for the LOS were derived manually by looking at the CXRS data from the different discharge phases. The numbers in the first columns indicate the optical heads (CMR-1, CMR-2 and CMR-3) and their respective LOS.

All inference settings were generally consistent with those used in all previously presented analyses and described in section 6.2.3. The equilibrium time points chosen for the individual discharge phases are specified in table 7.6. For the phases with significant ELM activity, care was again taken to ensure that these time points are within inter-ELM phases. The geometry parameters derived from these equilibria are also provided in table 7.6.

equilibrium time point	distance of last grid point to separatrix	distance of limiters to separatrix	connection length to limiters	connection length to divertor
3.025 s	7.2 cm	4.8 cm	0.5 m	31.0 m
3.660 s	7.0 cm	4.7 cm	0.5 m	31.4 m
4.060 s	7.0 cm	4.7 cm	0.5 m	31.1 m
4.460 s	7.0 cm	4.7 cm	0.5 m	30.9 m
4.865 s	7.0 cm	4.7 cm	0.5 m	30.4 m
5.265 s	7.2 cm	4.8 cm	0.5 m	30.1 m
5.659 s	7.2 cm	4.8 cm	0.5 m	29.9 m
6.060 s	7.3 cm	4.9 cm	0.5 m	29.5 m
6.460 s	7.5 cm	5.0 cm	0.5 m	29.4 m
6.850 s	7.4 cm	4.9 cm	0.5 m	27.0 m
7.260 s	7.3 cm	4.9 cm	0.5 m	24.9 m
7.825 s	7.2 cm	4.8 cm	0.5 m	23.1 m

Table 7.6: Inference settings for the edge geometry in the different phases of #40219. The SOL model parameters were approximated from the magnetic equilibria.

7.2.2 Results

Figure 7.12 demonstrates the good agreement with the data that was achieved in the inferences for all data in all phases of the discharge, despite the limited number of data points, particularly in the transitional phases with large but very high-frequent ELMs. In these phases, many edge CXRS frames were deselected, leaving only a few usable frames within the respective 400 ms time intervals. Figure 7.13 shows the posterior distributions for D and $\frac{v}{D}$, compared to the neoclassical transport calculated with `NEOART` from the posterior mean Ne densities, as explained in section 6.3. The first 2 plasma phases are QCE regimes with very small ELMs, similar to the discharges #39456 and #39461 studied in section 7.1. The inferred pedestal diffusion coefficients in these phases are slightly lower than those in #39456 and #39461, which are presented in figure 7.7. However, the presence of a significant anomalous transport contribution is equally evident. This enhanced diffusion again results in a strongly reduced Ne peaking with respect to the type-I ELMy H-modes in the last 2 discharge phases. This reduction is apparent in the $\frac{v}{D}$

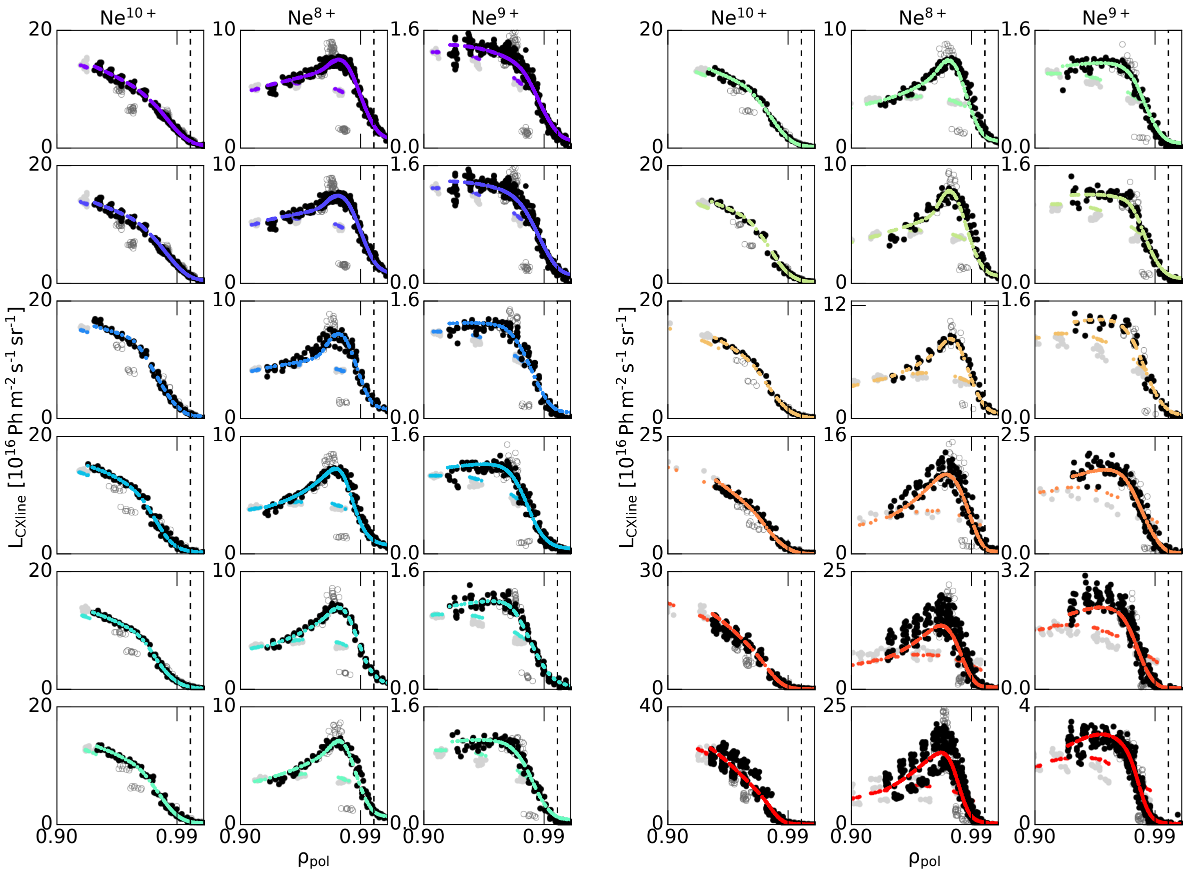

Figure 7.12: Comparison of the inference MAP with the data for the different phases of #40219. The data and inference results are plotted in the same way as in figure 7.6, i.e., the core CXRS data (light grey dots), the uncorrected edge CXRS data (open grey circles), the corrected edge CXRS data (black dots) and the inference MAP (colored smaller dots). The colors indicate the corresponding analysis time ranges, as shown in figure 7.9.

profiles, and more directly in the pedestal Ne peaking factors, which were calculated according to equation 6.2 and are plotted in figure 7.14. The last 2 plasma phases are type-I ELMy H-modes, similar to the discharges #39084 and #39086 studied in chapter 6. The transport coefficients in these phases align closely with the neoclassical predictions across large parts of the pedestal, in contrast to the QCE phases and similar to the results for #39084 and #39086, which are presented in figure 6.9. This neoclassical transport leads to a strong pedestal Ne peaking.

The analyses of the discharge phases in-between indicate a threshold-like behavior of the transport coefficients. Although the ELM activity is already significantly enhanced in the time range between 3.9–6.6 s compared to the initial QCE phases, the transport coefficients show no clear changes. A notable change occurs only once the plasma current is ramped up in the last 3 discharge phases, which coincides with a strong decrease in the ELM frequency. In these phases, the pedestal Ne transport converges towards the neoclassical solution. However, it is important to consider the limitations of the analyses in the intermediate time interval. As described in section 7.2.1, no proper ELM synchronization was possible in the phases up to 6.6 s due to the high ELM frequencies. The ELM time ranges were deselected from the data base, but parts of the ELM onset and termination phases were inevitably included in the data due to the finite exposure times of the spectrometers. This most likely results in a larger diffusion coefficient in the inference result than present in the actual inter-ELM phases.

(a)

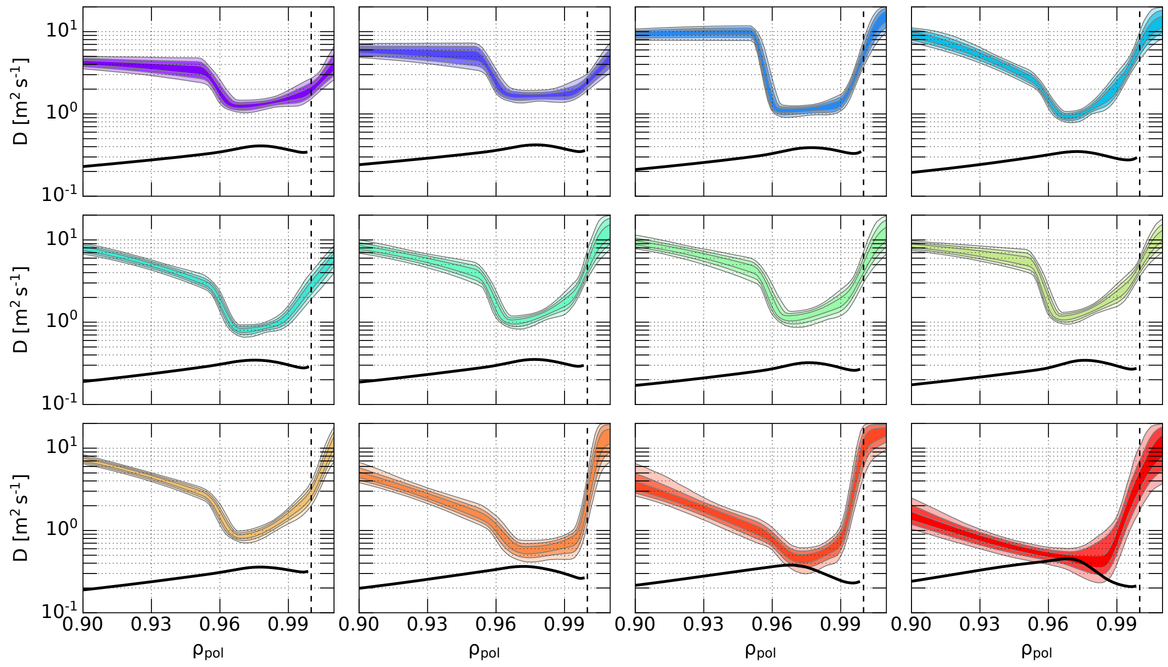

(b)

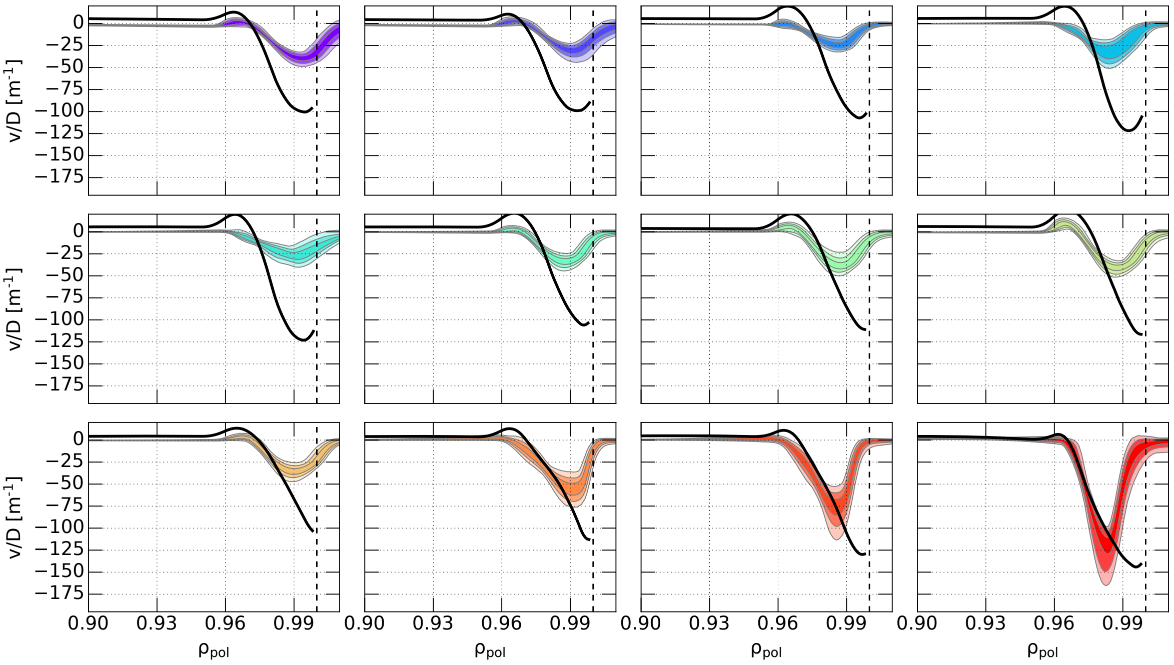

Figure 7.13: Inferred transport coefficients at the plasma edge compared to `NEOART` simulations for the different phases of #40219. The posterior distributions (colored shadings) and `NEOART` calculations (black lines) are plotted in the same way as in figure 7.7. The colors indicate the corresponding analysis time ranges, as shown in figure 7.9. (a) Diffusion coefficient D. (b) Ratio of the convection and diffusion coefficients $\frac{v}{D}$.

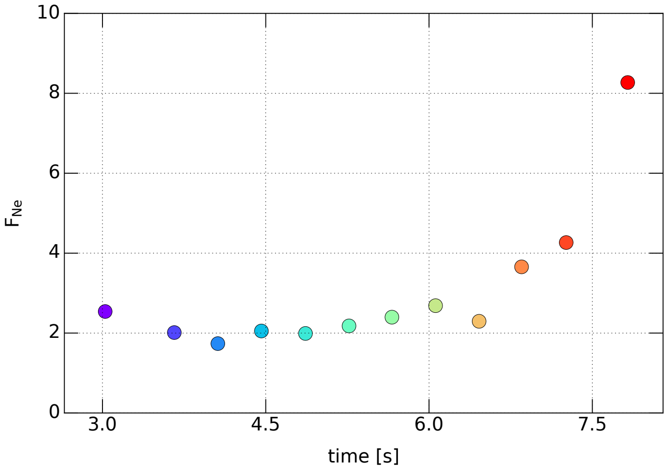

Figure 7.14: Pedestal Ne peaking factors in the different phases of #40219. The factors were calculated according to equation 6.2 from the posterior mean Ne densities.

The derived scaling factors for the edge CXRS spectrometer calibrations are expected to be the same in all discharge phases as they should correct for calibration errors. However, they show some variation as illustrated in figure 7.15, where the univariate posterior probability distributions are overplotted for all phases. Notably, a slight trend is visible, with the results for the last discharge phases differing most strongly from the first discharge phases. However, despite these inaccuracies, the transport coefficients remain highly consistent with the results presented in chapter 6 and in section 7.1, which suggests that the impact on the inferred transport coefficients is small. The other scalar free parameters, namely the thermal neutral D density at the separatrix, which is included in figure 7.10, and the Ne and O particle sources, also change throughout the different discharge phases. However, these variations can be attributed to changes in the physics due to the regime transition, such as modifications in the recycling and particle losses in the SOL. Finally, as in all previously presented analysis results, the inferred Ne content aligns well with the Z_{eff} obtained from IDZ in all discharge phases.

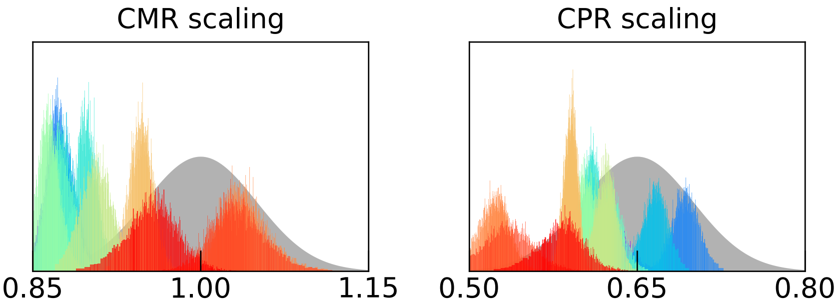

Figure 7.15: Posterior distributions for the scaling factors of the edge CXRS spectrometers in the different phases of #40219. The colors indicate the corresponding analysis time ranges, as shown in figure 7.9. The normalized prior distributions are plotted in grey.

7.3 Discussion

The results presented in this chapter, in comparison with those of chapter 6, show that the impurity peaking in the pedestal of both the QCE regime and the EDA H-mode is indeed reduced with respect to inter-ELM phases in the type-I ELMy H-mode. This is in line with experimental experience finding favorable impurity behavior without accumulation in these regimes. The inferred transport coefficients and their comparison with neoclassical simulations are able to explain this effect for the QCE regime by significant anomalous diffusion which is present throughout the whole pedestal. In a discharge transitioning from the QCE-regime to a type-I ELMy H-mode, it could be shown that this enhanced diffusion persists during phases with medium-sized but high-frequent ELMs. However, an effect of the ELM transport being partially included in the selected edge CXRS data frames, which were acquired with 2.5 ms exposure time, cannot be fully separated. Once the ELM frequency decreases to values $\lesssim 150\,\mathrm{Hz}$ and the ELM amplitude increases, reflected in a peak divertor current $\gtrsim 10\,\mathrm{kA}$, the diffusion in the now clearly separable inter-ELM phases progressively decreases, until it reaches the neoclassical level. Consistent with the results presented in chapter 6, the pedestal Ne peaking is stronger and closer to the neoclassical level the longer the inter-ELM phases and the larger the ELM amplitudes. In the EDA H-mode, in contrast to the QCE regime, a turbulent contribution to the inferred diffusion is less clearly indicated. Instead, the neoclassical diffusion is enhanced with respect to the studied ELMy discharges, and the neoclassical inward convection is weaker due to a decreased main ion density peaking contribution. This likewise results in a reduced impurity density gradient in the pedestal. However, it should be kept in mind, that this was a single-discharge analysis, and that the correction of calibration errors in individual channels, although done with care, substantially influences the inferred transport coefficients for this discharge. Hence, this result should be confirmed in future work.

The results for the QCE regime can be interpreted in view of the local high-n ballooning mode nature of the small type-II ELMs, and their location just inside the separatrix, as recently proposed by Harrer et al., 2022 and Radovanovic et al., 2022. Filamentary transport across the separatrix, driven by these ballooning modes, is assumed to flatten the pedestal gradients sufficiently to maintain peeling-ballooning stability (Harrer et al., 2018). This transport is further assumed to explain the observed quasi-coherent mode (Griener et al., 2020), which has indeed been shown to exhibit properties consistent with ballooning modes (Kalis et al., 2023). The small ELMs cannot be resolved individually with the CXRS diagnostic, but their impurity transport is reflected in the observed overall enhanced diffusion. From the inferred profiles, it is however not evident that the impurity transport is specifically enhanced at the pedestal foot around $\rho_{\mathrm{pol}} \approx 0.99$. This is likely not due to a lack of radial resolution in the results since the framework is in principle capable of resolving radially localized structures in the transport coefficient profiles, as demonstrated in section 5.1. Radovanovic et al., 2022 have also shown that the location of the ballooning instability at the pedestal foot is not equally clear in all QCE discharges. Future work could therefore include ballooning stability analyses for the presented discharges, in order to compare the location of the enhanced impurity diffusion with that of the pedestal instability on an individual discharge basis. Notably, the pedestal middle may also be more ballooning unstable if it is not in the second stability region. This scenario typically reduces the confinement of such discharges, as the entire pedestal is then affected by a reduced pressure gradient (Radovanovic et al., 2022).

As discussed in section 6.6 regarding the impact of large ELMs, enhanced diffusion provokes favorable impurity behavior, avoiding accumulation, in most standard scenarios on present-day devices. However, in reactor-like devices, including ITER, strong neoclassical temperature screening is expected to cause hollow impurity density profiles. This likely applies to the QCE regime as well, given that the results presented here do not indicate significant additional inward convection. In such a scenario, a diffusive action of any transport mechanism will drive inward impurity transport since diffusion always acts flattening on the impurity density profile. Consequently, enhanced impurity diffusion in the QCE regime would not be beneficial, but would rather weaken the effect of the temperature screening.

The hollowness of the impurity density profile, and thus the strength of the impurity diffusion, which acts proportionally to the impurity density gradient, will depend on the neoclassical convection, which scales linearly with the impurity charge. Therefore, high-Z elements, such as W, are expected to have more pronounced hollow profiles. Furthermore, the strength of the neoclassical transport depends on the collisionality, which will vary across the pedestal. While it will be low at the hot pedestal top, it will remain similar to current devices at the pedestal foot since high separatrix densities are required for a viable power exhaust (Kukushkin et al., 2013), and the high parallel heat conduction in the SOL limits the temperature rise at the separatrix. In current devices, the QCE regime cannot be established with such a gradient of collisionality in the pedestal. Thus, it is not possible to measure the relative importance of anomalous transport in different regions of the pedestal under reactor-like conditions. However, a reduced neoclassical transport due to low collisionalities towards the pedestal top, could potentially further enhance the role of turbulent diffusion in the QCE pedestal.

8 Conclusions

8.1 Summary and implications for reactor-like devices

This thesis contributes to overcoming the challenge of experimentally quantifying radial impurity transport in the pedestal of tokamak plasmas. It has introduced a novel framework to infer impurity diffusion and convection profiles, which is optimized for analyzing AUG data. The approach is based on CXRS observations of impurity line radiation in stationary discharges, applying the charge-stage method to determine the individual transport coefficients. Therefore, a tailored diagnostic setup is employed to enable measurements of multiple charge stages. Moreover, the transport results are inferred using Bayesian sampling, with settings specifically designed for this task. This method yields the full probability distribution of the free parameters, which provides a particularly robust and precise uncertainty quantification.

A strength of the framework is its inherent ability to handle high-dimensional non-Gaussian shapes of the probability distribution. They can easily arise due to the complex, non-linear nature of the forward model, which incorporates the coupled system of transport equations for the individual charge stage densities given in equation 1.13. Furthermore, the framework has been thoroughly tested using the method of manufactured solutions, and the parameterization of the transport coefficient profiles has been optimized through model selection. Hence, it fulfills all the criteria outlined by Chilenski et al., 2019 as most important for inferences of impurity transport coefficient profiles. In addition, relevant error sources, specifically for inferences based on the charge stage balance, were assessed. It has been demonstrated how systematic errors in the calibration of individual channels, misalignment of the kinetic plasma background profiles, or imperfections in the atomic data determining the charge stage balance can affect the results. In contrast, the approximations made for impurity sources and parallel transport in the SOL do not influence the results in the confined plasma pedestal. This is essential as the SOL processes are not well described.

For the first time, high-resolution profiles of D and v were inferred for Ne in a set of dedicated AUG discharges. The impurity transport was found to be close to the neoclassical level in the region of the turbulence suppressing ETB during inter-ELM phases of type-I ELMy H-mode discharges. This behavior was observed across pulses with different ELM frequencies and amplitudes. The ELMs themselves, instead, were qualitatively shown to act as anomalous diffusion. Impurity diffusion that significantly exceeds the neoclassical predictions in the pedestal was moreover inferred for the QCE regime, averaged over its small type-II ELMs that suppress large ELMs. These findings reinforce the hypothesis that the QCE regime prevents impurity accumulation in present-day devices due to a weakened ETB. The anomalous transport involved is assumed to be driven by the ballooning-like modes that narrow the pedestal and thereby keep it away from the peeling-ballooning boundary for type-I ELMs (Radovanovic et al., 2022). Furthermore, the analysis of a single EDA H-mode discharge also showed a moderate peaking of the Ne density in the pedestal, comparable to the QCE results and significantly weaker than in the inter-ELM phases of the ELMy pulses. However, the comparison to neoclassical calculations revealed that the neoclassical peaking itself is reduced due to a larger diffusion and smaller main ion density peaking contribution compared to the ELMy discharges. The anomalous contribution to the pedestal diffusion is much less pronounced than in the QCE regime. Yet, this result requires further validation in future work.

The methods and results of this thesis make a next step towards predicting impurity transport dynamics in the pedestal of future tokamak fusion devices, including ITER. Pedestal impurity transport sets the boundary conditions for the impurity densities in the plasma core, which are crucial for confinement, and in the plasma edge, which are essential for power exhaust. Accurate predictions of these boundary conditions require the impurity transport to be characterized in terms of neoclassical and anomalous diffusion and convection, as their individual effects depend on the background plasma profiles, which will differ in future tokamaks. Notably, the direction of the neoclassical convection reverses in reactor-like conditions with steep pedestal temperature gradients due to the dominant influence of the temperature screening contribution (Dux et al., 2014; Dux et al., 2017). This reversal results in fundamentally different impurity dynamics as neoclassical transport results in hollow impurity density profiles. The degree of this hollowness, however, depends on the amount of neoclassical and anomalous diffusion, both of which act to flatten the impurity density profile, and on the strength and direction of potential additional turbulent convection.

This thesis confirms the established conception of predominantly neoclassical impurity transport in the ETB region of H-mode plasmas between large ELMs (Pütterich et al., 2011). It also fits in with the observation of neoclassically dominated ion heat transport in the H-mode ETB, in particular in highly collisional pedestals as those investigated in this thesis (Viezzer et al., 2016; Haskey et al., 2022). Moreover, the presented results consolidate the characterization of the ELM impact as enhanced diffusion (Dux et al., 2011; Pütterich et al., 2011; van Vugt et al., 2019). These findings strengthen the expectation of hollow impurity profiles in type-I ELMy H-modes in ITER, and the consequent inward flushing effect of ELMs on impurities (van Vugt et al., 2019; Garcia et al., 2022; Field et al., 2022).

However, the detrimental impact of type-I ELMs on the PFCs in ITER necessitates operation in alternative regimes. A promising candidate is the QCE regime due to its favorable characteristics in terms of energy confinement and divertor detachment. The anomalous impurity diffusion identified in the QCE pedestal in this thesis, that is, the observation that the small type-II ELMs also act as enhanced diffusion, suggests that the impurity density profiles may be less hollow in ITER compared to those in inter-ELM phases prior to large ELM crashes. The general hollowness, however, is probably retained since no significant additional anomalous inward convection was found. A different picture emerges in the studied EDA H-mode plasma from the increased neoclassical diffusion and the reduced main ion density peaking contribution to the neoclassical convection while the turbulent diffusion is smaller. A tentative conclusion based on this discharge could be that the EDA H-mode might feature more hollow impurity density distributions in ITER than the QCE regime, as the diffusion that counteracts the outward-directed neoclassical convection might be less pronounced.

8.2 Directions for future work

The neoclassical impurity transport in all analyzed discharges was strongly in the Pfirsch-Schlüter regime. Therefore, further studies are needed to confirm that the impurity transport remains close to the neoclassical level in the ETB region of type-I ELMy H-modes in discharges with lower collisionalities. While the collisionalities at the pedestal foot will be similar in ITER, the predicted pedestal top collisionalities are much lower, making this differentiation particularly relevant. However, a replication of ITER-like collisionality profiles cannot be achieved at AUG. Instead, multiple discharges are needed to study low and high collisionalities separately.

Inferences of impurity transport for species with different charges could help to disentangle neoclassical and anomalous convection even more precisely since the neoclassical convection scales linearly with the impurity charge. Suitable candidates are especially N and Ar, as they are easily puffed and have sufficiently small masses to neglect poloidal density asymmetries. For the particularly interesting higher-Z species Ar, however, the currently available atomic data are limited. While the effective CX-emission rate coefficients for observing Ar^{16+} with CXRS have been accurately determined by McDermott et al., 2020, they are still lacking for other charge stages.

In addition to the confinement modes already studied, further investigations of other reactor-relevant regimes are planned. A high priority for ITER is specifically to gain knowledge about the pedestal impurity transport in H-modes with ELM suppression by resonant magnetic perturbations (RMPs), as this is the envisaged operational regime. But the complex 3-D geometry and low-density conditions pose significant challenges for both experimental investigations and neoclassical modeling. Due to its high reactor relevance and naturally high impurity levels, the X-point radiator (XPR) regime is also a strong candidate for further investigation. However, similar to RMP ELM-suppressed plasmas, analyses of the XPR regime are more complex due to pronounced poloidal impurity density asymmetries caused by the strong localization of the radiating region near the X-point.

Improvements to the inference procedure can also be explored. For example, switching from the region-based sampling in MultiNest to a step-sampling algorithm (Buchner, 2022) for inferences with many spline knots could easily reduce the computational cost. Since the runtime is currently mitigated by using the constant efficiency mode of `MultiNest`, which compromises the Bayesian evidence estimates, this could also improve model selection studies. The adoption of the `UltraNest` code (Buchner, 2021) in the framework is therefore being examined.

Generally, accurate predictions of impurity density distributions in future fusion devices beyond the qualitative statements made above require further steps besides the experimental studies of pedestal transport coefficient profiles presented in this thesis. The mechanisms behind the individual transport contributions must be well understood and accurately modeled to be able to extrapolate the transport coefficients to other plasma profiles. While neoclassical transport in the plasma edge can be easily predicted for ITER profiles, simulations of anomalous transport in the pedestal remain a developing field. Results for pedestal turbulence in different confinement regimes achieved with emerging gyrokinetic and gyrofluid edge codes, such as those presented in Zholobenko et al., 2024, should be validated by comparison to experimental results as provided by this thesis. For the QCE regime, radially resolved ballooning stability analyses for the pedestal could additionally help to attribute the observed impurity transport to its underlying edge instabilities.

Finally, the gained understanding of pedestal impurity transport should be embedded in a larger picture, eventually allowing integrated modeling of impurity densities from the divertor and SOL to the core. Especially, studies of impurity transport in the complex 3-D geometry outside the confined plasma, which are outside the scope of the presented framework, are a challenging task. Therefore, insight into SOL impurity transport is often obtained in terms of simpler quantities such as the impurity enrichment (Kallenbach et al., 2020). A comprehensive understanding of the global impurity behavior in tokamak plasmas will ultimately be key to assessing the core-edge integration of future tokamaks in different operating regimes.

Bibliography

Angioni, C. and Helander, P. (2014a). Neoclassical transport of heavy impurities with poloidally asymmetric density distribution in tokamaks. *Plasma Physics and Controlled Fusion* **56** (12), 124001. DOI: `10.1088/0741-3335/56/12/124001`.

Angioni, C., Camenen, Y., Casson, F. J., Fable, E., McDermott, R. M., Peeters, A. G., and Rice, J. E. (2012). Off-diagonal particle and toroidal momentum transport: a survey of experimental, theoretical and modelling aspects. *Nuclear Fusion* **52** (11), 114003. DOI: `10.1088/0029-5515/52/11/114003`.

Angioni, C., Mantica, P., Pütterich, T., Valisa, M., Baruzzo, M., Belli, E. A., Belo, P., Casson, F. J., Challis, C., Drewelow, P., et al. (2014b). Tungsten transport in JET H-mode plasmas in hybrid scenario, experimental observations and modelling. *Nuclear Fusion* **54** (8), 083028. DOI: `10.1088/0029-5515/54/8/083028`.

Angioni, C., Sertoli, M., Bilato, R., Bobkov, V., Loarte, A., Ochoukov, R., Odstrcil, T., Pütterich, T., Stober, J., and the ASDEX Upgrade Team (2017). A comparison of the impact of central ECRH and central ICRH on the tungsten behaviour in ASDEX Upgrade H-mode plasmas. *Nuclear Fusion* **57** (5), 056015. DOI: `10.1088/1741-4326/aa6453`.

Angioni, C. (2021). Impurity transport in tokamak plasmas, theory, modelling and comparison with experiments. *Plasma Physics and Controlled Fusion* **63** (7), 073001. DOI: `10.1088/1361-6587/abfc9a`.

Arbon, R., Candy, J., and Belli, E. A. (2020). Rapidly-convergent flux-surface shape parameterization. *Plasma Physics and Controlled Fusion* **63** (1), 012001. DOI: `10.1088/1361-6587/abc63b`.

ASDEX Team (1989). The H-Mode of ASDEX. *Nuclear Fusion* **29** (11), 1959. DOI: `10.1088/0029-5515/29/11/010`.

Ashton, G., Bernstein, N., Buchner, J., Chen, X., Csányi, G., Fowlie, A., Feroz, F., Griffiths, M., Handley, W., Habeck, M., et al. (2022). Nested sampling for physical scientists. *Nature Reviews Methods Primers* **2** (38). DOI: `10.1038/s43586-022-00132-8`.

`Aurora` Github Repository (2024). `https://github.com/fsciortino/aurora` [Accessed: 17th of November 2024].

`Aurora` Website (2024). `https://aurora-fusion.readthedocs.io/en/latest/` [Accessed: 17th of November 2024].

Austin, M. E., Marinoni, A., Walker, M. L., Brookman, M. W., deGrassie, J. S., Hyatt, A. W., McKee, G. R., Petty, C. C., Rhodes, T. L., Smith, S. P., et al. (2019). Achievement of Reactor-Relevant Performance in Negative Triangularity Shape in the DIII-D Tokamak. *Phys. Rev. Lett.* **122** (11), 115001. DOI: `10.1103/PhysRevLett.122.115001`.

Behringer, K. (1987). *Description of the impurity transport code STRAHL.* JET-R(87)08.

Belli, E. A. and Candy, J. (2008). Kinetic calculation of neoclassical transport including self-consistent electron and impurity dynamics. *Plasma Physics and Controlled Fusion* **50** (9), 095010. DOI: `10.1088/0741-3335/50/9/095010`.

Belli, E. A. and Candy, J. (2009). An Eulerian method for the solution of the multi-species drift-kinetic equation. *Plasma Physics and Controlled Fusion* **51** (7), 075018. DOI: `10.1088/0741-3335/51/7/075018`.

Belli, E. A. and Candy, J. (2011). Full linearized Fokker–Planck collisions in neoclassical transport simulations. *Plasma Physics and Controlled Fusion* **54** (1), 015015. DOI: `10.1088/0741-3335/54/1/015015`.

Bernert, M., Eich, T., Kallenbach, A., Carralero, D., Huber, A., Lang, P. T., Potzel, S., Reimold, F., Schweinzer, J., Viezzer, E., et al. (2014). The H-mode density limit in the full tungsten

ASDEX Upgrade tokamak. *Plasma Physics and Controlled Fusion* **57** (1), 014038. DOI: `10.1088/0741-3335/57/1/014038`.

Bernert, M., Janky, F., Sieglin, B., Kallenbach, A., Lipschultz, B., Reimold, F., Wischmeier, M., Cavedon, M., David, P., Dunne, M. G., et al. (2020). X-point radiation, its control and an ELM suppressed radiating regime at the ASDEX Upgrade tokamak. *Nuclear Fusion* **61** (2), 024001. DOI: `10.1088/1741-4326/abc936`.

Bernert, M., Wiesen, S., Février, O., Kallenbach, A., Koenders, J. T. W., Sieglin, B., Stroth, U., Bosman, T. O. S. J., Brida, D., Cavedon, M., et al. (2023). The X-Point radiating regime at ASDEX Upgrade and TCV. *Nuclear Materials and Energy* **34**, 101376. DOI: `https://doi.org/10.1016/j.nme.2023.101376`.

Bernert, M., Wischmeier, M., Huber, A., Reimold, F., Lipschultz, B., Lowry, C., Brezinsek, S., Dux, R., Eich, T., Kallenbach, A., et al. (2017). Power exhaust by SOL and pedestal radiation at ASDEX Upgrade and JET. *Nuclear Materials and Energy* **12**. 111–118. DOI: `https://doi.org/10.1016/j.nme.2016.12.029`.

Bethe, H. A. and Salpeter, E. E. (1977). *Quantum Mechanics of One- and Two-Electron Atoms*. 1st edition. Springer New York.

Beurskens, M. N. A., Schweinzer, J., Angioni, C., Burckhart, A., Challis, C. D., Chapman, I., Fischer, R., Flanagan, J., Frassinetti, L., Giroud, C., et al. (2013). The effect of a metal wall on confinement in JET and ASDEX Upgrade. *Plasma Physics and Controlled Fusion* **55** (12), 124043. DOI: `10.1088/0741-3335/55/12/124043`.

Braginskii, S. I. (1965). Transport processes in a plasma. *Reviews of plasma physics* **1**, 205.

Bruhn, C., McDermott, R. M., Angioni, C., Ameres, J., Bobkov, V., Cavedon, M., Dux, R., Kappatou, A., Lebschy, A., Manas, P., et al. (2018). A novel method of studying the core boron transport at ASDEX Upgrade. *Plasma Physics and Controlled Fusion* **60** (8), 085011. DOI: `10.1088/1361-6587/aac870`.

Buchner, J. (2021). UltraNest - a robust, general purpose Bayesian inference engine. *Journal of Open Source Software* **6** (60), 3001. DOI: `10.21105/joss.03001`.

Buchner, J. (2022). Comparison of Step Samplers for Nested Sampling. *Physical Sciences Forum* **5** (1). DOI: `10.3390/psf2022005046`.

Buchner, J. (2023). Nested sampling methods. *Statistics Surveys* **17**, 169–215. DOI: `10.1214/23-SS144`.

Buchner, J., Georgakakis, A., Nandra, K., Hsu, L., Rangel, C., Brightman, M., Merloni, A., Salvato, M., Donley, J., and Kocevski, D. (2014). X-ray spectral modelling of the AGN obscuring region in the CDFS: Bayesian model selection and catalogue. *A&A* **564**, A125. DOI: `10.1051/0004-6361/201322971`.

Burrell, K. H. (1997). Effects of E×B velocity shear and magnetic shear on turbulence and transport in magnetic confinement devices. *Physics of Plasmas* **4** (5), 1499–1518. DOI: `10.1063/1.872367`.

Burrell, K. H., Austin, M. E., Brennan, D. P., DeBoo, J. C., Doyle, E. J., Fenzi, C., Fuchs, C., Gohil, P., Greenfield, C. M., Groebner, R. J., et al. (2001). Quiescent double barrier high-confinement mode plasmas in the DIII-D tokamak. *Physics of Plasmas* **8** (5), 2153–2162. DOI: `10.1063/1.1355981`.

Burrell, K. H., Barada, K., Chen, X., Garofalo, A. M., Groebner, R. J., Muscatello, C. M., Osborne, T. H., Petty, C. C., Rhodes, T. L., Snyder, P. B., et al. (2016). Discovery of stationary operation of quiescent H-mode plasmas with net-zero neutral beam injection torque and high energy confinement on DIII-D. *Physics of Plasmas* **23** (5), 056103. DOI: `10.1063/1.4943521`.

Burrell, K. H., Chen, X., Chrystal, C., Ernst, D. R., Grierson, B. A., Haskey, S. R., Osborne, T. H., Paz-Soldan, C., and Wilks, T. M. (2020). Creation and sustainment of wide pedestal quiescent H-mode with zero net neutral beam torque. *Nuclear Fusion* **60** (8), 086005. DOI: `10.1088/1741-4326/ab940d`.

Camenen, Y., Pochelon, A., Behn, R., Bottino, A., Bortolon, A., Coda, S., Karpushov, A., Sauter, O., Zhuang, G., and the TCV Team (2007). Impact of plasma triangularity and collisionality on electron heat transport in TCV L-mode plasmas. *Nuclear Fusion* **47** (7), 510. DOI: `10.1088/0029-5515/47/7/002`.

Campbell, D. J., Loarte, A., Boilson, D., Bonnin, X., Vries, P. de, Giancarli, L., Gribov, Y., Kim, S. H., Lehnen, M., Luce, T., et al. (2024). *ITER Research Plan within the Staged Approach (Level III — Final Version).* Tech. rep. ITER Organization. URL: `https://www.iter.org/technical-reports?id=26`.

Cathey, A., Hoelzl, M., Gil, L., Dunne, M. G., Harrer, G. F., Huijsmans, G. T. A., Kalis, J., Lackner, K., Pamela, S. J. P., Wolfrum, E., et al. (2023). Probing non-linear MHD stability of the EDA H-mode in ASDEX Upgrade. *Nuclear Fusion* **63** (6), 062001. DOI: `10.1088/1741-4326/acc818`.

Cavedon, M., Pütterich, T., Viezzer, E., Laggner, F. M., Burckhart, A., Dunne, M. G., Fischer, R., Lebschy, A., Mink, F., Stroth, U., et al. (2017). Pedestal and Er profile evolution during an edge localized mode cycle at ASDEX Upgrade. *Plasma Physics and Controlled Fusion* **59** (10), 105007. DOI: `10.1088/1361-6587/aa7ad0`.

Cavedon, M., Dux, R., Pütterich, T., Viezzer, E., Wolfrum, E., Dunne, M. G., Fable, E., Fischer, R., Harrer, G. F., Laggner, F. M., et al. (2019). On the ion and electron temperature recovery after the ELM-crash at ASDEX upgrade. *Nuclear Materials and Energy* **18**, 275–280. DOI: `https://doi.org/10.1016/j.nme.2018.12.034`.

`CGYRO` homepage (2024). `https://gafusion.github.io/doc/cgyro.html` [Accessed: 13th of December 2024].

Chilenski, M. A., Greenwald, M., Marzouk, Y., Rice, J. E., and White, A. E. (2019). On the importance of model selection when inferring impurity transport coefficient profiles. *Plasma Physics and Controlled Fusion* **61** (12), 125012. DOI: `10.1088/1361-6587/ab4e69`.

Creely, A. J., Greenwald, M. J., Ballinger, S. B., Brunner, D., Canik, J., Doody, J., Fülöp, T., Garnier, D. T., Granetz, R., Gray, T. K., et al. (2020). Overview of the SPARC tokamak. *Journal of Plasma Physics* **86** (5), 865860502. DOI: `10.1017/S0022377820001257`.

Degeling, A. W., Martin, Y. R., Lister, J. B., Villard, L., Dokouka, V. N., Lukash, V. E., and Khayrutdinov, R. R. (2003). Magnetic triggering of ELMs in TCV. *Plasma Physics and Controlled Fusion* **45** (9), 1637. DOI: `10.1088/0741-3335/45/9/306`.

Dolgov-Saveliev, G. G., Ivanov, D. P., Mukhovatov, V. S., Razumova, K. A., Strelkov, V. S., Shepelyev, M. N., and Yavlinsky, N. A. (1958). Investigations of the stability and heating of plasmas in toroidal chambers. *Proceedings of the Second United Nations International Conference on the Peaceful Uses of Atomic Energy* **32**, 82–91.

Dunne, M., Faitsch, M., Radovanovic, L., Wolfrum, E., and ASDEX Upgrade Team, the (2024). Quasi-continuous exhaust operational space. *Nuclear Fusion* **64** (12), 124003. DOI: `10.1088/1741-4326/ad89da`.

Dunne, M. G. (2016). Impact of impurity seeding and divertor conditions on transitions, pedestal structure and ELMs. *Nuclear Fusion* **57** (2), 025002. DOI: `10.1088/0029-5515/57/2/025002`.

Dux, R., Loarte, A., Fable, E., and Kukushkin, A. (2014). Transport of tungsten in the H-mode edge transport barrier of ITER. *Plasma Physics and Controlled Fusion* **56** (12), 124003. DOI: `10.1088/0741-3335/56/12/124003`.

Dux, R., Neu, R., Peeters, A. G., Pereverzev, G., Mück, A., Ryter, F., Stober, J., and the ASDEX Upgrade Team (2003). Influence of the heating profile on impurity transport in

ASDEX Upgrade. *Plasma Physics and Controlled Fusion* **45** (9), 1815. DOI: `10.1088/0741-3335/45/9/317`.

Dux, R. and Peeters, A. G. (2000). Neoclassical impurity transport in the core of an ignited tokamak plasma. *Nuclear Fusion* **40** (10), 1721. DOI: `10.1088/0029-5515/40/10/304`.

Dux, R., Bobkov, V., Herrmann, A., Janzer, A., Kallenbach, A., Neu, R., Mayer, M., Müller, H. W., Pugno, R., Pütterich, T., et al. (2009). Plasma-wall interaction and plasma behaviour in the non-boronised all tungsten ASDEX Upgrade. *Journal of Nuclear Materials* **390-391**. 858–863. DOI: `https://doi.org/10.1016/j.jnucmat.2009.01.225`.

Dux, R., Cavedon, M., Kallenbach, A., McDermott, R. M., Vogel, G., and the ASDEX Upgrade Team (2020). Influence of CX-reactions on the radiation in the pedestal region at ASDEX Upgrade. *Nuclear Fusion* **60** (12), 126039. DOI: `10.1088/1741-4326/abb748`.

Dux, R., Janzer, A., Pütterich, T., and the ASDEX Upgrade Team (2011). Main chamber sources and edge transport of tungsten in H-mode plasmas at ASDEX Upgrade. *Nuclear Fusion* **51** (5), 053002. DOI: `10.1088/0029-5515/51/5/053002`.

Dux, R., Loarte, A., Angioni, C., Coster, D., Fable, E., and Kallenbach, A. (2017). The interplay of controlling the power exhaust and the tungsten content in ITER. *Nuclear Materials and Energy* **12**. 28–35. DOI: `https://doi.org/10.1016/j.nme.2016.10.013`.

Dux, R. (2003). Chapter 11: Impurity Transport in ASDEX Upgrade. *Fusion Science and Technology* **44** (3), 708–715. DOI: `10.13182/FST03-A409`.

Dux, R. (2004). "Impurity transport in Tokamak plasmas". Max-Planck-Institut für Plasmaphysik (IPP 10/27). Habilitation. Universität Augsburg.

Dux, R. (2010). *Plasmaphysik und Fusionsforschung. Teil II: Fusionsforschung.* Vorlesungsskript Universität Augsburg.

Dux, R. (2021). *STRAHL User Manual.* Max-Planck-Institut für Plasmaphysik.

Eich, T., Manz, P., and the ASDEX Upgrade Team (2021). The separatrix operational space of ASDEX Upgrade due to interchange-drift-Alfvén turbulence. *Nuclear Fusion* **61** (8), 086017. DOI: `10.1088/1741-4326/ac0412`.

EUROfusion (2024a). `https://euro-fusion.org/eurofusion-news/dte3record/` [Accessed: 14th of August 2024].

EUROfusion (2024b). `https://euro-fusion.org/faq/breakeven-point-to-actually-produce-power/` [Accessed: 14th of August 2024].

EUROfusion (2024c). `https://euro-fusion.org/fusion/history-of-fusion/` [Accessed: 14th of August 2024].

Evans, T. E., Moyer, R. A., Thomas, P. R., Watkins, J. G., Osborne, T. H., Boedo, J. A., Doyle, E. J., Fenstermacher, M. E., Finken, K. H., Groebner, R. J., et al. (2004). Suppression of Large Edge-Localized Modes in High-Confinement DIII-D Plasmas with a Stochastic Magnetic Boundary. *Phys. Rev. Lett.* **92** (23), 235003. DOI: `10.1103/PhysRevLett.92.235003`.

Fable, E., Kallenbach, A., McDermott, R. M., Bernert, M., Angioni, C., and the ASDEX Upgrade Team (2021). High-confinement radiative L-modes in ASDEX Upgrade. *Nuclear Fusion* **62** (2), 024001. DOI: `10.1088/1741-4326/ac3e81`.

Faitsch, M., Dunne, M., Lerche, E., Lomas, P., Balboa, I., Bilkova, P., Bohm, P., Gil, L., Harrer, G. F., Kappatou, A., et al. (2025). The Quasi-Continuous Exhaust regime in ASDEX Upgrade and JET. *submitted to Nuclear Materials and Energy.*

Faitsch, M., Eich, T., Harrer, G. F., Wolfrum, E., Brida, D., David, P., Dunne, M. G., Gil, L., Labit, B., Stroth, U., et al. (2023). Analysis and expansion of the quasi-continuous exhaust (QCE) regime in ASDEX Upgrade. *Nuclear Fusion* **63** (7), 076013. DOI: `10.1088/1741-4326/acd464`.

Faitsch, M., Eich, T., Harrer, G. F., Wolfrum, E., Brida, D., David, P., Griener, M., Stroth, U., the ASDEX Upgrade Team, and the EUROfusion MST1 Team (2021). Broadening of the power fall-off length in a high density, high confinement H-mode regime in ASDEX Upgrade. *Nuclear Materials and Energy* **26**, 100890. DOI: `https://doi.org/10.1016/j.nme.2020.100890`.

Fajardo, D., Angioni, C., Casson, F. J., Field, A. R., Maget, P., Manas, P., the ASDEX Upgrade Team, and JET Contributors (2023). Analytical model for the combined effects of rotation and collisionality on neoclassical impurity transport. *Plasma Physics and Controlled Fusion* **65** (3), 035021. DOI: `10.1088/1361-6587/acb0fc`.

Fajardo, D., Angioni, C., Maget, P., and Manas, P. (2022). Analytical model for collisional impurity transport in tokamaks at arbitrary collisionality. *Plasma Physics and Controlled Fusion* **64** (5), 055017. DOI: `10.1088/1361-6587/ac5b4d`.

Fajardo, D., Angioni, C., Fable, E., Tardini, G., Bilato, R., Luda, T., McDermott, R. M., Samoylov, O., and the ASDEX Upgrade Team (2024). Integrated modelling of tungsten accumulation control with wave heating: validation in ASDEX Upgrade and predictions for ITER. *Nuclear Fusion* **64** (10), 104001. DOI: `10.1088/1741-4326/ad6f26`.

Fajardo, D. (2024). "Experimental Inference of Particle Transport in Tokamak Plasmas". Dissertation. Ludwig Maximilians Universität München.

FARO Technologies (2024). `https://www.faro.com/` [Accessed: 30th of October 2024].

Feroz, F. and Hobson, M. P. (2008). Multimodal nested sampling: an efficient and robust alternative to Markov Chain Monte Carlo methods for astronomical data analyses. *Monthly Notices of the Royal Astronomical Society* **384** (2), 449–463. DOI: `https://doi.org/10.1111/j.1365-2966.2007.12353.x`.

Feroz, F., Hobson, M. P., and Bridges, M. (2009). MultiNest: an efficient and robust Bayesian inference tool for cosmology and particle physics. *Monthly Notices of the Royal Astronomical Society* **398** (4), 1601–1614. DOI: `10.1111/j.1365-2966.2009.14548.x`.

Feroz, F., Hobson, M. P., Cameron, E., and Pettitt, A. N. (2019). Importance Nested Sampling and the MultiNest Algorithm. *The Open Journal of Astrophysics* **2**. DOI: `10.21105/astro.1306.2144`.

Field, A. R., Casson, F. J., Fajardo, D., Angioni, C., Challis, C. D., Hobirk, J., Kappatou, A., Kim, H.-T., Lerche, E., Loarte, A., et al. (2022). Peripheral temperature gradient screening of high-Z impurities in optimised 'hybrid' scenario H-mode plasmas in JET-ILW. *Nuclear Fusion* **63** (1), 016028. DOI: `10.1088/1741-4326/aca54e`.

Fischer, R., Fuchs, C. J., Kurzan, B., Suttrop, W., Wolfrum, E., and the ASDEX Upgrade Team (2010). Integrated Data Analysis of Profile Diagnostics at ASDEX Upgrade. *Fusion Science and Technology* **58** (2), 675–684. DOI: `10.13182/FST10-110`.

Fischer, R., Bock, A., Dunne, M. G., Fuchs, J. C., Giannone, L., Lackner, K., McCarthy, P. J., Poli, E., Preuss, R., Rampp, M., et al. (2016). Coupling of the Flux Diffusion Equation with the Equilibrium Reconstruction at ASDEX Upgrade. *Fusion Science and Technology* **69** (2), 526–536. DOI: `10.13182/FST15-185`.

Fußmann, G. (1992). "Teilchentransport in magnetisch eingeschlossenen Plasmen". Max-Planck-Institut für Plasmaphysik (IPP 1/273). Habilitation. Universität Augsburg.

Futatani, S., Cathey, A., Hoelzl, M., Lang, P. T., Huijsmans, G. T. A., Dunne, M. G., the JOREK Team, the ASDEX Upgrade Team, and the EUROfusion MST1 Team (2021). Transition from no-ELM response to pellet ELM triggering during pedestal build-up—insights from extended MHD simulations. *Nuclear Fusion* **61** (4), 046043. DOI: `10.1088/1741-4326/abdfb4`.

Garcia, J., Luna, E. de la, Sertoli, M., Casson, F. J., Mazzi, S., Štancar, Ž., Szepesi, G., Frigione, D., Garzotti, L., Rimini, F., et al. (2022). New H-mode regimes with small ELMs and high thermal confinement in the Joint European Torus. *Physics of Plasmas* **29** (3), 032505. DOI: `10.1063/5.0072236`.

Geiger, B. (2013). “Fast-ion transport studies using FIDA spectroscopy at the ASDEX Upgrade tokamak”. Dissertation. Ludwig Maximilians Universität München.

GENE homepage (2024). `https://genecode.org/` [Accessed: 17th of November 2024].

Giacomin, M., Pau, A., Ricci, P., Sauter, O., Eich, T., the ASDEX Upgrade Team, JET Contributors, and the TCV Team (2022). First-Principles Density Limit Scaling in Tokamaks Based on Edge Turbulent Transport and Implications for ITER. *Phys. Rev. Lett.* **128** (18), 185003. DOI: `10.1103/PhysRevLett.128.185003`.

Gil, L., Silva, C., Happel, T., Birkenmeier, G., Conway, G. D., Guimarais, L., Kallenbach, A., Pütterich, T., Santos, J., Schneider, P. A., et al. (2020). Stationary ELM-free H-mode in ASDEX Upgrade. *Nuclear Fusion* **60** (5), 054003. DOI: `10.1088/1741-4326/ab7d1b`.

Goldston, R. J., White, R. B., Hahm, T. S., and Kaye, S. (2012). “Physics of Confinement”. In: *Fusion Physics*. Ed. by M. Kikuchi, K. Lackner, and M. Q. Tran. International Atomic Energy Agency (IAEA). Chap. 2. URL: `http://www-pub.iaea.org/MTCD/Publications/PDF/Pub1562_web.pdf`.

Greenwald, M., Boivin, R., Bonoli, P., Budny, R., Fiore, C., Goetz, J., Granetz, R., Hubbard, A., Hutchinson, I., Irby, J., et al. (1999). Characterization of enhanced Dα high-confinement modes in Alcator C-Mod. *Physics of Plasmas* **6** (5), 1943–1949. DOI: `10.1063/1.873451`.

Greenwald, M., Terry, J. L., Wolfe, S. M., Ejima, S., Bell, M. G., Kaye, S. M., and Neilson, G. H. (1988). A new look at density limits in tokamaks. *Nuclear Fusion* **28** (12), 2199. DOI: `10.1088/0029-5515/28/12/009`.

Greenwald, M. (2002). Density limits in toroidal plasmas. *Plasma Physics and Controlled Fusion* **44** (8), R27. DOI: `10.1088/0741-3335/44/8/201`.

Griener, M., Wolfrum, E., Birkenmeier, G., Faitsch, M., Fischer, R., Fuchert, G., Gil, L., Harrer, G. F., Manz, P., Wendler, D., et al. (2020). Continuous observation of filaments from the confined region to the far scrape-off layer. *Nuclear Materials and Energy* **25**, 100854. DOI: `https://doi.org/10.1016/j.nme.2020.100854`.

Grierson, B. A., Burrell, K. H., Nazikian, R. M., Solomon, W. M., Garofalo, A. M., Belli, E. A., Staebler, G. M., Fenstermacher, M. E., McKee, G. R., Evans, T. E., et al. (2015). Impurity confinement and transport in high confinement regimes without edge localized modes on DIII-Da). *Physics of Plasmas* **22** (5). DOI: `10.1063/1.4918359`.

GYRO homepage (2024). `https://gafusion.github.io/doc/gyro.html` [Accessed: 17th of November 2024].

Handley, W. (2023). “The scaling frontier of nested sampling”. Talk at the 42nd International Workshop on Bayesian Inference and Maximum Entropy Methods in Science and Engineering – Meeting-withing-a-meeting: Frontiers of Nested Sampling, 5th of July 2023, Garching, Germany.

Happel, T., Manz, P., Ryter, F., Bernert, M., Dunne, M., Hennequin, P., Hetzenecker, A., Stroth, U., Conway, G. D., Guimarais, L., et al. (2016). The I-mode confinement regime at ASDEX Upgrade: global properties and characterization of strongly intermittent density fluctuations. *Plasma Physics and Controlled Fusion* **59** (1), 014004. DOI: `10.1088/0741-3335/59/1/014004`.

Happel, T., Pütterich, T., Told, D., Dunne, M., Fischer, R., Hobirk, J., McDermott, R. M., Plank, U., and the ASDEX Upgrade Team (2022). Overview of initial negative triangularity plasma studies on the ASDEX Upgrade tokamak. *Nuclear Fusion* **63** (1), 016002. DOI: `10.1088/1741-4326/ac8563`.

Harrer, G. F., Faitsch, M., Radovanovic, L., Wolfrum, E., Albert, C., Cathey, A., Cavedon, M., Dunne, M. G., Eich, T., Fischer, R., et al. (2022). Quasicontinuous Exhaust Scenario for a

Fusion Reactor: The Renaissance of Small Edge Localized Modes. *Phys. Rev. Lett.* **129** (16), 165001. DOI: `10.1103/PhysRevLett.129.165001`.

Harrer, G. F., Wolfrum, E., Dunne, M. G., Manz, P., Cavedon, M., Lang, P. T., Kurzan, B., Eich, T., Labit, B., Stober, J., et al. (2018). Parameter dependences of small edge localized modes (ELMs). *Nuclear Fusion* **58** (11), 112001. DOI: `10.1088/1741-4326/aad757`.

Harrer, G. F. (2020). "On the origin and transport of small ELMs". Dissertation. Technische Universität Wien.

Haskey, S. R., Ashourvan, A., Banerjee, S., Barada, K., Belli, E. A., Bortolon, A., Candy, J., Chen, J., Chrystal, C., Grierson, B. A., et al. (2022). Ion thermal transport in the H-mode edge transport barrier on DIII-D. *Physics of Plasmas* **29** (1), 012506. DOI: `10.1063/5.0072155`.

Helander, P. and Sigmar, D. J. (2002). *Collisional Transport in Magnetized Plasmas.* Vol. 4. Cambridge monographs on plasma physics. Cambridge University Press.

`HELENA` homepage (2024). `https://pb3d.github.io/helena.html` [Accessed: 14th of December 2024].

Hinton, F. L. and Hazeltine, R. D. (1976). Theory of plasma transport in toroidal confinement systems. *Rev. Mod. Phys.* **48** (2), 239–308. DOI: `10.1103/RevModPhys.48.239`.

Hirshman, S. P. and Sigmar, D. J. (1981). Neoclassical transport of impurities in tokamak plasmas. *Nuclear Fusion* **21** (9), 1079–1201. DOI: `10.1088/0029-5515/21/9/003`.

Hoelzl, M., Huijsmans, G. T. A., Pamela, S. J. P., Bécoulet, M., Nardon, E., Artola, F. J., Nkonga, B., Atanasiu, C. V., Bandaru, V., Bhole, A., et al. (2021). The JOREK non-linear extended MHD code and applications to large-scale instabilities and their control in magnetically confined fusion plasmas. *Nuclear Fusion* **61** (6), 065001. DOI: `10.1088/1741-4326/abf99f`.

Houlberg, W. A., Shaing, K. C., Hirshman, S. P., and Zarnstorff, M. C. (1997). Bootstrap current and neoclassical transport in tokamaks of arbitrary collisionality and aspect ratio. *Physics of Plasmas* **4** (9), 3230–3242. DOI: `10.1063/1.872465`.

Howard, N. T., Greenwald, M., Mikkelsen, D. R., Reinke, M. L., White, A. E., Ernst, D., Podpaly, Y., and Candy, J. (2012). Quantitative comparison of experimental impurity transport with nonlinear gyrokinetic simulation in an Alcator C-Mod L-mode plasma. *Nuclear Fusion* **52** (6), 063002. DOI: `10.1088/0029-5515/52/6/063002`.

Illerhaus, J. (2017). "Estimation, Validation and Uncertainty of the Position of the Separatrix Contour at ASDEX Upgrade". Diploma Thesis. Technische Universität München.

IPP (2023). `https://www.ipp.mpg.de/987491/AUG_en_2023.pdf` [Accessed: 19th of August 2024].

IPP (2024a). `https://www.ipp.mpg.de/1471827/asdex_upgrade/` [Accessed: 19th of August 2024].

IPP (2024b). `https://www.ipp.mpg.de/5426473/facilities_review_report?c=5405906/` [Accessed: 19th of August 2024].

Isler, R. C. (1994). An overview of charge-exchange spectroscopy as a plasma diagnostic. *Plasma Physics and Controlled Fusion* **36** (2), 171. DOI: `10.1088/0741-3335/36/2/001`.

ITER (2024). `https://www.iter.org/mach/divertor/` [Accessed: 04th of September 2024].

ITER Physics Expert Group on Confinement and Transport, ITER Physics Expert Group on Confinement Modelling and Database, and ITER Physics Basis Editors (1999). Chapter 2: Plasma confinement and transport. *Nuclear Fusion* **39** (12), 2175. DOI: `10.1088/0029-5515/39/12/302`.

Janev, R. K. and Smith, J. J. (1993). *Cross Sections for Collision Processes of Hydrogen Atoms with Electrons, Protons, and Multiply Charged Ions.* Atomic and Plasma–Material Interaction

Data for Fusion 4. International Atomic Energy Agency (IAEA). URL: `https://www.iaea.org/publications/1839/atomic-and-plasma-material-interaction-data-for-fusion`.

Jeffreys, H. (1998). *The Theory of Probability.* Oxford Classic Texts in the Physical Sciences. Oxford University Press.

`JOREK` homepage (2024). `https://www.jorek.eu/` [Accessed: 14th of December 2024].

Kalis, J., Birkenmeier, G., Manz, P., Eich, T., Griener, M., Goti, R., Cavedon, M., Gil, L., Faitsch, M., Radovanovic, L., et al. (2023). Experimental characterization of the quasi-coherent mode in EDA H-Mode and QCE scenarios at ASDEX Upgrade. *Nuclear Fusion* **64** (1), 016038. DOI: `10.1088/1741-4326/ad0d32`.

Kalis, J. (2024). "Characterization of Edge Modes in Different Confinement Regimes of Fusion Plasmas". Dissertation. Technische Universität München.

Kallenbach, A., Bernert, M., Dux, R., Casali, L., Eich, T., Giannone, L., Herrmann, A., McDermott, R. M., Mlynek, A., Müller, H. W., et al. (2013). Impurity seeding for tokamak power exhaust: from present devices via ITER to DEMO. *Plasma Physics and Controlled Fusion* **55** (12), 124041. DOI: `10.1088/0741-3335/55/12/124041`.

Kallenbach, A., Dux, R., Fuchs, J. C., Fischer, R., Geiger, B., Giannone, L., Herrmann, A., Lunt, T., Mertens, V., McDermott, R. M., et al. (2010). Divertor power load feedback with nitrogen seeding in ASDEX Upgrade. *Plasma Physics and Controlled Fusion* **52** (5), 055002. DOI: `10.1088/0741-3335/52/5/055002`.

Kallenbach, A., Balden, M., Dux, R., Eich, T., Giroud, C., Huber, A., Maddison, G. P., Mayer, M., McCormick, K., Neu, R., et al. (2011). Plasma surface interactions in impurity seeded plasmas. *Journal of Nuclear Materials* **415** (1, Supplement). S19–S26. DOI: `https://doi.org/10.1016/j.jnucmat.2010.11.105`.

Kallenbach, A., Bernert, M., David, P., Dunne, M. G., Dux, R., Fable, E., Fischer, R., Gil, L., Görler, T., Janky, F., et al. (2020). Developments towards an ELM-free pedestal radiative cooling scenario using noble gas seeding in ASDEX Upgrade. *Nuclear Fusion* **61** (1), 016002. DOI: `10.1088/1741-4326/abbba0`.

Kallenbach, A., Bernert, M., Eich, T., Fuchs, J. C., Giannone, L., Herrmann, A., Schweinzer, J., Treutterer, W., and the ASDEX Upgrade Team (2012). Optimized tokamak power exhaust with double radiative feedback in ASDEX Upgrade. *Nuclear Fusion* **52** (12), 122003. DOI: `10.1088/0029-5515/52/12/122003`.

Kallenbach, A., Dux, R., Henderson, S. S., Tantos, C., Bernert, M., Day, C., McDermott, R. M., Rohde, V., Zito, A., and the ASDEX Upgrade Team (2024). Divertor enrichment of recycling impurity species (He, N2, Ne, Ar, Kr) in ASDEX Upgrade H-modes. *Nuclear Fusion* **64** (5), 056003. DOI: `10.1088/1741-4326/ad3139`.

Kallenbach, A., Lang, P. T., Bernert, M., Dux, R., Eberl, T., Gleiter, T., McDermott, R. M., Piccinni, C., Ploeckl, B., Rohde, V., et al. (2022). Argon doped pellets for fast and efficient radiative power removal in ASDEX Upgrade. *Nuclear Fusion* **62** (10), 106013. DOI: `10.1088/1741-4326/ac888a`.

Kappatou, A., McDermott, R. M., Pütterich, T., Dux, R., Geiger, B., Jaspers, R. J. E., Donné, A. J. H., Viezzer, E., and and, M. C. (2018). A forward model for the helium plume effect and the interpretation of helium charge exchange measurements at ASDEX Upgrade. *Plasma Physics and Controlled Fusion* **60** (5), 055006. DOI: `10.1088/1361-6587/aab25a`.

Kirk, A., Asakura, N., Boedo, J. A., Beurskens, M., Counsell, G. F., Eich, T., Fundamenski, W., Herrmann, A., Kamada, Y., Leonard, A. W., et al. (2008). Comparison of the spatial and temporal structure of type-I ELMs. *Journal of Physics: Conference Series* **123** (1), 012011. DOI: `10.1088/1742-6596/123/1/012011`.

Knuth, K. H., Habeck, M., Malakar, N. K., Mubeen, A. M., and Placek, B. (2015). Bayesian evidence and model selection. *Digital Signal Processing* **47**. 50–67. DOI: `https://doi.org/10.1016/j.dsp.2015.06.012`.

Korving, S. Q., Mitterauer, V., Huijsmans, G. T. A., Loarte, A., Hoelzl, M., the JOREK Team, and the ASDEX Upgrade Team (2024). Simulation of neoclassical heavy impurity transport in ASDEX Upgrade with applied 3D magnetic fields using the nonlinear MHD code JOREK. *Physics of Plasmas* **31** (5), 052504. DOI: `10.1063/5.0198299`.

Kramer, G. J., Bortolon, A., Diallo, A., and Maingi, R. (2024). The formation of an radial edge electric field due to finite ion orbit width effects is the possible root cause of the H-mode edge. *Nuclear Fusion* **64** (10), 106035. DOI: `10.1088/1741-4326/ad7275`.

Krasheninnikov, S. I. and Kukushkin, A. S. (2017). Physics of ultimate detachment of a tokamak divertor plasma. *Journal of Plasma Physics* **83** (5), 155830501. DOI: `10.1017/S0022377817000654`.

Kuang, A. Q., Cao, N. M., Creely, A., Dennett, C., Hecla, J., Labombard, B., Tinguely, R., Tolman, E., Hoffman, H., Major, M., et al. (2018). Conceptual design study for heat exhaust management in the ARC fusion pilot plant. *Fusion Engineering and Design* **137**, 221–242. DOI: `10.1016/j.fusengdes.2018.09.007`.

Kukushkin, A. S., Pacher, H. D., Pacher, G. W., Kotov, V., Pitts, R. A., and Reiter, D. (2013). Impact of potential narrow SOL heat flux on H-mode access in ITER. *Nuclear Fusion* **53** (12), 123024. DOI: `10.1088/0029-5515/53/12/123024`.

Kurzan, B. and Murmann, H. D. (2011). Edge and core Thomson scattering systems and their calibration on the ASDEX Upgrade tokamak. *Review of Scientific Instruments* **82** (10), 103501. DOI: `10.1063/1.3643771`.

Labit, B., Eich, T., Harrer, G. F., Wolfrum, E., Bernert, M., Dunne, M. G., Frassinetti, L., Hennequin, P., Maurizio, R., Merle, A., et al. (2019). Dependence on plasma shape and plasma fueling for small edge-localized mode regimes in TCV and ASDEX Upgrade. *Nuclear Fusion* **59** (8), 086020. DOI: `10.1088/1741-4326/ab2211`.

LaBombard, B. (2001). *KN1D: A 1-D Space, 2-D Velocity, Kinetic Transport Algorithm for Atomic and Molecular Hydrogen in an Ionizing Plasma.* PSFC-RR-01-3.

Lang, P. T., Baylor, L. R., Day, C., Dux, R., McDermott, R. M., Giegerich, T., Gleiter, T., Kallenbach, A., Ploeckl, B., Rohde, V., et al. (2023). Admixed pellets for fast and efficient delivery of plasma enhancement gases: Investigations at AUG exploring the option for EU-DEMO. *Fusion Engineering and Design* **196**, 114020. DOI: `https://doi.org/10.1016/j.fusengdes.2023.114020`.

Lang, P. T., Conway, G. D., Eich, T., Fattorini, L., Gruber, O., Günter, S., Horton, L. D., Kalvin, S., Kallenbach, A., Kaufmann, M., et al. (2004). ELM pace making and mitigation by pellet injection in ASDEX Upgrade. *Nuclear Fusion* **44** (5), 665. DOI: `10.1088/0029-5515/44/5/010`.

Lebschy, A. (2014). “Electron density reconstruction using beam emission spectroscopy on a heating beam – A feasibility study”. Master Thesis. Ludwig Maximilians Universität München.

Lennholm, M., McKean, R., Mooney, R., Tvalashvili, G., Artaserse, G., Baruzzo, M., Belonohy, E., Calabro, G., Carvalho, I. S., Challis, C. D., et al. (2021). Statistical assessment of ELM triggering by pellets on JET. *Nuclear Fusion* **61** (3), 036035. DOI: `10.1088/1741-4326/abd861`.

Linder, O., Fable, E., Jenko, F., Papp, G., Pautasso, G., the ASDEX Upgrade Team, and the EUROfusion MST1 Team (2020). Self-consistent modeling of runaway electron generation in massive gas injection scenarios in ASDEX Upgrade. *Nuclear Fusion* **60** (9), 096031. DOI: `10.1088/1741-4326/ab9dcf`.

Loarte, A., Huijsmans, G., Futatani, S., Baylor, L. R., Evans, T. E., Orlov, D. M., Schmitz, O., Becoulet, M., Cahyna, P., Gribov, Y., et al. (2014). Progress on the application of ELM control schemes to ITER scenarios from the non-active phase to DT operation. *Nuclear Fusion* **54** (3), 033007. DOI: `10.1088/0029-5515/54/3/033007`.

Loarte, A., Pitts, R. A., Wauters, T., Nunes, I., Köchl, F., Polevoi, A. R., Kim, S.-H., Lehnen, M., Artola, J., Chen, L., et al. (2024). *Initial evaluations in support of the new ITER baseline and Research Plan.* Tech. rep. ITER Organization. URL: `https://www.iter.org/technical-reports?id=25`.

Lunt, T., Bernert, M., Brida, D., David, P., Faitsch, M., Pan, O., Stieglitz, D., Stroth, U., and Redl, A. (2023). Compact Radiative Divertor Experiments at ASDEX Upgrade and Their Consequences for a Reactor. *Phys. Rev. Lett.* **130** (14), 145102. DOI: `10.1103/PhysRevLett.130.145102`.

Makarov, S. O., Coster, D. P., Gleiter, T., Brida, D., Muraca, M., Dux, R., David, P., Kurzan, B., Bonnin, X., O'Mullane, M., et al. (2024). First SOLPS-ITER simulations of ASDEX Upgrade partially detached H-mode with boron impurity: The missing radiation at the outer strike-point region. *Contributions to Plasma Physics* **64** (7-8), e202300139. DOI: `https://doi.org/10.1002/ctpp.202300139`.

Manz, P., Eich, T., Grover, O., and ASDEX Upgrade Team, the (2023). The power dependence of the maximum achievable H-mode and (disruptive) L-mode separatrix density in ASDEX Upgrade. *Nuclear Fusion* **63** (7), 076026. DOI: `10.1088/1741-4326/acd9db`.

Manz, P. (2018). "The Microscopic Picture of Plasma Edge Turbulence". Habilitation. Technische Universität München.

Marinoni, A., Sauter, O., and Coda, S. (2021). A brief history of negative triangularity tokamak plasmas. *Reviews of Modern Plasma Physics* **5** (6), 115001. DOI: `10.1007/s41614-021-00054-0`.

Marmar, E., Boivin, R. L., Fiore, C. L., Goetz, J. A., Granetz, R., Greenwald, M., Hubbard, A. E., Hughes, J., Hutchinson, I. H., Irby, J., et al. (2000). Enhanced D-Alpha H-mode Studies in the Alcator C-Mod Tokamak. *International Atomic Energy Agency (IAEA), IAEA-CN-77/EX2/5.* URL: `https://www-pub.iaea.org/mtcd/publications/pdf/csp_008c/pdf/ex2_5.pdf`.

Martin, Y. R., Takizuka, T., and the ITPA CDBM H-mode Threshold Database Working Group (2008). Power requirement for accessing the H-mode in ITER. *Journal of Physics: Conference Series* **123** (1), 012033. DOI: `10.1088/1742-6596/123/1/012033`.

Matthews, G. F. (1995). Plasma detachment from divertor targets and limiters. *Journal of Nuclear Materials* **220-222**. 104–116. DOI: `https://doi.org/10.1016/0022-3115(94)00450-1`.

Mattioli, M., Mazzitelli, G., Finkenthal, M., Mazzotta, P., Fournier, K. B., Kaastra, J., and Puiatti, M. E. (2007). Updating of ionization data for ionization balance evaluations of atoms and ions for the elements hydrogen to germanium. *Journal of Physics B: Atomic, Molecular and Optical Physics* **40** (18), 3569. DOI: `10.1088/0953-4075/40/18/002`.

McCarthy, P. J. (1999). Analytical solutions to the Grad–Shafranov equation for tokamak equilibrium with dissimilar source functions. *Physics of Plasmas* **6** (9), 3554–3560. DOI: `10.1063/1.873630`.

McCarthy, P. J., Martin, P., and Schneider, W. (1999). *The CLISTE Interpretive Equilibrium Code.* Max-Planck-Institut für Plasmaphysik (IPP 5/85). URL: `https://hdl.handle.net/11858/00-001M-0000-0027-6025-9`.

McDermott, R. M., Dux, R., Guzman, F., Pütterich, T., Fischer, R., Kappatou, A., and the ASDEX Upgrade Team (2020). Development of Ar+16 charge exchange recombination spectroscopy measurements at ASDEX Upgrade. *Nuclear Fusion* **61** (1), 016019. DOI: `10.1088/1741-4326/abc07f`.

McDermott, R. M., Dux, R., Pütterich, T., Geiger, B., Kappatou, A., Lebschy, A., Bruhn, C., Cavedon, M., Frank, A., Harder, N. den, et al. (2018). Evaluation of impurity densities from charge exchange recombination spectroscopy measurements at ASDEX Upgrade. *Plasma Physics and Controlled Fusion* **60** (9), 095007. DOI: `10.1088/1361-6587/aad256`.

McDermott, R. M., Angioni, C., Cavedon, M., Kappatou, A., Dux, R., Fischer, R., Manas, P., and the ASDEX Upgrade Team (2021). Validation of low-Z impurity transport theory using boron perturbation experiments at ASDEX upgrade. *Nuclear Fusion* **62** (2), 026006. DOI: `10.1088/1741-4326/ac3cd9`.

Meneghini, O., Smith, S. P., Lao, L. L., Izacard, O., Ren, Q., Park, J. M., Candy, J., Wang, Z., Luna, C. J., Izzo, V. A., et al. (2015). Integrated modeling applications for tokamak experiments with OMFIT. *Nuclear Fusion* **55** (8), 083008. DOI: `10.1088/0029-5515/55/8/083008`.

Meneghini, O. and Lao, L. (2013). Integrated Modeling of Tokamak Experiments with OMFIT. *Plasma and Fusion Research* **8**, 2403009.

Michels, D., Stegmeir, A., Ulbl, P., Jarema, D., and Jenko, F. (2021). GENE-X: A full-f gyrokinetic turbulence code based on the flux-coordinate independent approach. *Computer Physics Communications* **264**, 107986. DOI: `https://doi.org/10.1016/j.cpc.2021.107986`.

`MultiNest` Github Repository (2024). `https://github.com/farhanferoz/MultiNest` [Accessed: 17th of November 2024].

Murmann, H., Götsch, S., Röhr, H., Salzmann, H., and Steuer, K. H. (1992). The Thomson scattering systems of the ASDEX upgrade tokamak. *Review of Scientific Instruments* **63** (10), 4941–4943. DOI: `10.1063/1.1143504`.

`NEO` homepage (2024). `https://gafusion.github.io/doc/neo.html` [Accessed: 17th of November 2024].

Neu, R., Kallenbach, A., Balden, M., Bobkov, V., Coenen, J. W., Drube, R., Dux, R., Greuner, H., Herrmann, A., Hobirk, J., et al. (2013). Overview on plasma operation with a full tungsten wall in ASDEX Upgrade. *Journal of Nuclear Materials* **438**. S34–S41. DOI: `https://doi.org/10.1016/j.jnucmat.2013.01.006`.

Nishizawa, T., Dux, R., McDermott, R. M., Sciortino, F., Cavedon, M., Schuster, C., Wolfrum, E., Toussaint, U. von, Jansen Van Vuuren, A., Cruz-Zabala, D. J., et al. (2022). Nonparametric inference of impurity transport coefficients in the ASDEX Upgrade tokamak. *Nuclear Fusion* **62** (7), 076021. DOI: `10.1088/1741-4326/ac60e8`.

Odstrčil, T., Pütterich, T., Angioni, C., Bilato, R., Gude, A., Odstrčil, M., the ASDEX Upgrade Team, and the EUROfusion MST1 Team (2017). The physics of W transport illuminated by recent progress in W density diagnostics at ASDEX Upgrade. *Plasma Physics and Controlled Fusion* **60** (1), 014003. DOI: `10.1088/1361-6587/aa8690`.

Odstrčil, T., Howard, N. T., Sciortino, F., Chrystal, C., Holland, C., Hollmann, E., McKee, G., Thome, K. E., and Wilks, T. M. (2020). Dependence of the impurity transport on the dominant turbulent regime in ELM-y H-mode discharges on the DIII-D tokamak. *Physics of Plasmas* **27** (8), 082503. DOI: `10.1063/5.0010725`.

`OMFIT` Website (2024). `https://omfit.io/` [Accessed: 31st of October 2024].

Oost, G. van, ed. (2023). *Fundamentals of Magnetic Fusion Technology.* 1st edition. International Atomic Energy Agency (IAEA).

OPEN ADAS (2024). `https://open.adas.ac.uk/` [Accessed: 19th of August 2024].

Pedersen, T. S., Granetz, R. S., Hubbard, A. E., Hutchinson, I. H., Marmar, E. S., Rice, J. E., and Terry, J. (2000). Radial impurity transport in the H mode transport barrier region in Alcator C-Mod. *Nuclear Fusion* **40** (10), 1795. DOI: `10.1088/0029-5515/40/10/310`.

Peeters, A. G. (2000). Reduced charge state equations that describe Pfirsch Schlüter impurity transport in tokamak plasma. *Physics of Plasmas* **7** (1), 268–275. DOI: `10.1063/1.873812`.

Pitts, R. (2024). Private communication, IPP E2/E2M Seminar at Kloster Seeon, 18th–20th of March 2024.

Plank, U., Brida, D., Conway, G. D., Happel, T., Hubbard, A. E., Pütterich, T., Angioni, C., Cavedon, M., Dux, R., Eich, T., et al. (2023). Experimental study of the edge radial electric field in different drift configurations and its role in the access to H-mode at ASDEX Upgrade. *Physics of Plasmas* **30** (4), 042513. DOI: `10.1063/5.0102763`.

Plassche, K. L. van de, Citrin, J., Bourdelle, C., Camenen, Y., Casson, F. J., Dagnelie, V. I., Felici, F., Ho, A., Van Mulders, S., and Contributors, J. (2020). Fast modeling of turbulent transport in fusion plasmas using neural networks. *Physics of Plasmas* **27** (2), 022310. DOI: `10.1063/1.5134126`.

Pütterich, T., Dux, R., Janzer, M. A., McDermott, R. M., and the ASDEX Upgrade Team (2011). ELM flushing and impurity transport in the H-mode edge barrier in ASDEX Upgrade. *Journal of Nuclear Materials* **415** (1, Supplement). S334–S339. DOI: `https://doi.org/10.1016/j.jnucmat.2010.09.052`.

Pütterich, T., Fable, E., Dux, R., O'Mullane, M., Neu, R., and Siccinio, M. (2019). Determination of the tolerable impurity concentrations in a fusion reactor using a consistent set of cooling factors. *Nuclear Fusion* **59** (5), 056013. DOI: `10.1088/1741-4326/ab0384`.

Radovanovic, L., Dunne, M. G., Wolfrum, E., Harrer, G. F., Faitsch, M., Fischer, R., Aumayr, F., the ASDEX Upgrade Team, and the EUROfusion MST1 Team (2022). Developing a physics understanding of the quasi-continuous exhaust regime: pedestal profile and ballooning stability analysis. *Nuclear Fusion* **62** (8), 086004. DOI: `10.1088/1741-4326/ac6d6a`.

Rathgeber, S. K., Barrera, L., Eich, T., Fischer, R., Nold, B., Suttrop, W., Willensdorfer, M., Wolfrum, E., and the ASDEX Upgrade Team (2012). Estimation of edge electron temperature profiles via forward modelling of the electron cyclotron radiation transport at ASDEX Upgrade. *Plasma Physics and Controlled Fusion* **55** (2), 025004. DOI: `10.1088/0741-3335/55/2/025004`.

Rathgeber, S. K., Fischer, R., Fietz, S., Hobirk, J., Kallenbach, A., Meister, H., Pütterich, T., Ryter, F., Tardini, G., Wolfrum, E., et al. (2010). Estimation of profiles of the effective ion charge at ASDEX Upgrade with Integrated Data Analysis. *Plasma Physics and Controlled Fusion* **52** (9), 095008. DOI: `10.1088/0741-3335/52/9/095008`.

Rodriguez-Fernandez, P., Creely, A. J., Greenwald, M. J., Brunner, D., Ballinger, S. B., Chrobak, C. P., Garnier, D. T., Granetz, R., Hartwig, Z. S., Howard, N. T., et al. (2022). Overview of the SPARC physics basis towards the exploration of burning-plasma regimes in high-field, compact tokamaks. *Nuclear Fusion* **62** (4), 042003. DOI: `10.1088/1741-4326/ac1654`.

Rosenthal, A. M., Hughes, J. W., Laggner, F. M., Odstrčil, T., Bortolon, A., Wilks, T. M., and Sciortino, F. (2023). Inference of main ion particle transport coefficients with experimentally constrained neutral ionization during edge localized mode recovery on DIII-D. *Nuclear Fusion* **63** (4), 042002. DOI: `10.1088/1741-4326/acb95a`.

Ryan, D. P., Dunlap, M. K., Gelfand, M. P., Werner, J. H., Van Orden, A. K., and Goodwin, P. M. (2021). A gain series method for accurate EMCCD calibration. *Scientific Reports* **11**, 18348. DOI: `10.1038/s41598-021-97759-6`.

Ryter, F., Fischer, R., Fuchs, J. C., Happel, T., McDermott, R. M., Viezzer, E., Wolfrum, E., Barrera Orte, L., Bernert, M., Burckhart, A., et al. (2016). I-mode studies at ASDEX

Upgrade: L-I and I-H transitions, pedestal and confinement properties. *Nuclear Fusion* **57** (1), 016004. DOI: `10.1088/0029-5515/57/1/016004`.

Ryter, F., Orte, L. B., Kurzan, B., McDermott, R. M., Tardini, G., Viezzer, E., Bernert, M., Fischer, R., and the ASDEX Upgrade Team (2014). Experimental evidence for the key role of the ion heat channel in the physics of the L–H transition. *Nuclear Fusion* **54** (8), 083003. DOI: `10.1088/0029-5515/54/8/083003`.

Salmon, N. A. (1994). First electron temperature edge measurements on the asdex upgrade tokamak using a heterodyne radiometer. *International Journal of Infrared and Millimeter Waves* **15** (1), 53–60. DOI: `10.1007/BF02265876`.

Schmidtmayr, M., Hughes, J. W., Ryter, F., Wolfrum, E., Cao, N., Creely, A. J., Howard, N., Hubbard, A. E., Lin, Y., Reinke, M. L., et al. (2018). Investigation of the critical edge ion heat flux for L-H transitions in Alcator C-Mod and its dependence on B_T. *Nuclear Fusion* **58** (5), 056003. DOI: `10.1088/1741-4326/aaaed0`.

Schweinzer, J., Wolfrum, E., Aumayr, F., Pockl, M., Winter, H., Schorn, R. P., Hintz, E., and Unterreiter, A. (1992). Reconstruction of plasma edge density profiles from Li I (2s-2p) emission profiles. *Plasma Physics and Controlled Fusion* **34** (7), 1173. DOI: `10.1088/0741-3335/34/7/001`.

Sciortino, F., Howard, N. T., Odstrčil, T., Austin, M., Bykov, I., Chrystal, C., Haskey, S. R., Lore, J. D., Marinoni, A., Marmar, E. S., et al. (2022). Investigation of core impurity transport in DIII-D diverted negative triangularity plasmas. *Plasma Physics and Controlled Fusion* **64** (12), 124002. DOI: `10.1088/1361-6587/ac94f6`.

Sciortino, F., Odstrčil, T., Cavallaro, A., Smith, S. P., Meneghini, O., Reksoatmodjo, R., Linder, O., Lore, J. D., Howard, N. T., Marmar, E. S., et al. (2021a). Modeling of particle transport, neutrals and radiation in magnetically-confined plasmas with Aurora. *Plasma Physics and Controlled Fusion* **63** (11), 112001. DOI: `10.1088/1361-6587/ac2890`.

Sciortino, F., Howard, N. T., Marmar, E. S., Odstrcil, T., Cao, N. M., Dux, R., Hubbard, A. E., Hughes, J. W., Irby, J. H., Marzouk, Y. M., et al. (2020). Inference of experimental radial impurity transport on Alcator C-Mod: Bayesian parameter estimation and model selection. *Nuclear Fusion* **60** (12), 126014. DOI: `10.1088/1741-4326/abae85`.

Sciortino, F., Howard, N. T., Reksoatmodjo, R., Foster, A. R., Hughes, J. W., Marmar, E. S., Miller, M. A., Mordijck, S., Odstrčil, T., Pütterich, T., et al. (2021b). Experimental inference of neutral and impurity transport in Alcator C-Mod using high-resolution x-ray and ultra-violet spectra. *Nuclear Fusion* **61** (12), 126060. DOI: `10.1088/1741-4326/ac32f2`.

Sciortino, F. (2020). *Aurora Documentation, Release 1.0.0.*

Sciortino, F. (2021). "Experimental Inference of Particle Transport in Tokamak Plasmas". Dissertation. Massachusetts Institute of Technology.

Sertoli, M., Angioni, C., Dux, R., Neu, R., Pütterich, T., Igochine, V., and the ASDEX Upgrade Team (2011). Local effects of ECRH on argon transport in L-mode discharges at ASDEX Upgrade. *Plasma Physics and Controlled Fusion* **53** (3), 035024. DOI: `10.1088/0741-3335/53/3/035024`.

Sertoli, M., Angioni, C., Odstrcil, T., the ASDEX Upgrade Team, and the EUROFusion MST1 Team (2017). Parametric dependencies of the experimental tungsten transport coefficients in ICRH and ECRH assisted ASDEX Upgrade H-modes. *Physics of Plasmas* **24** (11), 112503. DOI: `10.1063/1.4996412`.

Silvagni, D., Eich, T., Happel, T., Harrer, G. F., Griener, M., Dunne, M., Cavedon, M., Faitsch, M., Gil, L., Nille, D., et al. (2020). I-mode pedestal relaxation events at ASDEX Upgrade. *Nuclear Fusion* **60** (12), 126028. DOI: `10.1088/1741-4326/abb423`.

Sivia, D. S. and Skilling, J. (2006). *Data Analysis – A Bayesian Tutorial.* 2nd edition. Oxford University Press.

Skilling, J. (2004). Nested Sampling. *AIP Conference Proceedings* **735** (1), 395–405. DOI: `10.1063/1.1835238`.

Skilling, J. (2006). Nested sampling for general Bayesian computation. *Bayesian Analysis* **1** (4), 833–859. DOI: `10.1214/06-BA127`.

Snyder, P. B., Groebner, R. J., Hughes, J. W., Osborne, T. H., Beurskens, M., Leonard, A. W., Wilson, H. R., and Xu, X. Q. (2011). A first-principles predictive model of the pedestal height and width: development, testing and ITER optimization with the EPED model. *Nuclear Fusion* **51** (10), 103016. DOI: `10.1088/0029-5515/51/10/103016`.

Snyder, P. B., Groebner, R. J., Leonard, A. W., Osborne, T. H., and Wilson, H. R. (2009). Development and validation of a predictive model for the pedestal height. *Physics of Plasmas* **16** (5), 056118. DOI: `10.1063/1.3122146`.

Sorbom, B. N., Ball, J., Palmer, T. R., Mangiarotti, F. J., Sierchio, J. M., Bonoli, P., Kasten, C., Sutherland, D. A., Barnard, H. S., Haakonsen, C. B., et al. (2015). ARC: A compact, high-field, fusion nuclear science facility and demonstration power plant with demountable magnets. *Fusion Engineering and Design* **100**, 378–405. DOI: `https://doi.org/10.1016/j.fusengdes.2015.07.008`.

Staebler, G., Bourdelle, C., Citrin, J., and Waltz, R. (2024). Quasilinear theory and modelling of gyrokinetic turbulent transport in tokamaks. *Nuclear Fusion* **64** (10), 103001. DOI: `10.1088/1741-4326/ad6ba5`.

Stegmeir, A., Ross, A., Body, T., Francisquez, M., Zholobenko, W., Coster, D., Maj, O., Manz, P., Jenko, F., Rogers, B. N., et al. (2019). Global turbulence simulations of the tokamak edge region with GRILLIX. *Physics of Plasmas* **26** (5), 052517. DOI: `10.1063/1.5089864`.

Strait, E. J., Barr, J. L., Baruzzo, M., Berkery, J. W., Buttery, R. J., Vries, P. C. de, Eidietis, N. W., Granetz, R. S., Hanson, J. M., Holcomb, C. T., et al. (2019). Progress in disruption prevention for ITER. *Nuclear Fusion* **59** (11), 112012. DOI: `10.1088/1741-4326/ab15de`.

Stroth, U. (2022). Progress from ASDEX Upgrade experiments in preparing the physics basis of ITER operation and DEMO scenario development. *Nuclear Fusion* **62** (4), 042006. DOI: `10.1088/1741-4326/ac207f`.

Stroth, U., Bernert, M., Brida, D., Cavedon, M., Dux, R., Huett, E., Lunt, T., Pan, O., Wischmeier, M., and the ASDEX Upgrade Team (2022). Model for access and stability of the X-point radiator and the threshold for marfes in tokamak plasmas. *Nuclear Fusion* **62** (7), 076008. DOI: `10.1088/1741-4326/ac613a`.

Stroth, U. (2018). *Plasmaphysik. Phänomene, Grundlagen und Anwendungen.* 2nd edition. Springer Spektrum Berlin, Heidelberg.

Summers, H. P. (2004). *The ADAS User Manual, version 2.6.* URL: `http://www.adas.ac.uk`.

Suttrop, W., Maraschek, M., Conway, G. D., Fahrbach, H.-U., Haas, G., Horton, L. D., Kurki-Suonio, T., Lasnier, C. J., Leonard, A. W., Maggi, C. F., et al. (2003). ELM-free stationary H-mode plasmas in the ASDEX Upgrade tokamak. *Plasma Physics and Controlled Fusion* **45** (8), 1399. DOI: `10.1088/0741-3335/45/8/302`.

Toussaint, U. von (2011). Bayesian inference in physics. *Rev. Mod. Phys.* **83** (3), 943–999. DOI: `10.1103/RevModPhys.83.943`.

`UltraNest` Documentation (2024). `https://johannesbuchner.github.io/UltraNest` [Accessed: 4th of December 2024].

van Vugt, D. C., Huijsmans, G. T. A., Hoelzl, M., Loarte, A., the ASDEX Upgrade Team, and the EUROfusion MST1 Team (2019). Kinetic modeling of ELM-induced tungsten transport in a tokamak plasma. *Physics of Plasmas* **26** (4), 042508. DOI: `10.1063/1.5092319`.

Victor, B. S., Odstrcil, T., Paz-Soldan, C. A., Grierson, B. A., Hinson, E., Jarvinen, A., Hollmann, E. M., Chrystal, C., Collins, C. S., Thome, K. E., et al. (2020). Impurity transport in the pedestal of H-mode plasmas with resonant magnetic perturbations. *Plasma Physics and Controlled Fusion* **62** (9), 095021. DOI: `10.1088/1361-6587/aba4bd`.

Viezzer, E., Cavedon, M., Cano-Megias, P., Fable, E., Wolfrum, E., Cruz-Zabala, D. J., David, P., Dux, R., Fischer, R., Harrer, G. F., et al. (2020). Dynamics of the pedestal transport during edge localized mode cycles at ASDEX Upgrade. *Plasma Physics and Controlled Fusion* **62** (2), 024009. DOI: `10.1088/1361-6587/ab5b1d`.

Viezzer, E., Pütterich, T., Dux, R., McDermott, R. M., and the ASDEX Upgrade Team (2012). High-resolution charge exchange measurements at ASDEX Upgrade. *Review of Scientific Instruments* **83** (10), 103501. DOI: `10.1063/1.4755810`.

Viezzer, E. (2018). Access and sustainment of naturally ELM-free and small-ELM regimes. *Nuclear Fusion* **58** (11), 115002. DOI: `10.1088/1741-4326/aac222`.

Viezzer, E., Austin, M. E., Bernert, M., Burrell, K. H., Cano-Megias, P., Chen, X., Cruz-Zabala, D. J., Coda, S., Faitsch, M., Février, O., et al. (2023). Prospects of core–edge integrated no-ELM and small-ELM scenarios for future fusion devices. *Nuclear Materials and Energy* **34**, 101308. DOI: `https://doi.org/10.1016/j.nme.2022.101308`.

Viezzer, E., Fable, E., Cavedon, M., Angioni, C., Dux, R., Laggner, F. M., Bernert, M., Burckhart, A., McDermott, R. M., Pütterich, T., et al. (2016). Investigation of inter-ELM ion heat transport in the H-mode pedestal of ASDEX Upgrade plasmas. *Nuclear Fusion* **57** (2), 022020. DOI: `10.1088/0029-5515/57/2/022020`.

Viezzer, E., Fable, E., Pütterich, T., Bergmann, A., Cavedon, M., Dux, R., McDermott, R. M., Angioni, C., Churchill, R. M., Dunne, M. G., et al. (2015). Collisionality dependence of edge rotation and in–out impurity asymmetries in ASDEX Upgrade H-mode plasmas. *Nuclear Fusion* **55** (12), 123002. DOI: `10.1088/0029-5515/55/12/123002`.

Viezzer, E., Pütterich, T., Conway, G. D., Dux, R., Happel, T., Fuchs, J. C., McDermott, R. M., Ryter, F., Sieglin, B., Suttrop, W., et al. (2013). High-accuracy characterization of the edge radial electric field at ASDEX Upgrade. *Nuclear Fusion* **53** (5), 053005. DOI: `10.1088/0029-5515/53/5/053005`.

Viezzer, E. (2012). "Radial electric field studies in the plasma edge of ASDEX Upgrade". Dissertation. Ludwig Maximilians Universität München.

Vogel, G., Zhang, H., Shen, Y., Dai, S., Sun, Y., Huang, J., Gu, S., Fu, J., Hu, R., Chen, J., et al. (2021). Experimental and simulation study of impurity transport response to RMPs in RF-heated H-mode plasmas at EAST. *Journal of Plasma Physics* **87** (2), 905870213. DOI: `10.1017/S0022377821000222`.

Wagner, F., Becker, G., Behringer, K., Campbell, D., Eberhagen, A., Engelhardt, W., Fussmann, G., Gehre, O., Gernhardt, J., v. Gierke, G., et al. (1982). Regime of Improved Confinement and High Beta in Neutral-Beam-Heated Divertor Discharges of the ASDEX Tokamak. *Phys. Rev. Lett.* **49** (19), 1408–1412. DOI: `10.1103/PhysRevLett.49.1408`.

Wesson, J. (2011). *Tokamaks.* 4th edition. Vol. 149. International Series of Monographs on Physics. Oxford University Press.

Whyte, D. G., Hubbard, A. E., Hughes, J. W., Lipschultz, B., Rice, J. E., Marmar, E. S., Greenwald, M., Cziegler, I., Dominguez, A., Golfinopoulos, T., et al. (2010). I-mode: an H-mode energy confinement regime with L-mode particle transport in Alcator C-Mod. *Nuclear Fusion* **50** (10), 105005. DOI: `10.1088/0029-5515/50/10/105005`.

Wilcox, R. S., Baylor, L. R., Bortolon, A., Knolker, M., Lasnier, C. J., Shiraki, D., Bykov, I., Chrystal, C., Scotti, F., Paz-Soldan, C., et al. (2021). Pellet triggering of edge localized modes in low collisionality pedestals at DIII-D. *Nuclear Fusion* **62** (2), 026017. DOI: `10.1088/1741-4326/ac3b8b`.

Willensdorfer, M., Birkenmeier, G., Fischer, R., Laggner, F. M., Wolfrum, E., Veres, G., Aumayr, F., Carralero, D., Guimarãis, L., Kurzan, B., et al. (2014). Characterization of the Li-BES at ASDEX Upgrade. *Plasma Physics and Controlled Fusion* **56** (2), 025008. DOI: `10.1088/0741-3335/56/2/025008`.

Willensdorfer, M., Mitterauer, V., Hoelzl, M., Suttrop, W., Cianciosa, M., Dunne, M., Fischer, R., Leuthold, N., Puchmayr, J., Samoylov, O., et al. (2024). Observation of magnetic islands in tokamak plasmas during the suppression of edge-localized modes. *Nature Physics* **20**, 1745–2481. DOI: `10.1038/s41567-024-02666-y`.

Wingen, A., Lyons, B. C., Wilcox, R. S., Baylor, L. R., Ferraro, N. M., Jardin, S. C., and Shiraki, D. (2021). Simulation of pellet ELM triggering in low-collisionality, ITER-like discharges. *Nuclear Fusion* **61** (12), 126059. DOI: `10.1088/1741-4326/ac34d7`.

Zholobenko, W., Zhang, K., Stegmeir, A., Pfennig, J., Eder, K., Pitzal, C., Ulbl, P., Griener, M., Radovanovic, L., Plank, U., et al. (2024). Tokamak H-mode edge-SOL global turbulence simulations with an electromagnetic, transcollisional drift-fluid model. arXiv: `2403.10113`.

Zito, A., Wischmeier, M., Kappatou, A., Kallenbach, A., Sciortino, F., Rohde, V., Schmid, K., Hinson, E. T., Schmitz, O., Cavedon, M., et al. (2023). Investigation of helium exhaust dynamics at the ASDEX Upgrade tokamak with full-tungsten wall. *Nuclear Fusion* **63** (9), 096027. DOI: `10.1088/1741-4326/ace26e`.

Zohm, H., Alessi, E., Angioni, C., Arden, N., Artigues, V., Astrain, M., Asunta, O., Balden, M., Bandaru, V., Navarro, A. B., et al. (2024). Overview of ASDEX upgrade results in view of ITER and DEMO. *Nuclear Fusion* **64** (11), 112001. DOI: `10.1088/1741-4326/ad249d`.

Zohm, H. (2014). *Magnetohydrodynamic Stability of Tokamaks.* 1st edition. WILEY-VCH Verlag GmbH & Co.

Zohm, H. (2019). On the size of tokamak fusion power plants. *Philosophical Transactions of the Royal Society A: Mathematical, Physical and Engineering Sciences* **377** (2141), 20170437. DOI: `10.1098/rsta.2017.0437`.

A List of variables, constants and functions

This appendix lists all variables, constants and functions that were introduced in the above text and reused with the same meaning but without repeated explanation in subsequent sections. They are sorted by the section of their first appearance. Few variables are used twice and their meaning must be deduced from the context.

chapter	var./const./func.	physical meaning
1.1	τ_{E}	energy confinement time
	n_{e}	electron density
	Z_{eff}	effective plasma charge, cf. 1.3
	T	temperature (multiplied with the Boltzmann constant)
	I_{p}	plasma current
	ϕ	toroidal angle
	θ	poloidal angle
	q_{s}	safety factor, cf. 1.4
	r	minor radius
	R	major radius
	B_{T}	toroidal magnetic field strength
	B_{P}	poloidal magnetic field strength
	p	kinetic pressure
	$\vec{j}$	plasma current density
	$\vec{B}$	magnetic field
	ψ	poloidal magnetic flux
	ρ_{pol}	normalized radial coordinate, cf. 1.6
	R_0	major radius of the magnetic axis without plasma
	a	half the horizontal diameter of the poloidal vessel cross-section
	B	magnetic field strength
1.2	T_{e}	electron temperature
	T_{i}	ion temperature
1.3	Z	atomic number
		(but also used for atomic charge, i.e., ionization stage)
	$n_{\mathrm{I},Z}$	density of impurity charge stage Z
	t	time
	$\vec{\Gamma}_{\mathrm{I},Z}$	flux density of impurity charge stage Z
	$Q_{\mathrm{I},Z}$	source term of impurity charge stage Z
	r	radial coordinate, constant on a flux surface
	D	flux surface-averaged diffusion transport coefficient
	v	flux surface-averaged convection transport coefficient
	$\Gamma^r_{\mathrm{I},Z}$	radial flux density of impurity charge stage Z
	$n_{\mathrm{I,tot}}$	total impurity density
1.5	$n_{\mathrm{D+}}$	main ion density
2.1.1	$v_{\perp}$	particle velocity component perpendicular to the field lines
	q	particle charge
	m	particle mass
	r_{L}	Larmor radius, cf. 2.1
	ρ^*	ordering parameter, cf. 2.2
	$\vec{E}$	electric field

	$f(\vec{r}, \vec{v})$	particle distribution function in phase space
	$\vec{v}$	particle velocity
	$\vec{r}$	particle position
	n	density of particle species, cf. 2.5
	f_{M}	Maxwellian velocity distribution
	$\vec{u}_{\perp}^{(0)}$	equilibrium velocity, cf. 2.12
	ϵ	local inverse aspect ratio, cf. 2.17
	$\nu_{\mathrm{eff},b}$	effective 90° scattering frequency by collisions with another species, cf. 2.22
	ϵ_0	vacuum permittivity
	m_{red}	reduced mass, cf. 2.23
	ν^*	collisionality, cf. 2.27
2.1.4	r_{vol}	flux surface volume based radial coordinate, cf. 2.53
2.2.1	$\overline{n}$	line-integrated density
	n_{GW}	Greenwald density, cf. 2.56
2.2.2	μ_0	vacuum permeability
	n	toroidal mode number
	κ	elongation, cf. 2.63
	δ_{u}	upper triangularity, cf. 2.64
2.3.1	$\mathcal{P}$	parameters
	$\mathcal{I}$	prior information
	$\mathcal{D}$	data
	$\mathcal{M}$	(forward) model
	χ^2	goodness of fit measure, cf. 2.67
2.3.2	n_{live}	number of live points
	L_i	likelihood of sample at iteration i
	X_i	remaining prior volume at iteration i
3.1.1	$n_{\mathrm{b},n,j}$	density of NBI neutrals in an excitation state with main quantum number n and with a velocity indexed by j
	n	main quantum number
	$\langle \sigma_{\mathrm{CXline},n} u_j \rangle_{\mathrm{eff}}$	effective CX-emission rate coefficient
3.1.3.2	n_{c}	number of counts
3.1.4	R_{aus}	outermost radius on the separatrix
	l	orbital angular momentum quantum number
4.1.2.2	n_{D^0}	thermal neutral D density
	T_{D^0}	thermal neutral D temperature
	$n_{\mathrm{D}^0,\mathrm{sep}}$	n_{D^0} at the separatrix
4.1.2.3	n_{N}	fully stripped N density
4.1.1	W_{MHD}	kinetic stored energy
4.2.2	$\lambda_{\rho_{\mathrm{pol}}}$	radial correlation length

B List of abbreviations

This appendix lists all abbreviations that are used in the above text in alphabetical order.

abbreviation	meaning
AD	Analog-to-Digital
ADAS	Atomic Data and Analysis Structure
Alcator C-Mod	former tokamak of MIT in Cambridge, Massachusetts
Ar	Argon (chemical symbol)
ASDEX	Axially Symmetric Divertor Experiment
AUG	ASDEX Upgrade
BES	Beam Emission Spectroscopy
BP	Banana-Plateau
CAR	short name for core CXRS spectrometer
CCD	charge-coupled device
CER	short name for core CXRS optical head and spectrometer
CL	Classical
CMR	short name for spectrometer
CMR-1, CMR-2, CMR-3	short names for edge CXRS optical heads
CPR	short name for spectrometer (also optical head, but not used here)
CX	Charge-Exchange
CXRS	Charge-Exchange Recombination Spectroscopy
D	Deuterium (chemical symbol)
DIII-D	tokamak of General Atomics in San Diego
DCN	diagnostic name for Deuterium Cyanide laser interferometry
DEMO	Demonstration Power Plant
ECE	diagnostic name for Electron Cyclotron Emission radiometry
ECRH	Electron Cyclotron Resonance Heating
EDA	Enhanced D-Alpha (D_α)
ELM	Edge Localized Mode
EM-gain	Electron-Multiplying gain
ETB	Edge Transport Barrier
FWHM	Full Wdith at Half Maximum
He	Helium (chemical symbol)
HFS	High-Field Side
H-mode	High-confinement regime
ICRF	Ion Cyclotron Resonance Frequency (heating)
IDA	Integrated Data Analysis, also used as diagnostic name
ITER	International Thermonuclear Experimental Reactor
ITG	Ion Temperature Gradient
JET	Joint European Torus
KBM	Kinetic Ballooning Mode
LBO	Laser Blow-Off
LFS	Low-Field Side
L-mode	Low-confinement regime
LOS	Line Of Sight
MAP	Maximum A Posteriori

MCMC	Markov Chain Monte Carlo
MHD	Magnetohydrodynamic
MXH	Miller Extended Harmonic
N	Nitrogen (chemical symbol)
Ne	Neon (chemical symbol)
NBI	Neutral Beam Injection
O	Oxygen (chemical symbol)
PFC	Plasma Facing Component
PS	Pfirsch-Schlüter
QCE	Quasi-Continuous Exhaust
ROI	Region of Interest
RMP	Resonant Magnetic Perturbation
SOL	Scrape-Off Layer
SXR	Soft X-Ray
TSC	Temperature Screening Coefficient
VTC	diagnostic name for Vertical Thomson scattering in the Core
VTE	diagnostic name Vertical Thomson scattering in the Edge
VUV	Vacuum Ultraviolet
W	Tungsten (chemical symbol)
XPR	X-Point Radiator

Acknowledgements

This thesis would not have been possible without the help and support of many people. Therefore, I would like to take this opportunity to thank all of them!

First of all, I want to express my sincere thanks to my supervisor **Ralph Dux**. I am very grateful for the considerable amount of time you have invested in introducing me to fusion plasma physics, spectroscopy, and impurity transport, and in guiding me through the initial stages of this thesis. Your ideas and your experimental expertise have crucially contributed to this work, and you have helped me a lot with your profound answers to any questions and with the fast and detailed proofreading of this thesis. I also appreciate the freedom you gave me to explore Bayesian data analysis methods, and the continuous support on my way to the final results.

Moreover, my academic supervisor **Ulrich Stroth** deserves a big thank you for our regular discussions and for his pragmatic suggestions, which helped me to complete this thesis. A special thank you also goes to **Rachael McDermott** for her genuine interest in my work, for encouraging me to become involved in the international research community, and for the flexibility in extending my contract as my department head. Further, I would like to thank **Hartmut Zohm** for his efforts to find a PhD position for me at IPP and for the interesting lectures on MHD.

I would like to extend my heartfelt thanks to **Francesco Sciortino** for motivating me to pursue Bayesian data analysis, for introducing me to previous work in the field and in particular to the `OMFIT ImpRad` module, and for his spirit of encouragement, inspiration, and dedication. My gratitude also goes to **Tomáš Odstrčil** for generously sharing his insights on experimental impurity transport inference and Bayesian methods, and especially for the detailed review of parts of my code. The development of the Bayesian framework was furthermore supported by valuable advice from **Johannes Buchner**, for which I am grateful.

For any diagnostic issues and beyond, I could always rely on the helping hands of all other spectroscopists and CXRS operators. So I want to say a big thank you to **Pilar Cano Megias**, **Marco Cavedon**, **Ralph Dux**, **Athina Kappatou**, **Hannah Lindl**, **Rachael McDermott**, **Ulrike Plank**, **Lidija Radovanovic**, **Roxána Takács**, **Benedikt Zimmermann**, and the Seville group, in particular **Diego Cruz Zabala**, **Kiera McKay**, **Julia Perez Gonzalez**, and **Eleonora Viezzer**. Much of the data analysis presented in this thesis was performed on IPP's TOK cluster. For their support in installing and maintaining the `OMFIT` and `MultiNest` softwares, I am very grateful to the **TOK cluster support team**, especially to **Thomas Hayward-Schneider**.

Many more colleagues deserve my thanks for their help at various stages of this thesis. First and foremost, I am thankful to the entire **AUG team**, and more specifically, without claiming completeness, to **Clemente Angioni**, **Mike Dunne**, **Michael Faitsch**, **Daniel Fajardo**, **Rainer Fischer**, **Michael Griener**, **Georg Harrer**, **Arne Kallenbach**, **Thomas Pütterich**, **Thilo Romba**, **Dirk Stieglitz**, **Giovanni Tardini**, and **Elisabeth Wolfrum** for many discussions and technical support. In addition, it was a pleasure to collaborate with **Matthias Bernert**, **Georg Graßler**, **Peter Lang**, **Sergei Makarov**, **Wolfgang Suttrop**, and **Matthias Wil-**

lensdorfer on several projects during my PhD time whose results are not included in this thesis. I would also like to thank **Lucas Räß** for his passionate work that will complement my thesis results, and for his patience with my limited time budget for supervising his master's thesis during the writing process of this thesis. Finally, I want to say thank you to all the **technical, administrative and IT staff** for their dedicated work, in particular to **Anja Bauer** and **Birgit Perey**.

Life at IPP is very enjoyable thanks to the many great people working here. Above all, I am deeply grateful to my close friends **Magdalena Bauer** and **Jonas Puchmayr**, who are always there to support me with emotional advice or practical help, both inside and outside of IPP. A special thank you also goes to **Benedikt Zimmermann** for his trust and our extended conversations. Moreover, I was lucky to be assigned a desk in the 'PhD office', which made me part of many inspiring and entertaining discussions. The warm atmosphere owes to all those who have had their workplace here over the years or who have been regular guests, but in particular to **Daniel Fajardo**, **Teobaldo Luda di Cortemiglia**, **Andrew Moreau**, **Marco Muraca**, **Maximilian Reisner**, **Oleg Samoylov**, and **Federico Stefanelli**. Thank you all very much for your friendship and your support. Finally, I would also like to express my thanks to all the young colleagues with whom I shared many lunch, coffee, and after-work breaks, especially **Michael Bergmann**, **Manuel Herschel**, **Sebastian Hörmann**, **Lea Hollendonner**, **Joey Kalis**, **Felix Klossek**, **Simon Krumm**, **David Kulla**, **Alessandro Mancini**, **Michaela Mayer**, **Raphael Schramm**, **Christian Schuster**, **Michael Sieben**, **Fabian Solfronk**, **Bojana Stefanoska**, **Beatrice Tosto**, and **Daniel Wendler**. Thanks a lot for the great times we spent together!

Last but not least, I would like to thank those who have not directly contributed to my thesis or my time at IPP, but who have laid the foundations for this work through their personal support. I am sincerely grateful to **Franko Greiner**, who has been encouraging me like a mentor since I was a bachelor's student in his plasma physics group at Kiel University. I feel fortunate to have started my physics career with your guidance, and I am glad that we have been able to keep the contact over the past years as we met at multiple conferences. For even much longer, I can count on the support from my family, in particular my parents, **Elisabeth** and **Hermann**, and my siblings, **Ruben**, **Lion**, and **Celia**, who deserve a very special thank you. Moreover, I want to thank all my friends, especially **Anna**, **Katrin**, **Rebecca**, **Isabel**, **Julia**, **Line**, and **Mika**, who have kept my spirits up during my PhD time. And finally, I would like to express my deepest gratitude to my partner **Jakob**. Thank you for your unwavering support and encouragement throughout all these years – it has been truly invaluable to me!